



Universität Hamburg
DER FORSCHUNG | DER LEHRE | DER BILDUNG

FAKULTÄT
FÜR MATHEMATIK, INFORMATIK
UND NATURWISSENSCHAFTEN

From MHC characterization to screening approaches

Dissertation

with the aim of achieving a doctoral degree at the Faculty of
Mathematics, Informatics and Natural Sciences

Department of Chemistry

University of Hamburg

submitted by

Janine-Denise Kopicki

born in Henstedt-Ulzburg

Hamburg, 2023

Thesis reviewers

Prof. Dr. Charlotte Uetrecht

Leibniz Institute of Virology, Hamburg, Germany; Centre for Structural Systems Biology, Hamburg, Germany; University of Siegen, Siegen, Germany; Deutsches Elektronen-Synchrotron, Hamburg, Germany.

Prof. Dr. Hartmut Schlüter

Institute of Clinical Chemistry and Laboratory Medicine, Section Mass Spectrometry and Proteomics, University Medical Center Hamburg-Eppendorf, Hamburg, Germany.

Prof. Dr. Aneika Leney

School of Biosciences, University of Birmingham, Edgbaston, Birmingham, UK.

Examination board

Prof. Dr. Kay Grünewald

Leibniz Institute of Virology, Hamburg, Germany; Centre for Structural Systems Biology, Hamburg, Germany; Institute of Biochemistry and Molecular Biology, University of Hamburg, Hamburg, Germany.

Prof. Dr. Hartmut Schlüter

Institute of Clinical Chemistry and Laboratory Medicine, Section Mass Spectrometry and Proteomics, University Medical Center Hamburg-Eppendorf, Hamburg, Germany.

Maria Marta Garcia Alai, PhD

European Molecular Biology Laboratory Hamburg, Hamburg, Germany.

Thesis submission

20.03.2023

Thesis defense

16.06.2023



Leibniz-Institut
für Virologie

Leibniz
Leibniz-Gemeinschaft



CSSB
Centre for Structural
Systems Biology



This thesis was prepared from 2017 to 2023 under the supervision of Prof. Dr. Charlotte Uetrecht at the Leibniz Institute of Virology, the Centre for Structural Systems Biology, and the University of Siegen in the working group *Dynamics of Viral Structures*. The second supervisor was Prof. Dr. Kay Grünewald at Leibniz Institute of Virology, Centre for Structural Systems Biology, and the Institute of Biochemistry and Molecular Biology of the University of Hamburg.

Contents	
PUBLICATIONS	1
ABBREVIATIONS	2
LIST OF FIGURES	4
LIST OF TABLES	5
ABSTRACT	6
ZUSAMMENFASSUNG	8
1 INTRODUCTION	10
1.1 STRUCTURAL MASS SPECTROMETRY	10
1.1.1 <i>Native mass spectrometry</i>	12
1.1.1.1 Sample preparation	13
1.1.1.2 Nano-electrospray ionization	14
1.1.1.3 Mass analysis	17
1.1.1.3.1 Quadrupole	19
1.1.1.3.2 Time-of-Flight	20
1.1.1.3.3 Orbitrap™	22
1.1.1.4 Protein structures within the gas phase	23
1.1.1.4.1 Locked up in-solution structures	24
1.1.1.4.2 Protein-ligand interactions	24
1.1.1.4.3 Gas-phase dissociation of protein complexes	25
1.2 IMMUNE REGULATION VIA THE MAJOR HISTOCOMPATIBILITY COMPLEX	28
1.2.1 <i>MHC structure</i>	29
1.2.2 <i>MHC class I</i>	30
1.2.2.1 Peptide binding and editing	31
1.2.2.2 Peptide presentation	33
1.2.3 <i>Identifying epitopes for vaccines and immunotherapy</i>	33
2 OBJECTIVES	35
3 RESULTS AND DISCUSSION	37
3.1 MHC-I HEAVY CHAINS FORM NONCOVALENT DIMERS IN ABSENCE OF β_2M	37
3.1.1 <i>Results</i>	37
3.1.2 <i>Discussion</i>	41
3.2 PEPTIDE-FREE, DISULFIDE-STABILIZED MHC-I MOLECULES	45
3.2.1 <i>Results</i>	45
3.2.2 <i>Discussion</i>	54
3.3 MHC-I PEPTIDE BINDING	58
3.3.1 <i>Results</i>	58
3.3.1.1 Peak intensity in native MS reflects peptide-MHC binding affinity	58
3.3.1.2 Neutralizing the terminal charges of the peptide reduces binding efficiency	65
3.3.1.3 NV9 truncations disclose preferred binding positions in the peptide	67
3.3.1.4 The binding groove may be occupied simultaneously by two short peptides	70
3.3.2 <i>Discussion</i>	73
3.4 ESTABLISHING A HIGH-THROUGHPUT PEPTIDE SCREENING	77
3.4.1 <i>Results</i>	77
3.4.1.1 Charge state 13 ⁺ best resembles in-solution conditions	78
3.4.1.2 Saving time during buffer exchange	80
3.4.1.3 Selecting a suitable mass spectrometer	81
3.4.1.4 Choosing suitable temperature and energy settings	82
3.4.1.5 Choosing the optimal peptide concentration	84
3.4.1.6 Impact of incubation time and ethanol	87
3.4.1.7 Screening low-affinity peptides	89
3.4.1.8 Is resolution the limit?	91
3.4.2 <i>Discussion</i>	93

4	OUTLOOK	98
5	MATERIALS AND METHODS.....	100
5.1	SAMPLE PREPARATION	100
5.1.1	<i>Proteins</i>	100
5.1.1.1	Expression	100
5.1.1.2	Refolding and purification	101
5.1.1.3	Quality control	101
5.1.2	<i>Peptides</i>	102
5.2	NATIVE MASS SPECTROMETRY.....	103
5.2.1	<i>Buffer exchange</i>	103
5.2.2	<i>Instruments and settings</i>	104
5.2.2.1	Pressure settings.....	105
5.2.2.2	Voltage settings	105
5.2.3	<i>Other instrument-specific settings</i>	105
5.2.4	<i>Spectra analysis</i>	106
5.3	DIFFERENTIAL SCANNING FLUORIMETRY.....	107
5.3.1	<i>Thermal stability (nDSF)</i>	107
5.3.2	<i>Binding affinity (iDSF)</i>	107
5.4	MATHEMATICAL METHODS	108
5.4.1	<i>Eliminating nonspecific ESI clustering</i>	108
5.4.2	<i>Calculating affinities</i>	109
5.4.2.1	Calculating $K_{d,high}$	109
5.4.2.2	Calculating $K_{d,low}$	110
5.5	STATISTICS AND REPRODUCIBILITY	112
5.6	DATA VISUALIZATION	113
5.7	DATA AVAILABILITY	114
	REFERENCES	115
	SUPPLEMENT.....	130
	SUPPLEMENTAL FIGURES	130
	SUPPLEMENTAL TABLES.....	132
	EXEMPLARY EXPERIMENTAL FILES	139
	<i>Q-ToF 2</i>	139
	<i>Q Exactive™ UHMR Hybrid Quadrupole Orbitrap™</i>	140
	HAZARDOUS SUBSTANCES ACCORDING TO THE GHS	143
	CONTRIBUTIONS.....	150
	ACKNOWLEDGEMENTS.....	152
	DECLARATION OF AUTHORSHIP EIDESSTATTLICHE VERSICHERUNG.....	154

Publications

Parts of this thesis have been published or are in preparation for publication.

Chapter 1.1 Structural mass spectrometry

Dülfer, J., Kádek, A., **Kopicki, J.-D.**, Krichel, B., & Uetrecht, C. (2019). Structural mass spectrometry goes viral. *Advances in virus research*, 105, 189–238¹.

Chapter 1.2 Immune regulation via the major histocompatibility complex

Anjanappa, R., Garcia-Alai, M., **Kopicki, J.-D.**, Lockhauserbäumer, J., Aboelmagd, M., Hinrichs, J., Nemtanu, I. M., Uetrecht, C., Zacharias, M., Springer, S., & Meijers, R. (2020). Structures of peptide-free and partially loaded MHC class I molecules reveal mechanisms of peptide selection. *Nature communications*, 11(1), 1314².

Dirscherl, C., Löchte, S., Hein, Z., **Kopicki, J.-D.**, Harders, A. R., Linden, N., Karner, A., Preiner, J., Weghuber, J., Garcia-Alai, M., Uetrecht, C., Zacharias, M., Piehler, J., Lanzerstorfer, P., & Springer, S. (2022). Dissociation of β_2m from MHC class I triggers formation of noncovalent transient heavy chain dimers. *Journal of cell science*, 135(9), jcs259489³.

Kopicki, J.-D., Saikia, A., Niebling, S., Günther, C., Anjanappa, R., Garcia-Alai, M., Springer, S., & Uetrecht, C. (2022). Opening opportunities for K_d determination and screening of MHC peptide complexes. *Communications biology*, 5(1), 488⁴.

Chapter 3.1 MHC-I heavy chains form noncovalent dimers in absence of β_2m

Dirscherl, C., Löchte, S., Hein, Z., **Kopicki, J.-D.**, Harders, A. R., Linden, N., Karner, A., Preiner, J., Weghuber, J., Garcia-Alai, M., Uetrecht, C., Zacharias, M., Piehler, J., Lanzerstorfer, P., & Springer, S. (2022). Dissociation of β_2m from MHC class I triggers formation of noncovalent transient heavy chain dimers. *Journal of cell science*, 135(9), jcs259489³.

Chapter 3.2 Peptide-free, disulfide-stabilized MHC-I molecules

Anjanappa, R., Garcia-Alai, M., **Kopicki, J.-D.**, Lockhauserbäumer, J., Aboelmagd, M., Hinrichs, J., Nemtanu, I. M., Uetrecht, C., Zacharias, M., Springer, S., & Meijers, R. (2020). Structures of peptide-free and partially loaded MHC class I molecules reveal mechanisms of peptide selection. *Nature communications*, 11(1), 1314².

Chapter 3.3 MHC-I peptide binding

Kopicki, J.-D., Saikia, A., Niebling, S., Günther, C., Anjanappa, R., Garcia-Alai, M., Springer, S., & Uetrecht, C. (2022). Opening opportunities for K_d determination and screening of MHC peptide complexes. *Communications biology*, 5(1), 488⁴.

Chapter 3.4 Establishing a high-throughput peptide screening

Kopicki, J.-D., Springer, S., & Uetrecht, C. (in preparation).

Other Publications

Holm, T., **Kopicki, J.-D.**, Busch, C., Olschewski, S., Rosenthal, M., Uetrecht, C., Günther, S., & Reindl, S. (2018). Biochemical and structural studies reveal differences and commonalities among cap-snatching endonucleases from segmented negative-strand RNA viruses. *The Journal of biological chemistry*, 293(51), 19686–19698⁵.

Günther, S., Reinke, P. Y. A., Fernández-García, Y., Lieske, J., Lane, T. J., Ginn, H. M., Koua, F. H. M., Ehart, C., Ewert, W., Oberthuer, D., Yefanov, O., Meier, S., Lorenzen, K., Krichel, B., **Kopicki, J.-D.**, Gelisio, L., Brehm, W., Dunkel, I., Seychell, B., Gieseler, H., ... Meents, A. (2021). X-ray screening identifies active site and allosteric inhibitors of SARS-CoV-2 main protease. *Science (New York, N.Y.)*, 372(6542), 642–646⁶.

Abbreviations

°	degree (angle)	K	kelvin
°C	degree Celsius (temperature)	K_a	association constant
1G4	human anti-NY-ESO-1 T cell receptor	K^b	murine MHC-I
A2	HLA-A*02 or HLA-A*02:01	K_d	dissociation constant
A24	HLA-A*24 or HLA-A*24:02	kDa	kilodalton
AC	alternating current	LILRB	leukocyte immunoglobulin-like receptor subfamily B
Ac-	acetylated	m	meter
AUC	area under the curve	m	mass
BEX	buffer exchange	m_H	mass of a proton
CAS	chemical abstract service registry number	M	membrane protein (SARS-CoV-2)
CD4	cluster of differentiation 4	M	molecular weight
CD8	cluster of differentiation 8	M_{exp}	experimental molecular weight
CEM	chain ejection model	M^{pro}	main protease (SARS-CoV-2)
cf.	<i>confer/conferatur</i> , Latin for “compare”	M_{th}	theoretical molecular weight
CID	collision-induced dissociation	m/z	mass-to-charge
cm	centimeter	mA	milliampere
COL11A2	collagen alpha-2(XI) chain (gene)	MALDI	matrix-assisted laser desorption-ionization
CRM	charged residue model	mbar	millibar
CTL	cytotoxic T lymphocytes	MD	molecular dynamics
d	day	MHC	major histocompatibility complex
Da	dalton	MHC-I/II/III	major histocompatibility complex class I/II/III
DC	direct current	min	minute
DNA	deoxyribonucleic acid	mL	milliliter
dsA2	disulfide-stabilized HLA-A*20:01	mM	millimolar
DTT	dithiothreitol	mm	millimeter
e	elementary charge	MOG	myelin oligodendrocyte glycoprotein (gene)
E_{el}	electrical energy	mRNA	messenger ribonucleic acid
E_{kin}	kinetic energy	ms	millisecond
<i>E. coli</i>	<i>Escherichia coli</i>	MS	mass spectrometry
e.g.	<i>exempli gratia</i> , Latin for “for example”	MS^1	tandem mass spectrometry
EDTA	ethylenediaminetetraacetic acid	MS^2	two-stage mass spectrometry
EM	electron microscopy	MS^3	three-stage mass spectrometry
ER	endoplasmic reticulum	MWCO	molecular weight cut-off
ESI	electrospray ionization	n	number of charges
<i>et al.</i>	<i>et alii</i> , Latin for “and others”	N	nucleocapsid protein
EtOH	ethanol	NaCl	sodium chloride
eV	electronvolt	nDSF	nanoscale differential scanning fluorimetry
f	clustering factor	-NH ₂	amidated
FHC	free heavy chain of MHC-I	NH ₄ ⁺	ammonium cation
FRAP	fluorescence recovery after photobleaching	NK	natural killer (cells)
FWHM	full width at half maximum	nL	nanoliter
g	gravitational force equivalent	nM	nanomolar
GFP	green fluorescent protein	NMR	nuclear magnetic resonance (spectroscopy)
GHS	Globally Harmonized System of Classification and Labelling of Chemicals	P	precautionary (statement)
h	hour	pep	peptide
H	hazard (statement)	pH	potential of hydrogen
H ⁺	proton	PLC	peptide loading complex
H2	murine MHC (histocompatibility 2)	pMHC	peptide-MHC complex
H2-K1	H-2K ^b (gene)	PMSF	phenylmethylsulfonyl fluoride
H-2K ^b	murine MHC-I	pp65	phosphoprotein (cytomegalovirus)
HA	hemagglutinin tag	PTMs	post-translational modifications
HC	heavy chain	q	charge of an ion
HCl	hydrochloric acid	Q	quadrupole
HEPES	4-(2-hydroxyethyl)-1-piperazineethanesulfonic acid	QE-UHMR	Q Exactive™ UHMR Hybrid Quadrupole Orbitrap™
HLA	human leukocyte antigen	R	radius of the droplet
<i>i.e.</i>	<i>id est</i> , Latin for “that is”	R	resolution
iDSF	isothermal analysis nDSF	RFP	red fluorescent protein
IEM	ion evaporation model	RT-1	rat MHC
Ig	immunoglobulin	s	second
IPTG	isopropyl-β-D-1-thiogalactopyranosid	s	distance
ISD	in-source dissociation	S	spike protein (SARS-CoV-2)

Abbreviations

SARS-CoV-2	severe acute respiratory syndrome coronavirus type 2	TOF	time-of-flight
SD	standard deviation	Tris	tris(hydroxymethyl)aminomethane
SDS-PAGE	sodium dodecylsulfate	<i>U</i>	potential
	polyacrylamide gel electrophoresis	<i>v</i>	velocity
SEC	size-exclusion chromatography	V	Volt
SMT	single-molecule tracking	WHO	World Health Organization
SMCT	single-molecule co-tracking	wtA2	wild type HLA-A*02:01
STF-1	TAP2-deficient fibroblasts	<i>z</i> , <i>z_R</i>	number of elementary charges <i>e</i>
<i>t</i>	time	α	alpha chain, subdomain of MHC
<i>t</i> _{1/2}	half-life	β	beta chain, subdomain of MHC
<i>T</i> _m	melting temperature	β _{2m}	beta-2 microglobulin
TAP2	antigen peptide transporter 2	γ	surface tension
TCR	T cell receptors	ϵ_0	electric field constant
term.	terminal	μ L	microliter
		μ m	micrometer

In this thesis, amino acids are abbreviated according to the single-letter amino acid code.

alanine	Ala	A
arginine	Arg	R
asparagine	Asn	N
aspartic acid	Asp	D
cysteine	Cys	C
glutamic acid	Glu	E
glutamine	Gln	Q
glycine	Gly	G
histidine	His	H
isoleucine	Ile	I
leucine	Leu	L
lysine	Lys	K
methionine	Met	M
phenylalanine	Phe	F
proline	Pro	P
serine	Ser	S
threonine	Thr	T
tryptophan	Trp	W
tyrosine	Tyr	Y
valine	Val	V

List of figures

Figure 1 Basic components of any mass spectrometer.....	12
Figure 2 Schematic representation of the ESI process.....	15
Figure 3 Modeled ESI processes for different analytes.....	16
Figure 4 Charge state distribution in ESI.	17
Figure 5 Exemplary native ESI mass spectrum of a protein complex.	19
Figure 6 Schematic representation of a quadrupole mass analyzer.	20
Figure 7 Schematic representation of a TOF mass analyzer.....	21
Figure 8 Schematic representation of an Orbitrap™ mass analyzer.....	23
Figure 9 Representative MS ² spectra of a CID experiment.....	26
Figure 10 Schematic structures of MHC class I and II.....	29
Figure 11 Schematic of MHC-I states at the plasma membrane.	30
Figure 12 Overview of the MHC-I peptide binding groove.	31
Figure 13 The K ^b α ₃ domains form dimers.	38
Figure 14 Representative mass spectra of the K ^b α ₃ domain.....	38
Figure 15 Percentages of α ₃ monomer and dimer in two different SEC fractions.....	39
Figure 16 Analyzing the α ₃ dimers of two different SEC fractions via MS ²	40
Figure 17 Crystal structure of empty disulfide-stabilized HLA-A*02:01 (dsA2).....	45
Figure 18 Production of dsA2.....	46
Figure 19 Representative mass spectra of wtA2.....	47
Figure 20 Representative mass spectra of dsA2.....	48
Figure 21 MS ² analysis of empty dsA2.	49
Figure 22 Superstoichiometric binding of high-affinity peptide NV9 to dsA2.....	51
Figure 23 Substoichiometric binding of high-affinity peptide NV9 to dsA2.....	52
Figure 24 Erucamide detected in all dsA2 samples.....	53
Figure 25 Erucamide identified as contaminant using small molecule MS.....	54
Figure 26 dsA2 in absence of peptides.	58
Figure 27 Raw spectrum of dsA2+NV9.....	59
Figure 28 Determining the binding affinities of YF9, NV9 and GV9 to dsA2.	60
Figure 29 ISD causes linear dependence of the ligand-bound dsA2 fraction on cone voltage.....	61
Figure 30 Affinities determined via iDSF and native MS correlate.	62
Figure 31 Relation of thermal stability and affinity for dsA2+peptide complexes.	64
Figure 32 Determining the binding affinities of charge-reduced NV9 variants to dsA2.....	65
Figure 33 Analyzing the charge-reduced NV9 variants using native MS.....	66
Figure 34 dsA2 and charge-reduced NV9 variants at higher collision energies.....	67
Figure 35 Determining the binding affinities of truncated NV9 variants to dsA2.	68
Figure 36 dsA2 and truncated NV9 variants at higher collision energies.....	69
Figure 37 Detected dsA2 mass species in presence of two corresponding truncated NV9 variants.	70
Figure 38 <i>T_m</i> of dsA2 in presence of two corresponding truncated NV9 variants.....	71
Figure 39 Synergistic stabilization of dsA2 in presence of two corresponding truncated NV9 variants.....	72
Figure 40 dsA2 and two corresponding truncated NV9 variants at higher collision energies.....	73
Figure 41 Favored amino acid positions within the HLA-A*02:01 peptide-binding pocket.....	74
Figure 42 The idea for peptide screening using native MS.	77
Figure 43 Charge state 13 ⁺ best resembles in-solution conditions.....	79
Figure 44 Saving time during buffer exchange.....	80
Figure 45 Selecting a suitable mass spectrometer.....	81
Figure 46 Impact of the ISD energy.....	83
Figure 47 Impact of the capillary temperature.	84
Figure 48 Choosing the optimal peptide concentration.	85
Figure 49 Substoichiometric peptide concentration allows for determination of unbiased affinities.	86
Figure 50 Impact of incubation time and ethanol.....	87
Figure 51 Screening low-affinity peptides.....	90
Figure 52 Facing the limits of resolution for the peptide screening approach.....	91
Figure 53 The locked and unlocked states of the A and F pockets of A2.....	130
Figure 54 dsA2 is stable at very low dipeptide concentrations.....	131

List of tables

Table 1 Overview of all proteins used in this work.....	100
Table 2 Overview of all peptides used in this work.....	102
Table 3 Overview of all samples used in this work.....	104
Table 4 Overview of all pressure settings used in this work.....	105
Table 5 Overview of all voltage settings used in this work.....	105
Table 6 Overview of all relevant instrument-specific settings used in this work.....	106
Table 7 M_{exp} of the different α_3 domain protein species.....	132
Table 8 M_{exp} of the different wtA2 and dsA2 protein species.....	132
Table 9 AUC for the detected dsA2 mass species at different acceleration voltages.....	133
Table 10 Apparent K_d for dsA2 and different peptides obtained by native MS and iDSF.....	137
Table 11 T_m for dsA2 and different peptides obtained by nDSF.....	138
Table 12 Overview of all hazardous substances used in this work.....	143

Abstract

An essential element of adaptive immunity is the selective binding of peptide antigens by major histocompatibility complex class I (MHC-I) proteins. They present antigenic peptides to cytotoxic T cells at the plasma membrane of mammalian cells. MHC-I is a heterodimer consisting of the strongly conserved beta-2-microglobulin light chain (β_2m) and the heavy chain (HC), which has a highly variable region that forms a cleft to accommodate a peptide. As the peptide dissociates, the two noncovalently bound subunits fall apart. The resulting peptide-free state of MHC-I is not well understood, but it is known that free heavy chains (FHCs) can assemble in the plasma membrane to form homotypic complexes that perform various regulatory functions. In this work, the stoichiometry and dynamics of FHC assembly of murine MHC-I H-2K^b were investigated using native mass spectrometry (MS) and complementary methods (**Chapter 3.1**). The FHCs were found to form noncovalently bound dimers. Dimerization was shown to be mediated by the α_3 domain binding the α_3 domain of another FHC in a manner similar to binding the β_2m subunit.

The dynamics and structure of the peptide-free but natively assembled complex are of particular interest for understanding peptide-binding and -exchange processes. For this work, a disulfide-stabilized version of the human MHC-I molecule HLA-A*02:01 (dsA2) was thoroughly characterized by native MS and various supporting structural biological methods (**Chapter 3.2**). The dsA2 molecule was designed to be stable in the absence of peptides. Successful refolding of the heterogeneous protein complex was verified, and the dipeptide used for refolding was not detected either free or bound to dsA2 after removing it via buffer exchange (BEX). In striking contrast, only a minimal amount of folded wild type A2 (wtA2) was detected in the absence of dipeptide; however, wtA2 remained stable when dipeptide was present at millimolar concentrations. It was concluded that wtA2 is dependent on high concentrations of dipeptide to maintain its folded conformation, whereas dsA2 is conformationally and thermally stable in the absence of dipeptide. Nevertheless, dsA2 was still able to specifically bind or exchange peptides. Dipeptides were found to settle only in the A pocket or in both the A and F pockets. High-affinity nonapeptides were able to bind even at substoichiometric concentrations. The amino acid side chains lining the binding pockets switched in a coordinated manner between a peptide-free, unlocked state, and a peptide-bound, locked state.

Peptide binding to the empty dsA2 molecule was studied in detail, and because of its unique stability, it was possible to determine the binding affinities of complexes loaded with various peptides, including truncated or reduced-charge peptides (**Chapter 3.3**). It was

found that the two already known anchor positions could be stabilized independently. Further investigation revealed the contribution of additional amino acid positions to the binding strength.

In addition, it was observed that dsA2 could bind a variety of peptides from a mixture. From the relative ratio of the different signals of MHC-peptide complexes, the affinities of the peptides could be estimated directly and simultaneously (**Chapter 3.4**). It became clear that the 13⁺ charge state is the one least affected by dissociation processes and is therefore suitable for direct read-out of the relative affinity. Various parameters related to the mass spectrometer and the sample were optimized to screen peptides. For example, it was determined that the total peptide concentration should be lower than that of MHC-I to eliminate time-dependent competition effects. Native MS analysis of MHC-I molecules is presented as a versatile tool for peptide screening approaches. As a complement to computational prediction tools, the method presented in this work rapidly and efficiently estimates the binding strength of even peptides with low affinity for MHC-I complexes. It has enormous potential for eliminating binding affinity biases and thus accelerating drug discovery in infectious diseases, autoimmunity, vaccine development, and cancer immunotherapy.

Zusammenfassung

Ein wesentliches Element der adaptiven Immunität ist die selektive Bindung von Peptidantigenen durch Proteine des Haupthistokompatibilitätskomplexes Klasse I (MHC-I). An der Plasmamembran von Säugetierzellen präsentieren diese den zytotoxischen T-Zellen antigenische Peptide. MHC-I ist ein Heterodimer, das aus der hochkonservierten leichten Beta-2-Mikroglobulin-Kette (β_2m) und der schweren Kette besteht. Letztere weist einen hochvariablen Bereich auf, der eine Tasche zur Aufnahme eines Peptids bildet. Wenn das Peptid dissoziiert, fallen die beiden nicht kovalent gebundenen Untereinheiten auseinander. Der daraus resultierende peptidfreie Zustand von MHC-I ist nicht gut untersucht, es ist jedoch bekannt, dass sich die freien schwere Ketten (FHCs) in der Plasmamembran zu homotypischen Komplexen zusammenfinden können, die dann verschiedene regulatorische Funktionen erfüllen. In dieser Arbeit wurden die Stöchiometrie und die Dynamik der FHC-Assemblierung des murinen MHC-I H-2K^b mit nativer Massenspektrometrie (MS) und ergänzenden Methoden untersucht (**Kapitel 3.1**). Es wurde festgestellt, dass die FHCs nichtkovalent gebundene Dimere bilden. Es konnte gezeigt werden, dass die Dimerisierung durch die Bindung der α_3 -Domäne an die α_3 -Domäne eines anderen FHC erfolgt – auf ähnliche Weise wie bei der Bindung zu β_2m .

Die Dynamik und Struktur des peptidfreien, aber nativ assemblierten Komplexes sind von besonderem Interesse für das Verständnis von Peptidbindungs- und -austauschprozessen. Für diese Arbeit wurde eine Disulfid-stabilisierte Version des menschlichen MHC-I-Moleküls HLA-A*02:01 (dsA2) durch native MS und verschiedene unterstützende strukturbiologische Methoden gründlich charakterisiert (**Kapitel 3.2**). Das dsA2-Molekül wurde so konzipiert, dass es in Abwesenheit von Peptiden stabil ist. Die erfolgreiche Rückfaltung des heterogenen Proteinkomplexes wurde verifiziert und das zur Rückfaltung verwendete Dipeptid wurde weder frei noch gebunden an dsA2 nachgewiesen, nachdem es mittels Pufferaustausch (BEX) entfernt wurde. In auffälligem Kontrast dazu wurde in Abwesenheit des Dipeptids nur eine minimale Menge an gefaltetem Wildtyp-A2 (wtA2) nachgewiesen; wtA2 blieb jedoch stabil, wenn das Dipeptid in millimolaren Konzentrationen vorhanden war. Daraus wurde gefolgert, dass wtA2 auf hohe Konzentrationen von Dipeptid angewiesen ist, um seine gefaltete Konformation aufrechtzuerhalten, während dsA2 in Abwesenheit von Dipeptid konformationell und thermisch stabil ist. Dennoch war dsA2 immer noch in der Lage, Peptide spezifisch zu binden oder auszutauschen. Es wurde festgestellt, dass Dipeptide nur in der A-Bindungstasche oder sowohl in der A- als auch in der F-Bindungstasche gebunden waren. Hochaffine Nonapeptide konnten sogar in substöchiometrischen Konzentrationen binden.

Die Aminosäureseitenketten, die die Bindungstaschen auskleiden, wechseln in koordinierter Weise zwischen einem peptidfreien, nicht geschlossenen Zustand und einem peptidgebundenen, geschlossenen Zustand.

Die Peptidbindung an das leere dsA2-Molekül wurde eingehend untersucht und aufgrund seiner einzigartigen Stabilität war es möglich, die Bindungsaffinitäten von Komplexen zu bestimmen, die mit verschiedenen Peptiden beladen waren, einschließlich verkürzter oder ladungsreduzierter Peptide (**Kapitel 3.3**). Es wurde festgestellt, dass die beiden bereits bekannten Ankerpositionen unabhängig voneinander stabilisiert werden können. Weitere Untersuchungen ergaben, dass zusätzliche Aminosäurepositionen zur Bindungsstärke beitragen.

Darüber hinaus wurde festgestellt, dass dsA2 eine Vielzahl von Peptiden aus einem Gemisch binden kann. Aus dem relativen Verhältnis der Signale der verschiedenen MHC-Peptid-Komplexe konnten die Affinitäten der Peptide direkt und simultan abgeschätzt werden (**Kapitel 3.4**). Es zeigte sich, dass der 13^+ -Ladungszustand am wenigsten von Dissoziationsprozessen betroffen ist und sich daher für das direkte Ablesen der relativen Affinität eignet. Verschiedene Parameter in Bezug auf das Massenspektrometer und die Probe wurden für das Screenen von Peptiden optimiert. So wurde beispielsweise festgestellt, dass die Gesamtpeptidkonzentration niedriger sein sollte als die von MHC-I, um zeitabhängige kompetitive Effekte auszuschließen. Die native MS-Analyse von MHC-I-Molekülen wird als vielseitiges Instrument für Peptidscreening-Ansätze vorgestellt. Als Ergänzung zu computergestützten Vorhersagemethoden lassen sich mit der in dieser Arbeit vorgestellte Methode schnell und effizient die Bindungsstärke selbst von Peptiden mit geringer Affinität für MHC-I-Komplexe bestimmen. Die Technik hat ein enormes Potenzial zur Beseitigung von Verzerrungen bei der Ermittlung von Bindungsaffinität und damit zur Beschleunigung der Arzneimittelforschung in Hinblick auf Infektionskrankheiten, Autoimmunität, sowie der Impfstoffentwicklung und Krebsimmuntherapie.

1 Introduction

1.1 Structural mass spectrometry

Parts of this chapter have been published in the following book chapter:

Dülfer, J., Kádek, A., **Kopicki, J.-D.**, Krichel, B., & Uetrecht, C. (2019). Structural mass spectrometry goes viral. *Advances in virus research*, 105, 189–238¹.

Reprinted from DÜLFER *et al.* (2019) with permission from Elsevier. Copyright © 2019 Elsevier Inc. All rights reserved.

To completely grasp research problems in disciplines like health, medicine, or ecology, understanding living matter is crucial but just the fact that we ourselves are made of it is extraordinary fascinating to my mind. In the field of structural biology, we strive to identify its individual components, observe their interactions, and decipher the resulting functions *in vivo*. Processes that occur at the molecular level can be astonishingly complex. The biomolecules involved are rarely static, but occur in a wide variety of conformations, have diverse binding partners, and are also otherwise dynamic in terms of their structure. Unfortunately, there is no such thing as a single method that can give us all the important structural information, we need to comprehend a biological process. Therefore, structural biologists employ a broad range of methods to uncover the organization of biomolecules and to understand their function at the molecular level.

Macromolecular crystallography techniques as well as nuclear magnetic resonance (NMR) spectroscopy routinely provide three dimensional structures with resolution down to single atoms, while electron microscopy (EM)-based methods are fast approaching this boundary with cryogenic sample preparation and recent developments in detector technology⁷. However, all these techniques have their own challenges and limitations. These can range from the frustrating efforts to produce sufficiently large, diffracting crystals, through sample size limitations, up to often very significant demands on sample amount and homogeneity or limited ability to assign subunit positions or identify post-translational modifications (PTMs). Most importantly, however, there is very rarely a single technique to answer all the questions at hand. Therefore, structural biology is moving more and more in the direction of so-called integrative approaches, where high-resolution structural data from different methods are combined with lower resolution information. These data then ultimately feed into computational modeling in order to obtain the most detailed functional understanding possible of the biological system⁸⁻¹⁰.

One of the experimental techniques, which provide invaluable input for the integrative structural efforts, is mass spectrometry (MS). MS is a technique for identifying and

characterizing chemical compounds based on the masses of their atomic or molecular constituents. Analytes are ionized and transferred to the gas phase, separated based on their mass-to-charge ratio (m/z) and then detected¹¹. Due to the wide range of possible applications diverse scientific fields can benefit from MS. Originally belonging purely to the domains of physics and analytical chemistry, MS has changed significantly since the revolutionary developments of electrospray ionization (ESI) and matrix-assisted laser desorption-ionization (MALDI) in the late 1980s¹²⁻¹⁶. These two so-called “soft-ionization techniques” have enabled the analysis of biomolecules without their unwanted fragmentation and allowed MS to expand hugely into the field of biochemistry. There, it has ever since been used in proteomics as a method of choice for identifying proteins, quantifying them and for analyzing their PTMs^{17,18}. Moreover, and more importantly from the point of view of higher order macromolecular structure, so-called structural MS has also established itself especially in the last two decades as a powerful method to study proteins. This was enabled by two major lines of development. On one hand, pioneering works by the groups of Carol Robinson, Albert Heck and Joseph Loo have exploited the softness of the ESI process to transfer whole noncovalently bound protein assemblies into the gas phase inside a mass spectrometer without disrupting their stoichiometry and interactions in a process termed native MS¹⁹⁻²². Additionally, as was shown later, the conformations of such protein complex ions often survive largely unperturbed, which opened possibilities for further gas-phase structural studies and “gas-phase structural biology”²³⁻²⁵. On the other hand, many techniques were developed which probe protein conformations, interactions, and dynamics directly in solution. Usually, such methods use some form of chemical labeling, be it through isotopic exchange²⁶, chemical cross-linking²⁷ or radical chemistry²⁸, and capitalize from the use of MS as a detection method.

Together, all the various structural MS approaches offer a broad portfolio of experimental techniques, which can probe a wide range of protein structural features, while at the same time retrieving information about protein identity and PTMs. Moreover, structural MS nicely complements the three traditional high-resolution structural biology techniques, albeit with lower overall resolution. However, this is often more than balanced by the ability of MS to work with low amounts of samples, in low concentrations, and with high throughput. Importantly, structural MS can often work in complex mixtures, with several pioneering methods probing protein structures directly in cells²⁹⁻³⁴. Additionally, structural MS is in theory unlimited in terms of molecular weight, offering information on systems ranging from small, isolated protein domains all the way up to huge multi-megadalton assemblies. Perhaps most importantly, structural MS can also provide insight into protein

conformational dynamics and coexisting transient species in solution, which is frequently missing or can be very challenging to access by static averaged high-resolution structures provided by macromolecular crystallography techniques and EM.

1.1.1 Native mass spectrometry

The basic requirement for all MS measurements is a configuration that includes a sample introduction system, an ion source, a mass analyzer, and a detector, all of which are operated in vacuum except for the first component (**Figure 1**).

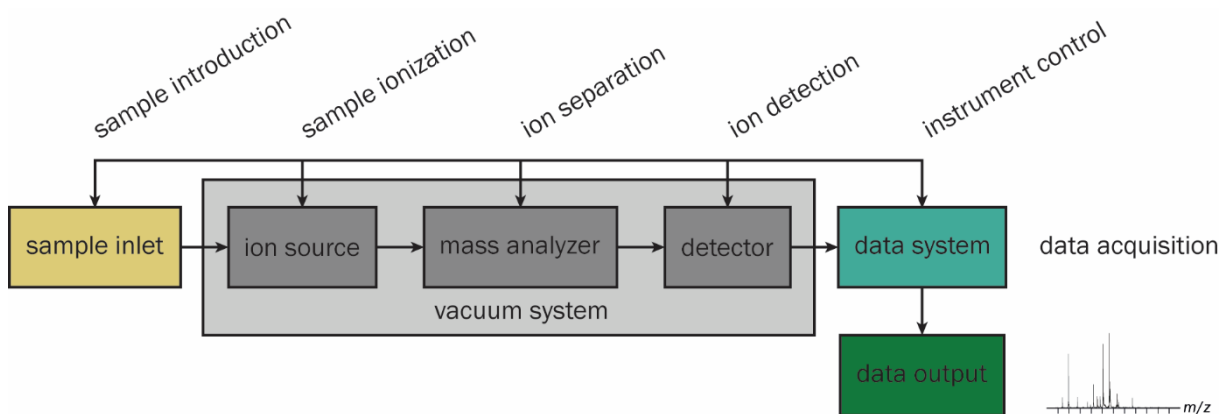


Figure 1 | Basic components of any mass spectrometer.

Samples can be injected at atmospheric pressure, while ion source, mass analyzer and detector operate under vacuum. The analyte is brought into the gas phase and ionized. A mass analyzer separates the ions according to their m/z values. Detected ions are visualized in the form of mass spectra.

For this reason, any samples must first be transferred to the gas phase. Neutral molecules are ionized at the ion source. In the mass analyzer, the analyte ions are separated according to their different m/z values. The separated ions reach the detector and generate a signal that is recorded and finally mapped in the mass spectrum, which shows the signal intensity as a function of the m/z value^{35,11}. In a mass spectrum, the signal intensity is displayed two-dimensionally depending on the associated m/z value. The displayed signals are called peaks. The position of a peak indicates the m/z value of a detected ion. The frequency of the detection events defines the intensity of the peak. In a conventional mass spectrum, the peak with the highest m/z value is the molecular peak, representing the intact molecule with single charge. The peak with the highest intensity, which shows the most abundant ion species, is called the base peak. Usually, mass spectra are normalized with respect to the base peak, so that the relative intensity is indicated on the ordinate.

In native MS, the term *native* refers to the state of biomolecules dictated by external conditions prior to mass analysis²². Proteins adopt three-dimensional structures depending on their amino acid sequence, chemical environment, and binding partners. Often, homo- or heterogeneous complexes are formed by noncovalent binding of other proteins. In

solution, this occurs under conditions that simulate a corresponding physiological environment. While the experimental preservation of physiological conditions is generally a hurdle in structural biology, it has been successfully demonstrated that the structure is still native-like after the transition to the gas phase, which is necessary for MS^{22,36}. Native MS therefore offers the possibility to analyze the topology, stoichiometry, dynamics, and interaction of native protein complexes with high sensitivity.

The basis of native MS is very soft ESI from volatile buffer surrogates. Nevertheless, other more exotic techniques exist, which have higher tolerance to salts or detergents³⁷. The main challenge is retaining noncovalent interactions of proteins and their stoichiometry in complexes upon transfer into the gas phase. However, ESI is soft enough that even intact viruses have been shown to survive the process and keep their infectivity^{38,39}.

1.1.1.1 Sample preparation

The better the sample quality, the more likely it is that high-quality spectra can be recorded. Similarly, the more homogeneous the sample, the easier it is to obtain well-resolved spectra. Having minimal impurities such as co-expressed proteins and as little glycosylation or other PTMs as possible contributes to a uniform mass distribution, which is reflected in clearly defined peak patterns. As recombinantly produced proteins are the typical sample for native MS, these are usually subjected to several (chromatographic) purification steps after expression. However, GAN *et al.* were able to show that this is not always necessarily required. They presented a protocol in which sample preparation for native MS is performed from crude cell extracts without further purification steps³⁰.

In general, the ideal protein ion is free of all solvent and buffer adducts but populated by multiple charges. The ESI process for native MS used in this work requires BEX into an MS-compatible solution of volatile salt. This step is usually performed after protein purification using centrifugal filters, desalting columns or via dialysis. Time-wise, it is advantageous to combine the BEX with the last purification step and thus elute the protein directly in the MS solution, for example.

Ammonium acetate solution is particularly suitable for native MS, due to its adjustable pH (4.6-10) and ionic strength (0 to several M), mimicking the natural environment and providing favorable conditions for the protein until its desolvation. The two salt components buffer the pH at 4.75 ± 1 (acetic acid) and 9.25 ± 1 (ammonia)⁴⁰. Small amounts of non-volatile salts or small molecules up to a few mM can be added when required, for example bivalent cations or co-factors, which can be essential in case of enzymes. Adduct formation

in the presence of non-volatile salts can be limited by the use of smaller diameter ESI emitter tips⁴¹. Furthermore, some applications require the addition of charge-reducing or charge-increasing substances. Here, for example, triethylammonium acetate, for charge-reduction, or *m*-nitrobenzyl alcohol, for supercharging, are suitable⁴²⁻⁴⁴. In the case of membrane proteins, further adjustments are usually necessary. For this, micelle-forming detergents or sophisticated systems such as nanodiscs or bicelles are used⁴⁵⁻⁴⁷.

Ammonium acetate solution is most widely used in native MS. However, there are of course also alternatives. One of them would be ammonium bicarbonate, though it has to be considered that CO₂ outgassing can occur at neutral pH, which in turn can lead to foam-induced protein unfolding⁴⁸. If slightly or completely denaturing conditions are required, organic solvents such as acetonitrile, methanol and formic acid are typically added for protein unfolding.

Immediately before the actual measurement, the concentration of the analyte is adjusted to about 1-10 μ M. The analyte concentration refers to the most prevalent species, which can be monomers but also large oligomers. For a new sample, the ideal concentration is usually evaluated first. Depending on the research question, the ionization efficiency of the analyte, or the instrument itself, the concentration may vary. The higher the concentration, the stronger the resulting signal, but the more likely it is that nonspecific artifacts will be formed during the ESI process.

1.1.1.2 Nano-electrospray ionization

In ESI, the protein sample is sprayed from an externally charged capillary into a mass spectrometer^{12,15,16}. More precisely, the sample solution is placed in an electrically conductive capillary, which is subjected to a potential of several kV (**Figure 2**). Depending on the technique, the capillary diameter and thus the flow rate can vary. In conventional ESI, the consumption of analyte solution ranges from one to hundreds of μ L/min, while nano ESI (capillary diameter < 4 μ m¹⁴) manages with a much lower flow rate of less than 10 nL/min. The physical background regarding desolvation, protein charging and structural integrity of gas-phase ions was unraveled experimentally and in molecular dynamics (MD) simulations^{49,50}. Due to the applied voltage, the sample solution takes the shape of a cone. At the tip of this so-called TAYLOR cone, ions with the same charge sign emerge surrounded by droplets⁴⁹. Then, because of COULOMB repulsion, the droplets drift apart, creating an aerosol, the actual electrospray.

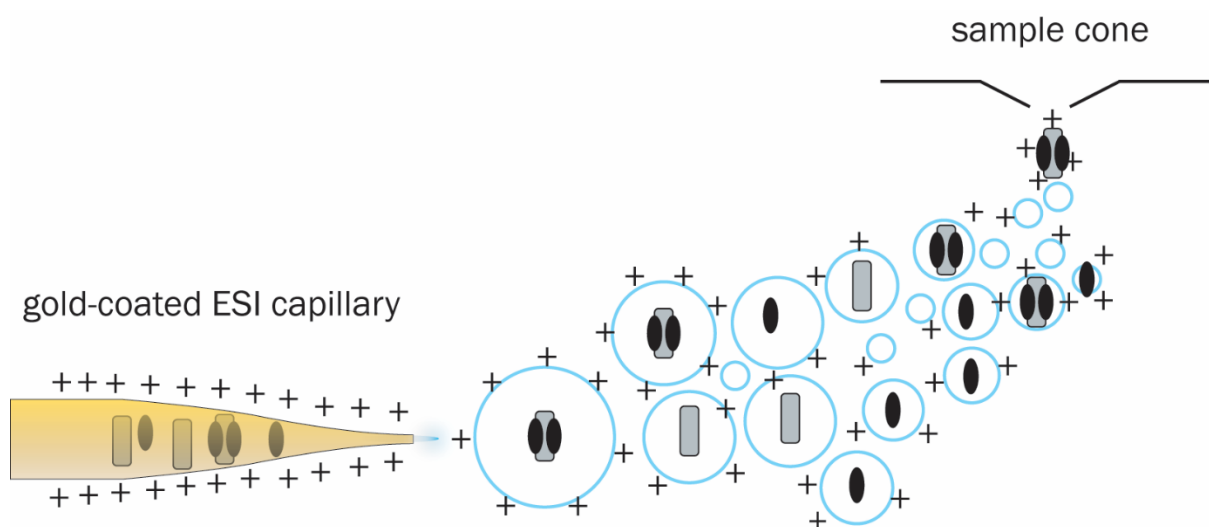


Figure 2 | Schematic representation of the ESI process.

By applying an electrical potential, the sample solution forms the TAYLOR cone at the tip of the ESI capillary, from which positively charged droplets are ejected. The solvent evaporates, forming even smaller droplets. Finally, the exposed, charged analyte reaches the mass spectrometer⁴⁹.

In positive ion mode, where a positively grounded potential is present, the capillary is the anode, and the mass spectrometer acts as the cathode. The droplets carry a positive charge due to the adduction of solvents (e.g., H^+ , NH_4^+)⁴⁹. After leaving the TAYLOR cone, the volatile solvents (e.g., aqueous ammonium acetate solution) evaporate very rapidly, with the charge density at the droplet surface increasing steadily until it bursts, and smaller droplets are formed¹¹. This process, controlled by surface tension and COULOMB repulsion, continues until the so-called RAYLEIGH limit is reached (**Equation 1**).

$$z_R = \frac{8 \cdot \pi}{e} \sqrt{\epsilon_0 \cdot \gamma \cdot R^3}$$

Equation 1 | Definition of the RAYLEIGH limit.

z_R – number of elementary charges e ; R – radius of the droplet; ϵ_0 – electric field constant; γ – surface tension⁴⁹.

Based on the assumption a protein's radius corresponds to the protein's molecular weight and its density is equivalent to the density of water, the equation can be simplified even further⁵¹.

$$z_R = 0.078 \cdot \sqrt{M}$$

Equation 2 | Simplified definition of the RAYLEIGH limit.

M – molecular weight of the analyte.

Continuous fission leaves highly charged droplets with diameters of only a few nanometers. From these, the gaseous ions detectable by MS are obtained. Depending on the size of the species to be ionized, the ionization process follows a distinct model. For low molecular weight analytes, the ion evaporation model (IEM) was proposed. Excess charge forces the analyte out of the droplet. A bridge of solvent forms, which shortly thereafter ruptures and

releases the ion (**Figure 3A**). Larger, globular molecules (e.g., natively folded proteins) are likely to be transferred to the gas phase using the charged residue model (CRM). In tiny droplets, that contain only one copy of the species to be analyzed, the solvent transfers the charge to the analyte, as evaporation proceeds (**Figure 3B**). For nonpolar polymer chains (e.g., unfolded proteins), the chain ejection model (CEM) is adopted. Hydrophobic interactions drive the molecule toward the droplet surface. Once a chain end penetrates the surface, more and more charges are delivered to the analyte until its complete ejection (**Figure 3C**)⁴⁹. The surface size and nature of a protein determines to a large extent the charge state of the molecule obtained by ESI^{38,49}.

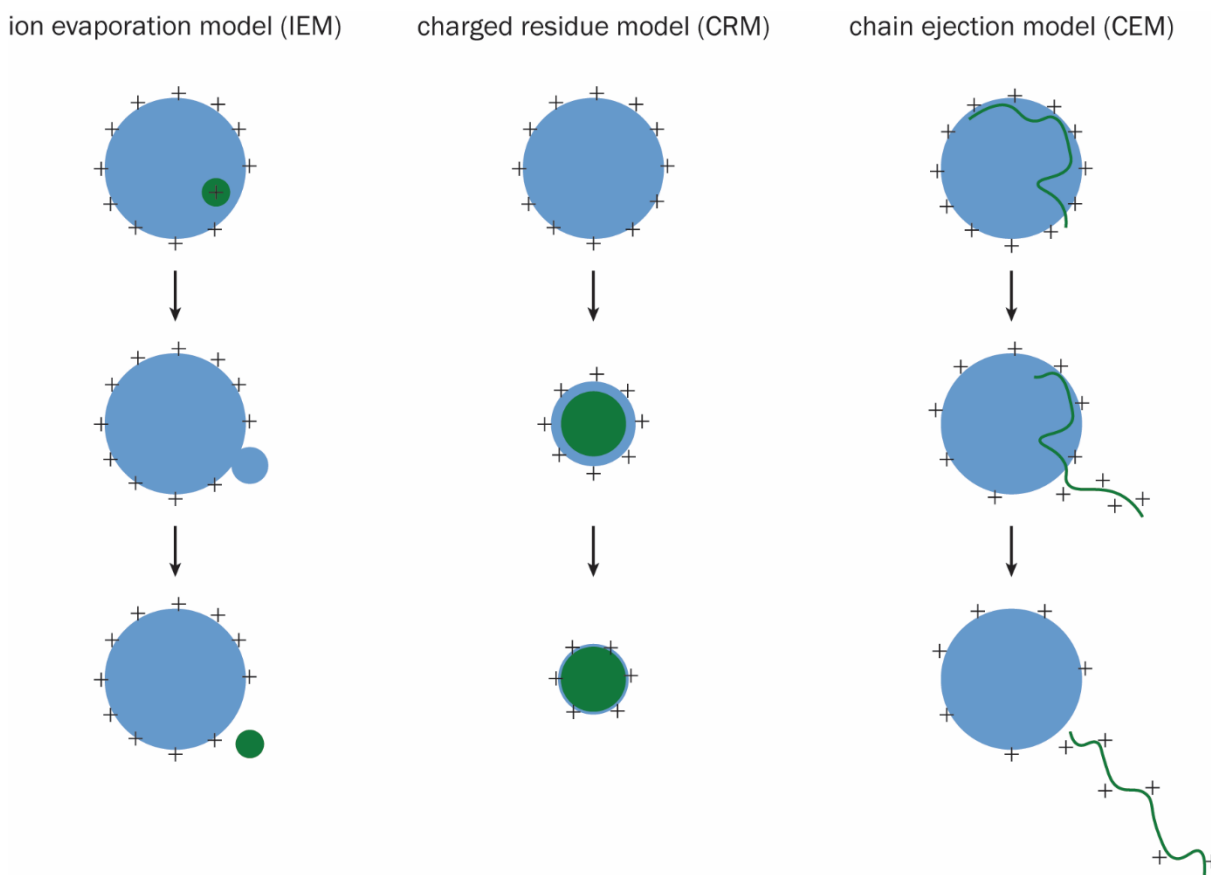


Figure 3 | Modeled ESI processes for different analytes.

IEM for small analytes; CRM for large analytes such as globular proteins or protein complexes; CEM for non-polar polymer chains such as denatured proteins.

The protein obtains its net positive charge at the molecular level through the protonation of basic amino acids or the *N*-terminus. Thus, proteins have significantly higher charge numbers in the unfolded state than in the folded state. The mass and charge of all protein ions can be described according to the following scheme: $[M + z\text{H}]^{z+}$ with $z \gg 1$ ³⁸. In accordance with the statistical frequency of the occurring charge numbers, a distribution of the charge states results that can be analyzed by MS.

1.1.1.3 Mass analysis

ESI mass spectra of proteins or protein complexes have unique characteristics. As described above, a protein can adopt different charge states. These are reflected in the resulting peak pattern, which is reminiscent of a GAUSS distribution (**Figure 4**). There again, the peak with the highest intensity represents the most frequently detected charge state of the molecule.

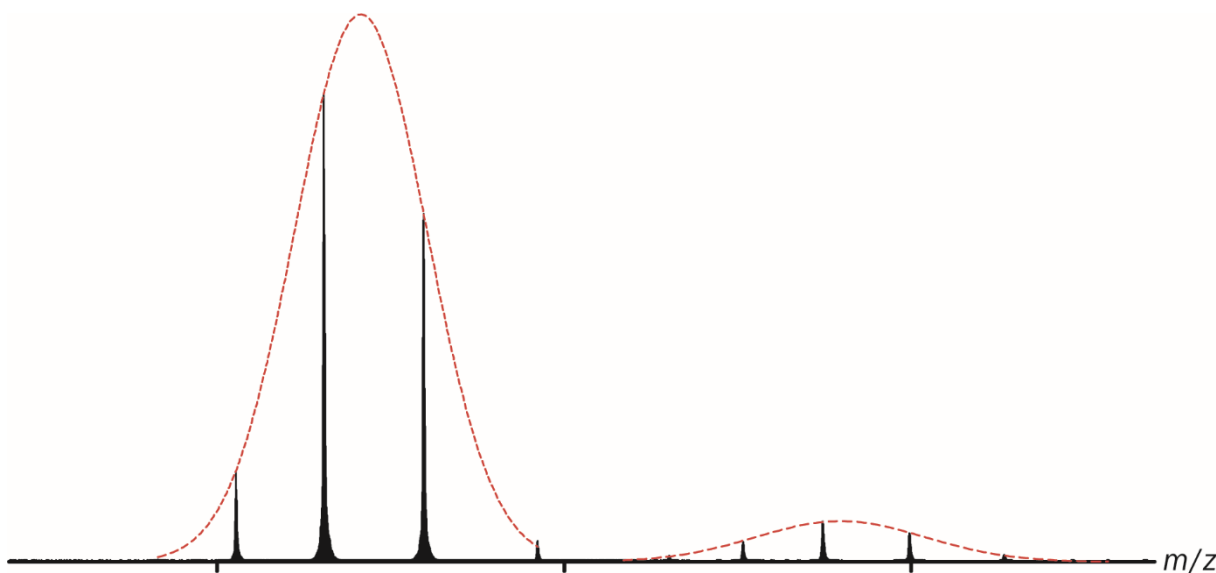


Figure 4 | Charge state distribution in ESI.

The charge states a protein adopts throughout an ESI process are distributed on a GAUSSIAN curve. The highest peak presents the most abundant charge state of the analyte.

Adjacent signals in a peak series have a charge difference of $\Delta z = 1$. From the m/z values of these peaks, the mass M of the signal-causing analyte can be calculated. The higher m/z value of the adjacent peaks is called $(m/z)_1$, the lower $(m/z)_2$. The numbers of charges are related as follows (**Equation 3**).

$$n_2 = n_1 + 1$$

Equation 3

In the following it is assumed that all charges are caused by protonation ($[M + zH]^{z+}$). Thus, using the mass of a proton m_H , we obtain $(m/z)_1$ (**Equation 4**).

$$\left(\frac{m}{z}\right)_1 = \frac{M + n_1 \cdot m_H}{n_1}$$

Equation 4

A substitution with **Equation 4** yields the following term for $(m/z)_2$ (**Equation 5**).

$$\left(\frac{m}{z}\right)_2 = \frac{M + n_2 \cdot m_{\text{H}}}{n_2} = \frac{M + (n_1 + 1) \cdot m_{\text{H}}}{n_1 + 1}$$

Equation 5

From this, the charge state n_1 can therefore be determined as follows (Equation 6).

$$n_1 = \frac{\left(\frac{m}{z}\right)_2 - m_{\text{H}}}{\left(\frac{m}{z}\right)_1 - \left(\frac{m}{z}\right)_2}$$

Equation 6

Last, once n_1 is determined, the molecular mass M can be calculated (Equation 7)¹¹.

$$M = n_1 \cdot \left(\left(\frac{m}{z}\right)_1 - m_{\text{H}}\right)$$

Equation 7

Proteins can pick up charge not only by adduction of a proton, but also by other ions present in solution, such as sodium, potassium, or ammonium. According to the mass of the respective adduct, the formula for mass calculation of the analyte needs to be adjusted. These calculations are usually performed for the whole peak series by special mass spectrometry software, with which the spectrum was previously processed in a suitable manner (calibration, smoothing, peak centering, baseline correction). This type of software also allows deconvolution of the signal, obtaining a spectrum that depends only on mass instead of m/z ⁵². Only in the case of excellent resolution, the charge state and thus the mass can be deduced from the isotopic pattern of the respective peak alone. The resolution for the signal in a (native) mass spectrum can generally be estimated using the full width half maximum (FWHM). Wide peaks thus indicate low and narrow peaks high resolution.

When discussing mass spectrometry, the resolution R is defined as the ability to separate ions of different m/z and can be calculated as follows.

$$R = \frac{m}{\Delta m} = \frac{\frac{m}{z}}{\Delta \frac{m}{z}}$$

Equation 8

In this, Δm or $\Delta(m/z)$ refers to the peak width of a specified fraction of the maximum peak height that is either 50%, 5%, or 0.5%^{53,54}. Resolution must not be confused with resolving power, which describes the ability of the instrument or method to distinguish between two adjacent peaks with very similar m/z . The peak width in mass units is given to express the resolving power⁵⁴.

Ideally, native MS reveals the charge-state distributions of all mass species, including any intermediates, present in the sample in solution (**Figure 5**). The mass can be deduced from the m/z values of neighboring peaks in a charge-state distribution, where charge states of the same species differ in z by 1. For similar sized analytes, the signal intensity is proportional to the analyte concentration. However, large oligomeric complexes deviate from this direct correlation at higher concentrations, which hampers a reliable quantification⁵⁵. Nevertheless, semi-quantification and hence characterizing binding affinities is possible as has been shown in antibody dimerization⁵⁶. Determining the mass of a species of interest is not always sufficient to deduce its stoichiometry so that further degrees of separation (e.g., ion mobility MS) or tandem MS (MS^n) fragmentation approaches are necessary.

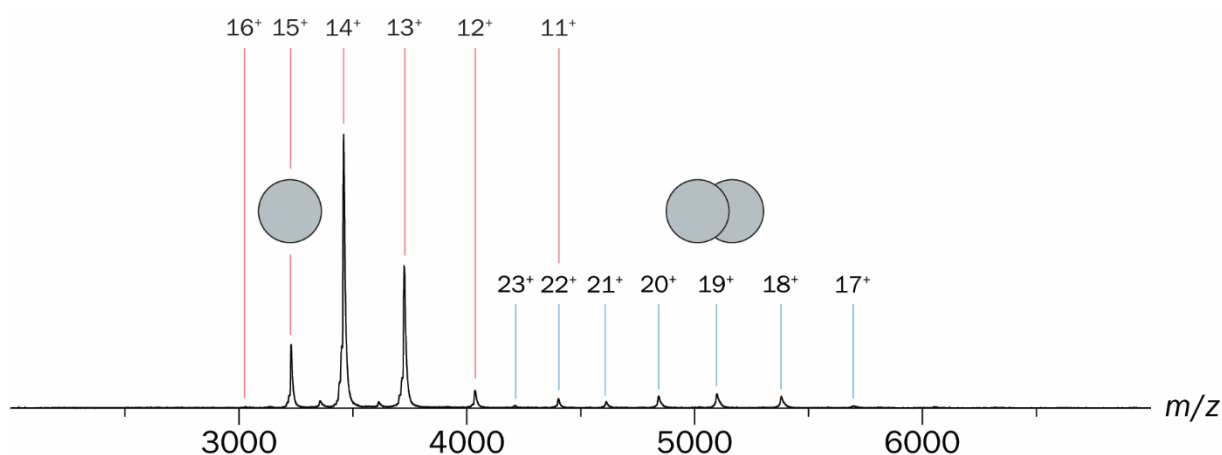


Figure 5 | Exemplary native ESI mass spectrum of a protein complex.
Dimeric (blue) and monomeric (red) state are detected simultaneously.

A mass analyzer separates the previously generated ions according to their m/z and passes them in focused state to the detector. The separation of the ions can be spatial or temporal, depending on the type of analyzer. The choice of mass analyzer affects the resolution, accuracy, and range of the measurement.

1.1.1.3.1 Quadrupole

A quadrupole (Q) analyzer (**Figure 6**) is able to pass on only ions with a certain m/z value over short time intervals (ms to s), thus providing temporal separation. A Q consists of four parallel rod electrodes, about 20 cm long, which are arranged in a square cross-section³⁵.

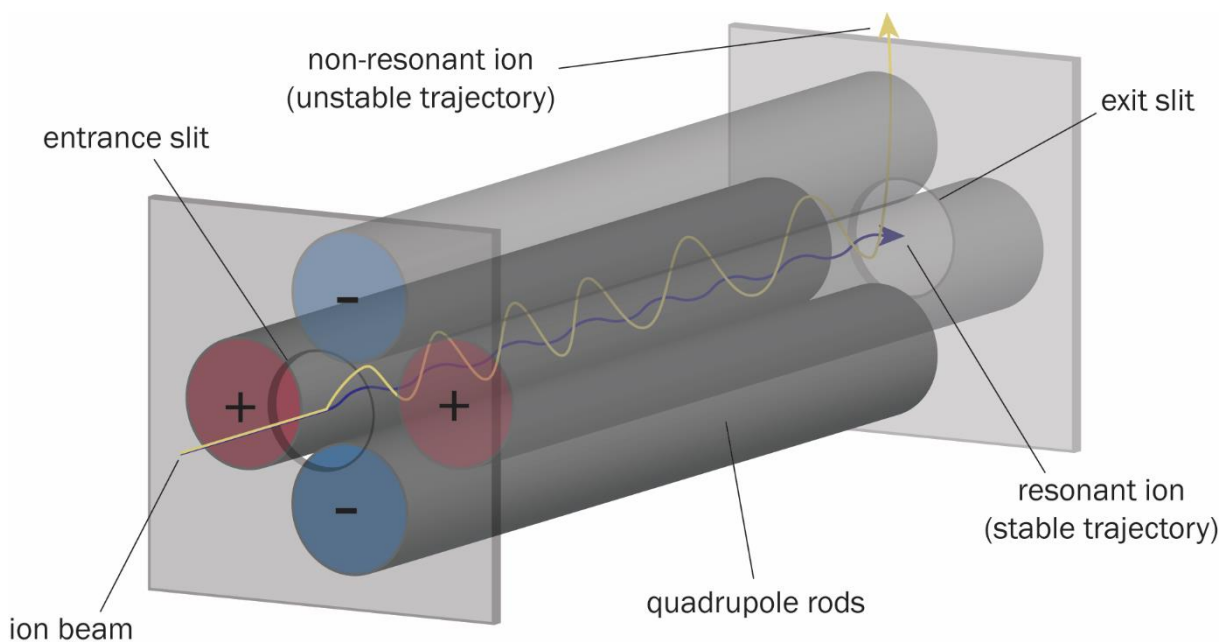


Figure 6 | Schematic representation of a quadrupole mass analyzer.

The voltage applied to the electrode rods causes entering ions to oscillate. Ions that oscillate too much have an unstable trajectory. They strike the rods or the housing of the Q. Only ions with a certain m/z value can pass through the Q.

The bars opposite each other are electrically coupled. They are each subject to the same electrical potential, which is composed of a DC and a high-frequency AC component. The applied voltage is periodic, generating inhomogeneous electric fields that allow the oscillating ions to propagate along the analyzer^{35,11}. Depending on how the voltages are applied, the Q can be used for simple transmission of the ions or as a mass filter. If voltages and radiofrequency is varied but their ratio is kept constant ions of different m/z will pass through the Q. In mass filter mode, the electric fields resulting from the voltages applied specifically separate the ions according to their m/z values³⁵. Only ions within the selected m/z range (resonant) will pass through, the non-resonant ions cannot pass due to an unstable trajectory^{57,58}.

1.1.1.3.2 Time-of-Flight

In a time-of-flight (TOF; **Figure 7**) mass analyzer, spatial separation of ions with different m/z values occurs along a field-free drift path of known length^{11,59}. Linear TOF analyzers are 1-2 m long evacuated tubes that the ions must pass through on their way to the detector³⁵. A *pusher* deflects the ion stream 90° so that all entering ions experience the same acceleration of the TOF^{35,11}. Ion separation occurs based on momentum, which in turn depends on the m/z value, since lighter ions can move faster than heavier ones.

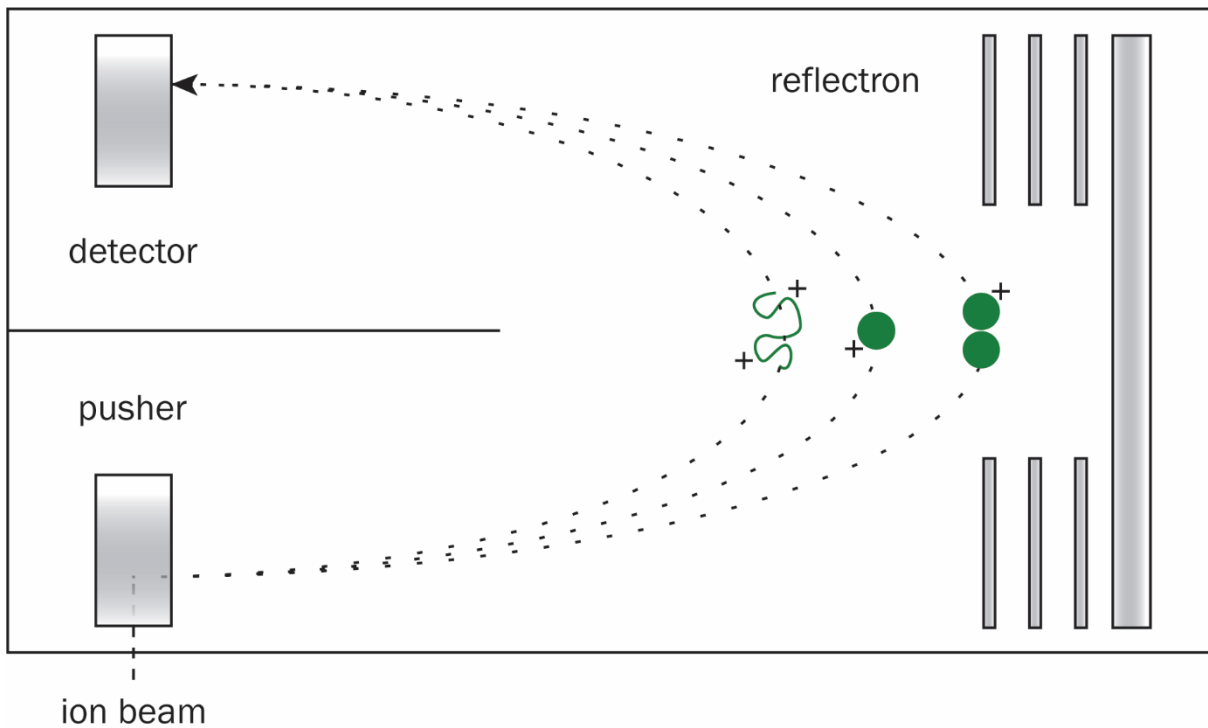


Figure 7 | Schematic representation of a TOF mass analyzer.

Bundled ions are introduced into the TOF by the pusher at a 90° angle. According to their m/z values, the ions develop different trajectories, allowing them to be detected at different times. A reflectron increases the resolution by improving the focusing of like ions.

The charge q of an ion of mass m is given by the number z of elementary charges e (**Equation 9**).

$$q = e \cdot z$$

Equation 9

The electric energy E_{el} of an ion under the influence of the electric potential U is defined as expressed in **Equation 10**.

$$E_{el} = q \cdot U = e \cdot z \cdot U$$

Equation 10

The acceleration of the ion in the electric field presents a transformation of the electric energy E_{el} into kinetic energy E_{kin} (**Equation 11**).

$$E_{el} = e \cdot z \cdot U = \frac{1}{2} \cdot m \cdot v^2 = E_{kin}$$

Equation 11

Assuming that the ion was at rest before the acceleration, the following mathematical relationship therefore applies to the velocity v (**Equation 12**).

$$v = \sqrt{\frac{2 \cdot e \cdot z \cdot U}{m}}$$

Equation 12

Applying the law of velocity to the equation results in the following expression for the time of flight t of the ion at constant velocity v (**Equation 13**).

$$t = \frac{s}{v} = \frac{s}{\sqrt{\frac{2 \cdot e \cdot z \cdot U}{m}}}$$

Equation 13

Therefore, the time t that the ion needs to traverse distance s is proportional to the square root of its m/z (**Equation 14**).

$$t = \frac{s}{\sqrt{2 \cdot e \cdot U}} \cdot \sqrt{\frac{m}{z}}$$

Equation 14

Thus, to calculate m/z of an ion, it is sufficient to record the time t required by the ion accelerated by the voltage U to cover the distance s (TOF length). The detection of ions takes place within microseconds. In mass spectrometers, ion detection is usually performed by using secondary electron multipliers, in which the ions strike a surface from which electrons are then emitted. The accelerated electrons in turn strike a surface, from which more electrons are subsequently released. Repeating this process many times creates a cascade of electrons that generates a current. This current can also be electronically amplified. The signal is recorded and eventually visualized³⁵.

Higher resolution can be achieved by using reflectors or orthogonal injection of the ions. Combinations of different analyzers (MS^n) such as Q-TOF can generate more information from one measurement and increase the sensitivity of the measurement³⁵.

1.1.1.3.3 Orbitrap™

The invention of the orbital ion trap, Orbitrap™, was a major breakthrough concerning high-resolution MS^{60-63} . Ion packets entering the Orbitrap™ are directed to orbit the spindle-shaped electrode located in the core by ramping the electrode's potential. A second outer barrel-like electrode encases the ion trap. The ions are injected off center, therefore they not only oscillate in a simple circular path, but also move axially along the inner electrode resulting in an intricate spiral trajectory^{60,61,64}. The motion of the ions along the longitudinal axis of the electrode corresponds to a harmonic oscillator whose frequency, unlike the

rotational or radial motion, is independent of the energy or spatial spread of the ions⁶⁰. The identification of the ions' m/z ratios is based only on the axial frequency. An image current is induced on the outer electrode by the oscillation, which is recorded and assigned to a corresponding m/z using Fourier transform operations^{60,62,65,66}.

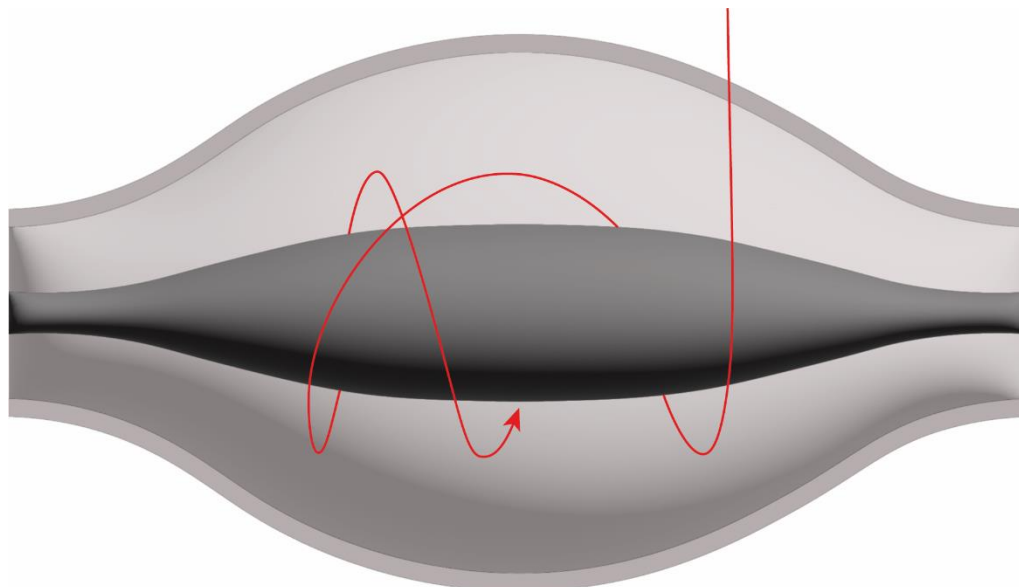


Figure 8 | Schematic representation of an Orbitrap™ mass analyzer.

The ion packets are injected into the ion trap at a remove from the center. They orbit around the core electrode on elliptical trajectories. From the frequency of the axial oscillation, the m/z of the ions can be determined.

The special design of the Orbitrap™ allows mass analysis with very high resolution and accuracy⁶⁴. With instruments optimized for high-mass ion analysis, even large biological complexes such as virus particles can be detected with high resolution⁶⁷⁻⁷¹.

1.1.1.4 Protein structures within the gas phase

The charge acquired during the ESI process allows protein manipulation and detection in the gas phase, opening the door to the application of methods that are incompatible with having the protein in solution. For example, to detect the stoichiometry unambiguously, a complex ion can be selected in a mass analyzer and dissociated subsequently. The first time a protein structure was analyzed by ESI-MS was in 1990 when CHOWDHURY *et al.* were able to show a correlation between the folding of bovine cytochrome C and the number of charges adopted⁷². As unfolding increased due to the addition of higher concentrations of acetic acid, the charge states found in the spectrum were significantly higher. This is due to the larger solvent-exposed surface area available^{73,74}. Higher charge states are usually the result of COLOUMB repulsion-induced unfolding into extended helical or ultimately string-like structures, whereas the protein remains compact at low charge states^{25,75-78}.

1.1.1.4.1 Locked up in-solution structures

Native MS is an appropriate technique for the analysis of proteins and protein complexes because their in-solution structures are largely preserved by ESI^{22,36,79}. As a result of evaporative cooling, compact structures can be kinetically trapped over several milliseconds, even if extended structures would be considered energetically preferable for gas phase^{80,81}. Using ion mobility MS, which can also distinguish ions of the same m/z but different shape, it was shown that the gas-phase conformations of proteins agreed well with structural models obtained by complementary in-solution methods^{23,76,82-84}. Furthermore, spectroscopic techniques were used to investigate conformational differences between proteins in gas phase and aqueous phase with the result that these were rather small and protein folding is maintained^{25,85-89}. In so-called soft-landing experiments, the native-like structure was verified by EM even after MS analysis^{90,91}. However, there are exceptions where either COULOMB-induced unfolding occurs, or the structures collapse in the gas phase⁹²⁻⁹⁴. For small proteins such as ubiquitin, secondary and tertiary gas-phase structures that were not consistent with a native state were also shown via electron capture dissociation⁹⁵. Although the degree to which the in-solution structure of a protein or complex is preserved by native MS is still controversial, it has been amply demonstrated that gas-phase structure can reflect many important aspects of the native structure.

1.1.1.4.2 Protein-ligand interactions

Since many biological processes such as transcriptional regulation, cell differentiation, immune response, cell adhesion, or inflammation rely on specific protein-ligand interactions, their investigation is of high importance, especially with regard to the identification of new drug targets^{96,97}. In addition to the exploration of protein-protein interactions in homo- or heterooligomeric complexes, native MS offers the possibility to probe the binding of a protein and its specific ligands^{79,97-101}. When a ligand, e.g., a peptide, nucleic acid, lipid, carbohydrate, or other small molecule, binds to the protein under investigation, a new peak appears in the spectrum that correlates with the mass of the resulting protein-ligand complex. Thus, the number of binding sites can be determined, the binding strength or affinity for known ligands can be estimated, or completely new ligands can be discovered. In all these analyses, it is mandatory to distinguish between specific binding and nonspecific clustering, which can occur as a result of artifact formation in the ESI process. The use of a non-associated reference species, protein or ligand, can help to accurately determine the effect of clustering and correct for it in the final analysis¹⁰²⁻¹⁰⁵.

Just recently, SCHULTE *et al.* reviewed in detail the ways in which native MS is used to determine binding affinities between protein and ligand¹⁰⁰. Briefly, this can be done either by titration experiments¹⁰⁶⁻¹¹⁴, by competition between two ligands for the same binding site¹¹⁵⁻¹²⁰, or by single point measurements where the peak height or area directly reflects the concentration of a component¹²¹⁻¹²³.

That native MS in the field of drug discovery can provide complementary data or entirely new insights compared to other techniques, some of them long established, such as isothermal titration calorimetry, surface plasmon resonance, NMR spectroscopy, X-ray crystallography, or cryo-EM, has been thoroughly discussed by GAVRIILIDOU *et al.*⁹⁶. Recently, in an extensive inhibitor screen for the SARS-CoV-2 main protease (M^{pro}) the binding of some compounds, which had previously been investigated by other techniques, could be verified by native MS⁶. This technique has advantages in terms of sensitivity, simplicity, speed, dynamic range, and sample consumption. Furthermore, there is the possibility of process automation, which even offers the potential for high-throughput drug discovery as seen in another recent ligand screen for M^{pro}^{96,124}.

1.1.1.4.3 Gas-phase dissociation of protein complexes

When analyzing protein complexes by MS, MSⁿ techniques, in which *m/z*-selected ions are selectively fragmented or dissociated, are indispensable¹²⁵. Herein, smaller product ions obtained from the precursor ions are subjected to mass spectrometric analysis yet again^{35,11}. This allows to identify the constituents of the complex and to understand its structure. A prerequisite for performing an MSⁿ experiment is a combined setup of the spectrometer that allows an at least two-step mass analysis (MS²). For this purpose, collision-induced dissociation (CID) is mostly used, in which additional energy is imparted to the analyte ions via high-velocity collisions with heavy inert gas atoms. As the ions collide with the collision gas (e.g., argon, xenon, or nitrogen), part of the kinetic energy of the ion is converted into vibrational energy. This gradually increases the internal energy of the ion until individual subunits of a noncovalent complex unfold and are eventually ejected from the complex one-by-one⁴³.

To employ CID, the mass spectrometer requires a collision cell upstream of the second mass analyzer, in which a constant pressure of about 1.5⁻²-10⁻² mbar is set with the help of the collision gas^{126,35,11}. Dissociation is usually not controlled by pressure, but by adjusting that voltage which accelerates the ions from the first analyzer into the collision chamber³⁵. At low energy, the MS² spectrum of a protein complex shows the peak of the selected ions (precursor) alone. With increased the collision energy, regulated via the

acceleration voltage, new signals emerge in the low- and high- m/z regions, representing the CID products. Initially, the weakest noncovalent bond will be broken, which is why small, peripherally localized subunits first exit the complex. While the smaller fragments can be detected in the lower m/z region, the residual complex loses charge due to the repulsion of a fragment and can therefore be found in the higher m/z region. (**Figure 9**)

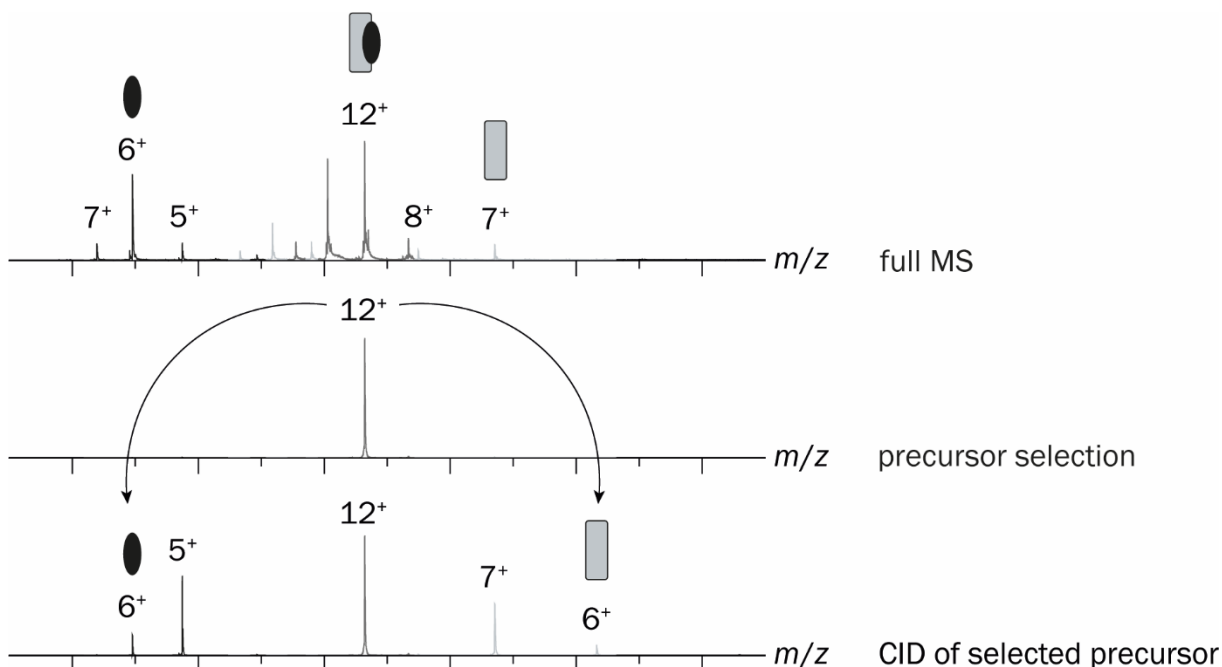


Figure 9 | Representative MS² spectra of a CID experiment.

The spectrum of the normal MS mode is shown at the **top**. The **middle** spectrum shows the peak of the ions selected in the Q. In the **bottom** spectrum, the same m/z region was selected, but the energy of the system was increased by raising the acceleration voltage. As a result, the signals of the dissociation products of the protein complex appear to the left and right of the parent peak, respectively.

Mass information obtained by the detection of the ejected subunits and the remaining subcomplexes unequivocally proves stoichiometry of the original complex. The order of subunit ejection also correlates with peripheral location in the complex and thus provides even more insight into complex architectures. Notably, this dissociation behavior is usually distinct from what is observed in solution, where it is a spontaneous (often reversible) equilibrium reaction rather than an irreversible consequence of physical collisions with gas molecules¹²⁷. The described method is especially informative if a specific complex species is singled out according to its m/z in the gas phase before CID occurs, so that dissociation products can be traced back to one single complex species.

In principle, any combination of protein fragmentation with (native) MS analysis of intact proteins is called top-down MS. When harsh CID conditions are used, backbone fragmentation of the intact protein occurs on top of subunit dissociation of the protein complex. At high collision energy, the selected ions are ruptured, *i.e.*, chemical bonds break, so that the intensity of the precursor peak decreases. In the case of CID, proteins

fragment along peptide bonds to form b and y ions. Additionally, these backbone fragmentations are often induced by other fragmentation techniques such as ultraviolet photodissociation and infrared multiphoton dissociation¹²⁸, impacts with a surface¹²⁹ or electron transfer reactions¹³⁰ in the gas phase. Thus, information about the primary structure of a protein, its PTMs as well as its presence in a complex can be obtained. For example, top-down approaches have been used to predict transmembrane regions of Hepatitis C virus p7 viroporin sprayed from detergent micelles based on the observed CID fragmentation pattern¹³¹. Furthermore, the existence of PTMs can be derived from fragmentation patterns, e.g., the complex glycosylation profile of influenza hemagglutinin¹³².

1.2 Immune regulation via the major histocompatibility complex

Parts of this chapter have been published in either of the following studies:

Anjanappa, R., Garcia-Alai, M., **Kopicki, J. D.**, Lockhauserbäumer, J., Aboelmagd, M., Hinrichs, J., Nemtanu, I. M., Uetrecht, C., Zacharias, M., Springer, S., & Meijers, R. (2020). Structures of peptide-free and partially loaded MHC class I molecules reveal mechanisms of peptide selection. *Nature communications*, 11(1), 1314².

Reprinted from ANJANAPPA *et al.* (2020). Copyright © 2020, The Author(s).

Dirscherl, C., Löchte, S., Hein, Z., **Kopicki, J. D.**, Harders, A. R., Linden, N., Karner, A., Preiner, J., Weghuber, J., Garcia-Alai, M., Uetrecht, C., Zacharias, M., Piehler, J., Lanzerstorfer, P., & Springer, S. (2022). Dissociation of β_2m from MHC class I triggers formation of noncovalent transient heavy chain dimers. *Journal of cell science*, 135(9), jcs259489³.

Reprinted from DIRSCHERL *et al.* (2022). Copyright © 2022, The Author(s).

Kopicki, J. D., Saikia, A., Niebling, S., Günther, C., Anjanappa, R., Garcia-Alai, M., Springer, S., & Uetrecht, C. (2022). Opening opportunities for K_d determination and screening of MHC peptide complexes. *Communications biology*, 5(1), 488⁴.

Reprinted from KOPICKI *et al.* (2022). Copyright © 2022, The Author(s).

Vertebrates are equipped with a complex system of immune defense. The specific or adaptive immune response refers to the organism's acquired cellular (T lymphocytes) and humoral (antibodies from B lymphocytes and plasma cells) immune response, which is directed against specific antigens such as certain proteins of a pathogenic microorganism. The reactions that occur as part of the specific immune response are based on the processing and presentation of these antigens. Responsible for the presentation are several cell surface proteins encoded in a highly polymorphic DNA locus, the major histocompatibility complex – named as such because of its first discovery during a study on transplanted tissue compatibility¹³³. In humans, the MHC region contains 224 genes with over 3.6 megabase pairs. The genes are located on the short arm of chromosome 6 between the flanking genetic markers MOG and COL11A2¹³⁴. The human MHC complex is more specifically referred to as human leukocyte antigen (HLA)¹³⁴. Specific terms for the MHC homologues in other species are e.g., H-2 in mice¹³⁵, RT-1 in rats^{136,137}, or B-locus in chickens¹³⁸.

There are three distinct subgroups in the MHC gene family: MHC class I, MHC class II and MHC class III (MHC-I/II/III). All nucleated cells bear immunogenic peptide+MHC-I complexes. Infected cells and tumor cells, which both produce aberrant proteins, are identified by peptide presentation on the cell surface via the MHC-I pathway before being eliminated by cytotoxic T cells (CD8⁺; CTL)¹³⁹. In turn, via the MHC-II pathway, T helper cells (CD4⁺) can stimulate the production of highly specific antibodies as well as the activity of phagocytes. These are then able to inactivate and eliminate pathogens in body fluids as part of the humoral immune response. MHC-II proteins are found on so-called professional antigen-presenting cells, *i.e.*, B cells, dendritic cells, and macrophages¹³⁹. Both classes

have in common that the respective MHC proteins present peptides on the cell surface, and subsequently, the clonotypic T cell receptor interacts with the respective peptide MHC protein complex. If necessary, cell-cell contact is sustained and the activation of T cells is induced.

1.2.1 MHC structure

In terms of structure, the proteins of MHC-I and MHC-II are highly similar (**Figure 10**). Both molecules are heterodimers comprised of two noncovalently linked polypeptide chains. Two α helices at the top and a slightly bent β sheet at the bottom together form a cavity, in which a peptide can bind. The respective domains are α_1 and α_2 in MHC-I or α_1 and β_1 in MHC-II.

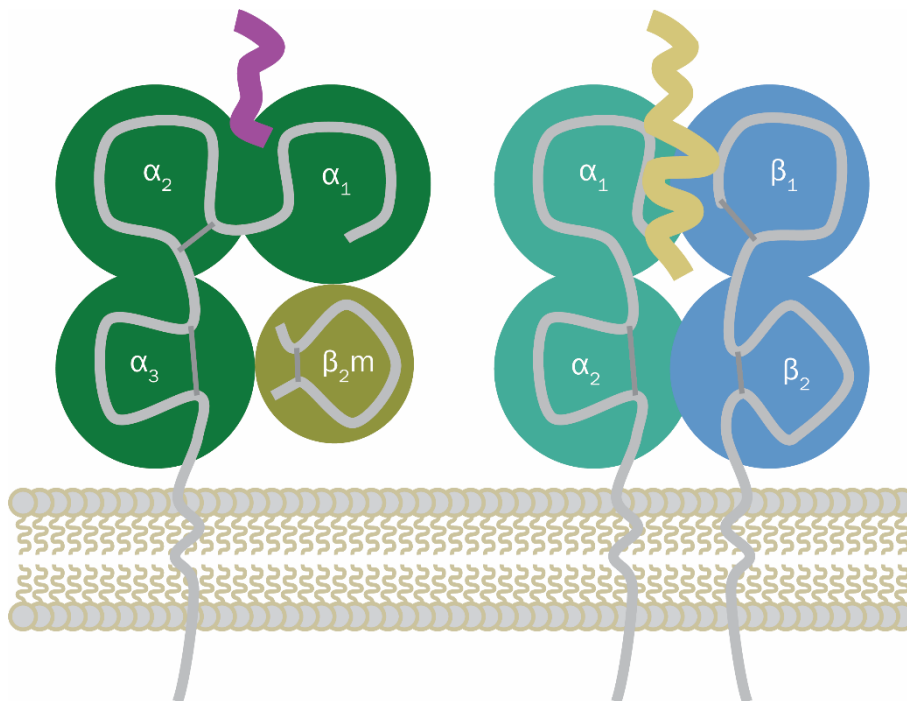


Figure 10 | Schematic structures of MHC class I and II.

Both protein complexes – MHC-I (left) and II (right) – have a transmembrane region and four distinct subunits (α_1 , α_2 , α_3 and β_2m vs. α_1 , α_2 , β_1 and β_2) corresponding to certain domains within the respective gene segment. Disulfide bridges are illustrated as dark gray lines.

This peptide-binding structure is supported by two membrane-proximal domains featuring an immunoglobulin-fold (Ig) structure. Each of the two chains in MHC-II contains one Ig domain, namely α_2 and β_2 . In MHC-I, the three subunits α_1 , α_2 and α_3 are connected covalently. Their entirety is also called the heavy chain (HC). Here, the Ig-type domains are given by the strongly conserved α_3 domain and the non-polymorphic, soluble light chain beta-2 microglobulin (β_2m), which interacts noncovalently with the HC. MHC-I HC and both MHC-II chains are anchored in the membrane via transmembrane helices¹³⁹. The peptide binding groove in MHC-I accommodates peptides derived from proteolysis of endogenously

expressed proteins, usually consisting of 8-10 amino acids¹⁴⁰. The size restriction is caused by two conserved tyrosine residues situated at both ends, which close the peptide-binding groove. In turn, the binding cleft of MHC-II has an open structure, allowing longer peptides (13-35 residues) to bind. Here, the peptidic *N* and *C*-termini protrude from the peptide-binding groove.

Due to the high allelic variation within the genetic regions encoding MHC-I (HLA-A, HLA-B and HLA-C) and MHC-II (HLA-DR, HLA-DP and HLA-DQ), the peptide-binding groove is very polymorphic. This eventually results in the diversity of peptides being bound and presented by MHC-I and -II, accordingly¹³⁹. About 16,000 MHC-I allotypes have been described to date, with nine of them found in > 75% of the Caucasian and Asian populations¹⁴¹.

Structure and function of MHC-III gene products is poorly defined compared to their counterparts in the first two subgroups. MHC-III proteins are not involved in antigen binding or presentation. Instead, MHC-III encodes diverse signaling molecules within but also outside the immune context. These include various tumor necrosis factors as well as heat shock proteins¹⁴²⁻¹⁴⁵.

1.2.2 MHC class I

Major histocompatibility class I molecules fulfil central tasks of the adaptive immune response against infections and malignancies by presenting antigenic peptides to T cells¹⁴⁶⁻¹⁴⁸. They bind peptides in the lumen of the endoplasmic reticulum (ER) and present tightly binding (high-affinity) peptides on the cell surface for recognition by CTLs, which detect non-self-peptide+MHC-I combinations and induce apoptosis in the presenting cell¹⁴⁶.

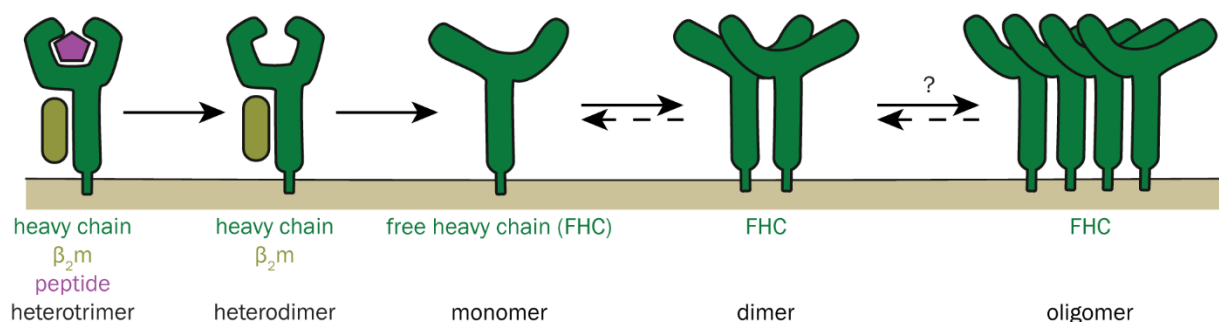


Figure 11 | Schematic of MHC-I states at the plasma membrane.

Dissociation of peptide from the HC+ β_2m +peptide trimer results in an “empty” HC+ β_2m heterodimer. Dissociation of β_2m then produces FHCs, which can form FHC associations (HC+HC dimer and oligomer shown)³.

MHC-I heterotrimers consist of the polymorphic transmembrane heavy α chain, the invariant light chain β_2m , and a peptide^{146,149}. In addition to this trimer, two more states of

MHC-I occur at the cell surface, the “empty” HC+ β_2m heterodimer that lacks a peptide^{150,151}, and the monomeric “free” heavy chain^{152,153}. Since the binding of peptide and β_2m is cooperative^{154,155}, HC+ β_2m heterodimers are conformationally unstable, and loss of the peptide leads to the rapid formation of FHCs (**Figure 11**) and to the subsequent endocytic removal of FHCs by a sorting mechanism that is not understood¹⁵¹.

For FHCs present at the cell surface, important regulatory functions mediated by homo- and heteromeric interactions in *cis* and *trans* have been proposed¹⁵⁶⁻¹⁵⁸, which suggest defined spatiotemporal organization and dynamics of FHC in the plasma membrane. Indeed, clustering and covalent dimerization of MHC-I have been identified using a variety of approaches including recombinant proteins and live cells¹⁵⁹⁻¹⁷². Complexes of different and largely unclear composition, size and type of intermolecular bonding were found.

1.2.2.1 Peptide binding and editing

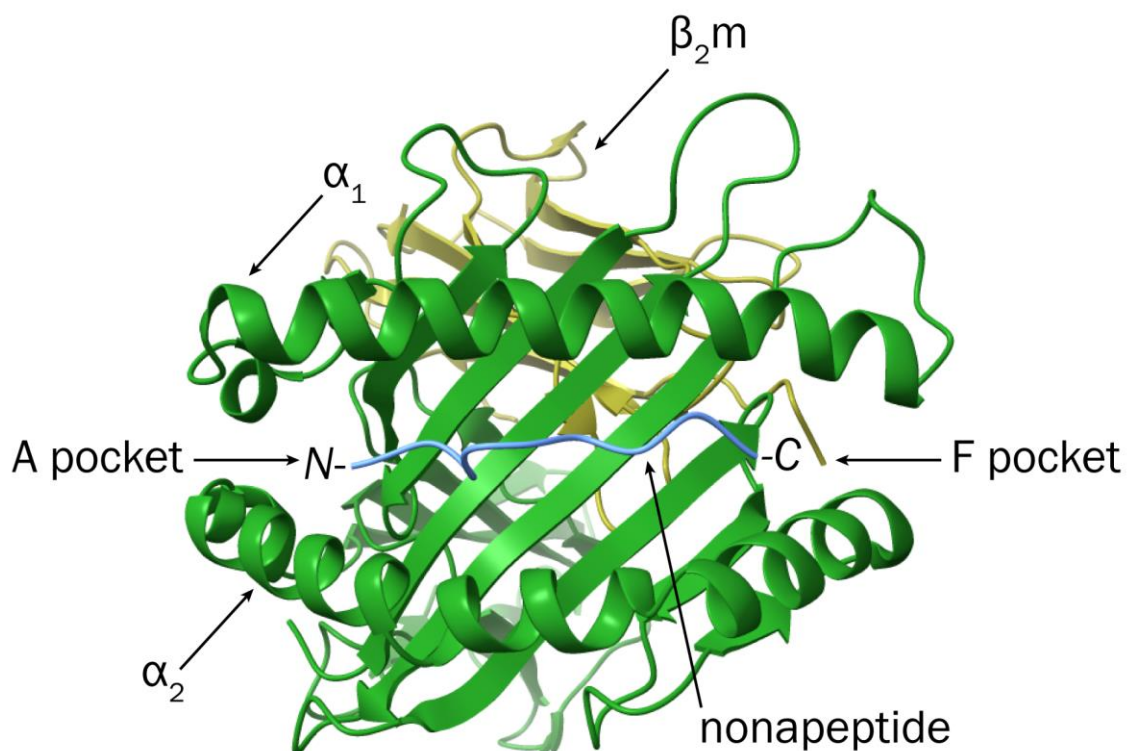


Figure 12 | Overview of the MHC-I peptide binding groove.

An exemplary MHC-I complex is seen as top view of the peptide pocket, which is edged by the two helices α_1 and α_2 . β_2m is shown in olive and the HC in green. The nonapeptide's (blue) N-terminus binds into the A pocket, its C-terminus is located in the F pocket. (PDB: 6Q3K^{173,174}).

A thorough understanding of binding and selection of high-affinity peptides by MHC-I molecules is essential for the design of peptide vaccines and for the analysis and prediction of CTL responses to infection and cancer¹⁷⁵. So far, the structural basis of MHC-I peptide binding is well understood¹⁷⁶, with > 1500 human MHC+peptide (pMHC) structures in the protein data bank¹⁷³. As briefly mentioned above, the peptide binds into a groove that

consists of eight β strands topped by two parallel α helices, with its *N*-terminus contacting the A pocket at one end of the groove¹⁷⁷ and the *C*-terminal carboxylate held by a network of hydrogen bonds at the other end^{140,178} (**Figure 12**). Further hydrogen bonds between the side chains of the MHC molecule and the backbone of the peptide contribute to the binding¹³⁹. In addition, side chains of the peptide, usually two, bind into other pockets at the bottom of the groove; one of them is always the F pocket – usually binding the hydrophobic side chain of the *C*-terminal amino acid. However, it will depend on the geometry, charge distribution, and hydrophobicity within the pocket how exactly the individual amino acid residues interact with the binding groove¹³⁹. Together, these interactions define the peptide-binding motif of a particular MHC-I allotype (such as xLxxxxxV for HLA-A*02:01). In general, these so-called anchor residues of the peptide are located in position 2,5 or 6 from the *N*-terminus, along with the *C*-terminally positioned amino acid¹⁷⁹. It was demonstrated that it is also possible for peptides longer than ten amino acids to bind into an MHC-I peptide groove. This inevitably bends the peptide and the central residues are pushed out of the pocket¹⁸⁰⁻¹⁸³.

An effective and specific immune response requires that pMHCs are kinetically stable for presentation at the cell surface^{184,185}. To ensure kinetic stability of pMHCs, high-affinity peptides must be acquired. Such high-affinity peptides have a low dissociation rate, which depends on tight binding to defined pockets of the binding groove, among them the A pocket (which binds the amino terminus of the peptide) and the F pocket (which binds the carboxy-terminal side chain of the peptide)¹⁷⁷. It is generally assumed that initially, just after folding of the HC and its association with β_2m in the lumen of the ER, the peptide-binding site is occupied by low-affinity peptides, followed by iterative peptide exchange and cellular quality control such that the MHC-I molecule is associated with high-affinity peptides when it reaches the cell surface¹⁸⁶⁻¹⁸⁸. This process, known as peptide editing, which removes unstably bound peptides and then replaces them with strongly binding peptides, is realized by the so-called peptide-loading complex (PLC)^{175,189-192}. Directly after expression, the heterodimer consisting of HC and β_2m is incorporated into the PLC¹⁸⁹. The transporters associated with antigen processing (TAP1 and TAP2) translocate proteasomal degradation products from the cytosol to the ER lumen, thereby maintaining high local peptide concentrations next to the MHC-I^{184,190,193}. Further components of the PLC are oxidoreductase ERp57 as well as chaperones calreticulin and tapasin^{190,192,194}. Tapasin supports peptide binding by two independent mechanisms, which is evident from the fact that the expression of tapasin increases the amount of long-lived pMHCs on cell surface. First, tapasin protects peptide-empty MHC-I molecules from denaturation (chaperone

function), and second, it catalyzes peptide binding and exchange (peptide optimization function). Binding of a high-affinity peptide triggers tapasin to release the pMHC, which is subsequently transported to the cell surface to present the antigenic peptide bound^{185,195-198}. It was shown that during both loading and exchange of peptides, MHC proteins undergo changes in conformational dynamics¹⁹⁹⁻²⁰².

1.2.2.2 Peptide presentation

Peptide presentation by MHC-I is a crucial process in the immune system to monitor the cell's entire proteome, and to identify and destroy abnormal cells, *i.e.*, virally and bacterially infected cells or cancer cells. The specificity of this immune response is determined by the peptide presented^{147,203-205}. The variety of peptides presented is in turn driven by the activity of proteasomes and peptide transporters in the cell. Once a kinetically stable pMHC is established in the ER and released by tapasin, the complex is recruited into cargo vesicles, and consequently transported via the Golgi apparatus to the plasma membrane where it can be recognized by CTLs^{196,204,206}. These carry T cell receptors (TCR) that bind the pMHC with their highly polymorphic complementary determining regions. The majority of all TCR+pMHC structures resolved so far show contact of the TCR with both the peptide and the MHC²⁰⁷. In addition, the CD8 co-receptor increases antigen recognition by stabilizing the TCR-pMHC-I binding. CD8 mainly binds the invariant region α_3 of the MHC-I, further interaction to α_2 and β_2m was shown²⁰⁸⁻²¹⁰. This recognition process between TCR and pMHC takes place at two different times in the life of a T cell: first, naïve T cells may be activated by antigen-presenting activated dendritic cells in the lymph nodes, leading to the activation of the T cell; and second, activated T cells probe tissue cells in the environment of an inflammation, and if they recognize a pMHC-I containing a non-self peptide, they destroy the infected or transformed cell. The first process also supports the development of immunological memory. Once a CTL was activated by encountering a particular pMHC-I, it divides to produce many daughter cells. Some of these daughter cells will differentiate into memory T cells that will be able to quickly respond if the same peptide is encountered in the future²¹¹⁻²¹³.

1.2.3 Identifying epitopes for vaccines and immunotherapy

The identification of high-affinity virus- or tumor-specific peptide epitopes is the key to novel immunotherapy approaches, in which antiviral or antitumor CTLs are identified, stimulated, and reintroduced into the patient, and to developing efficacious peptide vaccines (as prioritized by the WHO²¹⁴). In terms of production effort, shelf-life and mutation risk,

peptide vaccines outperform conventional vaccines. Finding important epitopes across alleles has been rather difficult due to the polymorphic nature of human MHC²¹⁵. This is currently achieved either by isolating pMHCs from patient samples, eluting the peptides, and sequencing them by MS²¹⁶; or by sequencing the virus or the exome of a tumor and predicting MHC-binding peptides²¹⁷. Since this approach is highly time- and resource-consuming, the research community has long sought to make accurate *in silico* predictions of allotype-specific antigen-MHC interactions¹³⁹. In the meantime, bioinformatics algorithms for such have been continuously optimized²¹⁸. Structural knowledge and extensive databases of eluted peptides have informed the computational methods that predict tumor epitopes²¹⁸. This approach, however, suffers from the uncertainty created by matching the eluted peptide to one of the 4-6 MHC-I allotypes present in a human being. The predictions to date are not precise enough, false positives occur, and the immunological significance of predicted epitopes is often not given^{219,220}. Hence, to accelerate biological testing, it is desirable to rank candidate peptides by their binding affinity using a direct approach. Yet, to date, simple equilibrium binding assays that support high-throughput screening are not available because they require empty peptide-receptive MHC-I molecules, which are conformationally unstable^{140,221}.

2 Objectives

The aim of this work was to structurally characterize the major histocompatibility complex class I in the presence and absence of peptides using native mass spectrometry and to develop a screening for potential T cell epitopes based on the findings.

Extensive research has been conducted to examine MHC-I molecules bound to either a full-length peptide or a partial peptide, but limited information was available on the structure of these molecules in the empty state so far. An empty wild type MHC-I molecule dissociates because the complex is not stabilized without a peptide in the binding pocket. However, since regulatory functions related to hormones, growth factors, cytokines, and neurotransmitters have already been postulated for the isolated heavy chain¹⁵⁶⁻¹⁵⁸, we took an integrative approach to shed light on the stoichiometry and conformation of the open conformer MHC-I. Since my collaborators had been able to stabilize MHC-I independently of peptides and only with the help of an additional disulfide bridge before²²², this allowed us to conduct structural investigations on the empty but closed conformation *i.e.*, the binding groove in its native form.

Furthermore, peptide binding to both, wild type and disulfide-stabilized MHC-I was ought to be investigated and compared. We were interested whether the empty, stabilized molecule can bind peptides as well as the wild type, and which properties at the sequence level of the peptide ensure particularly stable binding. Another goal was to quantify the binding, *i.e.*, to estimate the dissociation constants via a direct read-out of the native mass spectrum. It was already shown that peptides smaller than the optimal 8-11-mers bind MHC-I as well^{221,223}. We aimed to analyze whether two peptides can be accommodated within the binding groove at the same time, and if so, whether the peptide fragments would have a synergistic effect with respect to the binding energy, *i.e.*, whether this binding is cooperative, which could imply communication of both ends of the binding groove with each other.

Conventionally, peptide binding to MHC-I is probed by trying to fold the molecule *in vitro* with selected individual peptides, followed by testing whether the folding is facilitated, which is slow, tedious, and has a low-throughput. Another way is to elute peptides from MHC-I molecules isolated from cells, then identifying them by top-down mass spectrometry. At this, there is no way of probing a particular peptide of interest, and we are limited to the specific set of peptides produced by the cell. Additionally, eluted peptides will vary in solubility and ionization efficiency creating a bias. We therefore aimed to design a new

method to identify peptides that will bind to the MHC-I molecule of interest. The new concept would be to incubate empty MHC-I with any interesting mixture of peptides, and then detect high-affinity binders via the signal intensities of corresponding pMHCs in native MS. Ideally, bound peptides would be dissociated from the complex and fragmented afterwards for an unambiguous identification.

3 Results and discussion

3.1 MHC-I heavy chains form noncovalent dimers in absence of β_2m

Parts of the following chapter have been published in:

Dirscherl, C., Löchte, S., Hein, Z., **Kopicki, J. D.**, Harders, A. R., Linden, N., Karner, A., Preiner, J., Weghuber, J., Garcia-Alai, M., Uetrecht, C., Zacharias, M., Piehler, J., Lanzerstorfer, P., & Springer, S. (2022). Dissociation of β_2m from MHC class I triggers formation of noncovalent transient heavy chain dimers. *Journal of cell science*, 135(9), jcs259489³.

Reprinted from DIRSCHERL *et al.* (2022). Copyright © 2022, The Author(s).

3.1.1 Results

MHC class I complexes are heterogenic trimers, which are composed of a polymorphic transmembrane domain called heavy chain, a soluble light chain named beta-2-microglobulin, and a peptide^{146,149}. Other than this trimer, there are two additional states of MHC-I existing at the cell surface: the "empty" HC+ β_2m heterodimer, lacking the peptide^{150,151}, and the monomeric "free" HC^{152,153}. Given that peptide and β_2m binding is cooperative^{154,155}, HC+ β_2m heterodimers are conformationally unstable, and losing the peptide results in formation and subsequent endocytic removal of FHCs by a sorting mechanism that is not yet understood¹⁵¹. Important regulatory functions in connection with hormones, growth factors, cytokines, and neurotransmitters being mediated by homo- or heteromeric interactions have been proposed for FHCs residing at the cell surface¹⁵⁶⁻¹⁵⁸. Although both clustering and covalent dimerization of MHC-I have been identified numerous times¹⁵⁹⁻¹⁷², it was not possible to draw clear conclusions about the composition of the complexes or the nature of binding. DIRSCHERL *et al.* recently succeeded in directly detecting homomeric FHC interactions in the intact plasma membrane using a live-cell two-hybrid micropattern assay²²⁴, in which micrometer-sized patterns of anti-hemagglutinin tag monoclonal antibodies are printed on glass coverslips^{225,226}. These experiments showed that the formation of homomeric MHC-I occurs only in the absence of β_2m , *i.e.*, only between FHCs.

While my collaborators employed a combination of a micropattern assay with fluorescence recovery after photobleaching (FRAP), and single-molecule tracking (SMT) and co-tracking (SMCT) to further understand the molecular mechanisms of HC-HC interactions³, I used native MS to analyze the system structurally. The isolated, soluble α_3 domain of the murine MHC-I H-2K^b (K^b α_3), encoded by H2-K1, was expressed in *Escherichia coli* (*E. coli*), refolded *in vitro* and isolated by size-exclusion chromatography (SEC). The SEC chromatogram (**Figure 13A**) showed significant formation of homodimers, while no prominent higher-order

complexes were observed. Based on non-reducing gel electrophoresis, no disulfide bonds linked the detected α_3 homodimers (Figure 13B).

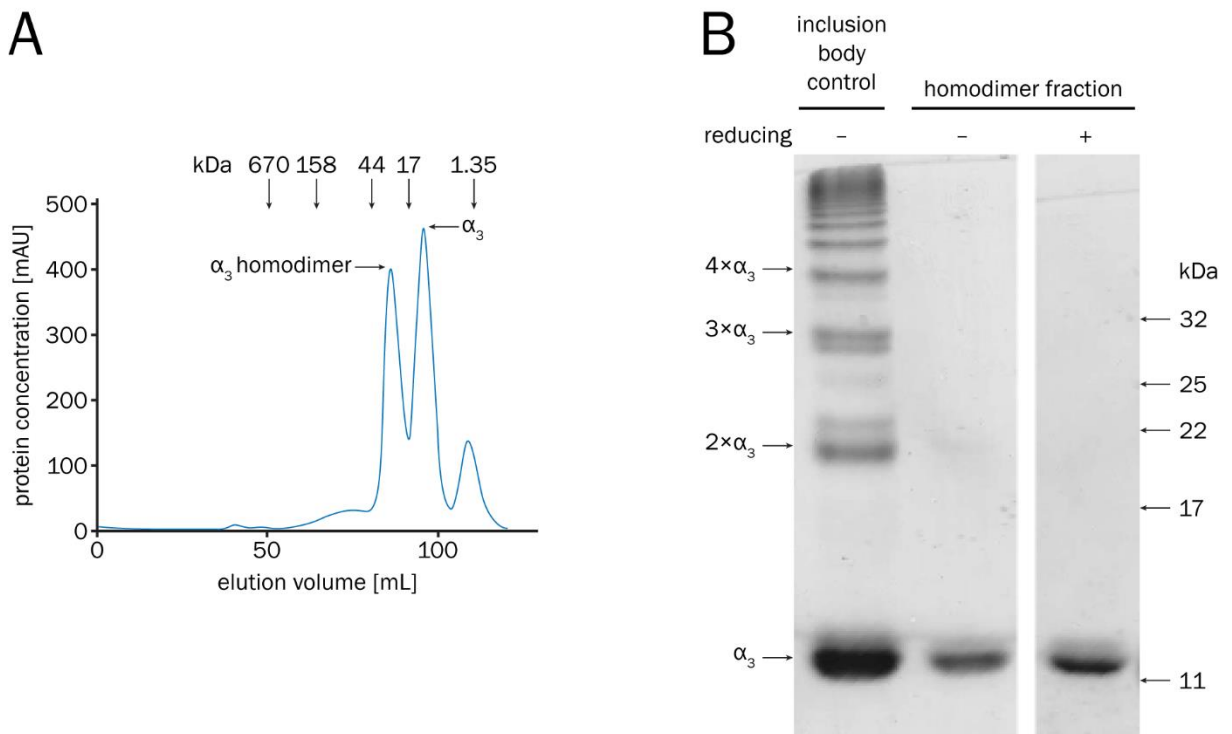


Figure 13 | The K^b α_3 domains form dimers.

A: Size-exclusion chromatography of the K^b α_3 domain expressed in *E. coli* and folded *in vitro*. **B:** Nonreducing SDS-PAGE of the α_3 domain homodimer fraction shows absence of disulfide linkage between the monomers. The positive control for disulfide-oligomer formation was α_3 inclusion bodies, isolated under oxidizing conditions, where some molecules are linked by disulfide bonds to form covalent oligomers as indicated on the left.

Both α_3 -containing SEC fractions were analyzed mass spectrometrically at three different concentrations – 5 μ M, 10 μ M and 20 μ M with respect to the α_3 monomer. Measurements were carried out at acceleration voltages of both, 10 V and 25 V to investigate potential CID effects as well.

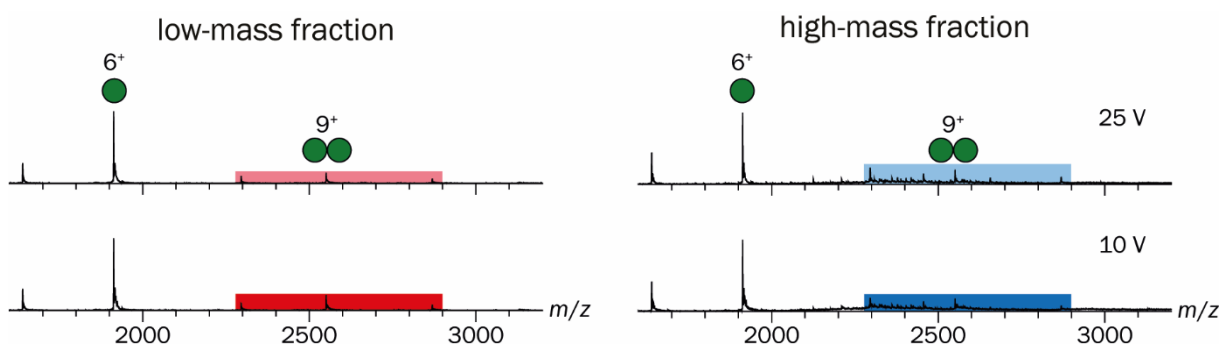


Figure 14 | Representative mass spectra of the K^b α_3 domain.

20 μ M α_3 domain was analyzed, respectively. Both spectra show the charge distributions of the α_3 monomer (single-spheres) and dimer (double-spheres). Dimers originating from the low-mass SEC fraction are highlighted in red shades. Dimers from the high-mass fraction are highlighted in blue shades. The acceleration voltage was ramped from 10 V to 25 V. For both samples, the most prevalent species was the monomer. One notable finding was that in addition to the mass of the expected dimer species, smaller mass species were also detected in the high-mass sample, presumably being degradation products.

Curiously, the analysis revealed the monomer ($M_{th} = 11,475$ Da vs. $M_{exp} = 11,472.7$ Da \pm 0.4 Da) to be the predominant species for each individual measurement of both, the lower (< 17 kDa) and higher (17-44 kDa) mass fraction as seen in the representative spectra (Figure 14). The low-mass fraction will be discussed at first. The fractions of the two occurring oligomeric protein states were determined via their overall peak areas under the curve (AUC) within the mass spectra. At a concentration of 5 μ M, essentially all protein ($98\% \pm 3\%$) was present as monomer.

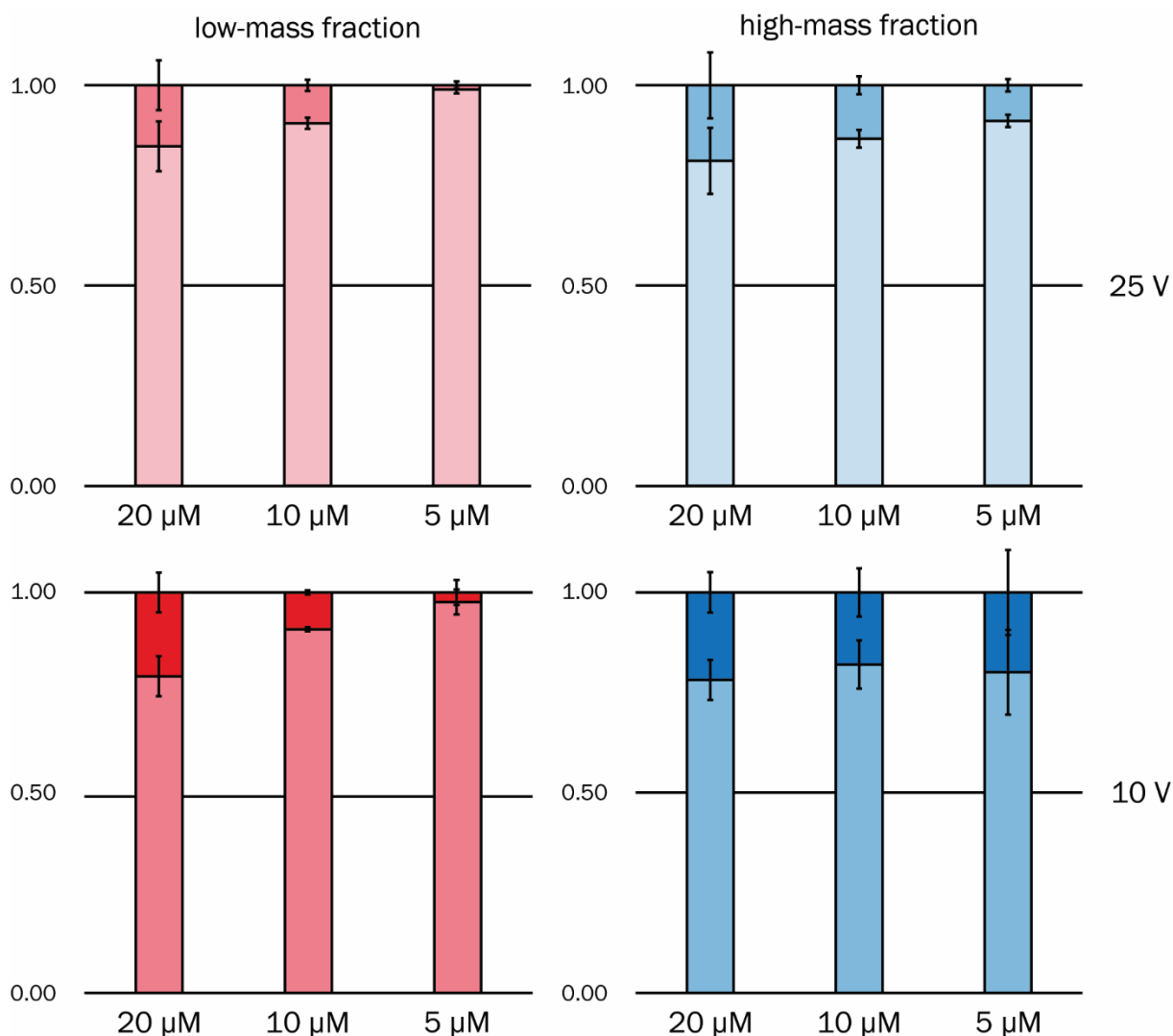


Figure 15 | Percentages of α_3 monomer and dimer in two different SEC fractions.

The AUC was determined over the entire spectrum for the α_3 monomeric and dimeric mass species. The mean value of the AUC from at least three independent measurements is depicted along with error bars that represent the corresponding standard deviation. While the dimeric proportion of the low-mass SEC fraction (red) was concentration dependent, the dimer originating from the high-mass fraction (blue) has a higher share and was not entirely depending on the α_3 domain concentration. Acceleration voltage was either 10 V or 25 V, respectively.

However, as the total concentration increased, the dimeric fraction ($M_{th} = 22,950$ Da vs. $M_{exp} = 22,947$ Da \pm 1 Da) became significantly higher. At 10 μ M its proportion made up $9\% \pm 1\%$, at 20 μ M already $21\% \pm 5\%$. Even at higher acceleration voltage (25 V) inside the collision cell, at which artificial electrospray-induced protein clusters are expected to

be less abundant, the concentration dependence of dimerization was evident. At 20 μM , the proportion of the dimer was increased as well with $15\% \pm 6\%$. Thus, the dimeric fraction present in the low-mass SEC sample was found to be concentration-dependent, whereas the dimer found in the high-mass sample presented a higher proportion and was not completely dependent on the concentration of the α_3 domain. At 10 V, the dimeric fraction appeared to be constant, $20\% \pm 10\%$, $18\% \pm 6\%$, and $22\% \pm 5\%$. At 25 V, on the other hand, when more nonspecific cluster products were already dissociated, slightly more dimer tended to form at higher concentration. There was $9\% \pm 2\%$ at 5 μM , $13\% \pm 2\%$ at 10 μM and finally $19\% \pm 8\%$ at 20 μM .

Dimeric species appearing in both samples were subjected to MS² analysis. For this purpose, the corresponding main peak – charge state 9⁺ at $m/z = 2551$ – was selected in both cases followed by a stepwise increase of the collision energy (Figure 16). In the spectrum of the low-mass sample, the precursor peak separated into the signals of the CID products at 50 V entirely. The newly appearing signals could be assigned to the 4⁺ and 5⁺ charge states of the monomer, confirming the presence of a noncovalently bound dimer. At higher acceleration voltage (100 V), the peptide chain partially fragmented, and a smaller mass species ($M_{\text{exp}} = 10,0621 \text{ Da} \pm 1 \text{ Da}$) could be additionally detected.

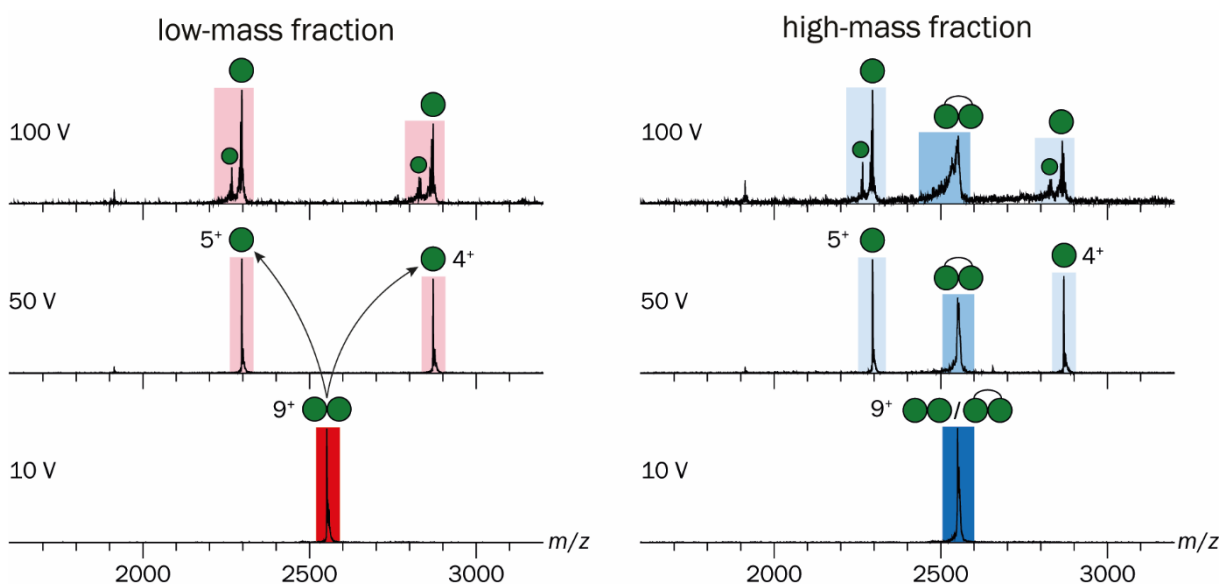


Figure 16 | Analyzing the α_3 dimers of two different SEC fractions via MS².

The 9⁺ peak at $m/z = 2551$ corresponding to the α_3 dimer was selected for MS² analysis at an acceleration voltage of 10 V, 50 V and 100 V. The low-mass SEC fraction dimers (double-spheres) easily dissociated in the gas phase indicating a noncovalent rather low-affinity binding event. Already at 50 V, no dimer was detectable anymore displaced by monomeric signal (single-spheres). Contrary to this, the dimeric signal was still significant at 100 V for the high-mass SEC fraction, where concurrently the monomer already started fragmenting (smaller spheres). The higher gas-phase stability suggested stronger binding presumably due to covalent bonds between two α_3 domains (connected double-spheres).

For the sample with the higher mass in the SEC, significant differences were seen in the MS² analysis. Although the same CID products and fragmentation patterns were detected,

a distinct signal of the dimeric parent peak was still evident at 50 V and evenly so at 100 V. This observation strongly suggested that this sample contained covalently linked dimers alongside the noncovalently bound ones.

The data certainly verified that just the α_3 domain of the MHC-I HC can form homodimeric interactions. Supplementary to my native MS analysis, a co-patterning experiment with an HA+K^b fusion protein that lacked the α_3 domain [HA-K^b($\Delta\alpha_3$)-RFP] and K^b-GFP was performed to investigate whether the α_3 domain is indeed required for FHC dimerization³. The interaction was significantly reduced, but still measurable, which suggested that the α_1 - α_2 domain is also involved in the interaction.

Furthermore, to image a possible arrangement of the K^b heavy chains in a dimer, my collaborators applied molecular docking³. A starting geometry was obtained by placing the α_3 domain of one K^b HC in the same position as the β_{2m} in the original K^b HC+ β_{2m} heterodimer and adjusting the α_1 - α_2 superdomain to avoid steric overlap. The structure was then energy-minimized and further refined by MD simulations. During MD simulations of 400 ns, no signs of dissociation were observed, and a stable root-mean-square deviation from the start structure was reached. In the model, the α_3 domain of one FHC substituted for β_{2m} , binding both the α_3 domain and the α_1 - α_2 superdomain of another FHC with a buried interface area of 2480 Å², which was comparable to the buried interface area of 2740 Å² between β_{2m} and the HC in heterodimers, and to other stable protein complexes²²⁷. Similar results were obtained with other arrangements of the two heavy chains.

Taken all techniques together, we found that the HC+HC complexes contain no β_{2m} and that the α_3 domain of the HC was sufficient for dimerization *in vitro* and in cells. The results suggest that FHC dimerization in the plasma membrane is at least partly based on the intrinsic affinity between the α_3 domains.

3.1.2 Discussion

Interactions of MHC-I FHC with FHC of the same allotype, of different allotypes, and even with other cell surface proteins have been proposed to play an important role in regulating adaptive and innate immune responses^{158,167} but the molecular principles that govern FHC interactions have remained unclear. In a highly integrative approach, my collaborators and I have shown that, after losing β_{2m} , murine H-2K^b MHC-I molecules at the cell surface

interact in a homotypic and heterotypic manner to form dimers, which are transient with a stability on the second timescale³.

As expected, the low-mass SEC fraction of the α_3 domain showed mostly monomeric α_3 . However, even at a for native MS moderate to rather low concentration of 5 μM , a small fraction of dimers was detected, which must have self-associated after SEC. This binding was easily disrupted by CID confirming the noncovalent nature of the interaction. As confirmed by the MS data, the α_3 domains of the FHCs alone are sufficient to form such interactions but it is conceivable that the α_1 - α_2 domain is also involved as suggested by the co-patterning study: In addition to the α_3 - α_3 interaction, the α_3 domain might also bind to the α_1 - α_2 domain of the other protein, or the α_1 - α_2 domains of the two proteins might interact with each other. These possibilities could currently not be distinguished.

Analysis of the high-mass SEC fraction was rather surprising. Based on peak's position within the chromatogram a large percentage of dimeric α_3 was assumed, though the spectra presented similar to those of the low-mass fraction. Again, mostly monomer was observed indicating dimers are transient and dimerization is a low-affinity binding process. At increased acceleration voltage (25 V), it was evident that the overall number of dimers was higher in the high-mass fraction than in the low-mass pendant. MS² analysis revealed the reason for this: The respective SEC fraction contained a significant amount of covalently bound dimers. Since immunoprecipitation experiments and micropatterning of FHC lacking free cysteine residues done by my collaborators clearly demonstrated that the FHC molecules at the plasma membrane were not covalently linked³, covalent dimers observed by native MS were likely refolding artifacts.

Although my collaborators observed a slightly increased tendency of FHCs to form higher oligomers, the data altogether identified noncovalent FHC dimers as the prevalent species at the cell surface³. The native MS data did not show any formation of higher oligomers even at higher concentrations of up to 20 μM , in fact with a maximum of about 20% even the dimeric fraction was rather low. Here, only the α_3 subunit was considered. This subunit separated from the rest of the FHC, therefore, does not seem to be capable of higher oligomerization. Direct detection of FHC interaction by SMCT corroborated transient noncovalent dimerization and only minor clustering into higher oligomers³.

By the use of SMCT, my collaborators estimated a lifetime of $t_{1/2} = 220 \text{ ms} \pm 150 \text{ ms}$ for the noncovalent FHC-FHC dimer³. The short half-life and the noncovalent monomer-dimer equilibrium observed by size exclusion chromatography at higher micromolar concentration

for the isolated α_3 domain, as well as the MS data presenting the α_3 monomer as the most prevalent species, pointed to a low-affinity interaction with a dimerization K_d of perhaps 10 μM to 20 μM . The weak and transient nature of HC-HC dimerization seen by SMT is similar to the nature of cell surface protein-protein association measured in other systems²²⁸.

In line with the observation of noncovalent dimerization in the plasma membrane, my collaborators obtained a robust structural model of a self-contained K^b FHC homodimer using molecular docking. The atomistic model was derived from the experimental findings that dissociation of $\beta_2\text{m}$ is required, that the α_3 domains are sufficient, and that a direct α_3 - α_3 interaction exists. Both latter findings were confirmed by native MS. We propose that $\beta_2\text{m}$ dissociation exposes a binding site on the FHC for the α_3 domain of another FHC. However, other arrangements of the two FHCs in a dimer are theoretically possible, and only experimental data will give a definitive answer.

Several findings in the literature are consistent with the formation of complexes of MHC-I HCs in the absence of $\beta_2\text{m}$ and peptide; this applies both to the “classical”, or class Ia, proteins HLA-A, HLA-B and HLA-C (and in mouse H-2D, H-2K and H-2L) as well as to the “non-classical”, or class Ib, protein HLA-F^{159,161,163,165,171}. Still, it is important to differentiate these HC-HC dimers from MHC-I associations described elsewhere¹⁵⁶⁻¹⁵⁸, namely homo- and heterotypic HC+ $\beta_2\text{m}$ +peptide trimers that are covalently dimerized via disulfide bonds in their cytosolic tails^{160,167}. They may play a role in binding the LILRB natural killer (NK) cell receptor¹⁶⁹. Other are noncovalent nano- and microscale clusters of HC+ $\beta_2\text{m}$ +peptide trimers that might stem from the fusion of exocytic vesicles with the plasma membrane and that might play a role in TCR recognition^{168,170,172,229}, macroscopic “clusters” of MHC-I molecules at the signaling interface between cells¹⁶⁴; and the covalent dimers of the HLA-B*27:05 heavy chain that are linked by disulfide bonds through C67²³⁰. The noncovalent HC+HC dimers described in this work may be a precursor to the formation of the latter.

The unexpected discovery that FHCs noncovalently associate into defined dimers allows exciting hypotheses of their distinct functional properties. FHC dimers might be responsible for the immunomodulatory functions contributed to cell surface heavy chains, *i.e.*, the stabilization of MHC-I trimers assist T cell activation^{153,231}, and also direct binding of FHCs to receptors on other cells – for example, FHCs of HLA-F binding to activating receptors on NK cell^{232,233}. Furthermore, dimerization of FHCs might enhance endocytosis in order to remove the nonfunctional FHCs, which themselves cannot activate T cells and are known

to be short-lived^{151,234}. Alternatively or additionally, such associated HCs may bind to other proteins in *cis* and promote their removal from the plasma membrane. Such endocytic removal might be achieved by altered endosomal routing, since the local density of membrane proteins in endosomes is higher than at the plasma membrane, and thus, efficient dimerization of MHC-I FHCs is expected. In such a scenario, even transient oligomerization in endosomes might prevent the return of internalized MHC-I FHCs to the cell surface¹⁵¹. Taken together, the presence of noncovalently bound transient FHC dimers points to exciting new aspects in the regulation of MHC-I functions with much potential for further investigation.

3.2 Peptide-free, disulfide-stabilized MHC-I molecules

Parts of this chapter have been published in either of the following studies:

Anjanappa, R., Garcia-Alai, M., **Kopicki, J. D.**, Lockhauserbäumer, J., Aboelmagd, M., Hinrichs, J., Nemtanu, I. M., Uetrecht, C., Zacharias, M., Springer, S., & Meijers, R. (2020). Structures of peptide-free and partially loaded MHC class I molecules reveal mechanisms of peptide selection. *Nature communications*, 11(1), 1314².

Reprinted from ANJANAPPA *et al.* (2020). Copyright © 2020, The Author(s).

Kopicki, J. D., Saikia, A., Niebling, S., Günther, C., Anjanappa, R., Garcia-Alai, M., Springer, S., & Uetrecht, C. (2022). Opening opportunities for K_d determination and screening of MHC peptide complexes. *Communications biology*, 5(1), 488⁴.

Reprinted from KOPICKI *et al.* (2022). Copyright © 2022, The Author(s).

3.2.1 Results

As peptide-free MHC-I molecules could not be crystallized so far, they have been modeled in various ways^{235,236}. In these modeling approaches, the conformations of the MHC-I side chains that line the peptide-binding groove were derived from peptide-loaded MHC-I structures²³⁷. Thus, such models cannot claim to represent the true shape of the peptide-free binding groove at the point of peptide recognition.

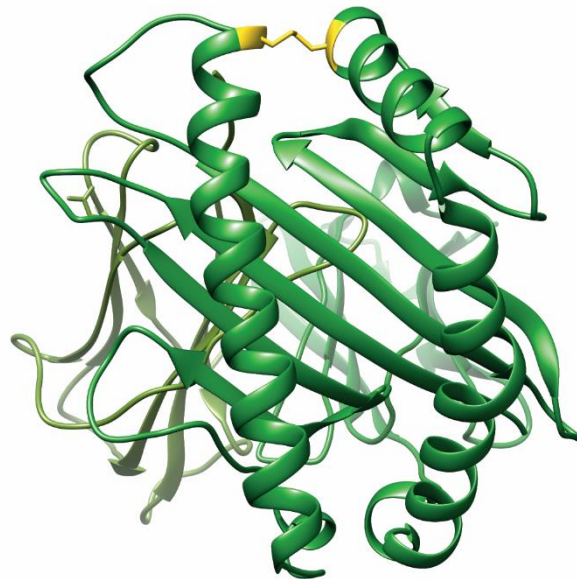


Figure 17 | Crystal structure of empty disulfide-stabilized HLA-A*02:01 (dsA2). The empty dsA2 complex is seen as top view of the peptide pocket. β_2m is shown in olive and the HC in green. The stabilizing disulfide bond (positions 84 and 139 mutated to cysteines) is depicted in yellow (PDB: 6TDR^{238,2}).

To better understand the peptide-binding process to MHC-I, HEIN *et al.* have stabilized MHC-I molecules by the introduction of a disulfide bond between the alpha helices in the vicinity of the F pocket²²². Such disulfide-stabilized MHC-I molecules can be folded *in vitro* with dipeptides to obtain recombinant soluble peptide-free MHC-I molecules that rapidly bind exogenous peptide²²¹. The dipeptide can subsequently be removed. Importantly, over a

hundred complexes of the disulfide-stabilized form of the frequent human MHC-I allotype HLA-A*02:01 (HLA-A*02:01(Y84C/A139C)), in the following named dsA2, with different peptides bind the T cell receptor with the same affinities as their wild type A*02:01 counterparts¹⁷⁴. The crystal structure of the complex dsA2 and the 1G4 T cell receptor with the cognate peptide shows that peptide binding and interaction with the T cell receptor are not affected by the disulfide bond²³⁹. Thus, the dsA2 molecule appears as an ideal model system to study empty MHC-I molecules.

For this thesis, a peptide-free dsA2 species (**Figure 17**) was investigated by native MS to demonstrate the absence of any peptide in the binding groove as well as the preservation of the ability to bind peptides. My work was part of a large integrative structural analysis of the molecule, in which my collaborators employed X-ray crystallography, MD simulations, and thermal denaturation assays². Their findings support the data obtained by native MS and are discussed as well.

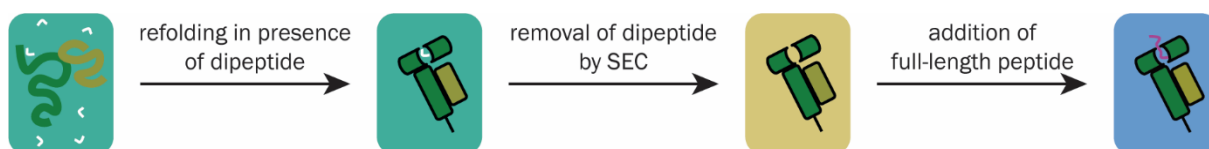


Figure 18 | Production of dsA2.

dsA2 is refolded in presence of GM or GL dipeptide, which is then removed via SEC. Afterwards, full-length peptides can bind into the empty binding groove.

Protein samples were provided by the Springer lab (Constructor University Bremen; **Figure 18**); wtA2 and dsA2 were bacterially expressed together with β_2m and refolded from inclusion bodies in presence of high concentrations of dipeptides but without any full-length peptide²²¹. Subsequently, the protein complexes were purified by SEC. Native MS of dsA2 was performed prior to and after removing any external dipeptide by SEC or filtration-based BEX. As a reference, wtA2 was subjected to the same experimental procedures.

In presence of 0.5 mM free GM (glycyl-methionine), resulting mass spectra (**Figure 19**, top spectrum) showed that the highest abundant species corresponded to the whole dsA2 protein complex ($45,834 \text{ Da} \pm 3 \text{ Da}$, **Figure 20**) and the whole wtA2 protein complex ($43,680 \text{ Da} \pm 2 \text{ Da}$), respectively, confirming a successful refolding. Additionally, the absence of other proteins verified sample purity. Presence of GM was confirmed as the corresponding peaks appeared in the low- m/z range when added to the solution.

To determine in which region of the dsA2-binding groove the dipeptides bind, my collaborators refolded dsA2 with dipeptide (GL or GM) and crystallized the complex with 2 mM free dipeptide present². The structures showed one dipeptide in the A pocket and in

addition one glycerol molecule from the buffer in the F pocket (**Figure 53, Supplement**). In terms of its conformation, the GL dipeptide in the A pocket was identical to the first two residues of the peptide in the wtA2+GLCPLVAML crystal structure (PDB: 3MRF)¹⁷³. Thus, the A pocket of A2 can bind a dipeptide in the same manner as it binds the first two residues of a longer peptide. In the structure dsA2+GM+GM, two GM dipeptides were present in the peptide-binding groove, one in the A pocket and one in the F pocket. The latter GM occupied positions P8 and P9 of a full-length nonamer peptide, and the C-terminus of the GM superimposed well with the C terminus of previously determined structures with full-length peptides that have a C-terminal leucine. In this crystal, there was no other ligand in the peptide-binding groove apart from the two dipeptides, and the rest of the groove was filled with solvent molecules. From this structure, it was concluded that dsA2 can accommodate two dipeptides at the same time, one in the A and one in the F pocket, and that they are bound like the *N*- and *C*-termini of a nonamer peptide.

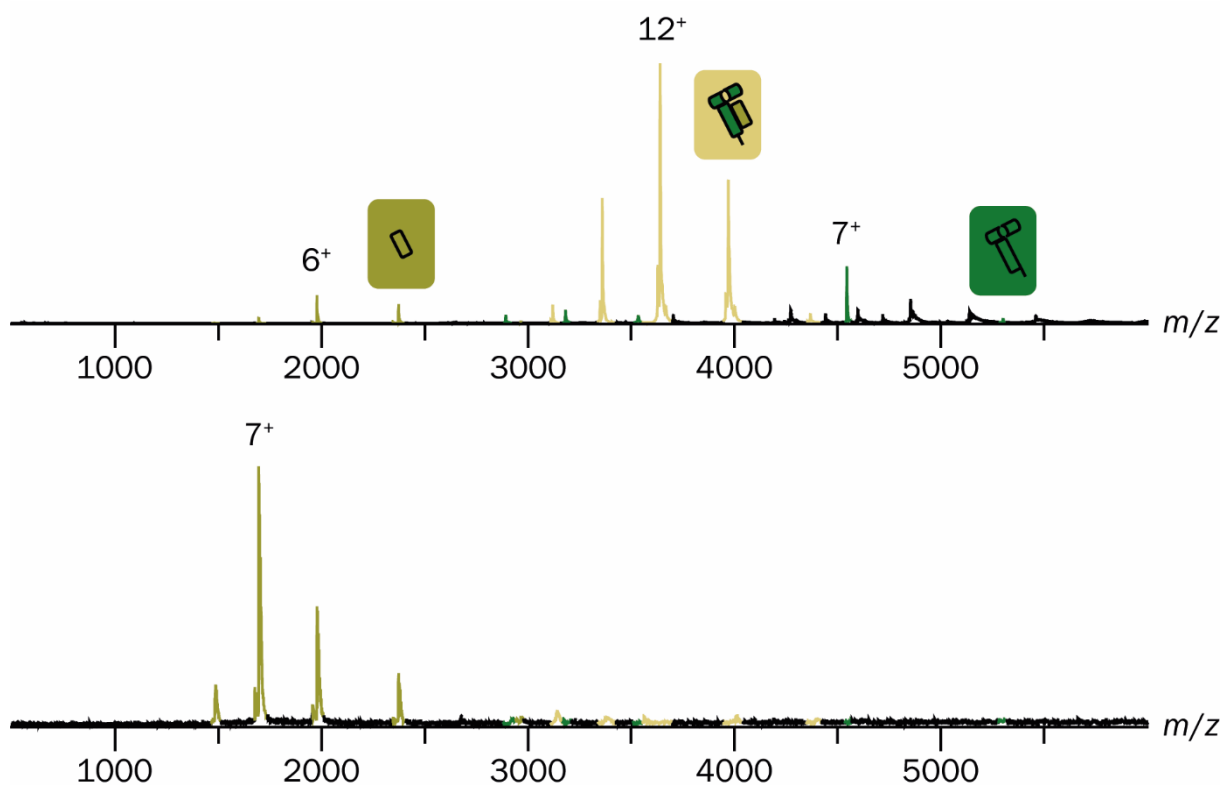


Figure 19 | Representative mass spectra of wtA2.

Spectra recorded in presence (**top**) and absence (**bottom**) of dipeptide GM. 10 μ M wtA2 in 250 mM ammonium acetate, pH 8, were recorded at an acceleration voltage of 50 V. In presence of 0.5 mM GM, the wtA2 complex (yellow) could be detected in high abundance, although the wtA2+GM complex was not observed. Note, the low-affinity dipeptide dissociated easily at the activation energies necessary to resolve the peaks sufficiently. Without GM, the HC (green) is not stable and unfolds already in solution. Thus, the wtA2 complex could not be maintained and both were hardly visible. The β_2 m subunit (olive) was more prevalent without GM.

After removing the external dipeptide, a vast difference between the resulting spectra of the two protein species was observed. As expected, the wtA2 complex could not be upheld without peptide. The folding of the HC in the absence of peptide cannot be maintained,

whereas the folding of β_2m is peptide-independent. This is reflected in the spectrum, where the signal of the free β_2m subunit could be detected but only minute amounts of folded HC and the entire wtA2 complex were observed when dipeptide was absent (**Figure 19**, bottom spectrum). In contrast, the spectrum of dsA2 remained unchanged – regardless of peptide presence or absence. Importantly, no dipeptide used for refolding, neither free nor bound to dsA2, was detected, which confirmed that the dsA2 complex is indeed empty and stable in absence of any peptide in the binding groove (**Figure 20**). The noncovalent binding showed to be quite robust and therefore withstood even when facing higher acceleration voltages of up to 125 V within in the mass spectrometer.

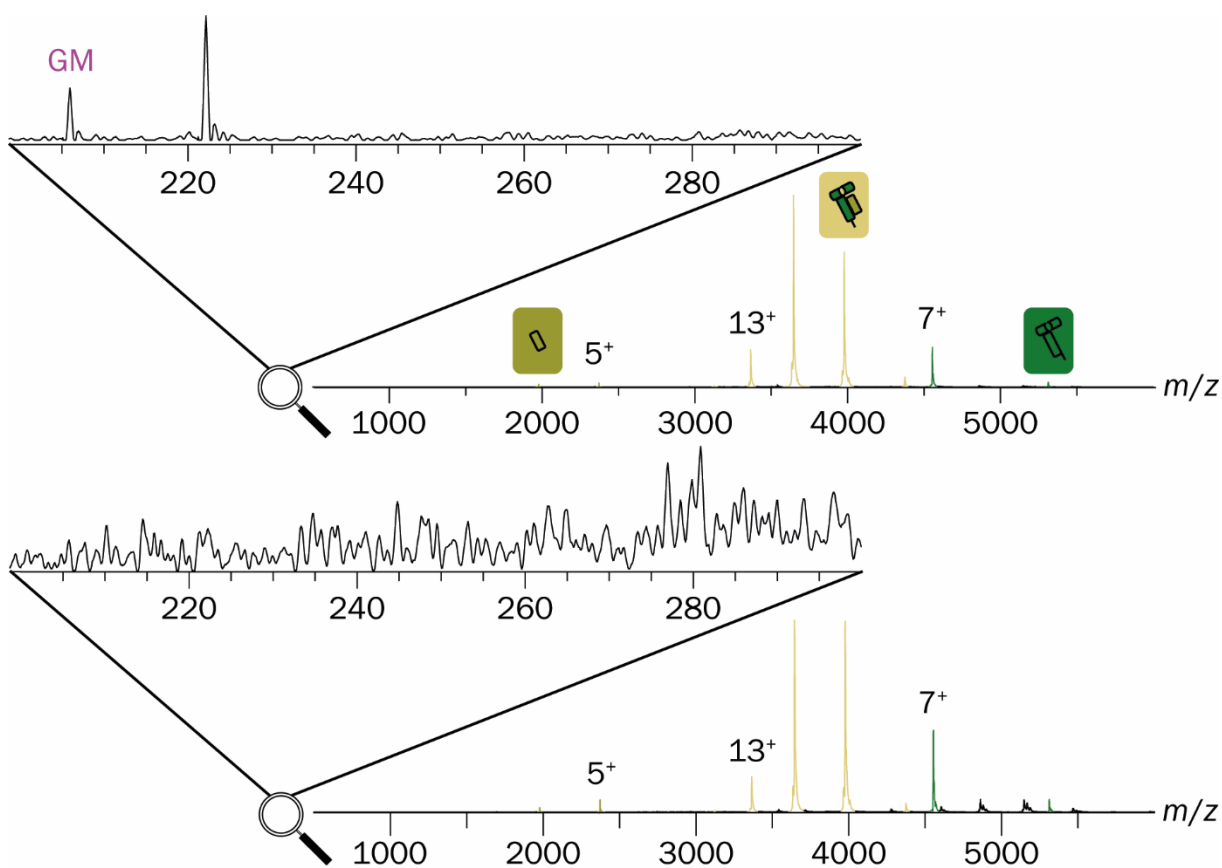


Figure 20 | Representative mass spectra of dsA2.

Spectra recorded in presence (**top**) and absence (**bottom**) of dipeptide GM. 10 μM dsA2 in 250 mM ammonium acetate, pH 8, were recorded at an acceleration voltage of 50 V. Comparing the spectrum of dsA2 alone with the spectrum of dsA2 in the presence of 0.5 mM GM, the low- m/z range (zoom) clearly showed that the protein complex no longer contained any dipeptide used for refolding. Note, the low-affinity dipeptide dissociated easily at the activation energies necessary to resolve the peaks sufficiently. The stability of dsA2 did not depend on the presence of dipeptide resulting in almost identical spectra.

Thus, it was concluded that although wtA2 was dependent on a high concentration of dipeptide to maintain its folded conformation, the dsA2 molecule was conformationally and thermally stable in the absence of any peptide or dipeptide in the binding groove.

To quantify the stabilization of dsA2 by the disulfide bond, my collaborators then performed thermal denaturation assays at different concentrations of free GM (glycyl-methionine)

dipeptide². In these assays, the characteristic decrease of tryptophan fluorescence upon protein unfolding was used to determine the transition midpoint of denaturation (melting temperature T_m) of the protein (**Figure 54, Supplement**). The fluorescence vs. temperature curves for both wtA2 and dsA2 showed two separate melting events, one at $T_m = 62$ °C for β_2m and another at lower temperature for the heavy chain. The melting event for the heavy chain was sensitive to the concentration of free GM, suggesting that GM binds to and stabilizes the peptide-binding site as predicted²²¹. The dependence of the T_m on dipeptide concentration matched previous observation for low-affinity ligands²⁴⁰. Remarkably, the dsA2 heavy chain gave a clear transition signal even at low dipeptide concentrations (at < 5 mM), whereas wtA2 did not give a distinct transition under these conditions. It was concluded that the C84-C139 disulfide bond of dsA2 enables it to remain folded even at low concentrations of dipeptide.

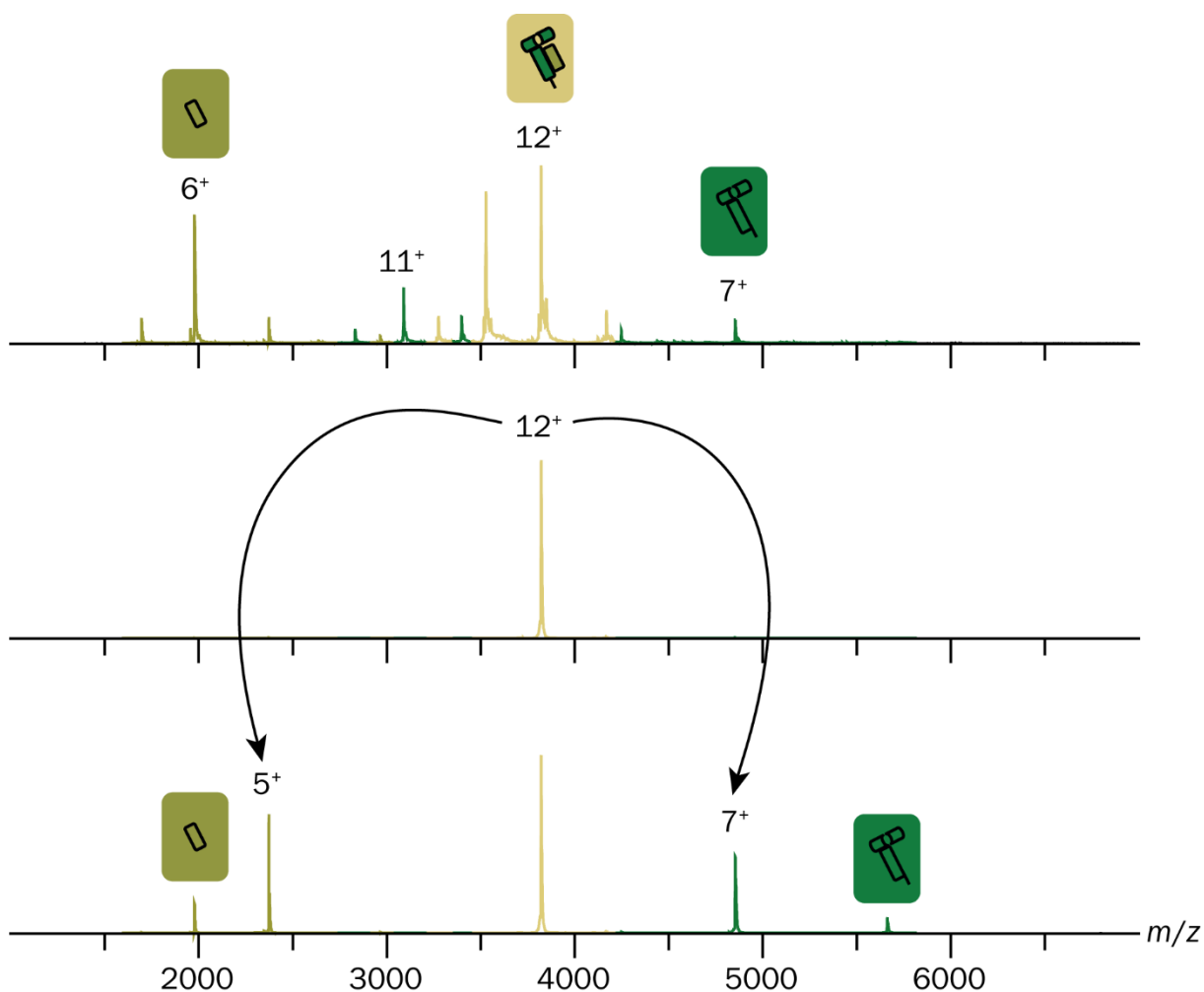


Figure 21 | MS² analysis of empty dsA2.

Top spectrum showed the empty dsA2 recorded in regular MS mode. The 12⁺ peak at $m/z = 3820$ resulting from a native mass spectrum of dsA2 (yellow) was selected for MS² analysis at an acceleration voltage of 50 V (**middle**). The **bottom** mass spectrum (100 V) showed the dissociation of the complex, which allowed an accurate mass determination of the HC (green) and β_2m (olive). The methionine-processed species could only be seen when zoomed in closely.

When dsA2 was further activated in the mass spectrometer, individual HC or β_2m molecules were released from the complex and appeared as individual peaks (**Figure 21; Table 8, Supplement**). MS² analysis revealed that both HC under investigation lacked a methionine suggesting the proteins were *N*-terminally processed during expression (dsA2: 33971 Da \pm 2 Da; wtA2: 31,799 Da \pm 4 Da). The same held true for the β_2m chain although here, the *N*-terminal methionine was processed only to some extent represented by adjacent peaks of diverging intensities (11729 Da \pm 1 Da vs. 11859.9 Da \pm 0.4 Da). Since the β_2m chain partially constitutes dsA2 and wtA2, this distinctive peak pattern reoccurred for the signals of the whole complex (dsA2: 45703 Da \pm 2 Da vs. 45,834 Da \pm 3; wtA2: 43,548 Da \pm 5 Da vs. 43,680 Da \pm 2 Da).

To obtain a peptide-free structure of dsA2 of the dsA2+GM crystals described above, my collaborators vacated the peptide-binding groove of the GM dipeptide applying a cycle of crystal washing in cryobuffer (lacking dipeptide) and crystal cryo-cooling². There was one molecule of 1,2-ethanediol, which was used as a cryo-protectant, in the A pocket mimicking the *N*-terminal amino group and the peptide backbone conformation. The lack of peptide in the A pocket of dsA2 was accompanied by a conformational change of some side chains. In the empty structure, the side chain of Y99 on the β sheet floor of the peptide-binding groove had changed its conformation to point further into the A pocket, away from H70 on the α_1 helix (**Figure 53, Supplement**). There was no longer a hydrogen bond network connecting these residues. The side chain of H70 had moved out of the B pocket into the C pocket. It occupied an area that in peptide-bound structures is filled with the side chain of the P6 residue. The side chain of F9, which was also situated on the β sheet floor, had turned perpendicular to the peptide-loaded conformation. The A pocket had expanded as a consequence of the rearrangements and thus appeared ready to accommodate an incoming peptide. This peptide-receptive conformation was proposed to be named “the unlocked state” of the A pocket, whereas the “locked” state described the peptide-bound conformation. Out of the 258 peptide-loaded structures in the PDB, only three structures showed a F9 side chain conformation that is similar to the empty dsA2 structures¹⁷³. Taken together, the comparison with the PDB structures demonstrated that the locked A pocket corresponds to the peptide-bound state and the unlocked A pocket corresponds to the peptide-receptive state of A2. Similar to that, the F pocket on the opposite side of the peptide-binding groove also rearranged a triad of side chains, R97-H114-Y116, to accommodate a bulky amino acid such as GM’s *C*-terminal methionine.

However, when comparing with the wtA2+peptide structures from the PDB database, it was found that in about 25% of the deposited wtA2+peptide structures the conformation of the F pocket was partially unlocked. In addition to that, my collaborators performed MD simulations. The results thereof reinforced the conclusions drawn from the crystal structures and suggested a significant energy barrier between the unlocked and the locked conformational states, and a concerted conformational change of the R97-H114-Y116 triad upon peptide binding.

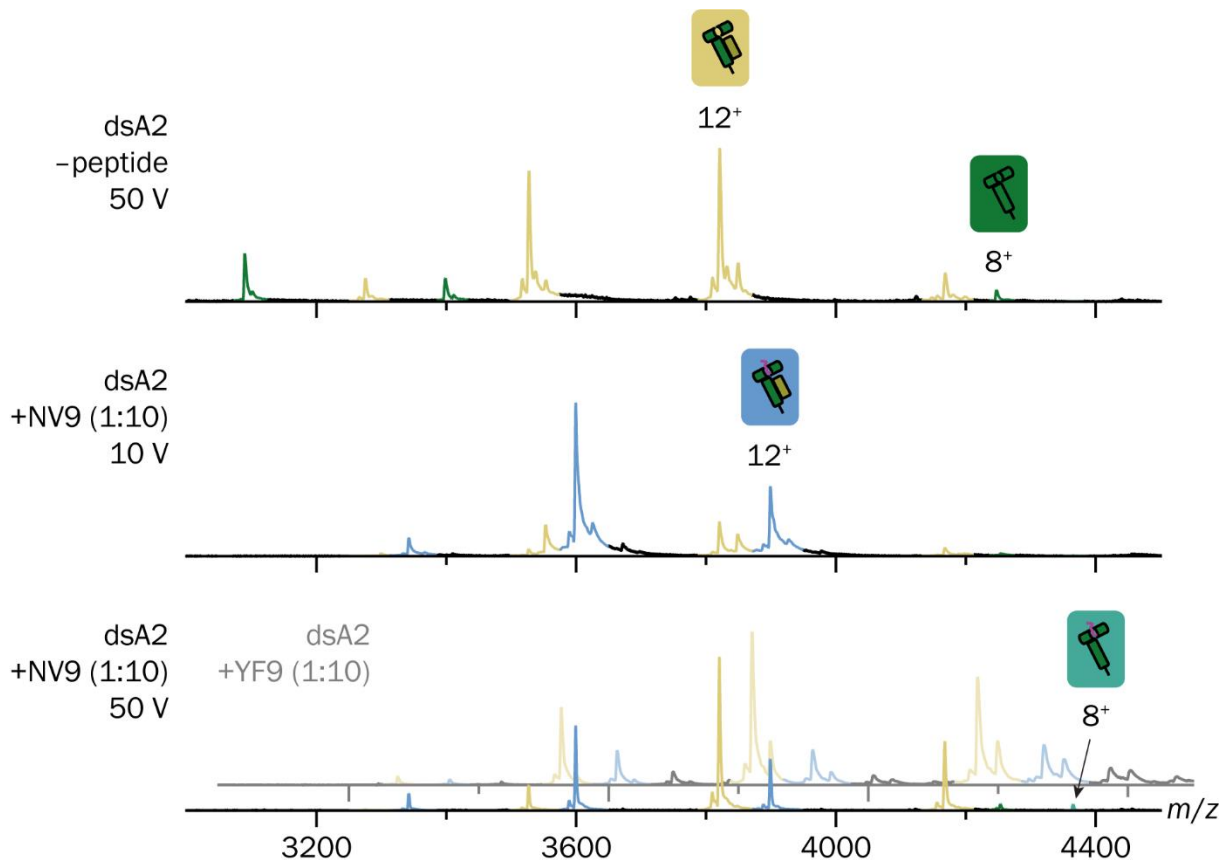


Figure 22 | Superstoichiometric binding of high-affinity peptide NV9 to dsA2.

A mass spectrum of 10 μ M dsA2 at acceleration voltage of 50 V is given as a reference (**top**). Upon addition of 0.1 mM NV9, the peptide-bound complex (blue) was the most abundant species at low acceleration voltage (10 V; **middle**). When the voltage was increased to 50 V (**bottom**), the complex began to dissociate into β_2 m (olive) and HC (green). However, some HC+NV9 complex could be detected (8⁺ peak; teal), indicating high stability. The low-affinity control YF9 recorded at same conditions is displayed in the **background**.

Since it was shown that dipeptide complexes of wild type MHC-I molecules can exchange bound dipeptide for a full-length high-affinity peptide²²¹, it was next investigated whether the artificial construct of empty dsA2 was able to bind cognate peptides. Being a high-affinity nonapeptide, A2 epitope NV9 from human cytomegalovirus pp65 (sequence NLVPMVATV) was the first control peptide of choice. A second nonapeptide (YPNVNIHNF, YF9) with low affinity was used as a negative control. A tenfold molar excess of respective peptides was added to dsA2, and the resulting complexes were analyzed (**Figure 22**). In presence of nonapeptide NV9 (1:10), peptide binding to dsA2 was observed showing that

the empty pocket could easily be filled again. As predicted, dsA2+NV9 ($46778 \text{ Da} \pm 1 \text{ Da}$) was by far the most-abundant species at low acceleration voltage. The NV9 peptide remained bound at higher activation up to 75 V suggesting a stable interaction. At tenfold molar excess of the peptide, ESI-clustering induced species like dsA2+NV9+NV9 ($47723 \text{ Da} \pm 3 \text{ Da}$) were observed. Therefore, measurements with substoichiometric peptide concentration (10:1) were performed to exclude the possibility of artifactual complex formation. Despite this low NV9 concentration, dsA2+NV9 was detected by native MS, whereas the low-affinity control YF9 was not visible (**Figure 23**).

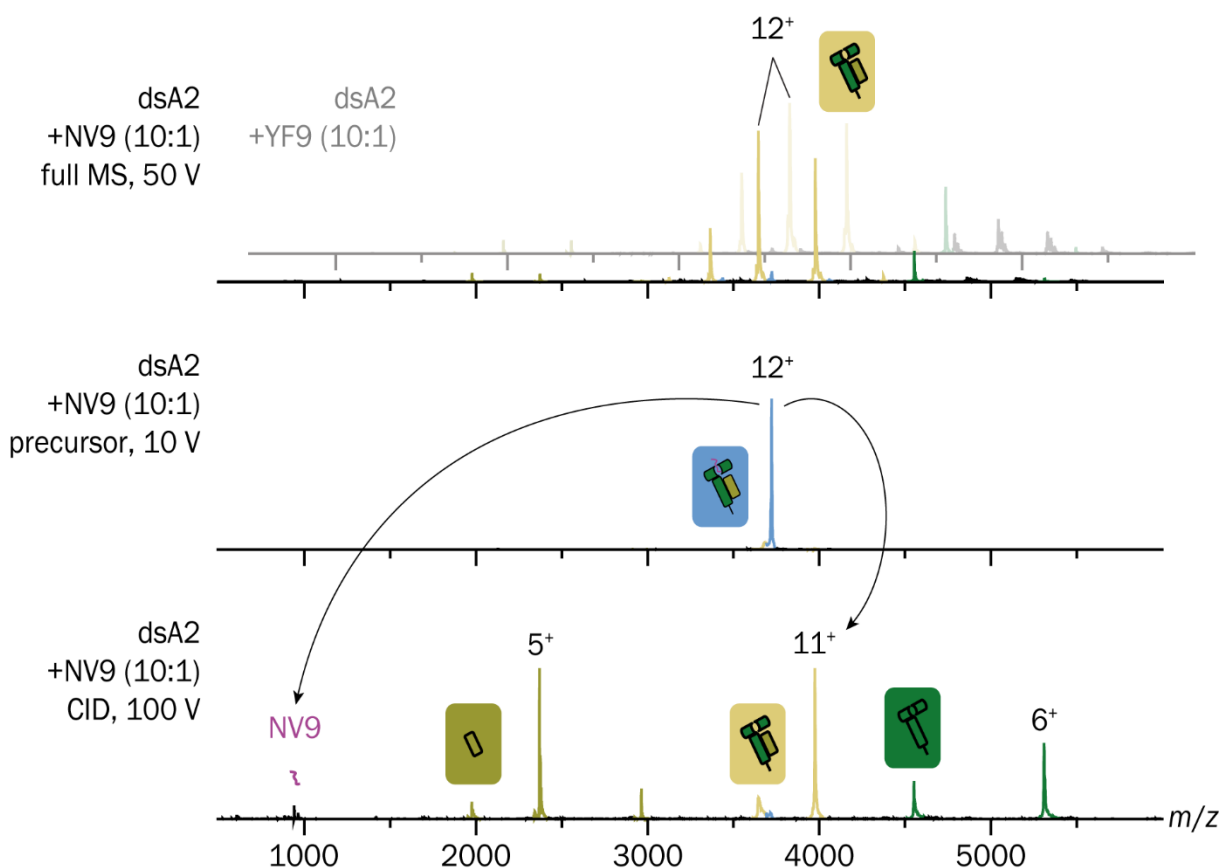


Figure 23 | Substoichiometric binding of high-affinity peptide NV9 to dsA2.

A mass spectrum of $10 \mu\text{M}$ dsA2 and $1 \mu\text{M}$ NV9 at acceleration voltage of 50 V is given as a reference (**top**). Peaks for dsA2+NV9 (blue) had a very low intensity, whereas the low-affinity control YF9 gave no signal for the peptide-bearing complex at all (**background**). The 12^+ peak of dsA2+NV9 at $m/z = 3723$ was selected for MS² analysis at 10 V (**middle**). The MS² spectrum measured at 100 V (**bottom**) clearly shows the dissociation of the complex into dsA2 as well as its subunits (β_2m , olive; HC, green) and NV9.

In MS² experiments, the selected protein-peptide complex dissociated into the dsA2 HC+ β_2m dimer (without the peptide) as well as into the individual subunits and the nonapeptide (**Figure 23**, bottom spectrum). Because signal for HC+NV9 (without β_2m) was still visible at high voltages, it could be concluded that the binding between dsA2 and NV9 is very strong. Thus, the two protein subunits partly dissociated first, before the peptide is released from the binding pocket. From these observations it is clear that the binding of full-length peptides to dsA2 is not affected by the presence of the C84-C139 disulfide bond.

In addition to all expected dsA2 mass species – empty dsA2, dsA2+peptide, HC, and β_2m – an additional species was detected whose origin was initially unknown (**Figure 24**). A fraction of dsA2 was found to carry a small molecule adduct, 337 Da by tandem MS analysis, that is easily released at ≥ 50 V by CID.

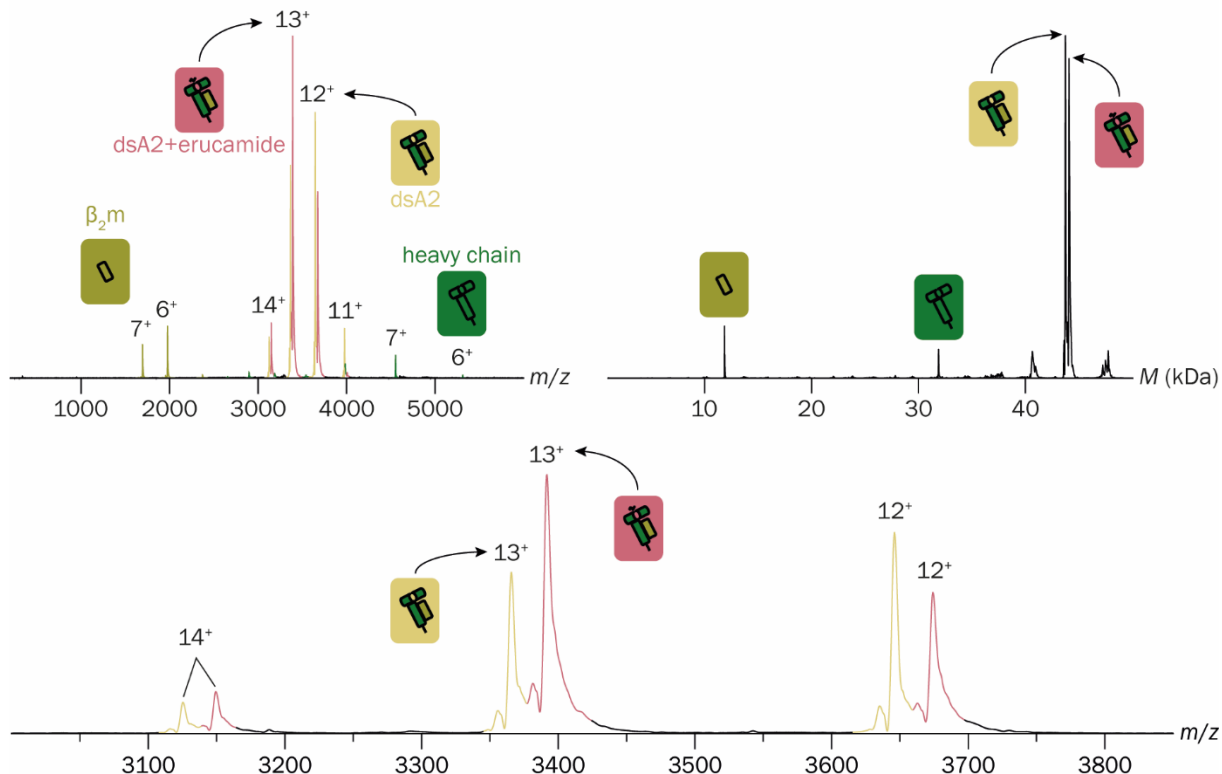


Figure 24 | Erucamide detected in all dsA2 samples.

Different spectra of the same measurement of 10 μ M dsA2 performed at 1.45 V at the capillary and 25 V in the collision cell in absence of any peptide are displayed. Full MS spectrum (**top, left**) shows the expected mass species, empty dsA2 (yellow), dissociated β_2m (olive) and heavy chain (green), but also the contaminant-carrying dsA2+erucamide (coral). The deconvoluted spectrum (**top, right**) illustrates its high proportion. The zoom (**bottom**) revealed that the proportion varies depending on the charge state.

By small-molecule MS (**Figure 25**), the compound was most likely identified as erucamide ((Z)-docos-13-enamide), probably originating from laboratory plastic ware as reported²⁴¹⁻²⁴³. This contaminant appeared consistently in all protein batches (dsA2 and wtA2) studied. Interestingly, the size of the respective erucamide-binding MHC-I fraction differed depending on the peptide introduced. This phenomenon, as well as details of the erucamide's binding position, will be discussed in more detail in the following chapter.

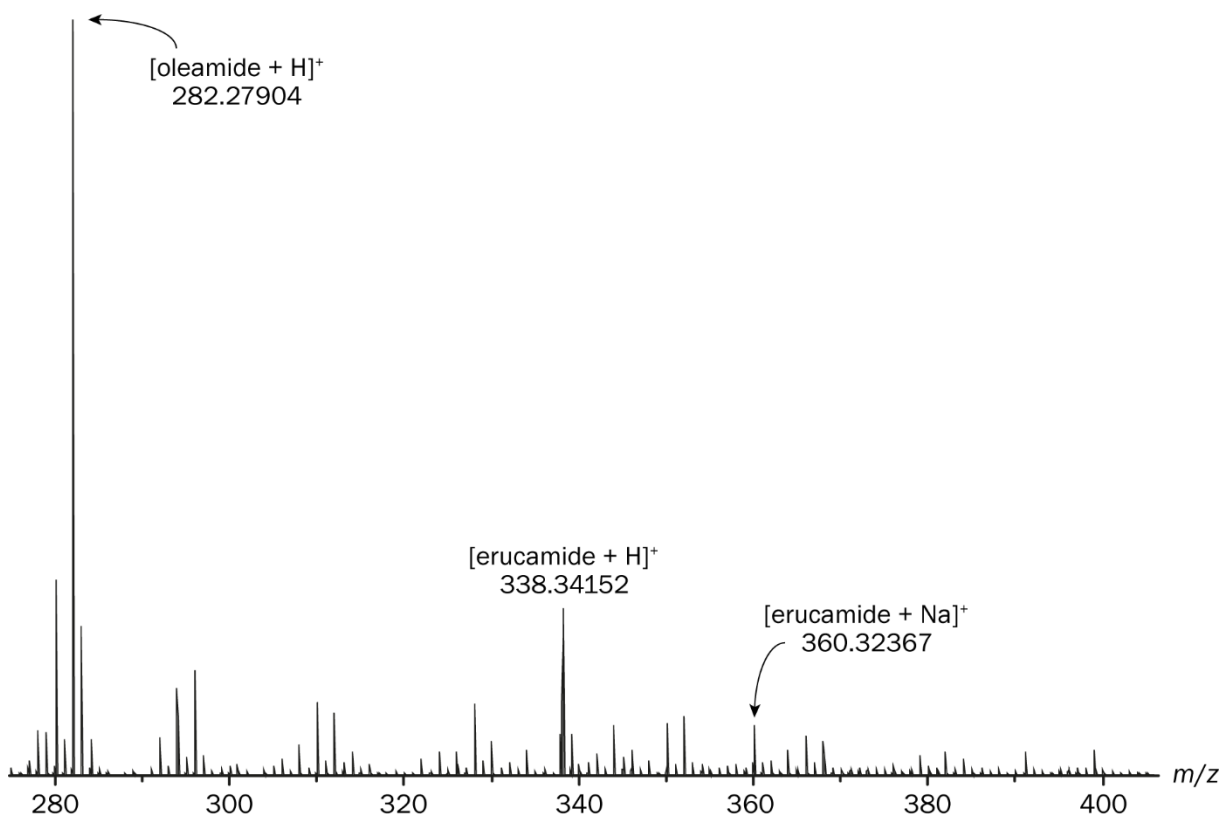


Figure 25 | Erucamide identified as contaminant using small molecule MS.

Small molecule MS² analysis verified that erucamide accounts for a large proportion of the contaminants found in dsA2 samples. Displayed is a spectrum resulting from the subtraction of the spectrum of plastic ware contaminants (empty vial) from the one of the dsA2 sample itself. Erucamide (337 Da) was hereby identified as the contaminant adducted to dsA2. Although oleamide is also found in the sample, there was no evidence of binding to the protein in the native MS analysis, unlike for erucamide.

3.2.2 Discussion

The binding of a peptide to a particular MHC-I allotype (and thus its surface presentation) depends on the match of its *N*-terminus and some of its amino acid side chains into the binding pockets of the peptide-binding groove. Until now, the study of the dynamic processes that accompany peptide binding has been hindered by the lack of a crystal structure of the peptide-free form of MHC-I. Using an integrative approach, my collaboration partners and I were able to present the structure of the disulfide-stabilized form of HLA-A*02:01. The molecule was thoroughly characterized by X-ray crystallography, MD simulations, thermal denaturation assays, and native MS – the latter serving to assess the proteins' quality, *i.e.*, correct folding and stoichiometry, but also to verify its peptide-free state as well as to confirm its ability to bind peptides.

Native MS analysis clearly demonstrated that the wild type A2 complex could not be maintained in the absence of a peptide ligand. However, stabilization by a dipeptide such as GM or GL was quite sufficient to observe the intact complex in the spectrum. Only few amounts of free HC or β 2m were observed which could be attributed to in-source

dissociation (ISD) or CID effects. In contrast, it was clearly demonstrated that a single genetically introduced disulfide bridge between the alpha helices near the F pocket stabilizes the peptide-binding groove in a manner that preserves the complex of HC and β_2m even in the absence of a ligand. Spectra of dsA2 in the presence or absence of a dipeptide effectively did not differ. In both cases, the protein complex appeared homogeneously and natively folded apart from the slight dissociation effects just mentioned with respect to wtA2.

The empty mutant complex could easily bind a new peptide added to the sample solution. In the case of a high-affinity peptide such as NV9, if the peptide was at least equimolar to the protein, the dsA2+peptide mass species became the new predominant signal in the spectrum. Interestingly, despite a clear excess of the peptide, we still saw a fraction of the empty protein complex. In the case of dipeptides, in fact, only the ligand-free complex was detected. This observation was also true for wtA2. Here we know that it is definitely unstable without peptide. Therefore, this mass species could only be the product of dissociation in the gas phase and could not have existed in solution before. In contrast to the high-affinity NV9, which gave a strong signal together with A2, GM and GL did not seem to be detectable when bound under the same conditions. The binding appeared to be too weak and could be easily disrupted by ISD, CID, or a combination of both. The relationship between the degree of occupancy of the protein and the affinity of the peptide is discussed in more detail in **Chapter 3.3**.

If ten times more NV9 as protein was present, dsA2+NV9+NV9 complexes were also detected. Accommodation of two nonapeptides within the peptide pocket of dsA2 is utterly inconceivable for steric reasons – especially considering the newly introduced disulfide bond, which makes a possibly imaginable opening of the pocket impossible. Furthermore, a complex of dsA2 and YF9 was also identified, although this peptide is unrelated to A2 and does not contain a binding motif of known epitopes. Both phenomena can be explained clustering¹⁰²⁻¹⁰⁵, *i.e.*, nonspecific attachment to the analyte, in the ESI process. In fact, these effects could be eliminated by reducing the peptide concentration. At 10 μM protein and only 1 μM peptide, no dsA2+YF9 and no dsA2+NV9+NV9 mass species were observed anymore. In contrast, the high-affinity binding between dsA2 and NV9 was still detectable at this substoichiometric condition.

Concerted conformational changes of the amino acid side chains lining the MHC-I peptide-binding groove that occur during peptide binding were described. It was found that both, the A and F pocket, contain side chain triads that undergo such concerted changes. In the

A pocket, peptide or dipeptide binding switched the F9-H70-Y99 triad into a locked state that affected other pockets. MD simulations on the empty dsA2 confirmed this. In the F pocket, however, GM-binding, with a methionine in the F pocket, supported the unlocked state of the R97-H114-Y116 triad that is otherwise found in the peptide-free structure. MD simulations indicated a considerable energy barrier between the locked and unlocked states in the absence of a ligand and hence supported the view of a concerted conformational switch between these two states, rather than a mere conformational fluctuation. The results concerning the F pocket explain why methionine is not a common C-terminal residue of A2-binding peptides. Methionine-binding switched the F pocket to the unlocked conformation, even with the peptide bound, which impacts the conformation such that it interferes with the binding of the peptide backbone. The binding of a peptide that inserts a C-terminal methionine into the F pocket is thus predicted to be weak, which potentially explains why there are only four A2 crystal structures in the PDB that contain methionine as the C-terminal peptide residue.

When the observations from native MS and X-ray crystallography are combined, it appears that, in the absence of peptides, small, organic molecules enter the binding pocket of dsA2. In the spectra, erucamide derived from the laboratory plastic was detected, and the crystal structures showed that glycerol or 1,2-ethanediol were embedded in the pocket. Glycerol molecules are known to bind into the MHC-I peptide-binding groove and to stabilize the MHC fold in partially empty crystal structures²⁴⁴. Structurally, of course, there are clear similarities between the glycerol and the 1,2-ethanediol, which makes the appearance of at least one of these molecules in the peptide pocket not surprising. It was observed that in the A pocket, the 1,2-ethanediol bound in a manner similar to that of the N-terminus of a peptide. Erucamide has great importance for the aspects discussed in **Chapter 3.3**, so its binding behavior will be further elaborated there. Taken together, it appears that although dsA2 does not rely on stabilizing ligands to maintain its own integrity, the exposed binding sites intended for peptides seem prone to form bonds to molecules that meet minimal requirements (free electron pairs, charge, size).

Of all MHC-I allotypes, A2 is most thoroughly studied in structural terms. This helped to conduct an extensive assessment of the changes in the conformational state of the peptide-binding groove after peptide removal by comparing our structures to 258 A2+peptide structures in the PDB. It was possible to define two states for both, the A and the F pocket – the locked state, which represents most peptide-loaded MHC structures, and the unlocked state, which is found in peptide-free MHC-I molecules. Crystal structures

and MD simulations allowed to conclude that upon binding of a full-length peptide to an empty MHC-I molecule, the A pocket switched to the locked state in nearly all cases, whereas the F pocket remained unlocked in 25% of A2 structures with full-length peptide.

The unlocked state of the F pocket is more open to the solvent. Thus, the lower tendency of the F pocket to switch to the locked state, even when high-affinity peptides are bound, supports the notion that peptide exchange at the F pocket can occur unassisted. This effect has been shown before for a number of MHC-I allotypes^{186,245}. The chaperones TAP-binding protein related (TAPBPR) and tapasin can further destabilize the peptide-binding groove to remove peptides from the F pocket and, in consequence, the binding groove¹⁹⁷. Indeed, recent structures of MHC-I in complex with TAPBPR^{246,247} or a tapasin loop fragment²⁴⁸ suggest that such a transition state at the F pocket contributes to peptide exchange. Taken together with the literature, our data confirmed the importance of the F pocket as the region of the protein where peptide binding can be modulated by external factors.

It is likely that the concerted switch to unlock the F pocket described above is not limited to A2 but may apply to many other allotypes. A similar movement upon the opening of the F pocket of HLA-B*44:02 has been suggested previously to contribute to chaperone-independent peptide exchange²⁴⁹. In addition, from a survey of MHC-I structures in the PDB, another series of structures that illustrate the presence of an allosteric switch in the F pocket is evident. HLA-A*24:02 (A24) binds the highly immunogenic peptide RYPLTFGWCF (PDB 3QZW)^{173,250}. The C-terminal peptide residue, phenylalanine, binds into the F pocket, which contains Y116 in a position identical to A2. The side chain of Y116 locks the F pocket by forming a hydrogen bond with D74 on the α_1 helix. Interestingly, a truncated octamer peptide with the sequence RYPLTFGW can also bind A24 in a stretched backbone conformation such that W8 fills the F pocket (PDB 5HGB)^{173,251}. The bulky side chain of W8 then unlocks the F pocket, and Y116 switches conformation to form a hydrogen bond with H114 on the β sheet floor. That very same hydrogen bond is formed in A2 when the F pocket unlocks. The third member of the allosteric triad in A24 is M97, which points upwards, out of the peptide-binding groove, when the F pocket is unlocked. These examples suggest that the concerted side chain switches involved in unlocking the F pocket may occur in many MHC-I allotypes.

3.3 MHC-I peptide binding

Parts of the following chapter have been published in:

Kopicki, J. D., Saikia, A., Niebling, S., Günther, C., Anjanappa, R., Garcia-Alai, M., Springer, S., & Uetrecht, C. (2022). Opening opportunities for K_d determination and screening of MHC peptide complexes. *Communications biology*, 5(1), 4884.

Reprinted from KOPICKI *et al.* (2022). Copyright © 2022, The Author(s).

3.3.1 Results

3.3.1.1 Peak intensity in native MS reflects peptide-MHC binding affinity

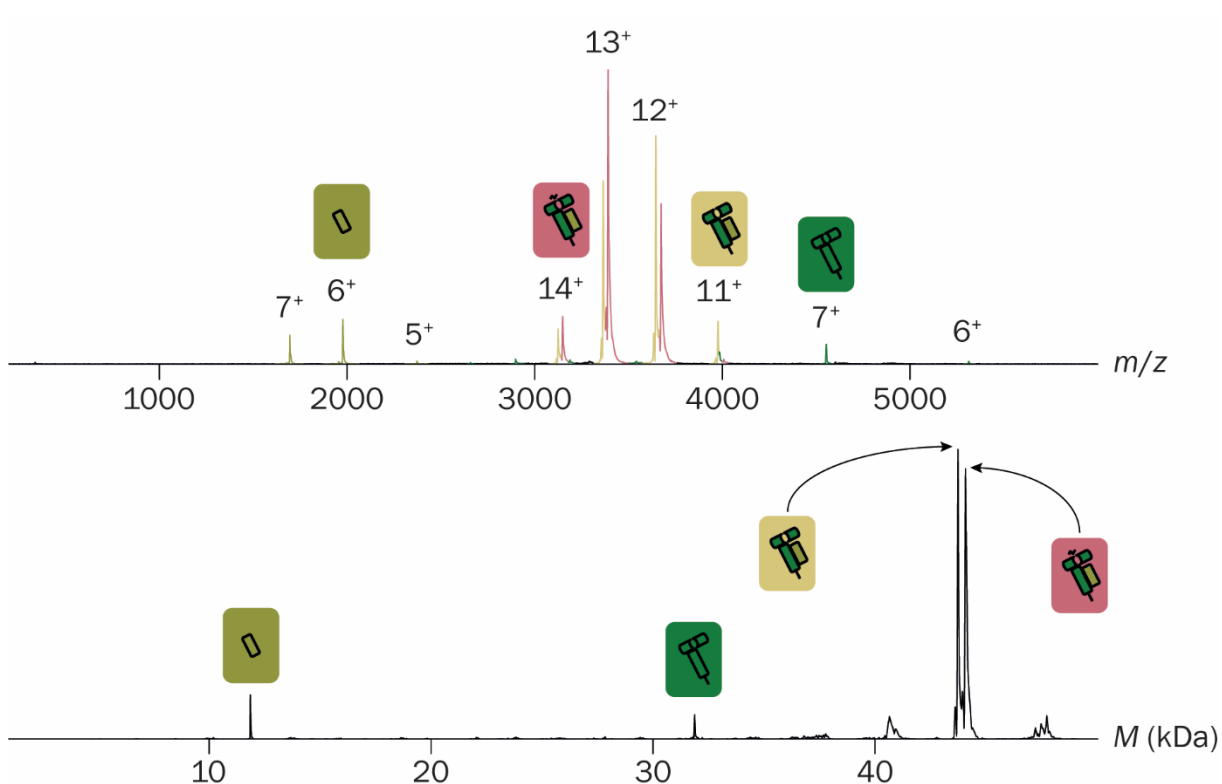


Figure 26 | dsA2 in absence of peptides.

Raw (**top**) and deconvoluted (**bottom**) native mass spectra of peptide-free dsA2 were recorded at an acceleration voltage of 25 V. The empty dsA2 was the predominant species (yellow). In addition, dsA2+erucamide (coral) and dissociated β_2m (olive) and HC (green) could be seen.

As already described in the previous **Chapter 3.2**, empty dsA2 consists of the disulfide-stabilized HC (HLA-A*02:01(Y84C/A139C)) and the light chain, beta-2 microglobulin (**Figure 17**). Bacterially expressed dsA2 HC and β_2m were folded *in vitro* into the dsA2 complex with dipeptides (GM or GL) and purified by SEC^{2,221}. Again, during SEC, the dipeptide was removed and was no longer detected by native MS, resulting in an empty binding groove (**Figure 18**). At a low acceleration voltage of 25 V in the collision cell, raw and deconvoluted spectra (**Figure 26**) demonstrated a stable complex of HC and β_2m in the absence of any peptide. Some minor ISD (< 5%) occurred upon activation in the mass

spectrometer, independently of either the addition of a peptide or the peptide characteristics.

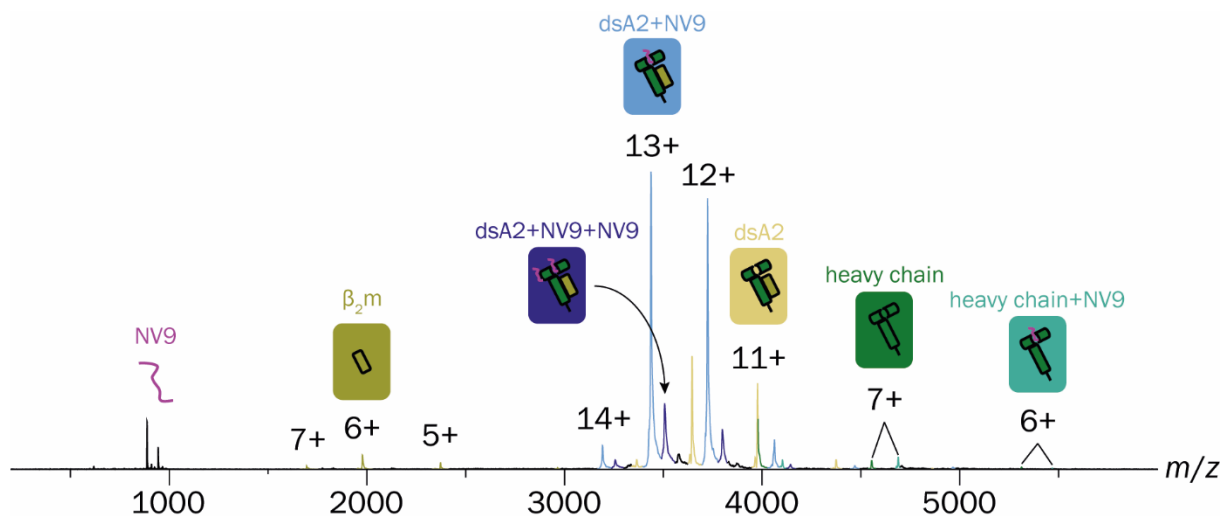


Figure 27 | Raw spectrum of dsA2+NV9.

A native mass spectrum dsA2 in presence of NV9 (protein-peptide ratio 1:5) recorded at an acceleration voltage of 25 V is shown. The dsA2+NV9 was the predominant species (light blue). In addition, peptide-free dsA2 (yellow), dissociated β_2m (olive) and HC (dark green) as well as free NV9 (purple) could be seen.

It was next examined whether native MS can differentiate the binding of high-affinity and low-affinity peptides by comparing the A2 epitope NV9 from human cytomegalovirus pp65 (sequence NLVPMVATV; theoretical dissociation constant, $K_{d,th} = 26$ nM predicted by NetMHC²¹⁸) with the irrelevant YF9 (YPNVNIHNF; $K_{d,th} = 27$ μ M) and with GV9 (GLGGGGGGV; $K_{d,th} = 2.7$ μ M), a simplified NV9 derivative that retains the anchor residues, L and V. After a short incubation, dsA2 with 5 \times excess peptide was subjected to native MS with increasing acceleration voltages. Since β_2m dissociated from the HC above 75 V² only results for 10 V, 25 V, and 50 V were considered. An exemplary spectrum of dsA2 and NV9 at 25 V is shown in **Figure 27**. While at 10 V and 25 V the distribution of the different mass species was very similar, the ratios changed significantly at 50 V. It is a frequent observation with the ESI process in native MS that noncovalent hydrophilic bonds such as those between dsA2 and high-affinity peptides are retained²⁵²⁻²⁵⁵, but hydrophobic interactions are weakened. By increasing the acceleration voltage, the dissociation of a protein-ligand complex usually does not occur gradually but spontaneously beyond a certain threshold, at which an energetic state is encountered that denatures the complex, here between 25 V and 50 V. Therefore, measurements at 10 V were used to calculate the K_d . In the presence of low-affinity YF9, the empty dsA2 molecule (43,733 Da \pm 4 Da) generated the largest signal (56% \pm 3% at 10 V; **Figure 28A**; reference spectra in **Figure 28B**). Most of the remaining dsA2 carried only erucamide (44,071 Da \pm 5 Da; 39% \pm 2%). There was very little dsA2+YF9 complex (4% \pm 2%), and because of the very low binding

affinity of YF9, it was assumed that this signal does not correspond to real binding but rather to an artifact of the ESI process.

Assuming that the other tested peptides cluster to the same extent, all native MS data were corrected for the clustering determined with YF9, for which thus no affinity can be calculated (raw data see **Table 9, Supplement**). For NV9, in contrast, strong binding is observed, with $64\% \pm 3\%$ for dsA2+NV9 at 10 V and $40\% \pm 4\%$ at 50 V.

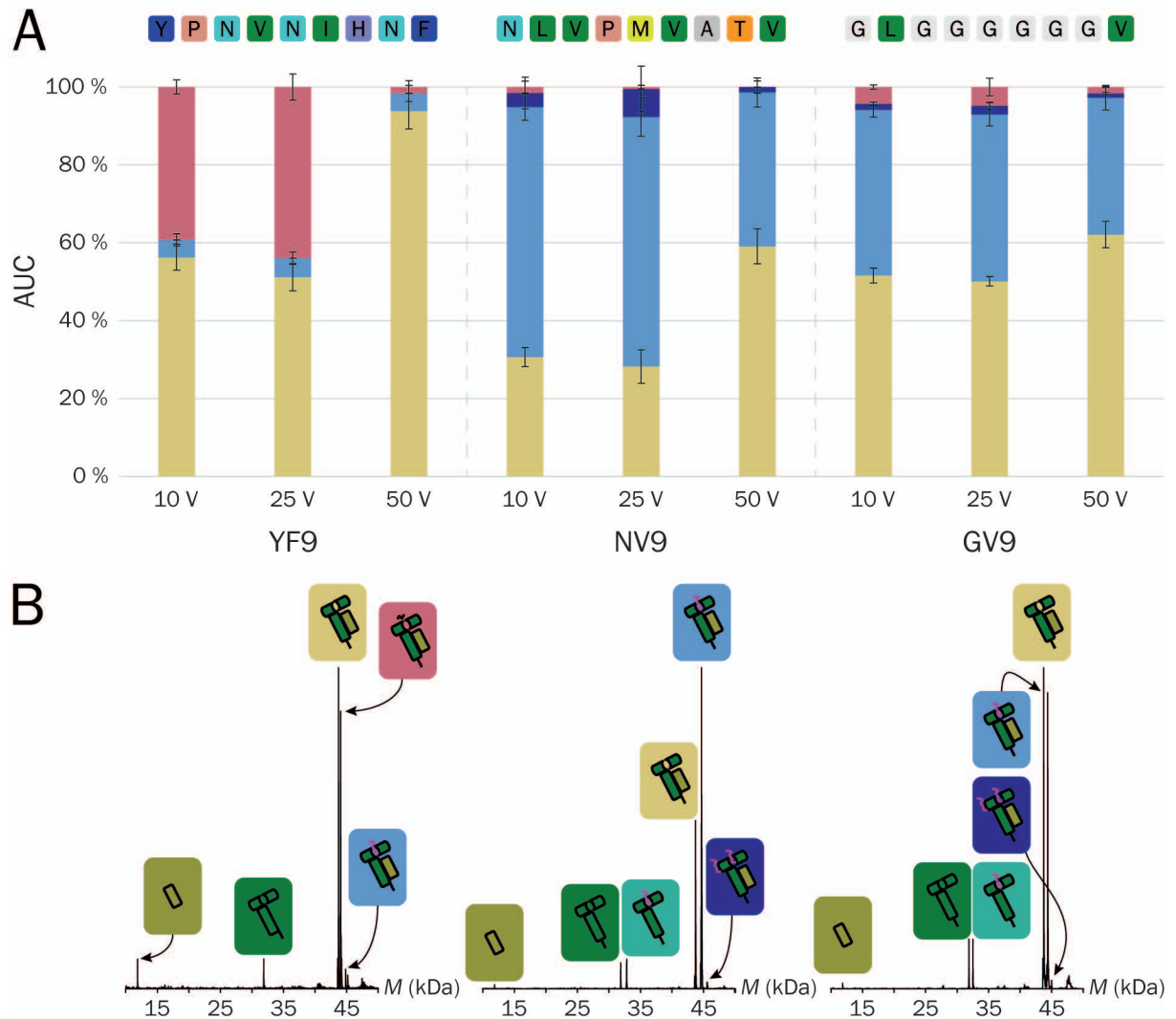


Figure 28 | Determining the binding affinities of YF9, NV9 and GV9 to dsA2.

A: The AUC was determined over the entire spectrum for the respective mass species at acceleration voltages of 10 V, 25 V, and 50 V. The cone voltage was kept constant at 150 V. The mean value of the AUC in the presence of the different peptides (protein-peptide ratio 1:5) from at least three independent measurements is depicted along with error bars that represent the corresponding standard deviation. The different complexes were assigned in yellow (empty dsA2), light blue (dsA2+pep), dark blue (dsA2+pep+pep), and coral (dsA2+erucamide). The negative control YF9 (uncorrected) barely associated with dsA2, whereas the positive control showed a high proportion of dsA2+NV9, indicating high affinity. GV9, which contains only the two anchor residues L2 and V9 of NV9, still showed a high affinity, and at 50 V, their dsA2+pep proportions were very similar, showing that their gas-phase stability is comparable. **B:** Representative charge-deconvoluted spectra of the distinct protein and protein-peptide complex species recorded at 25 V. Olive and dark green correspond to the free β_2m domain and HC, respectively. Teal corresponds to a FHC still attached to a peptide.

The dsA2+erucamide complex was completely absent, suggesting that erucamide was displaced by NV9. Hence, erucamide either bound into the peptide-binding groove, or

bound elsewhere and was displaced by a conformational change caused by peptide binding.

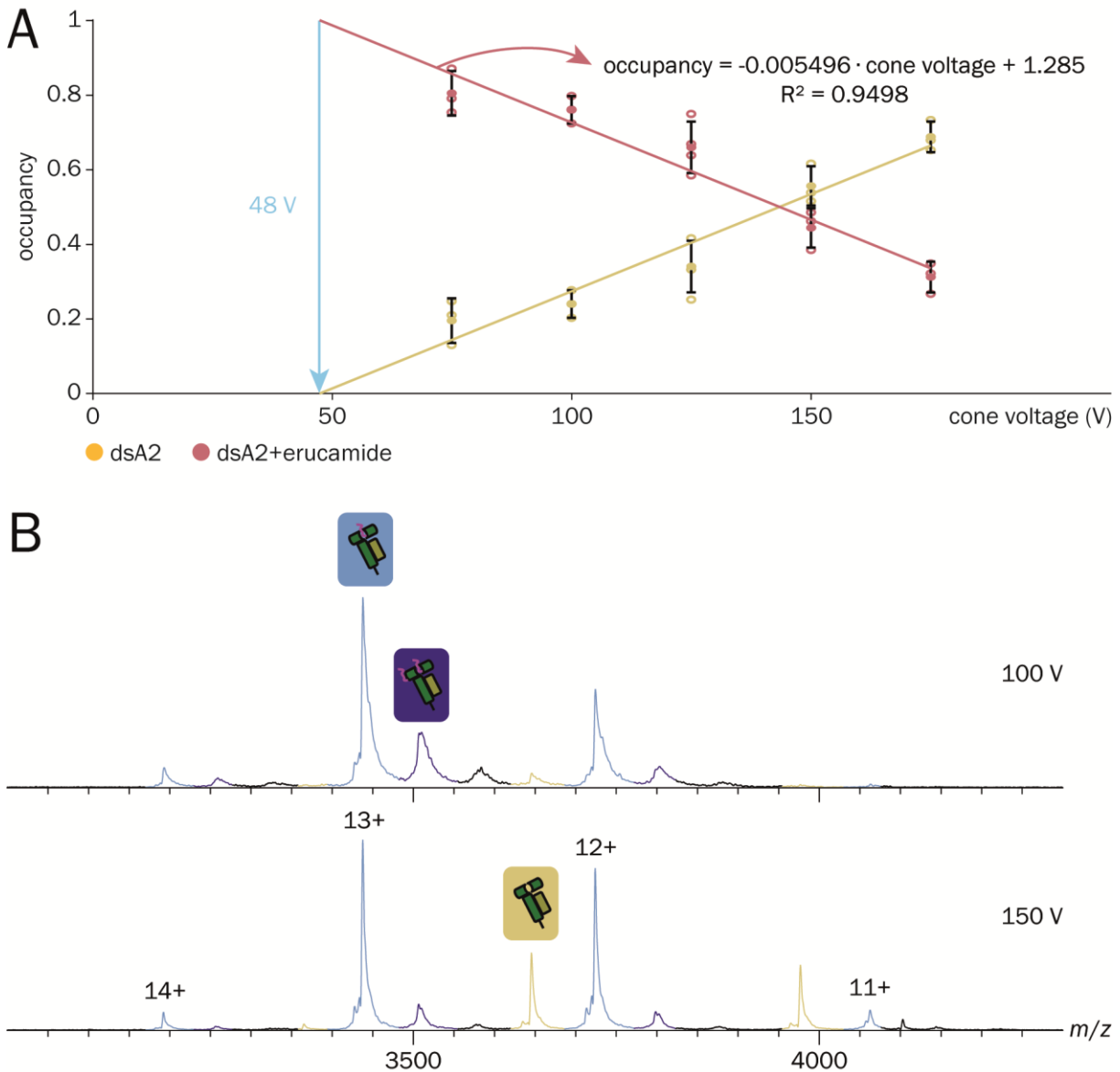


Figure 29 | ISD causes linear dependence of the ligand-bound dsA2 fraction on cone voltage.

A: Native MS fractions of empty dsA2 (yellow) and dsA2+erucamide (coral) were likewise dependent on the activation energy of the cone voltage. As the cone voltage was raised, the percentage of empty dsA2 increased because the adduct binding could not withstand the energy in the ion source and therefore dissociated. The proportionality was linear, and therefore a theoretical cone voltage of 48 V could be calculated at which a full occupancy with ligand would be reached. This voltage was too low to obtain stable electrospray and a resolved spectrum. **B:** Peptide binding was equally subject to ISD. NV9-bound dsA2 (light blue and dark blue annotated peaks) became less prominent with increasing cone voltage, while empty dsA2 (yellow) increased at the same time.

A small amount of another mass species ($45,624 \text{ Da} \pm 4 \text{ Da}$) corresponds to dsA2 with two molecules of NV9 (dsA2+NV9+NV9) with an abundance of $4\% \pm 4\%$ (10 V) and $1\% \pm 2\%$ at 50 V was also observed. The latter was likely the result of unspecific clustering, as the abundance correlated with the intensity of the first binding event and was similar to the intensity of unspecific YF9 clustering. Within NV9, the leucine in the second position and

the C-terminal valine bind into the B and F pocket of the peptide-binding groove, respectively^{256,257,174}.

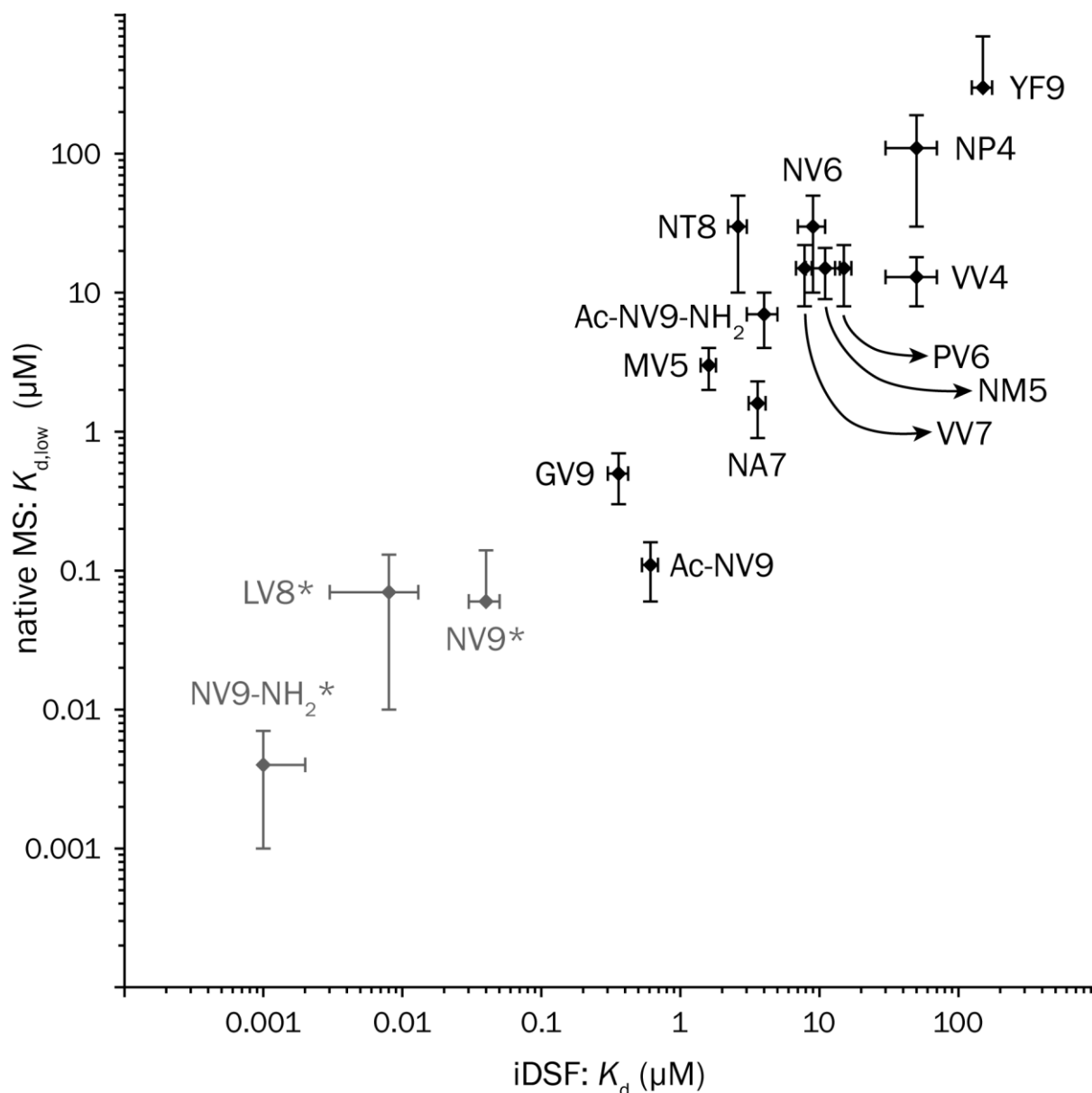


Figure 30 | Affinities determined via iDSF and native MS correlate.

Displayed data points represent the relationship of both apparent K_d for all different dsA2+peptide systems analyzed. The dsA2 complex and peptide were deployed in a ratio of 1:5. The native MS derived K_d for the various peptides is based on measurements performed at 10 V of acceleration voltage and 150 V of cone voltage. Both axes are scaled logarithmically. *iDSF reaches its limits at affinities below 200 nM, hence the values of grayed-out peptides are not reliable.

The proportion of dsA2 occupied with GV9 at 10 V ($43\% \pm 2\%$, and $1.5\% \pm 0.4\%$ for dsA2+GV9+GV9) was significantly lower than the proportion of dsA2+NV9. Thus, the minimal binding motif could not support the same affinity as NV9, suggesting that other amino acids contribute significantly to the binding. At 50 V, however, the abundance of the dsA2+pep complex was the same for GV9 and NV9. This indicates that the strong B and F pocket side chain interactions together with the binding of the termini determine pMHC

gas-phase stability. Despite strong binding with nM affinity²⁵⁸, the obtained K_d ($K_{d,high}$, defined below) for NV9 was only $8 \mu\text{M} \pm 2 \mu\text{M}$, and the expected fully occupied (> 99%) peptide-binding pocket was not observed (**Figure 28A**).

Protein denaturation due to storage or other stresses could be excluded from standard control experiments. Instead, ISD is the cause. Indeed, lower, *i.e.*, gentler, cone voltages^{259,260} increased the occupancy of the peptide-binding groove with both the peptide and erucamide. This linear relationship was most evident with dsA2 and erucamide in absence of any peptide (**Figure 29A**). The proportion of the dsA2+pep species was likewise linearly dependent on the cone voltage (**Figure 29B**). The extent to which the protein-peptide complex is affected by ISD depends on the gas-phase properties and the binding affinity of the peptide in question. Extrapolated data suggested that at a cone voltage of ≤ 48 V (which is unfeasible experimentally), dsA2 is 100% occupied with erucamide. Thus, erucamide was used as a reference species for peptide-binding measurements, assuming that in solution, all free dsA2 protein is initially bound to erucamide as suggested by the zero-cone voltage extrapolation, and that the peptide replaces it. This way, the fraction of peptide-free dsA2 (identical to the fraction of dsA2+erucamide complex) in the sample was calculated from a measurement at 150 V cone voltage using the correction factor of 2.2 (*cf.* **Chapter 5.4**), and from this, the fraction of dsA2+peptide could be inferred. The resulting K_d is a reliable approximation for binding in solution. Standardizing ISD to the dsA2+erucamide complex is advantageous since for individual pMHCs, the ISD is naturally influenced by peptide size and sequence, precluding compensation, while the ISD of the MHC-erucamide complex is invariant and peptide-independent. Therefore, for each peptide, both a K_d for the high cone voltage (150 V) based on the clustering-corrected pMHC signal ($K_{d,high}$) and another for the theoretical low cone voltage of 48 V based on the MHC-erucamide signal ($K_{d,low}$) were described (**Table 10, Supplement**). While the experimentally determined $K_{d,high}$ was overestimated due to ISD, the $K_{d,low}$ was a more reliable approximation, well demonstrated by the example of NV9. In the following figures, therefore, $K_{d,low}$ is given. Next, a series of sixteen peptides, most of them variations or truncations of the sequence of NV9, were compared in native MS and in the previously validated method, isothermal analysis of nanoscale differential scanning fluorimetry (iDSF)²⁶¹. K_d values from native MS and iDSF correlated very well over a wide range (**Table 9, Supplement, and Figure 30**). It has to be noted though that affinities below 200 nM have to be treated with caution as the peptide concentration, and hence the fraction of dsA2+pep, is very low in iDSF. It was also found

that K_d values from native MS correlated well with the thermal stabilization ΔT_m of dsA2 by peptide binding (protein-peptide ratio: 1:10, **Figure 31**), *i.e.*, the increase in the midpoint of thermal denaturation (melting temperature, T_m) above that of the empty dsA2 ($35.7 \text{ }^\circ\text{C} \pm 0.6 \text{ }^\circ\text{C}$) as measured by tryptophan nanoscale differential scanning fluorimetry (nDSF)^{240,262}.

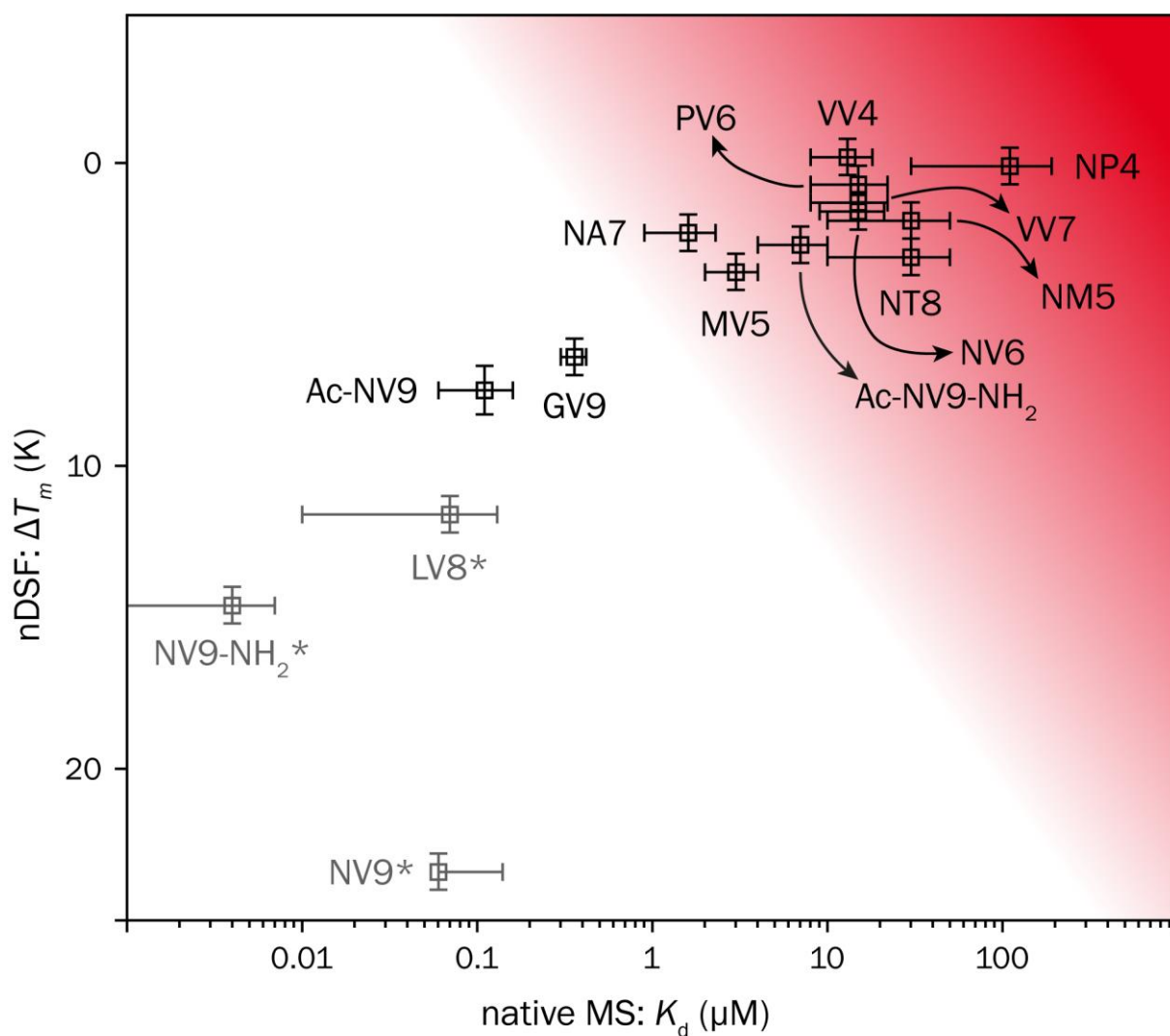


Figure 31 | Relation of thermal stability and affinity for dsA2+peptide complexes.

Thermal denaturation measurements availing intrinsic tryptophans' change in fluorescence were used to define protein complex stabilization upon peptide binding, whereas an apparent K_d for the various peptides was determined using native MS (10 V acceleration voltage and 150 V cone voltage). The dsA2 complex and peptide were deployed in a ratio of 1:10 (ΔT_m) or 1:5 (K_d) depending on the experiment. Peptides showing a small $K_{d,low}$ for binding dsA2 and being concomitantly able to stabilize the protein complex were defined as strong binders (white area). The remaining peptides (red area) lack crucial features, making them unable to form strong bonds to dsA2 indicated by low binding affinities and T_m . The standard deviation for both methods is displayed by error bars. The x coordinate is displayed logarithmically. *nDSF reaches its limits at affinities below 200 nM, hence the values of grayed-out peptides are not reliable.

While the negative control YF9 clearly showed no stabilization ($\Delta T_m = 1 \text{ K} \pm 1 \text{ K}$), the positive control NV9 showed a high ΔT_m ($23.4 \text{ K} \pm 0.6 \text{ K}$) in agreement with published data¹⁷⁴; this represented the maximum ΔT_m possible since NV9 stabilizes the binding groove so strongly that upon heating, other domains unfold first (**Figure 27**)^{240,262}. All other

peptides showed an excellent correlation between K_d and ΔT_m . Those identified as strong binders by their K_d exhibited a ΔT_m of at least $6.4 \text{ K} \pm 0.6 \text{ K}$ (GV9), while the ΔT_m for the low-affinity peptides ranged between $\approx 0 \text{ K}$ and $\approx 3 \text{ K}$ (Figure 31, red area). A closer evaluation of the data showed that peptides with a $K_{d,low} < 1 \mu\text{M}$ also had an increased gas-phase stability of the complex at 50 V ($\text{dsA2+pep} + \text{dsA2+pep+pep} > 35\%$) and presented only negligible amounts of dsA2+erucamide at any voltage. Therefore, we defined all peptides that fall within this range as strong binders for dsA2 (Figure 31, white area). These results demonstrated that by simply comparing the intensities in the native mass spectrum, it is possible to determine the K_d and hence high-affinity epitopes for HLA-A*02:01.

3.3.1.2 Neutralizing the terminal charges of the peptide reduces binding efficiency

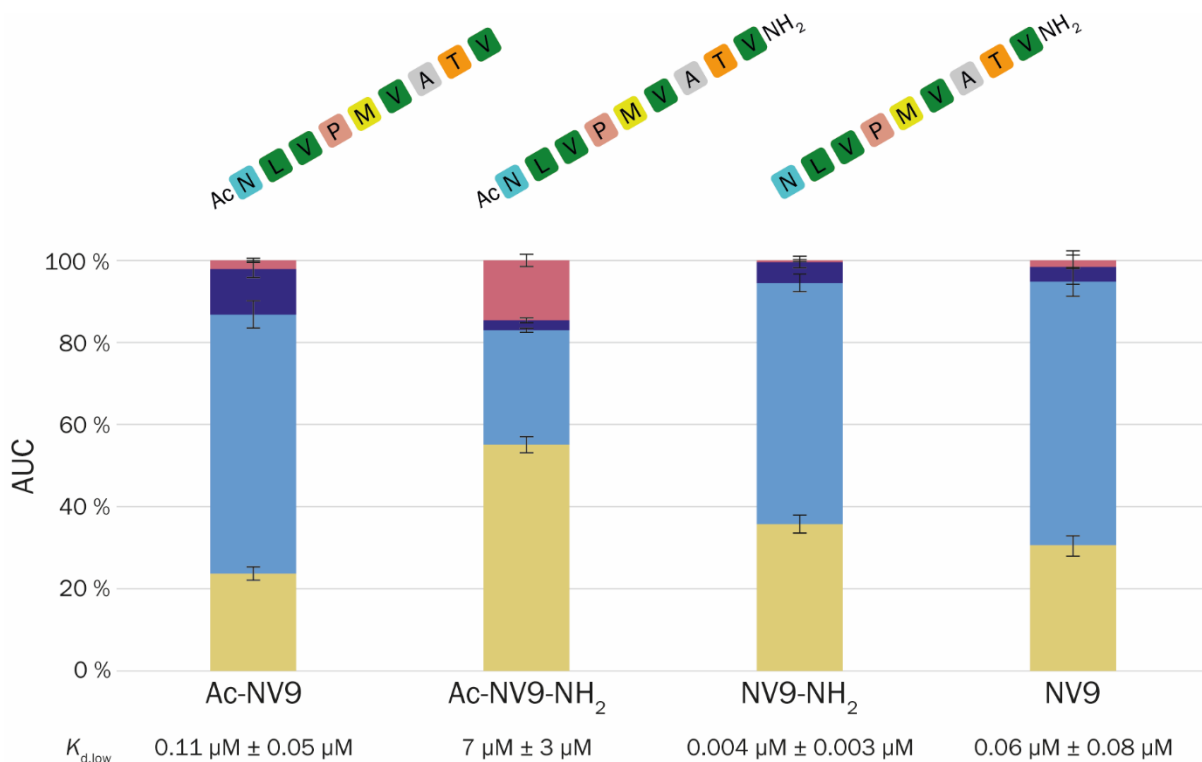


Figure 32 | Determining the binding affinities of charge-reduced NV9 variants to dsA2.

The AUC was determined over the entire spectrum for the respective mass species at an acceleration voltages of 10 V. The cone voltage was kept constant at 150 V. The mean value of the AUC in the presence of the different peptides (protein-peptide ratio 1:5) from at least three independent measurements is depicted along with error bars that represent the corresponding standard deviation. The corresponding $K_{d,low}$ is shown for respective peptides. The different complexes were assigned in yellow (empty dsA2), light blue (dsA2+pep), dark blue (dsA2+pep+pep), and coral (dsA2+erucamide). By modifying only one terminus (Ac-NV9 and NV9-NH₂), the affinity of the peptide to dsA2 changed only marginally, but if the charges on both termini were neutralized (Ac-NV9-NH₂), the peptide binding was greatly reduced.

Next, the influence of the charged termini of the peptide upon the K_d was analyzed. We hereby simulated the binding of deca- or undecapeptides but also peptides with common naturally occurring modifications in eukaryotes such as N^α -acetylation^{263,264}. For this

purpose, three variants of NV9 were designed: Ac-NV9-NH₂ has an acetylated *N*-terminus and an amidated *C*-terminus, whereas Ac-NV9 and NV9-NH₂ each carry only one of these modifications. For the dsA2+pep fraction at 10 V, Ac-NV9 and NV9-NH₂ showed only a small difference from unmodified NV9, with comparable apparent K_d values ($K_{d,low} = 0.11 \mu\text{M} \pm 0.05 \mu\text{M}$ and $0.004 \mu\text{M} \pm 0.003 \mu\text{M}$). Further, no increase of dsA2+erucamide was observed (Figure 32; reference spectra in Figure 33). For both peptides, the protein-ligand complex was still stable at 50 V (Figure 34). For Ac-NV9, the proportion of the occupancy was even higher than for NV9 itself ($57\% \pm 2\%$ and $8\% \pm 1\%$ vs. $40\% \pm 4\%$ and $1\% \pm 2\%$, Table 9, Supplement).

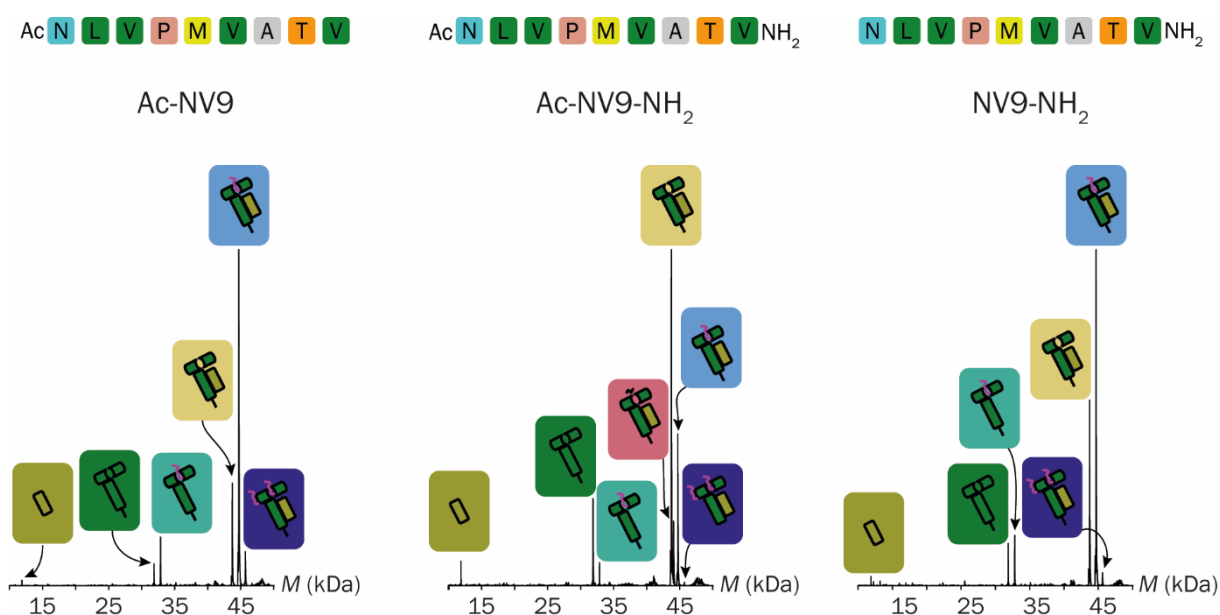


Figure 33 | Analyzing the charge-reduced NV9 variants using native MS.

Representative charge-deconvoluted spectra of the distinct protein and protein-peptide complex species recorded at an acceleration voltage of 10 V. Olive and dark green correspond to the free $\beta_2\text{m}$ domain and HC, respectively. Teal corresponds to a FHC still attached to a peptide. The different complexes were assigned in yellow (empty dsA2), coral (dsA2+erucamide), light blue (dsA2+pep), and dark blue (dsA2+pep+pep).

Remarkably, all modified peptides had an increased double occupancy. For the previously discussed peptides, dsA2+pep+pep was significantly lower with the result that correction for nonspecific clustering reduced it to a value below the threshold of meaningful signal. For Ac-NV9, this effect was significant, since even at 50 V the proportion of dsA2+pep+pep (dark blue) was still $8\% \pm 1\%$ indicating altered clustering or self-interaction. This clearly showed the benefit of the indirect erucamide approach.

However, the stabilization effect on dsA2 in a 1:10 thermal denaturation approach was rather moderate for Ac-NV9 ($\Delta T_m = 7.5 \text{ K} \pm 0.8 \text{ K}$), while it was very strong for NV9-NH₂ ($\Delta T_m = 14.6 \text{ K} \pm 0.6 \text{ K}$), indicating that the *N*-terminus has more relevance for tight peptide binding than the *C*-terminus. For Ac-NV9-NH₂, the affinity decreased significantly

($K_{d,low} = 7 \mu\text{M} \pm 3 \mu\text{M}$) due to the dual modification, and at an acceleration voltage of 50 V the complex was no longer stable. The nDSF measurements likewise showed that the stabilization effect ($\Delta T_m = 2.7 \text{ K} \pm 0.6 \text{ K}$) is rather weak. At the same time, there was no significant increase in double binding events. In summary, NV9-NH₂ was far better rated in terms of affinity and stabilizing effect (**Figure 30** and **Figure 31**), but Ac-NV9 still fell into the category of a strong binder. For Ac-NV9-NH₂, which no longer carries terminal charges, a loss of binding efficiency was observed, indicating that the respective hydrogen bonds are indispensable in the formation of the pMHC.

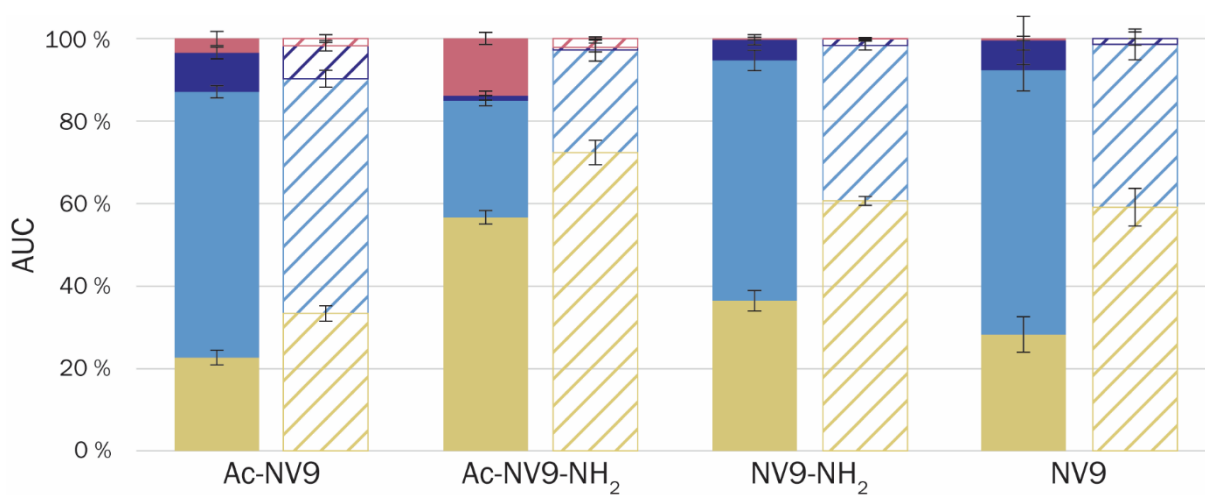


Figure 34 | dsA2 and charge-reduced NV9 variants at higher collision energies.

The AUC was determined over the entire spectrum for the respective mass species at acceleration voltages of 25 V (solid colors) and 50 V (diagonal pattern). The cone voltage was kept constant at 150 V. The mean value of the AUC in the presence of the different peptides (protein-peptide ratio 1:5) from at least three independent measurements is depicted along with error bars that represent the corresponding standard deviation. The different complexes were assigned in yellow (empty dsA2), coral (dsA2+erucamide), light blue (dsA2+pep), and dark blue (dsA2+pep+pep).

3.3.1.3 NV9 truncations disclose preferred binding positions in the peptide

Since the anchor residues do not determine affinity alone, the effect of stepwise truncation of NV9 from either terminus on binding was analyzed. Building on the knowledge from the dsA2+NV9 crystal structure^{2,174}, the peptide-binding groove can thus be mapped and further understood. *In vivo*, MHC-I predominantly binds peptides with a length of eight to eleven amino acids^{265,140,235}. It is therefore not surprising that octa- and nonapeptides showed the highest affinity (**Figure 35** and **Table 10, Supplement**). Still, the effects of the loss of either terminal amino acid were strikingly different. Without the N-terminal asparagine (LV8), the affinity ($K_{d,low} = 0.07 \mu\text{M} \pm 0.06 \mu\text{M}$) was still comparable to NV9, with considerable thermal stabilization (1:10, $\Delta T_m = 11.6 \text{ K} \pm 0.6 \text{ K}$). At 50 V, dsA2+LV8 even appeared to be more stable than dsA2+NV9. In contrast, loss of the C-terminal valine (NT8) strongly decreased affinity ($K_{d,low} = 30 \mu\text{M} \pm 20 \mu\text{M}$). The erucamide was no longer fully displaced by NT8, only a small fraction of the protein+peptide complex was resistant

to 50 V acceleration voltage, and no significant stabilization effect ($\Delta T_m = 3.1 \text{ K} \pm 0.6 \text{ K}$) was measured. Thus, the interactions of the C-terminal amino acid, an anchor residue, are more important for overall binding than those of the N-terminal amino acid. However, when the second amino acid from the N-terminus, leucine, was also eliminated (VV7), affinity and stabilization were strongly diminished as expected, since the second position is an anchor residue. Strong binding between peptide and A2 only occurred if both B and F pockets are occupied with peptide side chains.

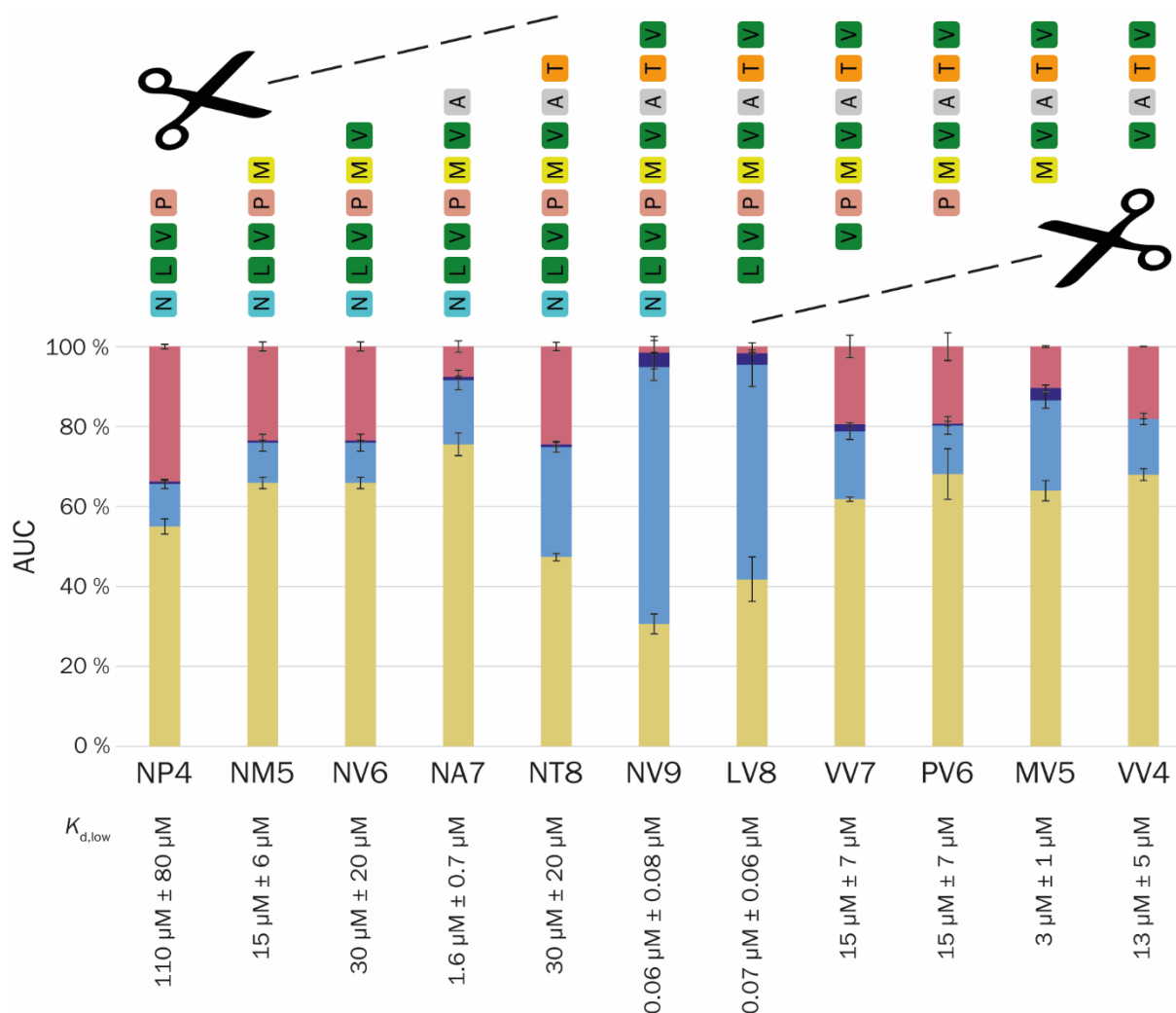


Figure 35 | Determining the binding affinities of truncated NV9 variants to dsA2.

The AUC was determined over the entire spectrum for the respective mass species at an acceleration voltages of 10 V. The cone voltage was kept constant at 150 V. The mean value of the AUC in the presence of the different peptides (protein-peptide ratio 1:5) from at least three independent measurements is depicted along with error bars that represent the corresponding standard deviation. The corresponding $K_{d,low}$ is shown for respective peptides. The different complexes were assigned in yellow (empty dsA2), coral (dsA2+erucamide), light blue (dsA2+pep), and dark blue (dsA2+pep+pep). Octa- and nonapeptides had the highest binding efficiency in accordance with their biological function. Without the anchor residues L2 and V9 in a truncated NV9 variant, the affinity decreased drastically. A terminal methionine appeared to enhance the affinity of the peptide to dsA2.

Still, the difference between GV9 and LV8 pointed towards an additional contribution of the other amino acids that is in sum larger than the N-terminal contribution. While none of the examined tetra- to heptapeptides were strong binders, VV7, still containing the C-

terminal anchor residue V9, performed worse than NA7, which in contrast carries L2. NA7 displaced more of the erucamide, and at 50 V, significantly more NA7 than VV7 was observed (**Figure 36**). Thus, L2 appeared to impart stronger binding than V9. Curiously, the *N*-terminally truncated pentapeptide MV5 performed significantly better than the corresponding hexa- (PV6) and heptapeptides (VV7). The increased proportion of dsA2+MV5 at 50 V (**Figure 36**) and the simultaneous occurrence of dsA2+MV5+MV5 (dark blue bars, **Figure 35**) strongly suggested that MV5 occupies an additional binding site within the peptide-binding groove. Because this effect was not apparent for the smaller VV4, the terminal methionine seemed to be decisive. Since no increased dual occupancy was observed for NM5, and binding at 50 V was weaker than for MV5, it seemed that the terminal methionine as such is not determinant on its own, but rather the relative position within the peptide. Considering the tetrapeptides, again the *N*-terminally truncated peptide, VV4, bound better than the *C*-terminally truncated NP4 at all acceleration voltages, pointing to the positioning of the erucamide within the peptide pocket. While NP4 carries only the anchor peptide L2, it seemed that VV4 has a higher chance to bind to the dsA2 peptide groove due to its two terminal valines.

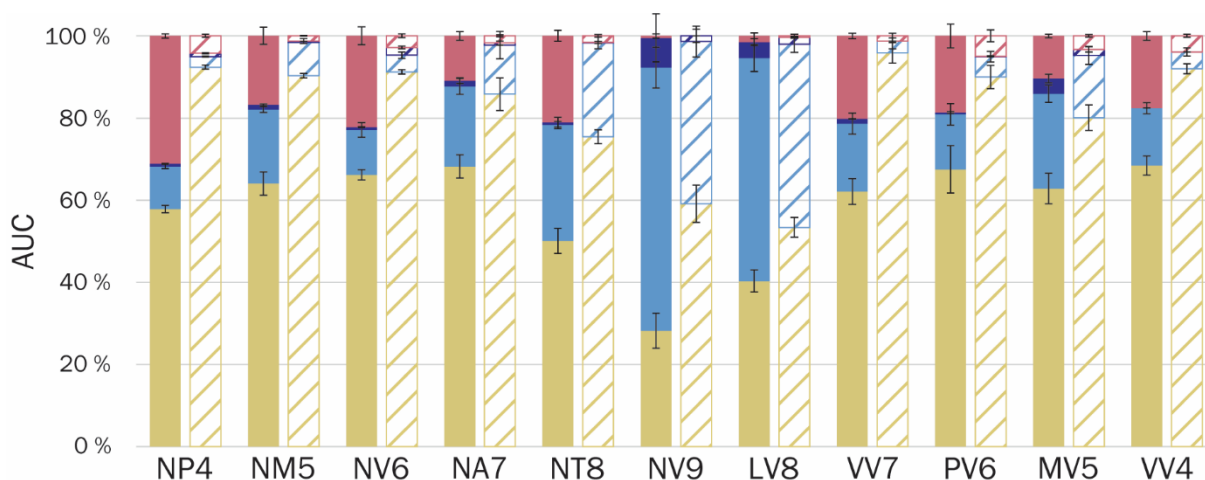


Figure 36 | dsA2 and truncated NV9 variants at higher collision energies.

The AUC was determined over the entire spectrum for the respective mass species at acceleration voltages of 25 V (solid colors) and 50 V (diagonal pattern). The cone voltage was kept constant at 150 V. The mean value of the AUC in the presence of the different peptides (protein-peptide ratio 1:5) from at least three independent measurements is depicted along with error bars that represent the corresponding standard deviation. The different complexes were assigned in yellow (empty dsA2), coral (dsA2+erucamide), light blue (dsA2+pep), and dark blue (dsA2+pep+pep).

3.3.1.4 The binding groove may be occupied simultaneously by two short peptides

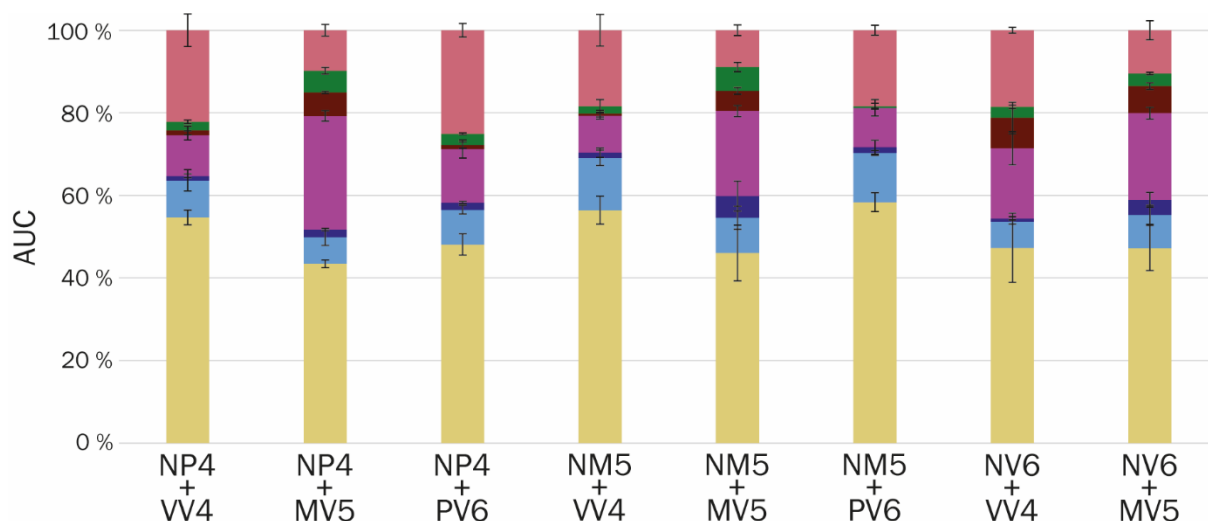


Figure 37 | Detected dsA2 mass species in presence of two corresponding truncated NV9 variants.

The native MS data suggested that the truncated peptides did not bind cooperatively as the amount of dsA2+pep1+pep2 remained small in all measurements. Rather, the affinity of the individual peptides was independent of each other. The AUC was determined over the entire spectrum for the respective mass species at 10 V. The mean value of the AUC in the presence of the different peptides (protein-peptide ratio 1:10:10) from at least three independent measurements is depicted along with error bars that represent the corresponding standard deviation. Yellow corresponds to the empty disulfide mutant complex (dsA2), light blue to dsA2 bound to one peptide (dsA2+pep1), dark blue to dsA2 bound to two molecules of this certain peptide (dsA2+pep1+pep1), purple to dsA2 bound to another peptide when two different peptides were present (dsA2+pep2), dark red to dsA2 bound to two molecules of the second peptide (dsA2+pep2+pep2), green to dsA2 bound to one molecule of each of both peptides (dsA2+pep1+pep2) and coral to dsA2 bound to the erucamide respectively.

Next, the simultaneous presence of two peptides in the binding pocket was further investigated²⁶⁶. Since native MS measures the binding of either peptide independently of the presence of the other in a single experiment, this allowed us to assess whether peptide binding to the two ends of the peptide-binding groove is cooperative. The truncated peptides of NV9 were combined with their corresponding counterparts from the opposite terminus.

Two short peptides that bind to different sites in the binding groove could either bind independently without any communication between the binding sites or in a cooperative manner, where the two binding sites communicate by a conformational or dynamic change in the protein and one peptide stabilizes (or destabilizes) the binding site for the other, such that the binding affinity for the second peptide is higher (or lower) in presence of the first. **Figure 37** shows single and double occupancy in native MS measurements for either peptide and for both together. The affinities of the two individual peptides found earlier are reflected well in this combined experiment.

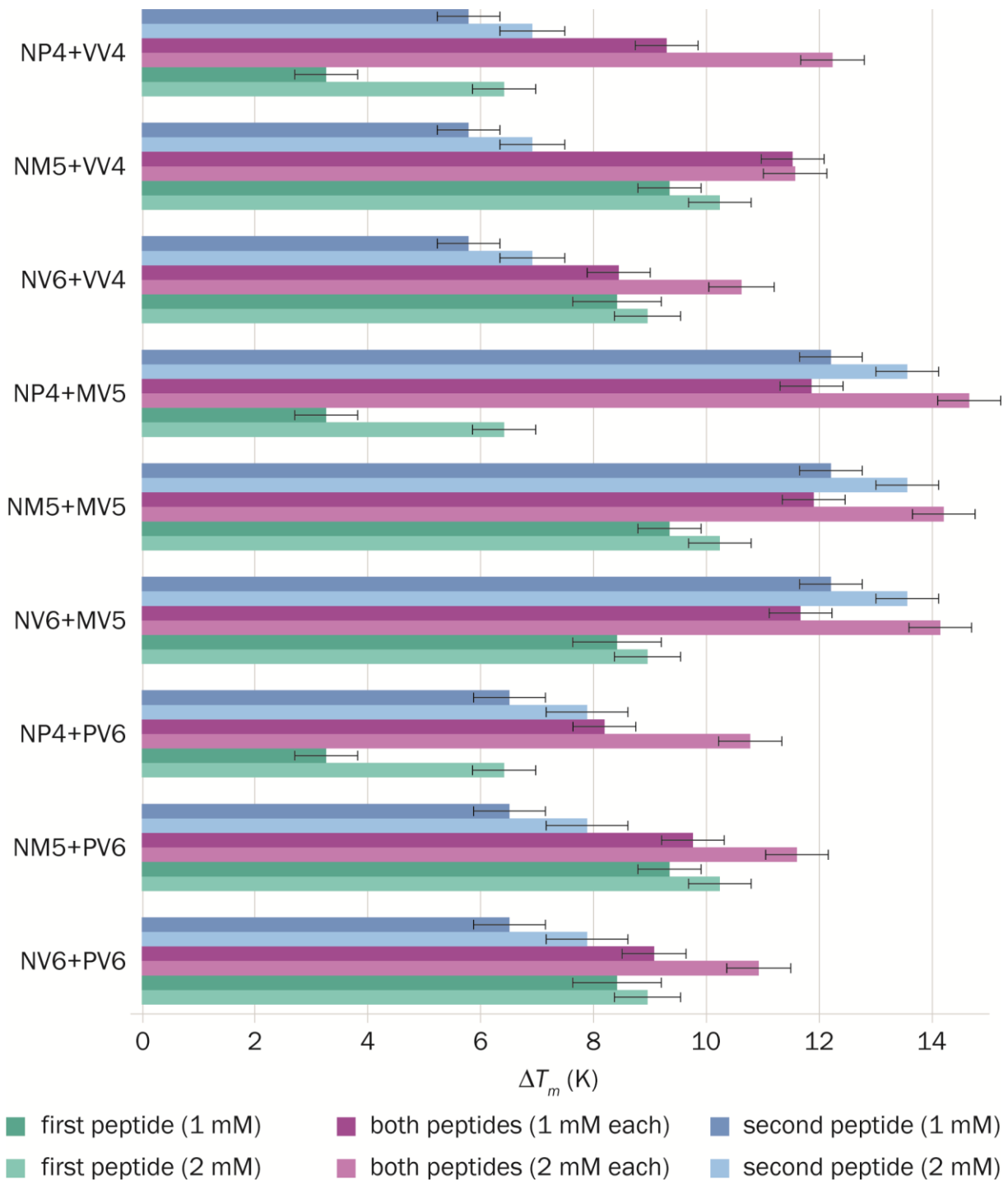


Figure 38 | T_m of dsA2 in presence of two corresponding truncated NV9 variants.

nDSF was employed to study thermal denaturation of dsA2 in presence of two peptides at once. 2 μM dsA2 were combined with either exclusively the N- (teal) or C-terminal peptide (blue) or both peptides together (purple) at different concentrations. Results for ΔT_m along with respective standard deviations are displayed.

No double-occupied complex could be detected in the pairing of the pentapeptide NM5 and the hexapeptide PV6, presumably, due to spatial restriction. In the other combinations, dsA2+pep1+pep2 was detected. Yet only when MV5 is involved in the binding, the complex could withstand higher acceleration voltages. It was assumed, however, that this is not due to a cooperative binding between NP4 and MV5, NM5 and MV5 or NV6 and MV5, but can rather be explained by the higher affinity of MV5 described above. Remarkably, VV4

achieved a significantly higher occupancy when combined with the corresponding hexapeptide (NV6), which was not the case for NP4 with PV6. This once again suggests that VATV appears to have more binding options due to its two terminal valines. In addition to the native MS measurements, nDSF measurements were performed with higher peptide excess to evaluate whether two peptides are able to synergistically stabilize dsA2.

ΔT_m for dsA2 (2 μ M) in K ($K_{d,low}$ in μ M)			N-terminal stabilization	C-terminal stabilization	synergistic effect	potential synergy
2 mM N- or C-term. pep.	1 mM N- or C-term pep.		9.0 \pm 0.6	10.2 \pm 0.6	6.4 \pm 0.6	
			8.4 \pm 0.8	9.4 \pm 0.6	3.3 \pm 0.6	
		1 mM N- and C-term pep.	NV6	NM5	NP4	
7.9 \pm 0.7	6.5 \pm 0.6	PV6	9.1 \pm 0.6	9.8 \pm 0.6 (60 \pm 20)	8.2 \pm 0.6 (130 \pm 60)	
13.6 \pm 0.6	12.2 \pm 0.6	MV5	11.7 \pm 0.6 (13 \pm 5)	11.9 \pm 0.6 (9 \pm 3)	11.9 \pm 0.6 (11 \pm 3)	
6.9 \pm 0.6	5.8 \pm 0.6	W4	8.5 \pm 0.6 (60 \pm 20)	11.5 \pm 0.6 (60 \pm 30)	9.3 \pm 0.6 (90 \pm 40)	

Figure 39 | Synergistic stabilization of dsA2 in presence of two corresponding truncated NV9 variants.

The matrix visualizes the changes of T_m in case half of the peptide amount was either exchanged for the corresponding N- (teal) or C-terminal (blue) peptide respectively or alternatively omitted. Teal marks the occurrence of major N-terminal stabilization whereas, for the light blue cells, the complex was primarily stabilized by the C-terminal peptide. Purple cells show peptide coupling with a significant synergistic effect or potential synergy (light purple). For respective peptide pairs, the $K_{d,low}$ is shown in brackets.

The T_m of dsA2 exposed to one of the truncated NV9 variants (**Figure 38**) was compared to the resulting T_m with two peptides, while the ratio of protein to total peptide concentration was kept constant at 1:1000. If no synergistic effect occurred, then the resulting T_m was expected less than or equal to that of the peptide complex with higher affinity. In line with the native MS results, most peptide pairs did not show additional stabilization by peptide combinations. Only for NP4 and W4 (and to a lesser extent for NP4 and PV6), a higher T_m was measured for both peptides together, which demonstrated that dsA2 can be stabilized

by two shorter peptides in a synergistic fashion if they do not compete with each other for binding (**Figure 39**).

Once again, MV5 stood out particularly in this experiment. Two parts of MV5 provided significantly more thermal stability to dsA2 than one part of MV5 together with one part of one of either of the corresponding *N*-terminal peptides, again suggesting that MV5 can bind into two positions in the binding groove. Taken together, these observations suggested that the unfolding of MHC-I (or at least of the disulfide mutant) can begin at either end of the peptide-binding groove and that the opposite ends of the groove cannot communicate conformationally, which was already described for the corresponding wild type²²².

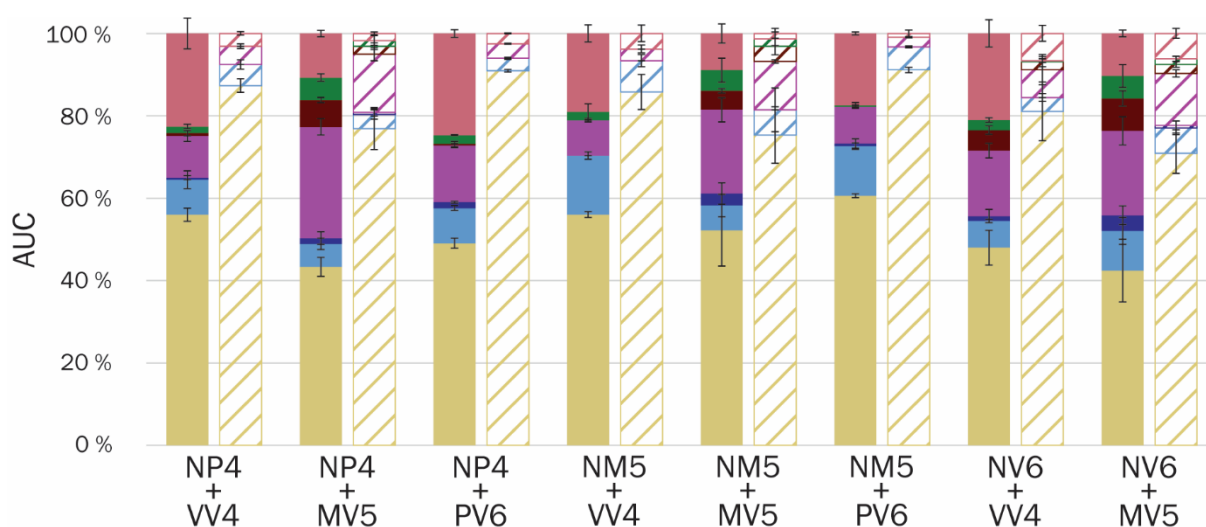


Figure 40 | dsA2 and two corresponding truncated NV9 variants at higher collision energies.

The AUC was determined over the entire spectrum for the respective mass species at acceleration voltages of 25 V (solid colors) and 50 V (diagonal pattern). The cone voltage was kept constant at 150 V. The mean value of the AUC in the presence of the different peptides (protein-peptide ratio 1:10:10) from at least three independent measurements is depicted along with error bars that represent the corresponding standard deviation. The different complexes were assigned in yellow (empty dsA2), light blue (dsA2+pep1), dark blue (dsA2+pep1+pep1), purple (dsA2+pep2), dark red (dsA2+pep2+pep2), green (dsA2+pep1+pep2), and coral (dsA2+erucamide).

3.3.2 Discussion

While only wild type pMHC had been studied by native MS so far²⁶⁷, we have recently demonstrated that peptides added to empty disulfide-stabilized MHC-I molecules can be detected as well². This work shows that this method, being fast and amenable to high-throughput approaches, can be used to measure MHC-I peptide-binding affinities and to map the contributions of parts of the peptide to high-affinity binding.

Our data affirmed the key interactions between dsA2 and its high-affinity ligand NV9 that were described previously²⁶⁸⁻²⁷⁰: The termini as well as L2 and the *C*-terminal V9, both binding into specific pockets, contribute the major portion of the binding energy. For the F pocket, it is well established that V or L are the strongest anchor residues with V being

the more preferred one, but our data suggest that MVATV can also stabilize the B pocket via its first valine similarly and possibly even simultaneously.

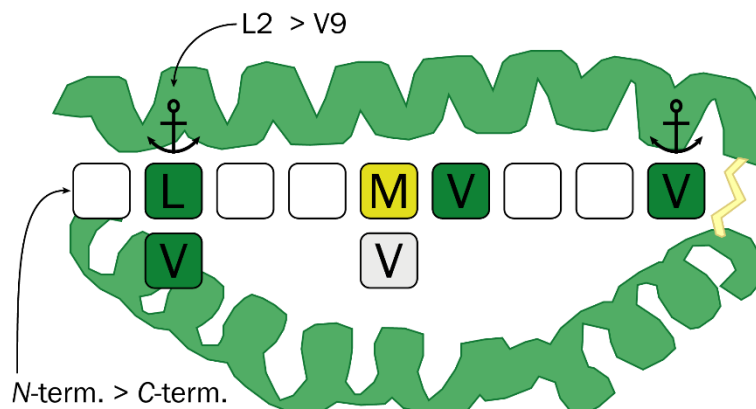


Figure 41 | Favored amino acid positions within the HLA-A*02:01 peptide-binding pocket.

Native MS confirmed L2 in the B pocket and V9 in the F pocket respectively as the main anchor positions of the pMHC. The analysis of truncated NV9 variants reveals that V2 is also a favored binding site. Moreover, M5 or V5, as well as V6, also contribute significantly to binding under certain circumstances. Among the anchor residues, L2 contributes significantly more to the binding than V9. Concerning the termini, the *N*-terminus is of greater importance for binding than the *C*-terminus.

The extraordinary thermal stabilization observed for dsA2+MV5, especially in comparison with potentially synergistic peptide pairs, gives rise to the assumption that even more than two binding modes are available for MV5. As reported before²¹⁵, along with leucine and methionine, valine is indeed one of the amino acid residues preferred by the HLA-A*02:01 and moreover by the entire A2 supertype as an anchor residue in the second position. Since proline in the *N*-terminal position was found to be a deleterious factor for binding, this could explain the poor performance of PV6 in our experiments despite the preferred methionine in the second position. Surprisingly, NV6 scored low in all our tests despite having leucine in the second position and a *C*-terminal valine. Given the two different binding modes, at least a higher proportion of singly-bound species would be expected here, similar to MV5, for statistical reasons. A potential explanation could be self-competition of the peptide for the two separate binding sites. Based on their sheer size, two NV6 molecules sterically hinder each other as opposed to the pentapeptide MV5.

As previously demonstrated², the F pocket can be occupied by GM with methionine as anchor residue. Methionine in the *C*-terminal position is not preferred but only tolerated by HLA-A*02:01, as reported before²¹⁵. Compared to MV5, which could bind with either valine, the second pentapeptide, NM5, therefore did not show the same strong binding behavior in our experiments. PARKER *et al.*²⁶⁹ claimed that GLGGGGGV, carrying the minimal binding motif, is not sufficient for the stabilization of HLA-A*02:01. However, GV9 bound well in our native MS experiment, and GV9 also increased thermal stability. Nevertheless,

the weaker binding compared to NV9 showed that other amino acids contribute substantially to the binding energy. From the shorter peptide-binding data, we propose that the disulfide-stabilized MHC-I molecule has at least two positions that can be stabilized independently upon peptide binding (**Figure 41**). Our findings with modified peptide termini support published observations¹⁴⁰ that the single-modified nonapeptides can indeed stabilize MHC-I, albeit to a lesser extent. In contrast, the weak binding of the double-modified Ac-NV9-NH₂ confirmed that one of the termini needs to be intact to form strong binding to either of the outer pockets. Thus, for example, undecapeptides with an overhang on both sides will have reduced affinity, as neither of the termini is intact. According to our data, the short, truncated peptides, which are unable to bind using both termini due to spatial limitations, could also stabilize their respective binding pocket individually, once again supporting our hypothesis concerning the independent stabilization of A and F pocket.

Binding of lipophilic small molecules into the MHC-I binding groove has been shown several times, sometimes quite tightly and (because of alteration of the bound peptidome) with medical consequences²¹⁵. In our MHC-I samples, erucamide was identified as the most prevalent contaminant, most likely from plastic ware²⁴³. It appeared to bind specifically into the peptide-binding groove, since it is displaced by peptides. An alternative explanation, binding outside the groove and displacement by a peptide-induced conformational change, we consider less likely due to the structural similarity of empty and peptide-bound dsA2². Thus, erucamide was used as a reference species to estimate the K_d of the peptides: an increase of dsA2+pep with a simultaneous decrease of dsA2+erucamide demonstrated that the corresponding peptide actually occupied the space in the peptide pocket due to its affinity to dsA2 instead of just clustering nonspecifically on the protein. Interestingly, other lipids have been shown to bind MHC-I^{271,272}, and since erucamide and related compounds are present in nutritional plants²⁷³ and produced by *E. coli*²⁷⁴, the binding could have biological relevance worth investigating.

HLA-A*02:01 is one of the most prevalent A2 allotypes among Caucasians and Asians, and it has been shown that high binding affinity to A*02:01 correlates with binding affinity to the entire A2 supertype, making A*02:01 a suitable candidate for comprehensive peptide screening²¹⁵. Epitope-based peptide vaccines offer various advantages regarding production, stability, and mutation risk. However, since HLA exhibits a strong polymorphism, the search for relevant, allele-spanning peptides has so far been challenging²¹⁵. With native MS, we have wide latitude in our approach to identify and

analyze potential epitopes. Measurements at low acceleration voltages yielded good estimates for the peptides' binding affinities. In contrast, prediction tools such as NetMHC cannot predict the K_d for shorter or modified peptides. Furthermore, we noted inconsistencies between our data and the affinities predicted by NetMHC. While this is reasonable in terms of the numerical values, the relative affinities for our fairly large number of peptides were also incongruent with the predictions (**Table 10, Supplement**). Moreover, the affinities determined by native MS and iDSF were in the same order of magnitude and correlate well. Thus, our work showed that the accuracy of affinity ranking by artificial neural networks needs to be debated.

Our measurements at higher energies yielded a simple test for strong peptide binding. We show that pMHC gas-phase stability is mainly determined by side chain interactions within the B and F pockets as well as by binding of the peptide termini. At an acceleration voltage of 50 V, only strongly bound ligands were retained. This value hence served as a cut-off value in our native MS approach that could easily be employed in a native MS-based screening. Apart from some attempts²⁷⁵⁻²⁷⁷, there is currently no high-throughput method for the identification of MHC-I binding peptides with immunogenic potential that is elaborated and reliable. Still, such high-throughput screenings are the ultimate key to the development of synthetic peptide vaccines that offer decisive advantages over conventional vaccines, as there is a lesser risk of unwanted host responses, no possibility of reversion to pathogenic phenotypes, and no limitation for target diseases^{214,278,279}. Vaccine production is rather easy and detached from the natural source itself, which may be challenging to culture^{214,278}. The greatest advantage of peptide vaccines lies in their stability. Especially in the context of the SARS-CoV-2 pandemic, mRNA vaccines have become very popular. However, especially these and other conventional vaccines are highly dependent on a continuous cold chain, whereas peptides show long-term thermal stability^{214,279,280}. This feature is of particular importance, as the need for vaccination is often especially high in tropical and hot climates with limited medical infrastructure. Taken together, our work provides a valid, sensitive, and rapid method to determine the K_d of the MHC-I-peptide complex and also the basis to develop a novel high-throughput peptide screen for MHC-I epitopes. Since our technique is based on MS, it allows working with very low sample consumption, and it also offers the possibility of simultaneous multi-species analysis.

3.4 Establishing a high-throughput peptide screening

Parts of the following chapter are in preparation for publication:

Kopicki, J. D., Springer, S., & Uetrecht, C. (in preparation).

3.4.1 Results

As MHC-I has already been characterized in detail in the previous chapters (3.2 & 3.3) and having demonstrated in particular that native MS is wonderfully suitable for providing qualitative as well as quantitative information on MHC peptide binding, we can now finally address the elaboration of an actual peptide screening, the prospective benefits of which have already been discussed previously. Once again, method development will be demonstrated using HLA-A*02:01 or its disulfide-stabilized counterpart as the exemplary MHC molecule.

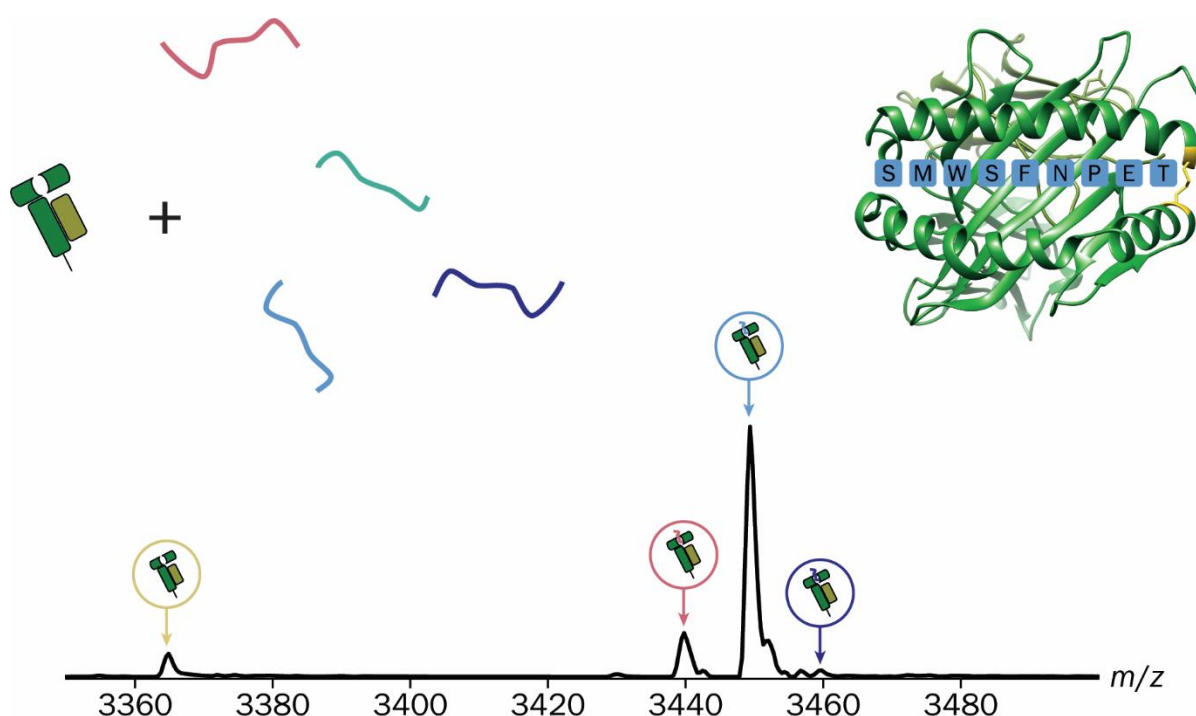


Figure 42 | The idea for peptide screening using native MS.

An MHC molecule in MS-compatible solution is incubated with the peptide pool in question and the mixture is analyzed with a mass spectrometer. The signals of the empty MHC and the different pMHCs are simultaneously displayed in the spectrum. The peak intensity reflects the affinity of the respective peptide ligand to the MHC molecule of interest. Based on the mass comprised of MHC and peptide, the peptides with the best binding properties can be accurately assigned. In the example spectrum, this would be the peptide shown in blue with the sequence SMWSFNPET, a peptide from the M protein of SARS-CoV-2.

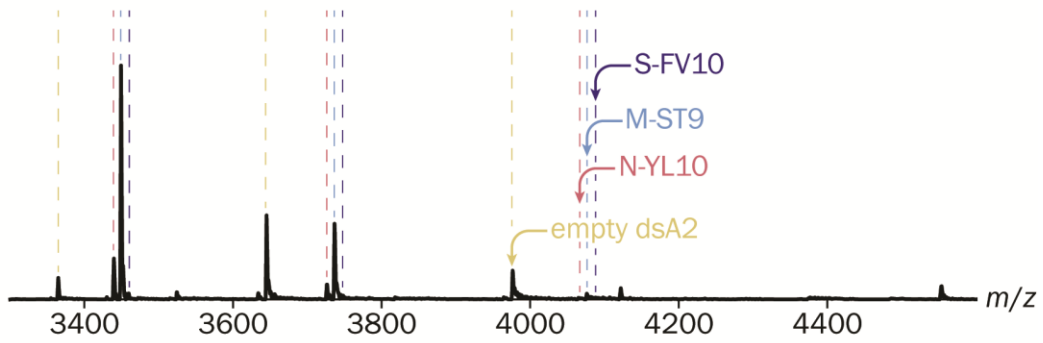
The ideal peptide screening for MHC-I should, above all, work quickly and with a high throughput rate while using only low amounts of sample; implementation and application should ideally be simple and inexpensive, and at best the process should even be automated. In the native MS approach (Figure 42), we strive to measure a mixture of the

MHC molecule of interest together with a pool of potential binding peptides and immediately identify the most affine candidates from the spectrum based on the peak intensities of the different pMHCs without bias.

3.4.1.1 Charge state 13⁺ best resembles in-solution conditions

All spectra analyzed for this work, when measured under the same conditions, showed the same distinct distribution of charge states. The charge state envelopes of the empty and peptide-bound MHC overlapped but are not congruent – there are clear differences depending on the charge state when comparing the respective signal intensity ratio of empty and peptide-bound MHC (**Figure 43**, full spectrum). While the relative intensity ratios of different pMHCs within a sample mixture did not differ significantly between charge states, the occupancy rate of the MHC molecule did vary a lot (*cf.* deconvoluted spectrum, 12⁺ and 13⁺ in **Figure 43**). Here, the fraction of pMHC decreased with declining charge state. Among all clearly prominent charge states, the 13⁺ was the one with the highest fraction of peptide-bound MHC molecule. As discussed earlier, in equimolar or superstoichiometric presence of affine peptides, high or complete occupancy of MHC molecules is expected when in solution. Thus, this native state was best represented by the 13⁺ charge state. In-source dissociation of the ligand resulted in the loss of one charge as the peptide drags it along explaining the higher proportion of empty MHCs at lower charge states. We therefore observed the least gas-phase and dissociation effects and consequently the best representation of the pMHC composition in solution at 13⁺, which allowed us to neglect the other charge states. By this, we avoid further steps like deconvoluting the spectrum providing a clear read-out of the intensity distribution directly from the regular spectrum. In the following, therefore, all further evaluation steps are based solely on the 13⁺ charge state.

full spectrum



deconvoluted spectrum

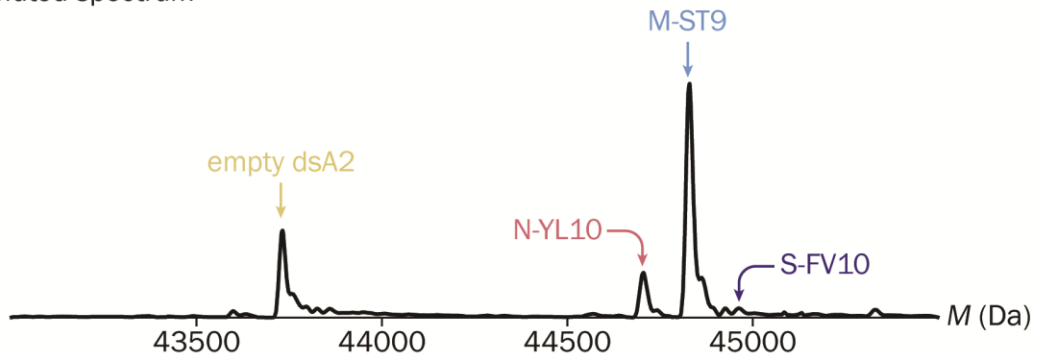
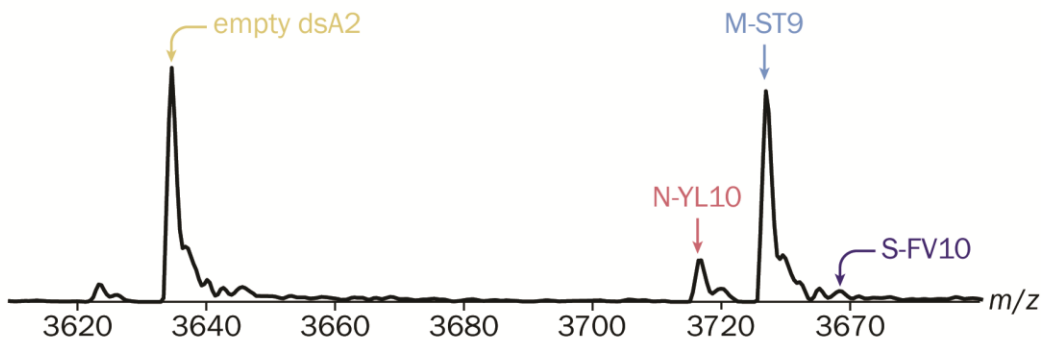
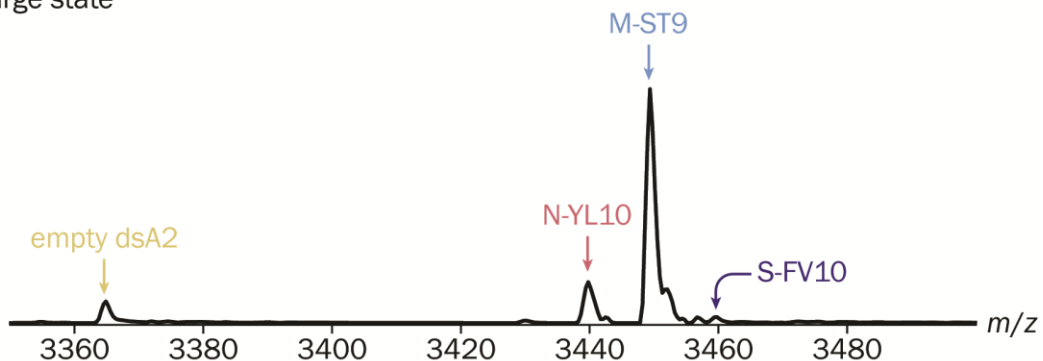
12⁺ charge state13⁺ charge state

Figure 43 | Charge state 13⁺ best resembles in-solution conditions.

Different spectra of the same measurement of 10 μM dsA2 together with the SARS-CoV-2 derived peptides N-YL10, M-ST9, S-FV10 and S-YL10 (10 μM each) are displayed. The latter was not detectable in bound form due to its low affinity for dsA2. The overview spectrum shows the most prevalent charge states 13⁺, 12⁺ and 11⁺. The level of occupancy of the MHC molecule decreased with decreasing charge state due to dissociation effects. The deconvoluted spectrum thus gives the average occupation level over all charge states – unlike the native state in solution, plenty of free MHC could be seen. Though, compared to 12⁺ and 13⁺, no differences concerning the relative intensities of the different pMHC fractions were observed. Hence, the only differences were in the degree of occupancy. Since at 13⁺, this degree was closest to the in-solution state, we neglected all other charge states and read the intensities exclusively from this m/z range.

3.4.1.2 Saving time during buffer exchange

The crucial step in sample preparation for native MS is the exchange of the buffer environment to a volatile and thus MS-compatible buffer surrogate such as ammonium acetate. Usually, this is also the most time-consuming step. In terms of a high-throughput screening, this step therefore offers great potential for saving time. For this reason, the first test was to determine whether combining MHC and peptides before or after BEX made a significant and effective difference. Two different mixtures of peptides – one with lower and one with higher average affinity – were assessed. Comparing the spectra for both BEX procedures, it was evident, especially with the low-affinity mix, that the overall occupancy of the protein decreased substantially (**Figure 44**).

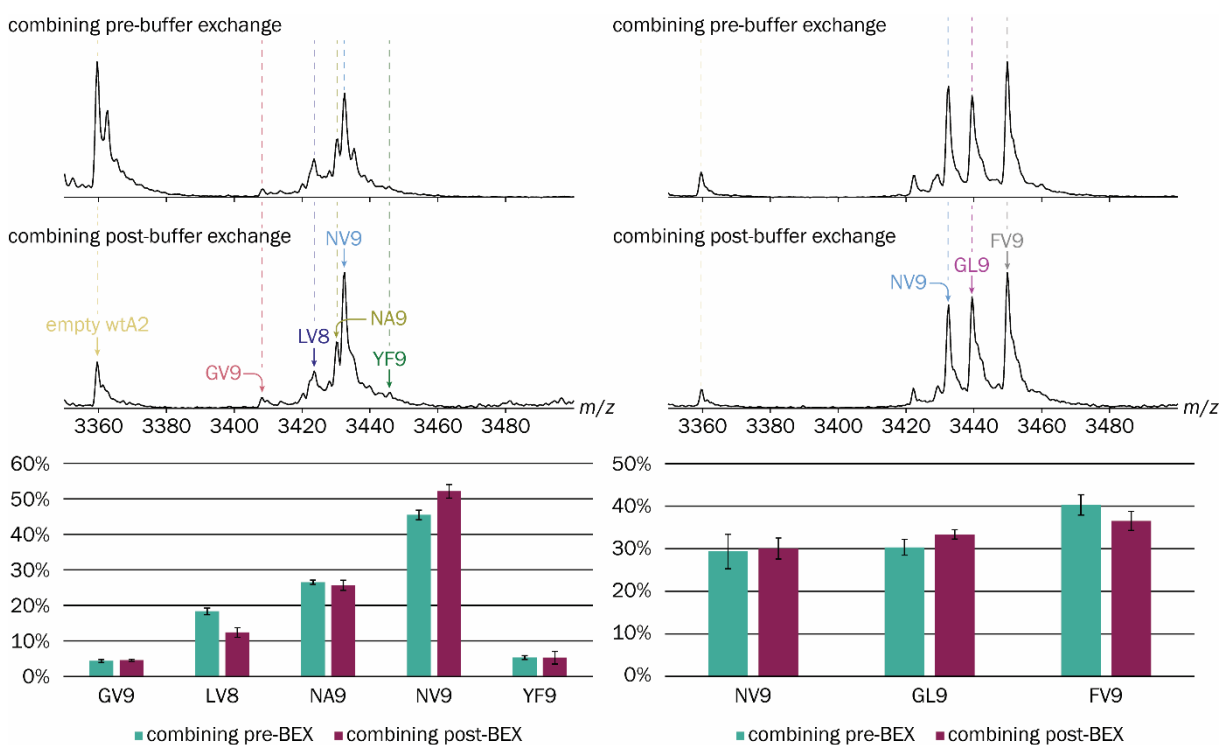


Figure 44 | Saving time during buffer exchange.

10 μ M wtA2 was incubated with 50 μ M of each peptide – GV9, LV8, NA9, NV9 and YF9 vs. NV9, GL9, AV9 (not visible), YF9 and FV9. The intensities of resulting pMHCs were compared. The components were mixed either before or after BEX for both peptide pools. For the spectra on the **left**, the high-affinity peptide NV9 was incubated with wtA2 together with the lower affinity peptides GV9, LV8, NA9 and YF9. The **right** side shows NV9 with two other high-affinity peptides (GL9 and FV9). The associated bar plots show the mean percentages of all peptide-bound MHC complexes based on the respective peak intensities of the 13⁺ charge state from at least three different measurements. The error bars symbolize the corresponding standard deviations. The teal columns show the intensity ratios for the measurements where BEX was performed only after incubation of protein and peptides. The dark pink columns show those where incubation happened after BEX.

For the high-affinity mix, the total occupancy decreased just slightly when BEX occurred after incubation of MHC, here wtA2, and peptide mixture. However, neither observation is relevant in terms of a successful screening approach as long as the intensity ratios among the pMHCs do not change. The changes observed are either not significant or minimal, as indicated by the graphs accompanying the spectra. In the case of LV8, the occupancy level

changed from $18.3\% \pm 0.9\%$ to $12\% \pm 1\%$, and in the case of NV9, there was a change from $45\% \pm 1\%$ to $52\% \pm 2\%$, depending on whether incubation or BEX was performed first. The fact that regardless of the procedure, the good binding partners could be reliably distinguished from the bad ones and that the best candidates were easily identified within the peptide pools supports the strength of the overall method. As a result, it is perfectly sufficient to exchange the buffer of the MHC protein of interest prior to screening and then add the respective peptides in the desired combinations directly ahead of the measurement. As mentioned, this saves a lot of time and allows much more flexibility with respect to the composition of the ligand pools.

3.4.1.3 Selecting a suitable mass spectrometer

QE-UHMR

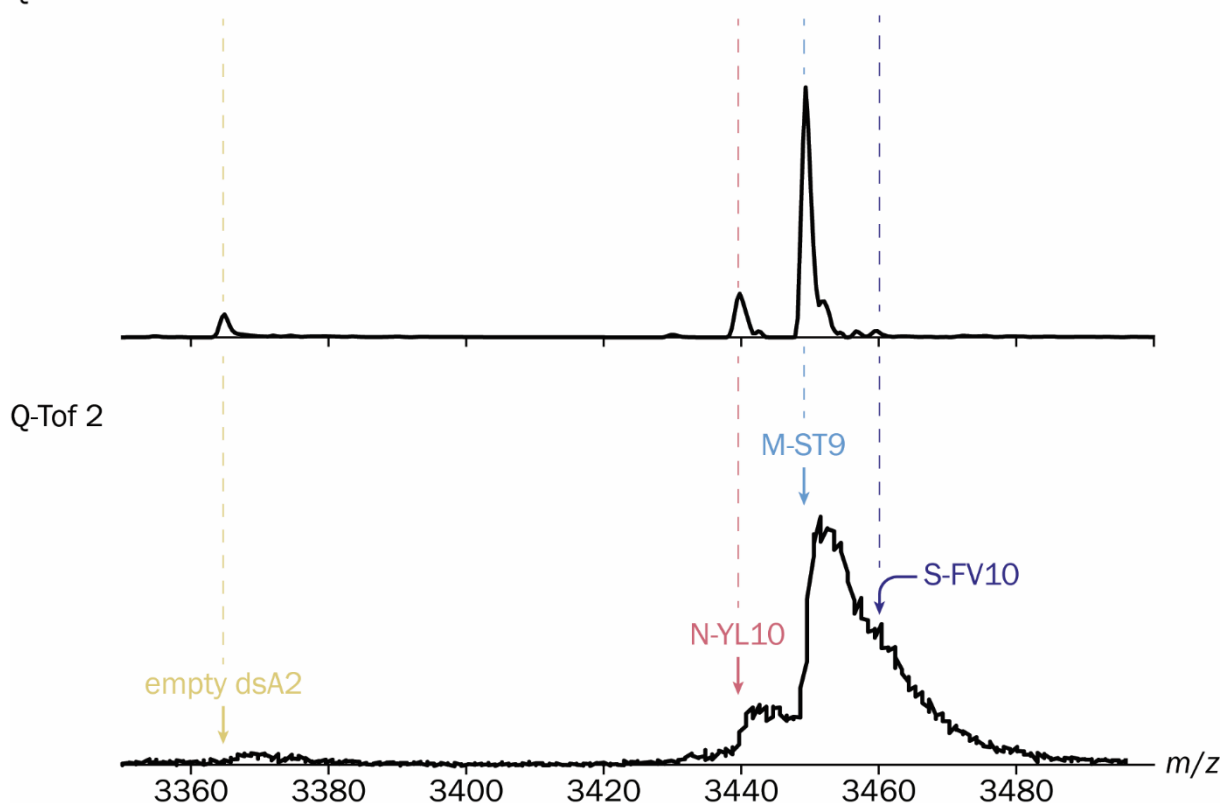


Figure 45 | Selecting a suitable mass spectrometer.

The spectrum must be sufficiently resolved – like the **top** spectrum, which was recorded on an Orbitrap™-bearing instrument (QE-UHMR) – to allow an easy and quick readout of relative affinity from the spectrum directly based on the peak heights of the pMHC signals. With insufficient resolution, as in the **bottom** Q-ToF 2 spectrum, low signals (here S-FV10) may be masked by those with high intensity (here M-ST9), making them difficult or impossible to detect. Both spectra were recorded with comparable energy settings (1.45 V at the capillary, 50 V in the collision cell), and dsA2 and all peptides (N-YL10, M-ST9, S-FV10 and S-YL10) had equimolar concentrations in both measurements (10 μ M each).

Experimentation was performed in parallel on two mass spectrometers, the Q Exactive™ UHMR Hybrid Quadrupole Orbitrap™ (QE-UHMR; *Thermo Fisher Scientific*) and the Q-ToF 2 (*Waters/Micromass*), to test robustness and universality of the method. As expected, the measurements on the QE-UHMR, which employs Orbitrap™ technology, all yielded spectra

with significantly better resolution. Although, as seen in the two example spectra in **Figure 45**, the ratio of relative peak intensities appears to be the same for both instruments, the lack of resolution on the Q-ToF 2 is critical, as the higher FWHM causes peaks to overlap. Consequently, if peptide masses and resultant m/z are rather close to each other, weaker signals will be lost in the large peaks and cannot be detected. This was the case for peptide S-FV10 in the example below, which could not be discriminated from the peptide corresponding to the main peak (M-ST9). The instrument must have sufficiently high resolution to ensure that the pMHCs of the entire ligand pool can be imaged simultaneously in terms of rapid screening. Further details of how the method can reach its limits in terms of resolution and how the problem can be circumvented are given below in **Chapter 3.4.1.8**. All the following data shown in this thesis were generated by measurements on the QE-UHMR.

3.4.1.4 Choosing suitable temperature and energy settings

In the following, the optimal energy and temperature settings of the mass spectrometer are evaluated for both instruments in use. In the complex instruments, there are of course various variables to establish a stable spray to represent the native environment. As shown in the previous chapters, suitable settings for well-resolved display of intact pMHCs have already been found. However, these were evaluated again for their suitability with respect to the peptide screening. In general, mild settings reflect the in-solution environment better due to smaller dissociation effects. The MHC-protein complex tends to remain intact, and more peptides occupy the binding pockets (*cf.* **Chapter 3.3.1**). Harsher conditions have the advantage that peptides clustering outside the binding pocket to the protein – *i.e.*, not representing real binding – can be easily stripped off. Similarly, peptides with poor affinity, in other words weak candidates, that are of no interest in screening anyway, can dissociate beforehand. A cut-off value could be set in the energy settings, at which the poorly performing peptides would not be detected at all and thus would not need to be evaluated further. Capillary temperature, ISD energy and collision energy are the variables that have the strongest impact with respect to the requirements mentioned above. In the previous chapters it was already shown how a change of the collision energy is manifested in the spectrum. If the acceleration voltage was higher than 50 V, the proportion of CID products was too high to ensure sufficient peptide-binding analysis. At lower voltages, the resolution was insufficient and the risk of detecting nonspecific binding was higher. With 50 V in the collision cell, we have thus found a good compromise that meets the demands of the screening.

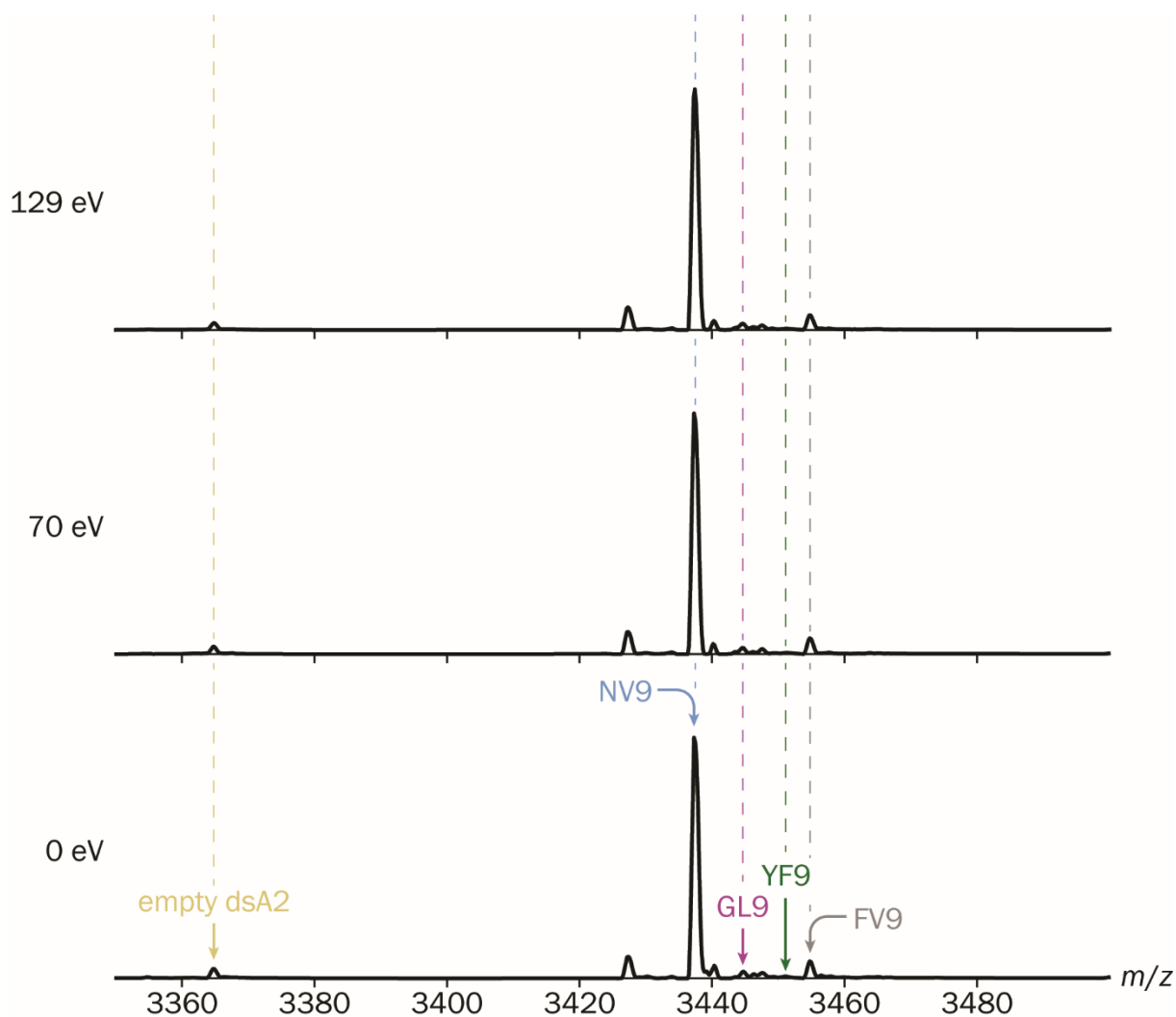


Figure 46 | Impact of the ISD energy.

10 μM dsA2 was incubated with 50 μM of each peptide – NV9, GL9, AV9 (not visible), YF9 and FV9. Measurements were performed on a QE-UHMR at 1.45 V and 50 $^{\circ}\text{C}$ at the capillary and 50 V in the collision cell. The ISD energy was increased stepwise from 0 eV to 129 eV (some intermediate steps are left out). This series of measurements showed that the ISD energy had no effect on the intensity ratios. Depicted is the 13⁺ charge state respectively.

Next, the impact of the ISD energy was assessed. The energy was gradually increased from 0 eV to a maximum of 129 eV (**Figure 46**). Apparently, the increase in ISD energy had no effect on the resulting spectra. The overall occupancy remained unchanged and the relative intensity ratios were constant, which is why we decided to use the mildest setting (0 eV) throughout all further measurements. Using the QE-UHMR, it was also possible to vary the temperature of the capillary. As shown in **Figure 47**, the temperature was increased from 50 $^{\circ}\text{C}$ to 300 $^{\circ}\text{C}$ in 50 K steps. The analysis clearly showed that 50 $^{\circ}\text{C}$ was the best setting for our purpose, since the degree of occupancy is drastically reduced at higher temperatures. The temperature therefore had a strong effect on peptide binding. Here, mild settings are certainly more beneficial for the screening approach.

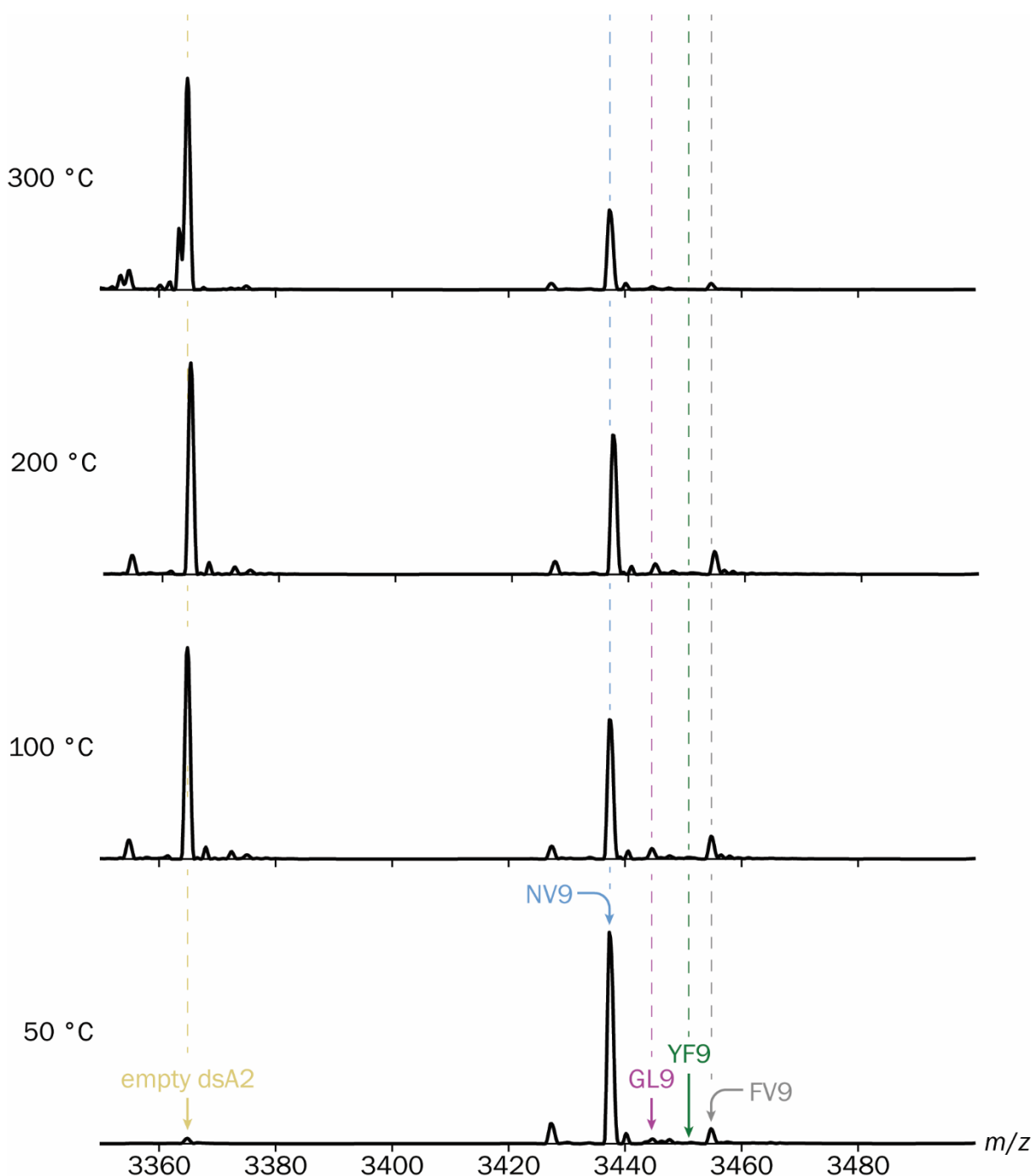


Figure 47 | Impact of the capillary temperature.

10 μM dsA2 was incubated with 50 μM of each peptide – NV9, GL9, AV9 (not visible) YF9 and FV9. Measurements were performed on a QE-UHMR at 1.45 V at the capillary and 50 V in the collision cell. In-source energy was set to 0 eV. The temperature of the capillary was increased stepwise from 50 $^{\circ}\text{C}$ to 300 $^{\circ}\text{C}$ (some intermediate steps are left out). This series of measurements shows that the capillary's temperature had a strong influence on the intensity ratios of the peaks. If the temperature was above 50 $^{\circ}\text{C}$, there was a large drop in the peptide occupancy rate. Depicted is the 13⁺ charge state respectively.

3.4.1.5 Choosing the optimal peptide concentration

The peptide concentration best suited for the screening approach was examined. Different peptide pools were tested both equimolar (10 μM each) and superstoichiometric (10 μM MHC vs. 50 μM for each peptide) to the MHC molecule. In general, higher (ligand) concentrations in native MS entail the risk of nonspecifically bound spray-induced artifacts.

This effect was also seen in the lower spectrum (**Figure 48**), where the peptides are present in 5-fold excess. The peaks in the range between $m/z = 3500$ and $m/z = 3550$ corresponded to the respective complexes, which carried a further peptide mass in addition to their specifically bound peptide ligand. As already discussed in the previous chapter, given the steric limitations within the peptide pocket, this was likely nonspecific clustering providing no additional value in terms of the screening. Direct comparison of the spectra showed that in presence of a high peptide excess the total occupancy of dsA2 was slightly higher and the signals of the low-affinity peptide complexes (here primarily S-FV10) were somewhat more prominent, which may also have arisen from nonspecific clustering.

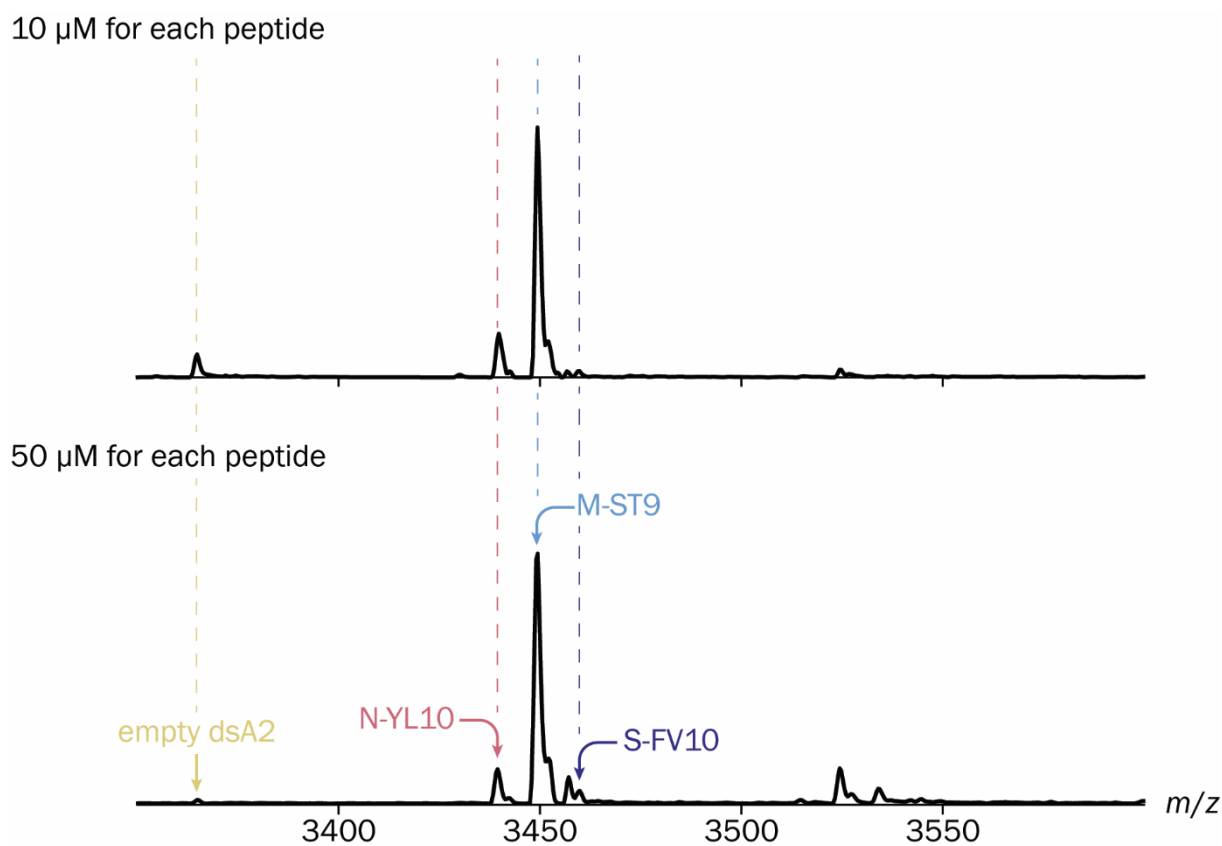


Figure 48 | Choosing the optimal peptide concentration.

10 μM dsA2 was incubated with SARS-CoV-2 derived peptides N-YL10, M-ST9, S-FV10 and S-YL10. Measurements were performed on a QE-UHMR at 1.45 V at the capillary and 50 V in the collision cell. Protein concentration was kept constant while the concentration of each peptide was either 10 μM or 50 μM . Depicted is the 13^+ charge state respectively. The overall appearance of both spectra is very similar. However, the degree of occupancy of MHC molecules and the occurrence of nonspecific peptide clusters increased with higher peptide concentrations – visible between $m/z = 3500$ and $m/z = 3550$.

Otherwise, both spectra appeared very similar. The peptide with the highest affinity in the peptide pool, M-ST9, was identified unambiguously. The weakly binding peptides, N-YL10 and S-FV10, showed comparable poor relative intensity in both measurements. S-YL10, which was also included in the peptide mixture, was not detected on either occasion due its low affinity. In summary, higher peptide concentration did not improve accuracy and

efficiency of the screening at all. There were fewer ESI artifacts when MHC and peptides were equimolar, yielding an image of primarily specific binding events.

1 μM for each peptide

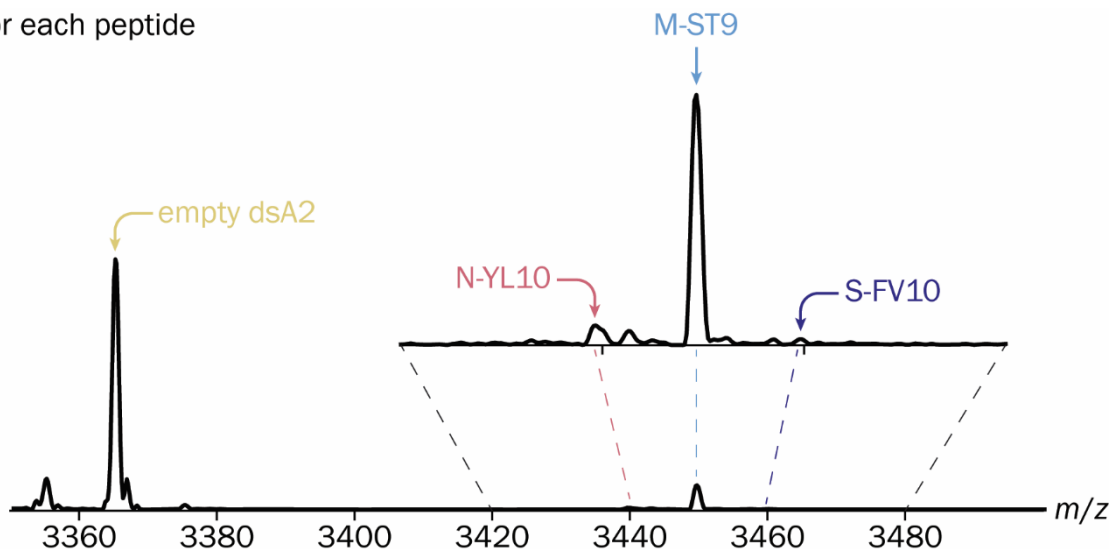


Figure 49 | Substoichiometric peptide concentration allows for determination of unbiased affinities.

This time, 10 μM dsA2 was incubated with just 1 μM of each peptide (N-YL10, M-ST9, S-FV10 and S-YL10). Measurements were performed on a QE-UHMR at 1.45 V at the capillary and 50 V in the collision cell. Depicted is the 13⁺ charge state respectively. We saw a drastic reduction of the population because there were now significantly more MHC molecules than ligands in the mixture. If only the occupied dsA2 were considered, we saw the affinity of the individual peptides represented by the peak height unaffected by ligand competition or ESI artifacts.

However, if the overall peptide concentration is lower than the concentration of the protein, then theoretically all peptide pockets can be filled, which would eliminate any competition effects, and thus the binding affinities of the individual peptides, as the only limiting factor, would be reflected completely unbiased in the signal heights. The result of such a measurement is shown in **Figure 49**. Here, as before, the protein concentration was 10 μM and the concentration of each peptide in the mixture was 1 μM . There were four peptides in the mixture, *i.e.*, the ratio was 10:1:1:1:1. With this vast excess of protein, a much larger percentage remained without ligand, hence a strong signal for empty dsA2 was observed this time. In contrast to what was described earlier, however, the low abundance of the peptide-bearing MHC molecules in this case did not result from energy-induced dissociation, but only due to the molar ratios, and is therefore not to be interpreted as a flaw. It was sufficient to focus on the MHC fraction binding peptides – in the range between $m/z = 3420$ and $m/z = 3480$ for the example in **Figure 49**. Not surprisingly, once again we saw that the peak corresponding to MHC+[M-ST9] had the highest intensity. Interestingly, the signal heights of the complexes binding N-YL10 and S-FV10, respectively, relatively decreased to some extent, again supporting the hypothesis on clustering effects at high peptides concentrations, but they could still be detected. As intended, at a total peptide concentration lower than that of the MHC, we obtained a simultaneous reflection of the

unbiased affinities of all ligands in the mixture as both competition effects and ESI artifacts were minimized.

3.4.1.6 Impact of incubation time and ethanol

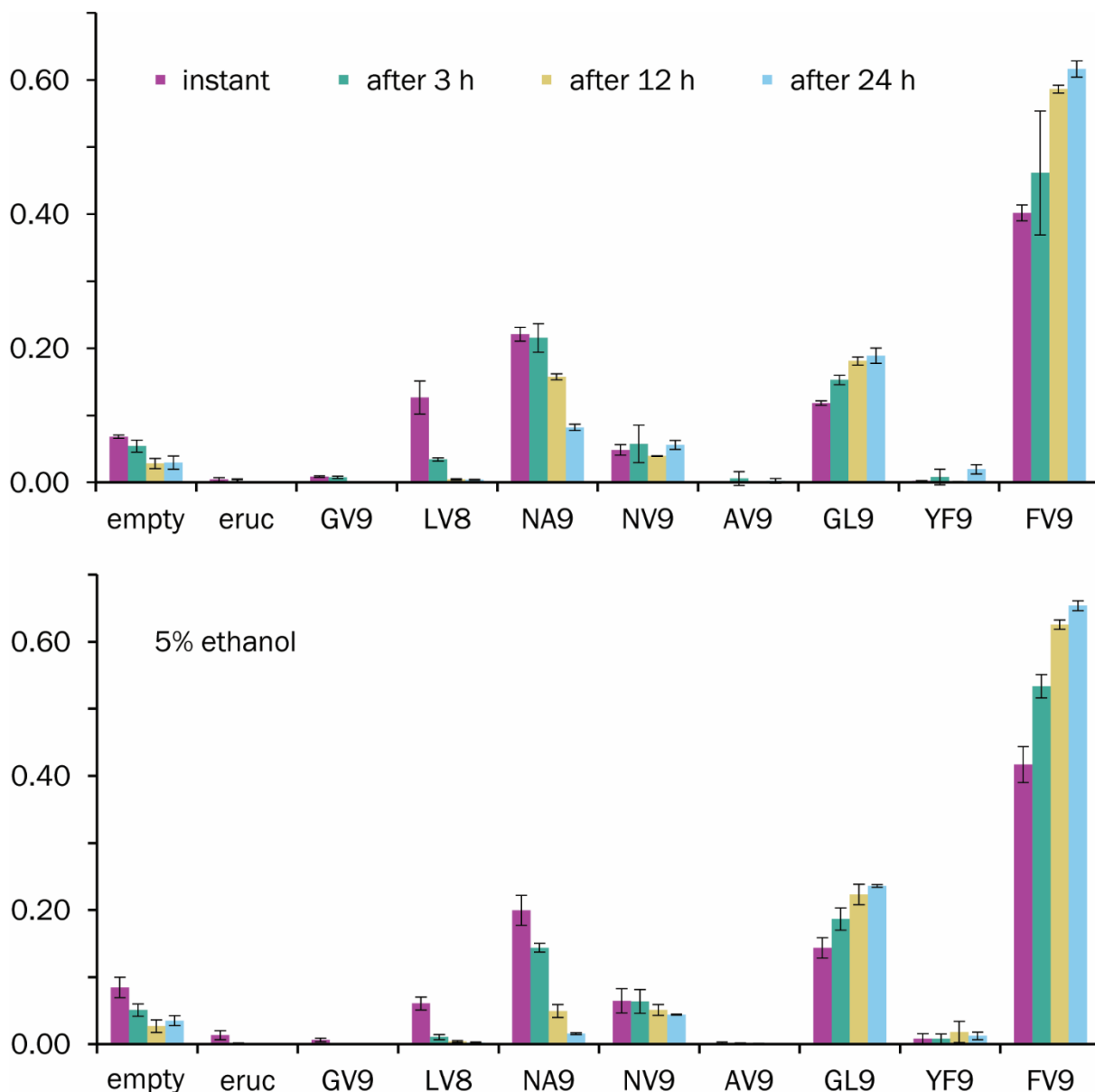


Figure 50 | Impact of incubation time and ethanol.

9.5 μM dsA2 was incubated with 9.5 μM of each of the eight peptides (GV9, LV8, NA9, NV9, AV9, GL9, YF9, FV9) and measured immediately (purple), after 3 h (teal), after 12 h (yellow), and after 24 h (light blue) using 1.45 V on the capillary and 50 V in the collision cell. The resulting intensities of all appearing MHC mass species in the 13⁺ peak were plotted according to their percentages (**top**). The entire series of experiments was repeated in the presence of 5% ethanol (**bottom**). Some peptides appeared to bind well initially (e.g., LV8 and NA9) but were then displaced by more affine peptides (e.g., GL9 and FV9). Ethanol slightly accelerated peptide exchange.

As mentioned in the previous section on searching for the appropriate peptide concentration (3.4.1.5), if the ligand concentration is too high, meaning if there are more ligands in total than available binding sites, competition may occur amongst the peptides. We first wanted to test whether the competition is time-dependent, *i.e.*, whether the relative

peak intensities of the different pMHCs remain constant or change over time. The hypothesis here is that the MHC molecules initially bind the most proximal peptides, but subsequently a peptide exchange to higher affinity ligands takes place at the binding sites. Such peptide exchange is known to be catalyzed by different factors – in the case of MHC-I for example by heat²⁸¹ or with the help of dipeptides²²³. For MHC-II, it has been shown that small organic molecules such as alcohols promote the exchange²⁸². While the native MS experiments for this thesis were designed, our collaborators used nDSF and fluorescence anisotropy to address the question of how small molecules affect the dynamics of peptide exchange²⁸³. To support these experiments, we analyzed the influence of ethanol (EtOH) as well.

Two mixtures of dsA2 and eight different peptides were prepared in parallel, each with a concentration of 9.5 μM for all components. In one of the mixtures, 5% EtOH was added, while the other was made up accordingly with more ammonium acetate solution. Then, using the previously evaluated settings (1.45 V, 50 V), spectra were recorded at different time points – immediately after preparation of the protein-peptide solution, after 3 h, after 12 h, and finally after 24 h of incubation on ice. For all recorded spectra, the percentages of total intensity of all dsA2 species – the empty MHC, all pMHC as well as MHC+erucamide – within the 13⁺ charge state were examined (**Figure 50**). Overall, the intensities of all species were heterogeneously distributed according to the peptide affinity. Due to the high total peptide concentration (76 μM vs. 9.5 μM dsA2), only few empty dsA2 were present. Over time, the fraction decreased even further. Since the peptide pool contained high-affinity candidates, the MHC+erucamide fraction was also very low or non-existent after 12 h at the latest. GV9, AV9, and YF9 were consistently low, without any temporal dependence observed. NV9 also tended to be in the lower intensity range, and again there was no change over time. This is not unexpected for YF9, since this peptide, as shown in **Chapter 3.3.1**, has no significant affinity for dsA2. For NV9, which with its known high affinity had previously served as a positive control, but also for GV9 and AV9, which had performed well to very well in the single experiment (K_d in **Table 10, Supplement**), these results were very surprising. LV8 and NA9 dropped dramatically over time, while the intensity of GL9 and FV9 increased accordingly. This indicated that although LV8 and NA9 initially bind dsA2 well, as soon as peptides with higher affinity appear, they easily displace LV8 and NA9. Thus, it may take time for the MHC molecule to bind the best available peptide. The results show that the equilibration may even take longer than 24 h. The bottom diagram in **Figure 50** depicts the same series of experiments when using 5% EtOH.

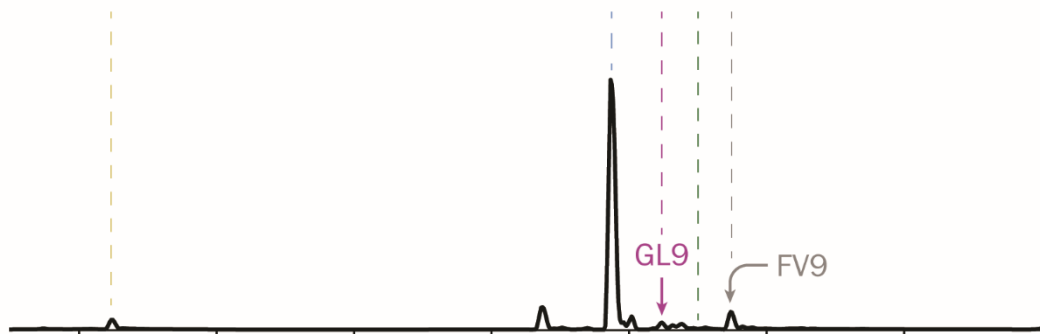
The intensities' percentage distribution in the immediate measurement (purple) nearly coincided with the measurement without EtOH. The occupation of the initially empty MHC occurred comparably fast in the presence of 5% EtOH, but the exchange of the lower affinity peptides (LV8 and NA9) and the simultaneous binding of the high affinity peptides (GL9 and FV9) was substantially faster. For example, the proportion of dsA2+NA9 after 12 h without EtOH is $15.8\% \pm 0.5\%$, with only $5.0\% \pm 1.0\%$, after 24 h it was $8.2\% \pm 0.5\%$ without, with already as low as $1.6\% \pm 0.1\%$. In contrast, the GL9 fraction after 12 h without EtOH was at $18.1\% \pm 0.6\%$, with already at $22\% \pm 2\%$. Another 12 h later it was $19\% \pm 1\%$ without and already $23.6\% \pm 0.2\%$ when using EtOH. Thus, the addition of 5% EtOH to the solution accelerated peptide selection and exchange when peptides were in a competitive situation due to a molar deficiency of MHC binding sites. NV9 but also LV8 both performed well in the single peptide experiment in terms of binding ability (cf. **Chapter 3.3.1.3**). The $K_{d,low}$ determined before are also in a similar range – $0.06 \mu\text{M} \pm 0.08 \mu\text{M}$ and $0.07 \mu\text{M} \pm 0.06 \mu\text{M}$, respectively. When both peptides were in competition, LV8 bound significantly better immediately after the addition of the protein; after equilibrium had been reached, significantly more binding sites were occupied by NV9 than LV8. In a competitive approach, peptides that bind well can be identified reliably, but there is a risk that other peptides, which also have good affinity remain undetected because the signal is suppressed by the more affine ligands. However, this problem can be easily circumvented by working with the MHC molecule in excess (cf. **Chapter 3.4.1.5**). That way, there are enough binding sites for all peptides and the affinities are directly and temporally independently represented by the peak intensity.

3.4.1.7 Screening low-affinity peptides

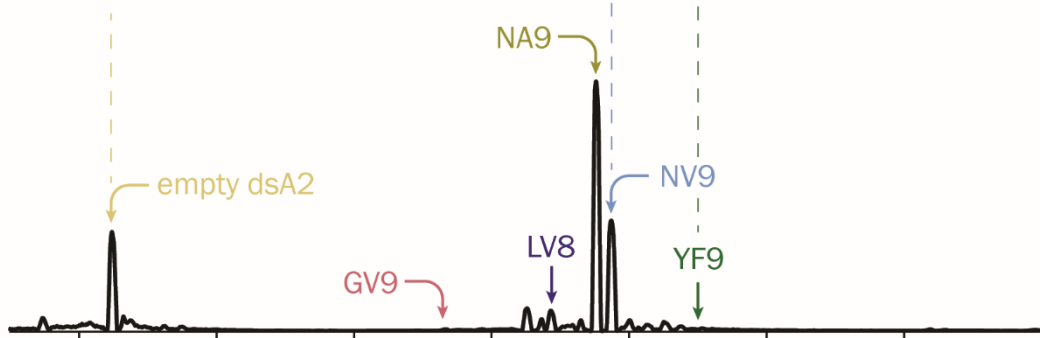
Since there is no high-throughput screening for MHC-I epitopes yet, a rapid alternative, as already mentioned above, is the use of neural networks to predict epitopes. However, these are only as accurate as the underlying databases. Poor or incomplete data can lead to biased predictions. For peptides shorter than the optimal length, K_d predictions can usually not be made at all. The same is true for modified peptides. With our method, however, we could easily analyze these peptides, as can be seen in **Figure 51**. Even peptides with very low or barely any affinity could be screened reliably. That nonapeptides in particular, which are known to bind well anyway, can be evaluated properly, which has now been demonstrated several times (top spectrum). GV9, LV8, NA9, YF9 are peptides of optimal length for MHC-I (middle spectrum). However, according to the prediction tool NetMHC, these have rather low affinities for HLA-A*02:01 ($188.84 \text{ nM} < K_{d,th} < 26704.52 \text{ nM}$). This

was indeed reflected in the overall occupancy of dsA2, the empty dsA2 peak was significantly higher than in the spectrum with the high-affinity mix. Nevertheless, we saw for each pMHC a nicely separated peak with an intensity corresponding to the respective affinity of the ligand to dsA2. Examination of the tetra- and pentamers, which have no effective affinity for MHC-I due to their length alone, was even more interesting (bottom spectrum).

high-affinity peptides



low-affinity peptides



no-affinity peptides

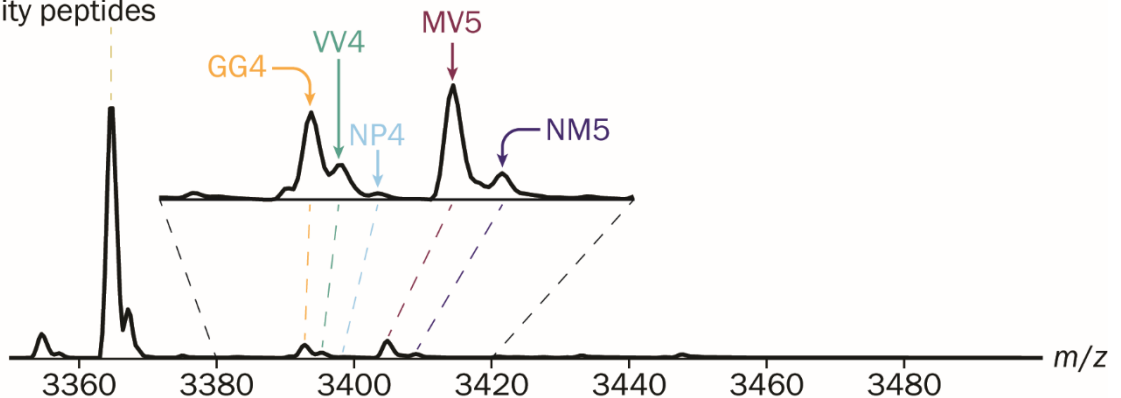


Figure 51 | Screening low-affinity peptides.

10 μM dsA2 was incubated with either of three mixtures: “high-affinity peptides” – NV9, GL9, AV9 (not visible), YF9, FV9; “low-affinity peptides” – GV9, LV8, NA9, NV9, YF9; “no-affinity peptides” – GG4, VV4, NP4, MV5, NM5. Peptide concentration was 10 μM of each peptide. Measurements were performed on a QE-UHMR at 1.45 V at the capillary and 50 V in the collision cell. Depicted is the 13⁺ charge state respectively. Even for very short peptides, we could estimate affinities easily.

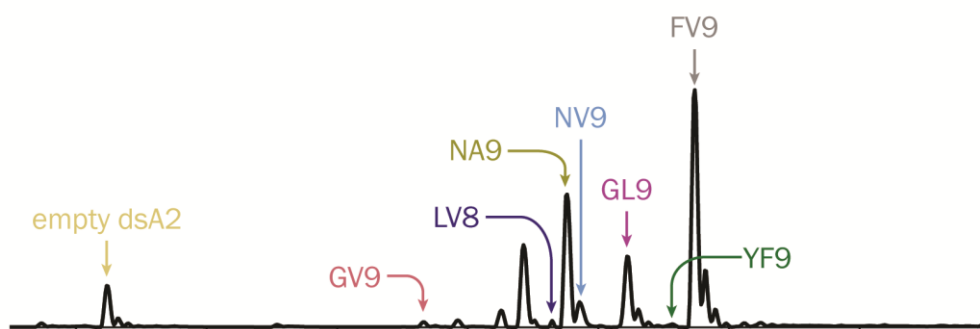
As expected, by far the most prevalent species is empty dsA2. A closer look at the region between $m/z = 3380$ and $m/z = 3420$ revealed the intensity distribution of the very few pMHCs. It is striking that MV5 performed significantly better in this mixture in contrast to the other pentamer NM5. This is in accordance with the results of the single peptide experiments from **Chapter 3.3.1.3**. In turn, NP4 also bound significantly worse than VV4, which is also consistent with the previous analyses. Thus, even for peptides exhibiting very low K_d , we could still obtain the individual values from the spectrum.

3.4.1.8 Is resolution the limit?

As mentioned earlier when discussing the selection of the appropriate mass spectrometer (cf. **Chapter 3.4.1.3**), resolution can be the bottleneck of this screening approach.

mixture of 7 peptides

M_{pep} (Da)	629.66	829.06	915.11	943.16	1034.14	1117.21	1169.24
m/z	3412.67	3428.00	3434.62	3436.77	3443.77	3450.15	3454.15



mixture of 20 NLVP?VATV derivatives

M_{pep} (Da) between 869.02 and 998.18 with minimal $\Delta M = 0.04$ Da

m/z between 3431.08 and 3441.01 with minimal $\Delta(m/z) < 0.00$

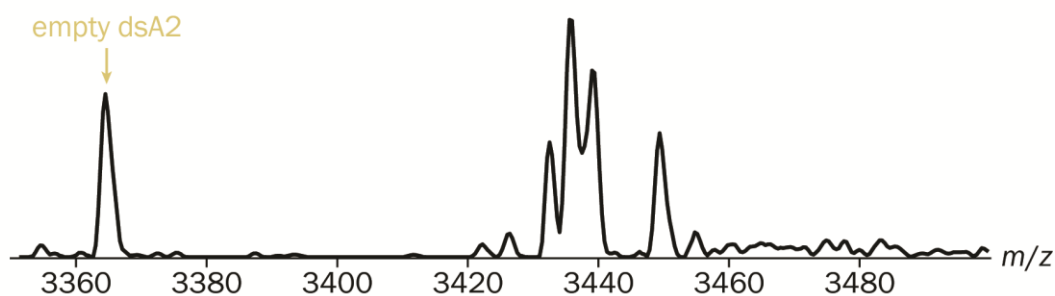


Figure 52 | Facing the limits of resolution for the peptide screening approach.

Top: 10 μM dsA2 was incubated with 10 μM of each of the peptides GV9, LV8, NA9, NV9, YF9 and FV9. The peptide masses M_{pep} are significantly distinct so that sufficient peak separation for the pMHC signals was achieved with the resolving power of the mass spectrometer used. **Bottom:** 10 μM dsA2 was incubated with 50 μM of a mixture of twenty NV9 derivatives differing in the amino acid in fifth position. Only three distinct pMHC signals were detected in the range of interest. These, however, could not be assigned to the respective peptides with sufficient certainty.

One problem may be instrument-specific resolving power or insufficient resolution due to a poor electrospray, which in turn can be caused by improper capillaries or an insufficient BEX, etc. On top of this, a proper protein quality is crucial for high-quality spectra. But leaving these points aside, there can still be problems if there are too many peptides in a pool to be tested – but especially if at least two peptides have too similar masses, so that the resulting m/z of the corresponding pMHCs are too close to each other. In order to evaluate the limits, first, a mixture of six different nonapeptides and one octapeptide was analyzed (**Figure 52**, top spectrum). Concentration of dsA2 was 10 μM as it was for each peptide. The peptide masses ranged from 629.66 Da to 1169.24 Da with the lowest mass difference of $\Delta M_{\text{pep}} = 28.05$ Da. The resulting m/z values were in the range of $m/z = 3412.67$ to $m/z = 3454.15$, and here the lowest calculated difference between two peaks was $\Delta m/z = 2.15$. Despite the short distance, the peaks of dsA2+NA9 and dsA2+NV9 could be easily distinguished from each other.

Furthermore, we examined a mix of twenty different variants of the peptide NLVPMVATV. The mixture contained equal parts of NV9 derivatives, in which the methionine (M5) of the peptide was replaced with all possible essential amino acids. For this sample, the maximum m/z range for all pMHCs ($\Delta m/z = 9.93$) and also the minimum differences between two individual masses or m/z values were significantly lower – $\Delta M_{\text{pep}} = 0.04$ Da and $\Delta(m/z) < 0.00$. The two peptides whose M5 have been substituted by leucine and isoleucine were not even included in this calculation, since the two amino acids have the same molecular mass anyway. For this experiment, the protein's concentration was 10 μM with a total peptide concentration of 50 μM , *i.e.*, 2.5 μM per peptide. We observe incomplete occupancy of the MHC, suggesting that several of the NV9 variants lose their binding affinity when M5 is substituted. In the range from $m/z = 3431.08$ to $m/z = 3441.01$ only three fairly separated peaks were detected: 3432.89, 3436.11 and 3439.53. The first one most likely corresponded to NAV9, which has a theoretical affinity of 37.04 nM. The base peak could not be assigned confidently since there were four possible candidates (NIV9, NLV9, NNV9 and NDV9) with very similar masses and predicted K_d . For the third peak, there were again two peptides worth considering: NRV9 with $K_{d,\text{th}} = 68.88$ nM and NYV9 with $K_{d,\text{th}} = 12.75$ nM. Unfortunately, with this particular situation it was not possible to make more accurate statements about the peptides' affinities by this experimental set-up.

3.4.2 Discussion

Knowledge of the immunopeptidome is the basis for developing both peptide vaccines and immunotherapy to treat cancer^{147,214,278-280,284-287}. T cell epitopes include a subset of MHC-binding peptides. Thus, the first step in identifying immunogenic epitopes is to search for these very MHC-binding peptides. Several methods have already been proposed to identify potential T cell epitopes based on predicting or measuring peptide binding to MHC-I molecules^{218,288-291}. The methods that measure binding usually rely on laborious low-throughput experiments while algorithmic approaches do not measure actual binding but are limited to evaluating the theoretical potential for epitope binding of common MHC allotypes²⁹². The algorithms are usually trained with affinity data of *in vitro* binding assays^{258,293,294}. Naturally, efforts to develop high-throughput approaches have already been made, such as by HAJ *et al.* using ultradense peptide arrays²⁷⁷. The screening was rapid and could provide large amount of peptide binding data but failed to identify many already known epitopes. Mass spectrometry is considered to be the method with the lowest bias for the identification of MHC-binding peptides^{216,295}. Apart from our approaches^{2,4} and the efforts of SCHACHNER *et al.* these MS-based methods are mostly non-native proteomics studies^{216,295}. Fragment ions are matched against previously acquired MHC peptidomics data. *De novo* methods are also possible but are less accurate. Another drawback here is that some peptides remain undetected due to their poor ionizability or inefficient fragmentation²⁹⁶.

The native MS screening approach for MHC epitopes presented here has great potential to fill this gap and counteract the bias of prediction tools. Native MS had already proven on many occasions to be an excellent method when searching for compatible protein ligands by quantifying upcoming protein-ligand complexes using respective intensities or areas of the peaks¹⁰⁰ either by titration¹⁰⁶⁻¹¹⁴, or using two ligands that compete for the same binding site¹¹⁵⁻¹²⁰. But native MS even enables to estimate affinities directly from single point measurements¹²¹⁻¹²³ as long as the ligand is significantly smaller than the protein, since response factors of complex and the hosting molecule are identical in this case, and there is enough knowledge on the amount of dissociation affecting the complex^{55,98,100,297}. In general, native MS has the advantage of reliably representing the entirety of all species present in the sample, even at low sample volume and concentration. At proper conditions, spectra can be recorded for many hours with only 1-2 μL of a sample solution of only about 1 μM . Thus, temporal dynamic changes can be observed quite easily. A few scans obtained within a few seconds are usually sufficient to directly display a current image of all

components of the solution, which results in an enormous advantage with regard to a high-throughput screening.

Soft ionization via electrospray can preserve noncovalent bonds, which is obligatory for analyzing ligand interactions. The less dissociation effects, source energy- or collision-induced, affect the analyte, the more the spectrum reflects the structures present in the solution. In the experiments presented here, excellent resolution was achieved for both instruments (Q-ToF 2 and QE-UHMR) at 1.45 kV at the capillary and 50 V in the collision cell while maintaining the quaternary structure of the pMHC. At the same time, these voltages were high enough to sufficiently decimate any occurrence of nonspecific adducts. An increase of the capillary temperature was not beneficial. Here, at more than 50 °C such noncovalent bonds could not be preserved (**Figure 47**). On the other hand, no effective change was observed at the QE-UHMR when the ISD energy was increased, which is why this was also omitted in the following (**Figure 46**).

The excellent resolution, especially obtained with the QE-UHMR, allowed us to estimate the quantity of abundant mass species using the peak intensity. However, for inhomogeneous samples (e.g., occurrence of multiple sodium adducts), the area of the peak would typically be the better choice, as it is much more accurate. The disadvantage in terms of screening is the extra time that has to be spent for additional analysis steps, since the area usually cannot be determined directly during the measurement. If this step can be bypassed with a software-based solution, the peak area is preferable to the peak intensity in terms of accuracy.

Interestingly, the overall occupancy of the MHC molecule was found to vary between the different charge states within a spectrum (**Figure 43**). Consequently, this means that each charge state represents a certain ion species, which was affected by dissociation effects to a different extent on its way through the instrument. The most prevalent charge state with the lowest proportion of empty MHC was the 13⁺ charge state. At 12⁺, there was already a significantly increased amount of empty MHC, which can be explained by the loss of the singly charged peptide. However, the relative distribution of peak intensities of all pMHCs contained in the sample did not change significantly. In subsequent analyses, only the 13⁺ charge state was considered. In addition to minimizing dissociation products, this also had the advantage of a very simple and fast read-out. In this work, only the system of disulfide-stabilized or wild type HLA-A*02:01 in combination with different synthetic peptides was analyzed. If the method is to be applied to another MHC molecule, for

example, a preliminary test must first be performed to determine which charge state is equivalent to the 13⁺ shown here. It is conceivable that for MHC molecules in the same size range the 13⁺ is also applicable, but this would have to be confirmed in further experiments.

The most time-consuming aspect in native MS is buffer exchange. Since peptide screening aims to combine an MHC molecule with different peptide combinations, it seemed advantageous to prepare only the protein alone with the MS-compatible solution and add the peptides afterwards instead of first preparing the MHC-peptide mixtures and then subject them to BEX – also to ensure flexibility regarding the peptide combinations in use. Especially if we think of the wild type, *i.e.*, non-stabilized, MHC, which would be the focus of the analyses if this screening were to be used more widely, the protein complex would disintegrate in the buffer exchange without the addition of peptides. So here the more cumbersome way could be taken – or the problem could be circumvented by adding a small stabilizer, in our case a dipeptide like GM or GL, to the MS solution. It was shown that this is indeed feasible. The peptide helped to maintain complex integrity and yet could be easily replaced by the high-affinity peptides of interest due to its weak affinity (**Figure 44**). For the two exemplary peptide combinations shown only minor decrease was observed for the total pMHC amount, in other words, slightly more free protein was detected. Since the relative intensities of the pMHC did not change significantly, this loss is completely negligible.

Working concentration for the peptides was assessed thoroughly. As expected, the higher the total amount of peptide within the sample the lesser empty MHC was observed. At the same time, in the case of strong excess (five times more peptides than protein *per peptide*), naturally more unspecific adducts were observed than with lower peptide concentrations. In **Figure 48**, this was evident from the appearance of dsA2+pep+pep species at higher *m/z*. In case the total amount of peptide is higher than that of the protein, there will inevitably be competition for the single binding site. In view of the screening, this has the disadvantage that in a mixture a peptide with satisfactorily high affinity together with at least one peptide with significantly higher affinity could remain undetected and missed. Furthermore, the peak intensities of pMHC were found to vary temporally in a competitive situation. In the setup with equimolar concentration of all components (MHC and eight peptides), equilibration took at least 24 h (**Figure 50**). The addition of 5% ethanol accelerated the process slightly. This observation was consistent with the findings of investigations by my collaborators, who identified ethanol as a good catalyst for peptide exchange²⁸³. It has been known for quite a while that dipeptides such as GM or GL, which

have been frequently mentioned here, accelerate the dissociation of peptides already bound to MHC-I by occupying the F pocket given a partially dissociated C-terminus, thus preventing rebinding²²³. Using 10% ethanol an even higher exchange rate was achieved compared to 10 mM GM, 20% methanol also led to a significant increase²⁸³. Longer alcohols such as propanol or butanol had no positive effect, so it was concluded that the catalyst cannot be larger than a certain size. Conversely, 1,2-ethanediol, which was shown to occupy A and F pocket (**Chapter 3.3**), had almost no catalytic effect on peptide exchange. Despite the similar size, this one carries another hydroxyl group, unlike methanol and ethanol, which seems to worsen the interaction with the peptide pocket here. We could speculate that other dipeptides, single amino acids, or small monothiols that are very similar to the alcohols could also help to increase the peptide exchange rate. *In vivo*, the exchange to higher affinity peptides is catalyzed by the cofactor tapasin^{194,198}. This can accelerate the dissociation of initially bound peptides – either by direct binding into the F pocket or by triggering a conformational change^{197,248,298,299}.

Analysis of the pMHC distribution at different time points showed that some of the peptides (here: LV8 and NA9) are replaced over time by stronger binding ones (here: GL9 and FV9). In this work and many times before, the structural aspects that make a peptide a good binder, from which a kinetically stable pMHC can emerge, have been discussed. However, it is unclear which properties a peptide must have in order to bind effectively *initially* or whether such properties do not exist at all and, at the first moment, all peptides are distributed statistically to all available MHC molecules. Continuing the thought, the question is whether all allotypes have the same initial binders or whether there are differences. Purely speculatively, peptides from the conserved region of the MHC itself could be considered due to the ultimate availability, but this needs to be verified in further peptide binding studies.

Finally, to avoid handling such competition effects in our screening in the first place, the total peptide concentration was set below that of the protein. In the substoichiometric situation, each peptide has at least one binding site available, eliminating competition effects, and allowing immediate identification of the peptides with the best affinity without having to wait for equilibrium to be established (**Figure 49**). Although only a low overall abundance was observed, highly affine as well as less affine peptides combined with dsA2 could be detected simultaneously. In order to further minimize sample consumption, the working concentration of MHC should be reduced to approximately 1 μM in the future with corresponding substoichiometric concentration of the peptide pool. With sufficiently high

concentration of available binding sites despite competing peptides, the only remaining variable affecting peak intensity under similar measuring conditions is the sequence-given affinity of the peptide to the respective MHC molecule. The low peptide concentration has the additional advantage that fewer ESI artifacts, *i.e.*, nonspecific adducts, occur.

Both, low and high-affinity peptides were reliably discriminated from different mixtures of peptides. We mainly used peptides whose affinities were known to us in order to be able to probe all possible ranges. In addition, we also successfully analyzed the first viral peptide pool with the mixture of synthetic peptides derived from SARS-CoV-2. The method has been successfully tested at two different mass spectrometers (Q-ToF 2 vs. QE-UHMR). However, it must be noted that the better the resolution, the easier the read-out. A mass spectrometer optimized for high-resolution analysis of proteins and protein complexes is therefore essential for this application. Even with very high resolving power of the mass spectrometer, there may still be the problem that the 13⁺ charge states of two pMHCs cannot be distinguished because the peptide masses are too close as it was the case for the different NV9 derivatives (**Figure 52**). One possibility to overcome the limitations owing to insufficient resolution could be achieved by applying an MS² approach. High-intensity signals corresponding to pMHCs containing the high-affinity peptides of interest would be isolated and subjected to CID in order to identify bound ligands. Furthermore, it is conceivable to verify a peptide's identity via fragmentation in a MS³ or pseudo MS³ experiment. Ideally, the whole screening process would also be automated here, for example with the aid of a pipetting robot. Then, in cases where signals inevitably overlap due to too similar peptide masses, one would be flexible enough to quickly create and analyze new mixtures that circumvent the problem.

4 Outlook

For this work, extensive structural characterizations were performed on MHC-I molecules. Aspects of the peptide-free state were investigated. Thus, the free heavy chains of murine H-2K^b were shown to form dimers by interaction of the α_3 domains. How α_1 and α_2 contribute to the binding can be determined in future native MS experiments. For human HLA-A*02:01, two variants were investigated with respect to peptide binding, exchange, but also within a peptide-free environment. The variants analyzed were the wild type on the one hand and on the other hand, a disulfide-stabilized molecule, which could maintain its structure even in the absence of a peptide. This molecule is an excellent candidate for a peptide screening approach due to its high prevalence and its unique role within the entire A2 supertype. It was shown that high-affinity peptides can be identified from a peptide pool using a simple native MS assay of the MHC molecule. Thereby, the straightforward reading of the peak intensity of the pMHCs from only one charge state was sufficient. No further data processing was necessary for this.

Some finishing touches still need to be made to finalize the screening approach. As analyzed in detail, the total concentration of all peptides in the mixture needs to be below the protein concentration in order to exclude competitive effects and to be able to doubtlessly detect all good peptide candidates of the pool. To waste as little as possible of the often rather valuable MHC samples, we will reduce the concentration to about 1-2 μM in future experiments with peptides still below that concentration. To overcome resolution-dependent limitations when analyzing two peptides of very similar mass simultaneously, extensive tandem MS experiments will be performed in the future. This will help to determine the best settings for isolation and dissociation of the pMHC of interest as well as fragmentation of the peptide in question. With regard to increasing the overall throughput, we are targeting the implementation of a pipetting robot. The commercially available TriVersa NanoMate® (*Advion*) is particularly suitable for this application, as it automates the entire preparation from sample mixing to establishment of the electrospray, which is achieved via a so-called ESI Chip® containing hundreds of nano-electrospray nozzles^{300,301,96}.

We will then put our method to the test with assorted synthetic peptide mixtures. We will focus on peptides of viral origin, for example derived from SARS-CoV-2 or Ebola virus, for which high affinities have been predicted or are already known, as well as other epitopes that seem promising in other ways. Since the screening approach presented here can

easily screen very short peptides, most of which have lower affinity, we will also look at small synthetic peptides that could potentially be used as peptidomimetic drugs^{302,303}.

After the principle of screening has been shown in detail with HLA-A*02:01, we will move on to other human, but also nonhuman MHC-I molecules soon. Selected disulfide-stabilized mutants of highly prevalent allotypes – HLA-A*11:01, HLA-A*24:02 and HLA-B*02:02 – are ready to be probed. As shown for wtA2, the method also works with wild type MHC-I as long as a stabilizing molecule such as a dipeptide is added to the protein solution, which is then exchanged with peptides from the analysis pool. At this point it should be mentioned that of course it will also be checked whether the analyses with MHC-I can be transferred to MHC-II.

Furthermore, we plan to study peptides produced *in vivo*. For example, it is rather simple to isolate pMHCs from human blood samples³⁰⁴. From this, mild acid elution³⁰⁵⁻³⁰⁷ can be used to obtain the peptides, which can then be mixed together with known MHC-I molecules and subsequently measured. In the case of an unknown set of peptides, the above-mentioned identification of the peptides by (pseudo) MS³ is obligatory. Peptidome analysis, for example in the context of a viral infection, is yet another conceivable application. Small animal models from which the corresponding pMHCs can be isolated may be used for this purpose.

The high-affinity peptides identified in this work are potential epitopes for the T cells, but an immune response provoked by these is not necessarily implied. Thus, further evaluation of T cell reactivity is required to confirm immunogenicity. This is usually done using flow or mass-cytometry³⁰⁸⁻³¹¹. Other approaches promising higher throughput have been suggested, e.g., by BENTZEN *et al.* who employed DNA-barcode labels for the identification of the peptides recognized by individual T cells³¹². How the native MS-based screening shown in this thesis can be linked to testing for immunogenicity has not been sufficiently evaluated to date. However, that T cell assays can be coupled downstream with native MS has indeed just been suggested by SCHACHNER *et al.*³¹³.

5 Materials and methods

Parts of this chapter have been published in either of the following studies:

Anjanappa, R., Garcia-Alai, M., **Kopicki, J. D.**, Lockhauserbäumer, J., Aboelmagd, M., Hinrichs, J., Nemtanu, I. M., Uetrecht, C., Zacharias, M., Springer, S., & Meijers, R. (2020). Structures of peptide-free and partially loaded MHC class I molecules reveal mechanisms of peptide selection. *Nature communications*, 11(1), 1314².

Reprinted from ANJANAPPA *et al.* (2020). Copyright © 2020, The Author(s).

Dirscherl, C., Löchte, S., Hein, Z., **Kopicki, J. D.**, Harders, A. R., Linden, N., Karner, A., Preiner, J., Weghuber, J., Garcia-Alai, M., Uetrecht, C., Zacharias, M., Piehler, J., Lanzerstorfer, P., & Springer, S. (2022). Dissociation of β_2m from MHC class I triggers formation of noncovalent transient heavy chain dimers. *Journal of cell science*, 135(9), jcs259489³.

Reprinted from DIRSCHERL *et al.* (2022). Copyright © 2022, The Author(s).

Kopicki, J. D., Saikia, A., Niebling, S., Günther, C., Anjanappa, R., Garcia-Alai, M., Springer, S., & Uetrecht, C. (2022). Opening opportunities for K_d determination and screening of MHC peptide complexes. *Communications biology*, 5(1), 488⁴.

Reprinted from KOPICKI *et al.* (2022). Copyright © 2022, The Author(s).

5.1 Sample preparation

5.1.1 Proteins

All protein samples were produced by my collaborators from the Springer lab (Constructor University Bremen) following the same protocol.

Table 1 | Overview of all proteins used in this work.

label	sequence	M_{th} (Da)
α_3 (H-2K ^b)	MAIQRSPKAH VTHHSRPEDK VTLRCWALGF YPADITLTWQ LNGEELIQDM ELVETRPAGD GTFQKWASVV VPLGKEQYYT CHVYHQGLPE PLTLRWDRDM	11,475
β_2m (HLA-A*02:01)	MIQRTPKIQV YSRHPAENGK SNFLNCYVSG FHPSDIEVDL LKNGERIEKV EHSDFSFSKD WSFYLLYYTE FTPTEKDEYA CRVNHVTLSQ PKIVKWDRDM	11,862
wtA2-HC (HLA-A*02:01)	GSHSMRYFFT SVSRPGRGEP RFIAVGVVDD TQFVRFSDSA ASQRMEPRAP WIEQEGPEYW DGETRKVKAH SQTHRVDLGT LRGYYNQSEA GSHTVQRMYG CDVGSDDWRFL RGYHQYAYDG KDYIALKEDL RSWTAADMAA QTTKHKWEAA HVAEQLRAYL EGTCVEWLRRL YLENGKETLQ RTDAPKTHMT HHAVSDHEAT LRCWALSFPY AEITLTWQRD GEDQTQDTEL VETRPAGDGT FQKWAAVVVP SGQEQRYSYTCV VQHEGLPKPL TLRWE	31,808
dsA2-HC (HLA-A*02:01)	GSHSMRYFFT SVSRPGRGEP RFIAVGVVDD TQFVRFSDSA ASQRMEPRAP WIEQEGPEYW DGETRKVKAH SQTHRVDLGT LRGYYNQSEA GSHTVQRMYG CDVGSDDWRFL RGYHQYAYDG KDYIALKEDL RSWTAADMCA QTTKHKWEAA HVAEQLRAYL EGTCVEWLRRL YLENGKETLQ RTDAPKTHMT HHAVSDHEAT LRCWALSFPY AEITLTWQRD GEDQTQDTEL VETRPAGDGT FQKWAAVVVP SGQEQRYSYTCV VQHEGLPKPL TLRWEP	33,977

5.1.1.1 Expression

The α_3 domain of H-2K^b (residues 205-295) was cloned into pET-3a (preceded by the residues MAIQR and followed by DRDM) and expressed in *E. coli* BL21(DE3)pLysS. Full-length HLA-A*02:01 HC as well as its corresponding HLA-A*02:01(Y84C/A139C) disulfide mutant were cloned into pGMT7 and expressed in *E. coli* RosettaTM (DE3)pLysS The β_2m light chain was cloned into pHN1+ and expressed in *E. coli* RosettaTM (DE3)pLysS.

Expression was induced with isopropyl- β -D-1-thiogalactopyranosid (IPTG), executed at 37 °C, and stopped after 4 h. The cells were harvested by centrifugation (5000 \times g, 4 °C, 10 min), the pellet was resuspended in 50 mM Tris-HCl pH 8.0, 25% sucrose, 1 mM ethylenediaminetetraacetic acid (EDTA), and frozen (-20 °C or -80 °C) afterwards. Cell lysis was achieved by thawing the pellet in a 30 °C water bath. 10 mM dithiothreitol (DTT) and 1 mM phenylmethylsulfonyl fluoride (PMSF) were added to the solution. This was followed by a sequence of sonication, centrifugation (40,000 \times g, 4 °C, 15 min), and removing supernatant (wash cycle). The protein-containing pellet was resuspended in 50 mM Tris-HCl pH 8.0, 25% sucrose, 1% Triton™ X-100, 5 mM EDTA, 2 mM DTT for a second wash cycle. Next, the pellet was resuspended in 50 mM Tris-HCl pH 8.0, 2 M NaCl, 2 M urea, 2 mM DTT for another wash cycle. Final wash cycle was done in 50 mM Tris-HCl pH 7.5, 150 mM NaCl, 0.5 mM PMSF. Finally, the pellet was resuspended by sonication in 50 mM HEPES pH 6.5, 6 M guanidine hydrochloride, 0.5 mM PMSF, 100 μ M 2-mercaptoethanol. The protein was solubilized by gently shaking for 48 h at 4 °C. Afterwards, the solution was centrifuged twice (40,000 \times g, 4 °C, 15 min) to remove remaining insoluble pellet.

5.1.1.2 Refolding and purification

For A2 complexes, the refolding was performed by slowly diluting 1 μ M of A2 heavy chain and 2 μ M of β 2m in a refolding buffer (100 mM Tris-HCl pH 8, 500 mM arginine, 2 mM EDTA, 0.5 mM oxidized glutathione, 5 mM reduced glutathione, 10 mM GM or GL, 100 μ M PMSF). The same procedure was followed for sole α 3. The solution was incubated for 4-5 d at 4 °C with constant stirring, followed by protein concentration using membrane filters (Vivaflow® 200; Sartorius) – 30 kDa cut-off for A2 complexes and 3 kDa cut-off for α 3, respectively. Concentrated protein was purified by SEC in 20 mM Tris-HCl pH 8.0, 150 mM NaCl on an ÄKTA™ system (Cytiva) using a Hiload Superdex 200 16/600 column (Cytiva). For A2 complexes a constant concentration of 10 mM dipeptide (GM or GL) was maintained. Peak fractions were pooled and concentrated to 15 mg/mL.

5.1.1.3 Quality control

While preparing α 3, molecular masses of the peaks were determined by comparison to SEC protein standards (Cytiva). Purified proteins were analyzed by SDS-PAGE with standard protein markers. For α 3, the fraction corresponding to the elution peak at \approx 20-30 kDa, was boiled with or without 600 mM DTT in sample buffer (350 mM Tris-HCl pH 6.8, 10.28% SDS, 36% glycerol, 0.012% bromophenol blue). Inclusion body extract boiled without DTT (nonreducing) served as the positive control for the formation of covalent oligomers.

Protein quality control after refolding and SEC was performed by nDSF (cf. **Chapter 5.3**) runs acquired with a Prometheus NT.48 fluorimeter (*NanoTemper Technologies*) controlled by PR.ThermControl 2.1.2 (*NanoTemper Technologies*).

5.1.2 Peptides

Peptides were custom-built. The majority was purchased from *GeneCust* with a minimal purity of 95%. GM and GL were purchased from *Bachem*.

Table 2 | Overview of all peptides used in this work.

label	sequence	M_{th} (Da)
GL	GL	188.12
GM	GM	206.07
GG4	GSFG	366.15
VV4	VATV	388.23
NP4	NLVP	441.26
MV5	MVATV	519.66
NM5	NLVPM	572.72
PV6	PMVATV	616.77
GV9	GLGGGGGGV	629.67
NV6	NLVPMV	671.85
VV7	VPMVATV	715.91
NA7	NLVPMVA	742.93
LV8	LVPVATV	829.07
NT8	NLVPMVAT	844.04
NGV9	NLVPGVATV	869.03
NAV9	NLVPAVATV	883.06
NSV9	NLVPSVATV	899.06
NPV9	NLVPPVATV	909.09
NVV9	NLVVVATV	911.11
NTV9	NLVPTVATV	913.08
NA9	NLVPMVATA	915.12
NCV9	NLVPCVATV	915.12
NIV9	NLVPIVATV	925.14
NLV9	NLVPLVATV	925.14
NNV9	NLVPNVATV	926.08
NDV9	NLVPDVATV	927.07
NQV9	NLVQVATV	940.11
NKV9	NLVPKVATV	940.15
NEV9	NLVPEVATV	941.09
NV9-NH ₂	NLVPMVATV-NH ₂	942.18
NV9	NLVPMVATV	943.17
NHV9	NLVPHVATV	949.12
NFV9	NLVPFVATV	959.15
NRV9	NLVPRVATV	968.16
NYV9	NLVPLYVATV	975.15
N-YL10	YLGTGPEAGL	977.08
Ac-NV9-NH ₂	Ac-NLVPMVATV-NH ₂	984.22
Ac-NV9	Ac-NLVPMVATV	985.20
NWV9	NLVPWVATV	998.19
AV9	ALFDIESKV	1021.18
GL9	GLYGDMEHL	1034.15
LV9	LLFGYPVYV	1070.30
M-ST9	SMWSFNPET	1098.20
YF9	YPNVNIHNF	1117.23
FV9	FLYDDNQRV	1169.26
YL9	YLLEMLWRL	1236.54
S-FV10	FIEDLLFNKV	1237.46
S-YL10	YIKWPWYIWL	1467.78

5.2 Native mass spectrometry

5.2.1 Buffer exchange

In advance of native MS measurements, different centrifugal devices were used to exchange purified protein samples to ammonium acetate (99.99% purity; *Sigma-Aldrich*) solution as sodium-free and volatile buffer surrogate. Ammonium hydroxide (extra pure, 25% solution in water; *Thermo Fisher Scientific*) and acetic acid (100%, extra pure; *Roth*) were used to adjust the pH.

Amicon® Ultra 0.5 mL centrifugal filter units (*Merck Millipore*)

According to the manual, 500 μL of sample and buffer surrogate were added to the filter unit and spun at $14,000 \times g$ and 4°C until a volume below 50 μL was reached which took approximately five to thirty minutes depending on the respective sample and the device's nominal molecular weight limit. This procedure was repeated applying new buffer surrogate five to six times in total to ensure quantitative desalting. The sample was recovered by placing the filter device upside down in a clean microcentrifuge tube and spinning for two minutes at $1000 \times g$ and 4°C .

Vivaspin® 500 Centrifugal Concentrators (*Sartorius*)

According to the manual, 500 μL of sample and buffer surrogate were added to the filter unit and spun at $14,000 \times g$ and 4°C until a volume below 50 μL was reached which took approximately five to thirty minutes depending on the respective sample and the device's nominal molecular weight limit. This procedure was repeated applying new buffer surrogate five to six times in total to ensure quantitative desalting. The sample was recovered directly from the concentrator.

Micro Bio-Spin 6 Columns (*Bio-Rad*)

The column was prepared according to the manufacturer's recommendations by resuspending the gel matrix and removing tip and cap to remove excess packing buffer by gravity drain. Remaining packing buffer was removed by spinning for two minutes at $1000 \times g$ and 4°C . 500 μL buffer surrogate was loaded onto the column, then the column was spun for one minute at $1000 \times g$ and 4°C . This step was performed four times in total. Next, 20 μL to 75 μL sample was applied to the center of the column, which was then spun for four minutes at $1000 \times g$ and 4°C . The whole procedure was repeated one more time using a fresh column for the same sample to ensure quantitative desalting. The particular device that had been used is listed in **Table 3**.

The final concentration of the analyte ranged between 1 μM and 20 μM with respect to the monomeric subunit. Refer to **Table 3** for the specific concentrations of each sample. The concentration of peptidic ligands was kept between 1 μM and 50 μM per ligand. In total, it ranged between 1 μM and 400 μM depending on the experiment.

Table 3 | Overview of all samples used in this work.

For each chapter, the samples used are listed together with their concentration. Furthermore, the BEX used, the corresponding molecular weight cut-off (MWCO) and the buffer surrogate used are given.

chapter	sample	concentration	BEX device	MWCO	buffer surrogate
3.1	α_3	5 μM 10 μM 20 μM	Amicon® Ultra 0.5 mL centrifugal filter units (<i>Merck Millipore</i>)	3 kDa	150 mM ammonium acetate, pH 7.2
3.2	wtA2 & dsA2	1 μM 10 μM	Vivaspin® 500 Centrifugal Concentrators (<i>Sartorius</i>)	10 kDa	250 mM to 1 M ammonium acetate, pH 8.0
3.3	dsA2	10 μM	Micro Bio-Spin 6 Columns (<i>Bio-Rad</i>)	6 kDa	250 mM ammonium acetate, pH 8.0
3.4	wtA2 & dsA2	9.5 μM 10 μM	Micro Bio-Spin 6 Columns (<i>Bio-Rad</i>)	6 kDa	250 mM ammonium acetate, pH 8.0
			Vivaspin® 500 Centrifugal Concentrators (<i>Sartorius</i>)	10 kDa	

5.2.2 Instruments and settings

Native MS analysis was either implemented on a Q-ToF 2 hybrid quadrupole time of flight mass spectrometer (*Waters/Micromass*) or a Q Exactive™ UHMR Hybrid Quadrupole Orbitrap™ mass spectrometer (*Thermo Fisher Scientific*) in positive ESI mode, respectively. Q-ToF 2 was modified to enable high mass experiments (*MS Vision*)³¹⁴.

Sample ions were introduced into the vacuum using homemade capillaries via a nanoESI source. Borosilicate glass tubes (inner diameter: 0.68 mm, outer diameter: 1.2 mm; *World Precision Instruments*) were pulled into closed capillaries in a two-step program using a squared box filament (2.5 mm \times 2.5 mm) within a micropipette puller (P-1000; *Sutter Instruments*). The capillaries were then gold-coated using a sputter coater (5.0 \times 10⁻² mbar, 30.0 mA, 100 s, 3 runs to vacuum limit 3.0 \times 10⁻² mbar argon, distance of plate holder: 5 cm; CCU-010; *safematic*). Capillaries were opened directly on the sample cone of the mass spectrometer or using precision tweezers.

When using Q-ToF 2, a spectrum of cesium iodide (25 g \cdot L⁻¹; 99.999% trace metals basis, *Sigma-Aldrich*) was recorded on the same day of the respective measurement to calibrate the data. QE-UHMR was calibrated monthly according to the manufacturer's recommendations.

5.2.2.1 Pressure settings

The experiments were carried out using argon (Q-ToF 2) or nitrogen (QE-UHMR) as collision gas.

The exact vacuum settings are stated in **Table 4**.

Table 4 | Overview of all pressure settings used in this work.

chapter	sample	instrument	source pressure (mbar)	collision cell pressure (mbar)
3.1	α_3	Q-ToF 2	10	1.2×10^{-2}
3.2	wtA2 & dsA2	Q-ToF 2	10	$1.2-2.0 \times 10^{-2}$
3.3	dsA2	Q-ToF 2	10	1.2×10^{-2}
3.4.1.1	dsA2	QE-UHMR	1.4-1.7	2.0×10^{-10}
3.4.1.2	wtA2	Q-ToF 2	10	1.2×10^{-2}
3.4.1.3	dsA2	QE-UHMR	1.4-1.7	$2.0-3.0 \times 10^{-10}$
		Q-ToF 2	10	1.2×10^{-2}
3.4.1.4	dsA2	QE-UHMR	1.4-1.7	$2.0-3.0 \times 10^{-10}$
3.4.1.5	dsA2	QE-UHMR	1.4-1.7	$2.0-3.0 \times 10^{-10}$
3.4.1.6	dsA2	QE-UHMR	1.4-1.7	$2.0-3.0 \times 10^{-10}$
3.4.1.7	dsA2	QE-UHMR	1.4-1.7	$2.0-3.0 \times 10^{-10}$
3.4.1.8	dsA2	QE-UHMR	1.4-1.7	$2.0-3.0 \times 10^{-10}$

5.2.2.2 Voltage settings

In regular MS mode, spectra were recorded at a capillary voltage between 1.2 kV and 1.45 kV and a cone voltage ranging from 75 V to 175 V. The settings were optimized to keep proteins and protein complexes in a folded state within the gas phase. Protein species with quaternary structure were assigned by MS² analysis. Hereby, the acceleration voltage ranged between 10 V and 100 V.

Applied voltages can be found in **Table 5**.

Table 5 | Overview of all voltage settings used in this work.

chapter	sample	instrument	capillary (kV)	cone (V)	collision cell (V)	in-source energy (eV)
3.1	α_3	Q-ToF 2	1.45	100-150	10-100	0
3.2	wtA2	Q-ToF 2	1.2-1.45	120-150	10-100	0
3.2	dsA2	Q-ToF 2	1.45	150	10-150	0
3.3.1	dsA2	Q-ToF 2	1.45	75-175	10-100	0
3.3.1.2	dsA2	Q-ToF 2	1.45	150	10-50	0
3.3.1.3	dsA2	Q-ToF 2	1.45	150	10-50	0
3.3.1.4	dsA2	Q-ToF 2	1.45	150	10-50	0
3.4.1.1	dsA2	QE-UHMR	1.45	150	50	0
3.4.1.2	wtA2	Q-ToF 2	1.45	150	50	0
3.4.1.3	dsA2	Q-ToF 2	1.45	150	50	0
3.4.1.3	dsA2	QE-UHMR	1.45	150	50	0
3.4.1.4	dsA2	QE-UHMR	1.45	150	50	0-129
3.4.1.5	dsA2	QE-UHMR	1.45	150	50	0
3.4.1.6	dsA2	QE-UHMR	1.45	150	50	0
3.4.1.7	dsA2	QE-UHMR	1.45	150	50	0
3.4.1.8	dsA2	QE-UHMR	1.45	150	50	0

5.2.3 Other instrument-specific settings

More instrument-specific settings are listed in Table 6.

Table 6 | Overview of all relevant instrument-specific settings used in this work.

chapter	sample	instrument	m/z interval	Q-Tof 2: pusher time (μ s) QE-UHMR: injection time (ms)	MS ² selection interval	capillary temperature ($^{\circ}$ C)
3.1	α_3	Q-Tof 2	100-10,000	192	0.2-10	
3.2	wtA2	Q-Tof 2	100-20,000	192	10	
3.2	dsA2	Q-Tof 2	100-10,000	192	10-20	
3.3.1	dsA2	Q-Tof 2	100-10,000	192	10-20	
3.3.1.2	dsA2	Q-Tof 2	100-10,000	192	10-20	
3.3.1.3	dsA2	Q-Tof 2	100-10,000	192	10-20	
3.3.1.4	dsA2	Q-Tof 2	100-10,000	192	10-20	
3.4.1.1	dsA2	QE-UHMR	500-15,000	100	5-100	
3.4.1.2	wtA2	Q-Tof 2	100-10,000	192	0-30	
3.4.1.3	dsA2	Q-Tof 2	100-10,000	192	10-20	
3.4.1.3	dsA2	QE-UHMR	500-15,000	100	5-100	50
3.4.1.4	dsA2	QE-UHMR	500-15,000	100	5-100	50-300
3.4.1.5	dsA2	QE-UHMR	500-15,000	100	5-100	50
3.4.1.6	dsA2	QE-UHMR	500-15,000	100	5-100	50
3.4.1.7	dsA2	QE-UHMR	500-15,000	100	5-100	50
3.4.1.8	dsA2	QE-UHMR	500-15,000	100	5-100	50

For each instrument, an exemplary experiment file including all available settings is given in the supplement (*cf.* **Exemplary experimental files**).

5.2.4 Spectra analysis

Peak assignment and mass analysis were executed via MassLynx 4.1 (Waters) and Massign (Nina Morgner)³¹⁵. The AUC of detected mass species was determined using UniDec 5.2.0 (Michael T. Marty)⁵². The software mMass 5.5.0 (Martin Strohaln)³¹⁶ was used to define the FWHM of the peaks. Narrow peak widths indicate rather homogeneous samples. The values of the shown averaged masses, FWHM, and AUC of the different species as well as the corresponding standard deviation result from at least three independent measurements.

5.3 Differential scanning fluorimetry

DSF experiments were executed by Ankur Saikia from the Springer lab (Constructor University Bremen) as well as Christian Günther and Stephan Niebling from the Garcia-Alai lab (EMBL Hamburg).

Thermal stability and binding affinity were determined using nanoscale differential scanning fluorimetry on a Prometheus NT.48 (*NanoTemper Technologies*). Capillaries were filled with 10 μL of respective samples in duplicates and loaded into the reading chamber. The scan rate was 1 $^{\circ}\text{C}/\text{min}$ ranging from 20 $^{\circ}\text{C}$ to 80 $^{\circ}\text{C}$ for thermal stability and 95 $^{\circ}\text{C}$ for binding affinity measurements. Protein unfolding was measured by detecting the temperature dependent change in intrinsic tryptophan fluorescence at emission wavelengths of 330 nm and 350 nm.

5.3.1 Thermal stability (nDSF)

About 2 μM of empty dsA2 were dissolved in citrate phosphate buffer, pH 7.6³¹⁷, and incubated with peptidic ligands (0.2 μM to 2 mM) on ice for 30 min. Melting curves and T_m values were generated by PR.ThermControl 2.1 (*NanoTemper Technologies*) using the first derivative of the fluorescence at 330 nm.

5.3.2 Binding affinity (iDSF)

Empty dsA2 dissolved in 20 mM Tris pH 8, 150 mM NaCl was incubated with peptidic ligands at different concentrations depending on their predicted or assumed K_d range. For each peptide, a twofold serial dilution series (11 concentrations) was prepared, while protein concentration was kept constant at 2.2 μM . A pure protein was analyzed as well. PR.ThermControl 2.1.2 (*NanoTemper Technologies*) was used to control the device. Data processing and evaluation was executed via the FoldAffinity web server (EMBL Hamburg, <https://spc.embl-hamburg.de/>)²⁶¹.

5.4 Mathematical methods

5.4.1 Eliminating nonspecific ESI clustering

In **Chapter 3.3**, AUC determined based on the spectral raw data were affected by nonspecific ESI clustering. In order to eliminate the clustering within the results, the raw data were corrected using the dsA2+pep fraction of the negative control YF9. For this, the clustering factor f was defined as quotient of the total AUC for the mass species “dsA2+YF9” and the total AUC of all other dsA2 mass species found (dsA2_{YF9-unbound}).

$$f = \frac{(\text{dsA2+YF9})}{\text{dsA2}_{\text{YF9-unbound}}}$$

Equation 15

All values used for the calculations are the respective arithmetic means of at least three replicates. “dsA2” corresponds to the empty HLA-A*02:01(Y84C/A139C) disulfide mutant complex, “dsA2+pep” to dsA2 bound to one peptide, “dsA2+pep+pep” to dsA2 bound to two molecules of this certain peptide, and “dsA2+erucamide” to dsA2 bound to the erucamide, respectively. The AUC fractions of dsA2, dsA2+pep and dsA2+pep+pep were corrected as follows.

$$\text{dsA2}_{\text{corr}} = \text{dsA2} + f \cdot (\text{dsA2+pep}) + f^2 \cdot (\text{dsA2+pep+pep})$$

Equation 16

$$(\text{dsA2+pep})_{\text{corr}} = (\text{dsA2+pep}) - f \cdot (\text{dsA2+pep}) + f \cdot (\text{dsA2+pep+pep})$$

Equation 17

$$(\text{dsA2+pep+pep})_{\text{corr}} = (\text{dsA2+pep+pep}) - f \cdot (\text{dsA2+pep+pep}) - f^2 \cdot (\text{dsA2+pep+pep})$$

Equation 18

Erucamide initially binds dsA2 when the protein solution is in contact with laboratory plastic ware. The compound is substituted by peptides introduced into the solution. Therefore, the total concentration of erucamide can never be high enough to cause significant clustering artifacts. As such, the AUC fraction of dsA2+erucamide does not need to be corrected.

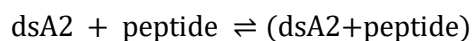
$$(\text{dsA2+erucamide})_{\text{corr}} = (\text{dsA2+erucamide})$$

Equation 19

The calculations presented were performed using Excel 2301 (*Microsoft*).

5.4.2 Calculating affinities

Peptide-binding affinities in **Chapter 3.3** were calculated using the law of mass action. Since MHC-I has exactly one binding groove for ligands, the binding process for dsA2 is defined as follows.



Equation 20

Association constant K_a describes the speed of the binding reaction and K_d that of the reverse reaction, hence the term dissociation constant. This is defined as follows.

$$K_d = \frac{[\text{dsA2}] \cdot [\text{peptide}]}{[\text{dsA2+peptide}]}$$

Equation 21

$[\text{dsA2}]$ represents the concentration of the empty dsA2 and equals the total concentration introduced to the sample $[\text{dsA2}]_0$ subtracted by all dsA2 occupied by a peptide ($\text{dsA2}_{\text{peptide-bound}}$). The latter value is extracted directly from the native mass spectrum using the AUC as read-out. This was done in different ways for $K_{d,\text{high}}$ and $K_{d,\text{low}}$. More information about this follows below.

$$[\text{dsA2}] = [\text{dsA2}]_0 - \text{dsA2}_{\text{peptide-bound}}$$

Equation 22

Concentration of the peptide $[\text{peptide}]$ is defined as the initial concentration $[\text{peptide}]_0$ minus $\text{peptide}_{\text{dsA2-bound}}$, which can equally be derived from AUC values of respective spectra.

$$[\text{peptide}] = [\text{peptide}]_0 - \text{peptide}_{\text{dsA2-bound}}$$

Equation 23

Conversely, the $[\text{dsA2+peptide}]$ is defined as the subtraction of $[\text{dsA2}]$ and $\text{dsA2}_{\text{peptide-unbound}}$. This variable can be retrieved from the spectrum as well.

$$[\text{dsA2+peptide}] = [\text{dsA2}]_0 - \text{dsA2}_{\text{peptide-unbound}}$$

Equation 24

The calculations presented were performed using Excel 2301 (*Microsoft*).

5.4.2.1 Calculating $K_{d,\text{high}}$

The affinity $K_{d,\text{high}}$ was calculated directly from AUC measured at 150 V cone voltage and 10 V acceleration voltage. The dsA2 and peptide concentrations used initially are known, i.e., $[\text{dsA2}]_0 = 10 \mu\text{M}$ and $[\text{peptide}]_0 = 50 \mu\text{M}$ in the single-peptide experiment. $\text{dsA2}_{\text{peptide-}}$

$bound$ is the summand of the (clustering-corrected) AUC for dsA2+pep and dsA2+pep+pep multiplied by $[dsA2]_0$. Thus, with regard to **Equation 22**, we define $[peptide]$ as follows.

$$[dsA2] = [dsA2]_0 - [dsA2]_0 \cdot (AUC_{dsA2+pep} + AUC_{dsA2+pep+pep})$$

Equation 25

Peptide concentration $[peptide]$ is similarly described.

$$[peptide] = [peptide]_0 - [peptide]_0 \cdot (AUC_{dsA2+pep} + AUC_{dsA2+pep+pep})$$

Equation 26

The variable $dsA2_{peptide-unbound}$ required to calculate $[dsA2+peptide]$ can be expressed as the summand of the (clustering-corrected) AUC for dsA2 and dsA2+erucamide multiplied by $[dsA2]_0$. Together with **Equation 24** we get the following description.

$$[dsA2+peptide] = [dsA2]_0 - [dsA2]_0 \cdot (AUC_{dsA2} + AUC_{dsA2+erucamide})$$

Equation 27

The calculations presented were performed using Excel 2301 (*Microsoft*).

5.4.2.2 Calculating $K_{d,low}$

The affinity $K_{d,low}$ was indirectly derived from the AUC of the dsA2+erucamide fraction. Since the cone voltage is linearly proportional to the ISD, the distribution of peptide-bound and peptide-unbound dsA2 at nondissociating conditions can be estimated. According to the equation derived from the linear relationship of cone voltage and occupancy, the binding groove is fully occupied at 48 V and thus reflects the in-solution conditions of the superstoichiometric mixture (*cf. Figure 29A*).

$$occupancy = -0.005496 \cdot \text{cone voltage} + 1.285$$

Equation 28

The peptide-free (erucamide-bound, dsA2+erucamide) fraction of the protein measured at a cone voltage of 150 V can be corrected using the linear equation. According to **Equation 28**, the occupation, which would be complete at a hypothetical cone voltage of 48 V, would in turn be only about 46% at 150 V. The factor for the loss is 2.2, when rounded. Thus, the AUC fraction of dsA2+erucamide was multiplied by this factor in order to eliminate the ISD effects, from which the variables $dsA2_{peptide-unbound}$ is derived. Subsequently, if this fraction is subtracted from the possible 100% occupancy, the fraction that binds the peptide is obtained providing the variables $dsA2_{peptide-bound}$ and $peptide_{dsA2-bound}$. Concentrations $[dsA2]$, $[peptide]$, and $[dsA2+peptide]$ are then defined as follows.

$$[\text{dsA2}] = [\text{dsA2}]_0 - [\text{dsA2}]_0 \cdot (1 - 2.2 \cdot \text{AUC}_{\text{dsA2+erucamide}})$$

Equation 29

$$[\text{peptide}] = [\text{peptide}]_0 - [\text{peptide}]_0 \cdot (1 - 2.2 \cdot \text{AUC}_{\text{dsA2+erucamide}})$$

Equation 30

$$[\text{dsA2+peptide}] = [\text{dsA2}]_0 - [\text{dsA2}]_0 \cdot 2.2 \cdot \text{AUC}_{\text{dsA2+erucamide}}$$

Equation 31

Linear regression was conducted using QtiPlot 1.1.3 (*Ion Vasilief*). Other calculations were performed using Excel 2301 (*Microsoft*).

5.5 Statistics and reproducibility

Concerning the native mass spectrometry data, the values of the shown averaged masses, FWHM, and AUC of the different species as well as the corresponding standard deviation result from at least three independent measurements. When feasible, all individual measured points are shown in addition to the mean value and the error bars representing the standard deviation.

Differential scanning fluorimetry was performed in duplicates.

In general, data is expressed as the mean \pm standard deviation of the mean.

For the presentation of indirectly determined quantities such as the K_d , the standard deviation was obtained according to the rules of GAUSSIAN error propagation.

5.6 Data visualization

Protein structure files were retrieved from the Protein Data Bank¹⁷³ at <https://www.rcsb.org/>, then viewed and adjusted using ChimeraX 1.4 (*Resource for Biocomputing, Visualization, and Informatics at UC San Francisco*)²³⁸.

Mass spectra were either copied from the spectrum window of MassLynx 4.1 (*Waters*) or generated using the Matplotlib library 3.2.2 (*Matplotlib Development Team, John Hunter*)^{318,319} and Python 3.8 (*Python Software Foundation, Guido van Rossum*)³²⁰, then modified using Adobe Illustrator 2022 (*Adobe*).

Diagrams were created using Excel 2301 (*Microsoft*) or Prism 5.03 (*GraphPad Software*).

All figures were prepared using Adobe Illustrator 2022 (*Adobe*).

5.7 Data availability

Native MS raw data of published datasets have been deposited to the ProteomeXchange Consortium³²¹ via the PRIDE partner repository³²².

Chapter 3.1 MHC-I heavy chains form noncovalent dimers in absence of β_2m

Dirscherl, C., Löchte, S., Hein, Z., **Kopicki, J.-D.**, Harders, A. R., Linden, N., Karner, A., Preiner, J., Weghuber, J., Garcia-Alai, M., Uetrecht, C., Zacharias, M., Piehler, J., Lanzerstorfer, P., & Springer, S. (2022). Dissociation of β_2m from MHC class I triggers formation of noncovalent transient heavy chain dimers. *Journal of cell science*, 135(9), jcs259489³.

Dataset identifier: **PXD033485**

Chapter 3.2 Peptide-free, disulfide-stabilized MHC-I molecules

Anjanappa, R., Garcia-Alai, M., **Kopicki, J.-D.**, Lockhauserbäumer, J., Aboelmagd, M., Hinrichs, J., Nemptanu, I. M., Uetrecht, C., Zacharias, M., Springer, S., & Meijers, R. (2020). Structures of peptide-free and partially loaded MHC class I molecules reveal mechanisms of peptide selection. *Nature communications*, 11(1), 1314².

Dataset identifier: **PXD016708**

Chapter 3.3 MHC-I peptide binding

Kopicki, J.-D., Saikia, A., Niebling, S., Günther, C., Anjanappa, R., Garcia-Alai, M., Springer, S., & Uetrecht, C. (2022). Opening opportunities for K_d determination and screening of MHC peptide complexes. *Communications biology*, 5(1), 488⁴.

Dataset identifier: **PXD027725**

References

- (1) Dülfer, J.; Kadek, A.; Kopicki, J.-D.; Krichel, B.; Uetrecht, C. Chapter Seven - Structural Mass Spectrometry Goes Viral. In *Advances in Virus Research*; Rey, F. A., Ed.; Academic Press, 2019; Vol. 105, pp 189–238. <https://doi.org/10.1016/bs.aivir.2019.07.003>.
- (2) Anjanappa, R.; Garcia-Alai, M.; Kopicki, J. D.; Lockhouserbaumer, J.; Aboelmagd, M.; Hinrichs, J.; Nemtanu, I. M.; Uetrecht, C.; Zacharias, M.; Springer, S.; Meijers, R. Structures of Peptide-Free and Partially Loaded MHC Class I Molecules Reveal Mechanisms of Peptide Selection. *Nat Commun* **2020**, *11* (1), 1314. <https://doi.org/10.1038/s41467-020-14862-4>.
- (3) Dirscherl, C.; Löchte, S.; Hein, Z.; Kopicki, J.-D.; Harders, A. R.; Linden, N.; Karner, A.; Preiner, J.; Weghuber, J.; Garcia-Alai, M.; Uetrecht, C.; Zacharias, M.; Piehler, J.; Lanzerstorfer, P.; Springer, S. Dissociation of B2m from MHC Class I Triggers Formation of Noncovalent Transient Heavy Chain Dimers. *J. Cell Sci.* **2022**, *135* (9), jcs259489. <https://doi.org/10.1242/jcs.259498>.
- (4) Kopicki, J.-D.; Saikia, A.; Niebling, S.; Günther, C.; Anjanappa, R.; Garcia-Alai, M.; Springer, S.; Uetrecht, C. Opening Opportunities for Kd Determination and Screening of MHC Peptide Complexes. *Commun. Biol.* **2022**, *5* (1), 488. <https://doi.org/10.1038/s42003-022-03366-0>.
- (5) Holm, T.; Kopicki, J. D.; Busch, C.; Olschewski, S.; Rosenthal, M.; Uetrecht, C.; Gunther, S.; Reindl, S. Biochemical and Structural Studies Reveal Differences and Commonalities among Cap-Snatching Endonucleases from Segmented Negative-Strand RNA Viruses. *J Biol Chem* **2018**. <https://doi.org/10.1074/jbc.RA118.004373>.
- (6) Günther, S.; Reinke, P. Y. A.; Fernández-García, Y.; Lieske, J.; Lane, T. J.; Ginn, H. M.; Koua, F. H. M.; Ehart, C.; Ewert, W.; Oberthuer, D.; Yefanov, O.; Meier, S.; Lorenzen, K.; Krichel, B.; Kopicki, J.-D.; Gelisio, L.; Brehm, W.; Dunkel, I.; Seychell, B.; Gieseler, H.; Norton-Baker, B.; Escudero-Pérez, B.; Domaracky, M.; Saouane, S.; Tolstikova, A.; White, T. A.; Hänle, A.; Groessler, M.; Fleckenstein, H.; Trost, F.; Galchenkova, M.; Gevorkov, Y.; Li, C.; Awel, S.; Peck, A.; Barthelmess, M.; Schluenzen, F.; Lourdu Xavier, P.; Werner, N.; Andaleeb, H.; Ullah, N.; Falke, S.; Srinivasan, V.; França, B. A.; Schwitzer, M.; Brognaro, H.; Rogers, C.; Melo, D.; Zaitseva-Doyle, J. J.; Knoska, J.; Peña-Murillo, G. E.; Mashhour, A. R.; Hennicke, V.; Fischer, P.; Hakanpää, J.; Meyer, J.; Gribbon, P.; Ellinger, B.; Kuzikov, M.; Wolf, M.; Beccari, A. R.; Bourenkov, G.; von Stetten, D.; Pompidor, G.; Bento, I.; Panneerselvam, S.; Karpics, I.; Schneider, T. R.; Garcia-Alai, M. M.; Niebling, S.; Günther, C.; Schmidt, C.; Schubert, R.; Han, H.; Boger, J.; Monteiro, D. C. F.; Zhang, L.; Sun, X.; Pletzer-Zelgert, J.; Wollenhaupt, J.; Feiler, C. G.; Weiss, M. S.; Schulz, E.-C.; Mehrabi, P.; Karničar, K.; Usenik, A.; Loboda, J.; Tidow, H.; Chari, A.; Hilgenfeld, R.; Uetrecht, C.; Cox, R.; Zaliani, A.; Beck, T.; Rarey, M.; Günther, S.; Turk, D.; Hinrichs, W.; Chapman, H. N.; Pearson, A. R.; Betzel, C.; Meents, A. X-Ray Screening Identifies Active Site and Allosteric Inhibitors of SARS-CoV-2 Main Protease. *Science* **2021**, eabf7945. <https://doi.org/10.1126/science.abf7945>.
- (7) Merk, A.; Bartesaghi, A.; Banerjee, S.; Falconieri, V.; Rao, P.; Davis, M. I.; Pragani, R.; Boxer, M. B.; Earl, L. A.; Milne, J. L. S.; Subramaniam, S. Breaking Cryo-EM Resolution Barriers to Facilitate Drug Discovery. *Cell* **2016**, *165* (7), 1698–1707. <https://doi.org/10.1016/j.cell.2016.05.040>.
- (8) Ward, A. B.; Sali, A.; Wilson, I. A. Biochemistry. Integrative Structural Biology. *Science* **2013**, *339* (6122), 913–915. <https://doi.org/10.1126/science.1228565>.
- (9) Politis, A.; Schmidt, C. Structural Characterisation of Medically Relevant Protein Assemblies by Integrating Mass Spectrometry with Computational Modelling. *J. Proteomics* **2018**, *175*, 34–41. <https://doi.org/10.1016/j.jprot.2017.04.019>.
- (10) Marklund, E. G.; Benesch, J. L. Weighing-up Protein Dynamics: The Combination of Native Mass Spectrometry and Molecular Dynamics Simulations. *Curr. Opin. Struct. Biol.* **2019**, *54*, 50–58. <https://doi.org/10.1016/j.sbi.2018.12.011>.
- (11) Gross, J. H. *Mass Spectrometry: A Textbook*, 3rd ed.; Springer International Publishing: Cham, Switzerland, 2017. <https://doi.org/10.1007/978-3-319-54398-7>.
- (12) Yamashita, M.; Fenn, J. B. Electrospray Ion Source. Another Variation on the Free-Jet Theme. *J. Phys. Chem.* **1984**, *88* (20), 4451–4459. <https://doi.org/10.1021/j150664a002>.
- (13) Karas, M.; Bachmann, D.; Bahr, U.; Hillenkamp, F. Matrix-Assisted Ultraviolet Laser Desorption of Non-Volatile Compounds. *Int. J. Mass Spectrom. Ion Process.* **1987**, *78*, 53–68. [https://doi.org/10.1016/0168-1176\(87\)87041-6](https://doi.org/10.1016/0168-1176(87)87041-6).
- (14) Tanaka, K.; Waki, H.; Ido, Y.; Akita, S.; Yoshida, Y.; Yoshida, T.; Matsuo, T. Protein and Polymer Analyses up to 100 000 by Laser Ionization Time-of-Flight Mass Spectrometry. *Rapid Commun. Mass Spectrom.* **1988**, *2* (8), 151–153. <https://doi.org/10.1002/rcm.1290020802>.
- (15) Fenn, J. B.; Mann, M.; Meng, C. K.; Wong, S. F.; Whitehouse, C. M. Electrospray Ionization for Mass Spectrometry of Large Biomolecules. *Science* **1989**, *246* (4926), 64–71. <https://doi.org/10.1126/science.2675315>.
- (16) Nguyen, S.; Fenn, J. B. Gas-Phase Ions of Solute Species from Charged Droplets of Solutions. *Proc. Natl. Acad. Sci. U. S. A.* **2007**, *104* (4), 1111–1117. <https://doi.org/10.1073/pnas.0609969104>.
- (17) Yates, J. R.; Ruse, C. I.; Nakorchevsky, A. Proteomics by Mass Spectrometry: Approaches, Advances, and Applications. *Annu. Rev. Biomed. Eng.* **2009**, *11* (1), 49–79. <https://doi.org/10.1146/annurev-bioeng-061008-124934>.

- (18) Luo, Y.; Muesing, M. A. Mass Spectrometry-Based Proteomic Approaches for Discovery of HIV–Host Interactions. *Future Virol.* **2014**, *9* (11), 979–992. <https://doi.org/10.2217/fvl.14.86>.
- (19) Loo, J. A. Observation of Large Subunit Protein Complexes by Electrospray Ionization Mass Spectrometry. *J. Mass Spectrom.* **1995**, *30* (1), 180–183. <https://doi.org/10.1002/jms.1190300127>.
- (20) Rostom, A. A.; Robinson, C. V. Detection of the Intact GroEL Chaperonin Assembly by Mass Spectrometry. *J. Am. Chem. Soc.* **1999**, *121* (19), 4718–4719. <https://doi.org/10.1021/ja990238r>.
- (21) Van Berkel, W. J. H.; Van Den Heuvel, R. H. H.; Versluis, C.; Heck, A. J. R. Detection of Intact MegaDalton Protein Assemblies of Vanillyl-Alcohol Oxidase by Mass Spectrometry. *Protein Sci.* **2008**, *9* (3), 435–439. <https://doi.org/10.1110/ps.9.3.435>.
- (22) Leney, A. C.; Heck, A. J. Native Mass Spectrometry: What Is in the Name? *J Am Soc Mass Spectrom* **2017**, *28* (1), 5–13. <https://doi.org/10.1007/s13361-016-1545-3>.
- (23) Ruotolo, B. T.; Giles, K.; Campuzano, I.; Sandercock, A. M.; Bateman, R. H.; Robinson, C. V. Evidence for Macromolecular Protein Rings in the Absence of Bulk Water. *Science* **2005**, *310* (5754), 1658–1661. <https://doi.org/10.1126/science.1120177>.
- (24) Uetrecht, C.; Versluis, C.; Watts, N. R.; Wingfield, P. T.; Steven, A. C.; Heck, A. J. R. Stability and Shape of Hepatitis B Virus Capsids In Vacuo. *Angew. Chem. Int. Ed.* **2008**, *47* (33), 6247–6251. <https://doi.org/10.1002/anie.200802410>.
- (25) Seo, J.; Hoffmann, W.; Warnke, S.; Bowers, M. T.; Pagel, K.; von Helden, G. Retention of Native Protein Structures in the Absence of Solvent: A Coupled Ion Mobility and Spectroscopic Study. *Angew. Chem. Int. Ed.* **2016**, *55* (45), 14173–14176. <https://doi.org/10.1002/anie.201606029>.
- (26) Katta, V.; Chait, B. T.; Carr, S. Conformational Changes in Proteins Probed by Hydrogen-Exchange Electrospray-Ionization Mass Spectrometry. *Rapid Commun. Mass Spectrom.* **1991**, *5* (4), 214–217. <https://doi.org/10.1002/rcm.1290050415>.
- (27) Rossi, V.; Gaboriaud, C.; Lacroix, M.; Ulrich, J.; Fontecilla-Camps, J. C.; Gagnon, J.; Arlaud, G. J. Structure of the Catalytic Region of Human Complement Protease C.Hivin.1s: Study by Chemical Crosslinking and Three-Dimensional Homology Modeling. *Biochemistry* **1995**, *34* (22), 7311–7321. <https://doi.org/10.1021/bi00022a004>.
- (28) Maleknia, S. D.; Ralston, C. Y.; Brenowitz, M. D.; Downard, K. M.; Chance, M. R. Determination of Macromolecular Folding and Structure by Synchrotron X-Ray Radiolysis Techniques. *Anal. Biochem.* **2001**, *289* (2), 103–115. <https://doi.org/10.1006/abio.2000.4910>.
- (29) Espino, J. A.; Mali, V. S.; Jones, L. M. In Cell Footprinting Coupled with Mass Spectrometry for the Structural Analysis of Proteins in Live Cells. *Anal. Chem.* **2015**, *87* (15), 7971–7978. <https://doi.org/10.1021/acs.analchem.5b01888>.
- (30) Gan, J.; Ben-Nissan, G.; Arkind, G.; Tarnavsky, M.; Trudeau, D.; Noda Garcia, L.; Tawfik, D. S.; Sharon, M. Native Mass Spectrometry of Recombinant Proteins from Crude Cell Lysates. *Anal Chem* **2017**, *89* (8), 4398–4404. <https://doi.org/10.1021/acs.analchem.7b00398>.
- (31) Chavez, J. D.; Lee, C. F.; Caudal, A.; Keller, A.; Tian, R.; Bruce, J. E. Chemical Crosslinking Mass Spectrometry Analysis of Protein Conformations and Supercomplexes in Heart Tissue. *Cell Syst.* **2018**, *6* (1), 136–141.e5. <https://doi.org/10.1016/j.cels.2017.10.017>.
- (32) Chorev, D. S.; Baker, L. A.; Wu, D.; Beilsten-Edmands, V.; Rouse, S. L.; Zeev-Ben-Mordehai, T.; Jiko, C.; Samsudin, F.; Gerle, C.; Khalid, S.; Stewart, A. G.; Matthews, S. J.; Grunewald, K.; Robinson, C. V. Protein Assemblies Ejected Directly from Native Membranes Yield Complexes for Mass Spectrometry. *Science* **2018**, *362* (6416), 829–834. <https://doi.org/10.1126/science.aau0976>.
- (33) Nguyen, T. T.; Sabat, G.; Sussman, M. R. In Vivo Cross-Linking Supports a Head-to-Tail Mechanism for Regulation of the Plant Plasma Membrane P-Type H⁺-ATPase. *J. Biol. Chem.* **2018**, *293* (44), 17095–17106. <https://doi.org/10.1074/jbc.RA118.003528>.
- (34) Garcia-Moreno, M.; Noerenberg, M.; Ni, S.; Järvelin, A. I.; González-Almela, E.; Lenz, C. E.; Bach-Pages, M.; Cox, V.; Avolio, R.; Davis, T.; Hester, S.; Sohler, T. J. M.; Li, B.; Heikel, G.; Michlewski, G.; Sanz, M. A.; Carrasco, L.; Ricci, E. P.; Pelechano, V.; Davis, I.; Fischer, B.; Mohammed, S.; Castello, A. System-Wide Profiling of RNA-Binding Proteins Uncovers Key Regulators of Virus Infection. *Mol. Cell* **2019**, *74* (1), 196–211.e11. <https://doi.org/10.1016/j.molcel.2019.01.017>.
- (35) Greaves, J.; Roboz, J. *Mass Spectrometry for the Novice*; Taylor & Francis Group, LLC: Boca Raton, FL, 2014.
- (36) Bakhtiari, M.; Konermann, L. Protein Ions Generated by Native Electrospray Ionization: Comparison of Gas Phase, Solution, and Crystal Structures. *J. Phys. Chem. B* **2019**, *123* (8), 1784–1796. <https://doi.org/10.1021/acs.jpcc.8b12173>.
- (37) Peetz, O.; Hellwig, N.; Henrich, E.; Mezhyrova, J.; Dötsch, V.; Bernhard, F.; Morgner, N. LILBID and NESI: Different Native Mass Spectrometry Techniques as Tools in Structural Biology. *J. Am. Soc. Mass Spectrom.* **2019**, *30* (1), 181–191. <https://doi.org/10.1007/s13361-018-2061-4>.
- (38) Siuzdak, G.; Bothner, B.; Yeager, M.; Brugidou, C.; Fauquet, C. M.; Hoey, K.; Chang, C. M. Mass Spectrometry and Viral Analysis. *Chem Biol* **1996**, *3* (1), 45–48.

- (39) Hogan, C. J.; Kettleson, E. M.; Ramaswami, B.; Chen, D.-R.; Biswas, P. Charge Reduced Electrospray Size Spectrometry of Mega- and Gigadalton Complexes: Whole Viruses and Virus Fragments. *Anal. Chem.* **2006**, *78* (3), 844–852. <https://doi.org/10.1021/ac051571i>.
- (40) Konermann, L. Addressing a Common Misconception: Ammonium Acetate as Neutral PH “Buffer” for Native Electrospray Mass Spectrometry. *J Am Soc Mass Spectrom* **2017**, *28* (9), 1827–1835. <https://doi.org/10.1007/s13361-017-1739-3>.
- (41) Susa, A. C.; Xia, Z.; Williams, E. R. Small Emitter Tips for Native Mass Spectrometry of Proteins and Protein Complexes from Nonvolatile Buffers That Mimic the Intracellular Environment. *Anal Chem* **2017**, *89* (5), 3116–3122. <https://doi.org/10.1021/acs.analchem.6b04897>.
- (42) Iavarone, A. T.; Williams, E. R. Mechanism of Charging and Supercharging Molecules in Electrospray Ionization. *J. Am. Chem. Soc.* **2003**, *125* (8), 2319–2327. <https://doi.org/10.1021/ja021202t>.
- (43) Pagel, K.; Hyung, S.-J.; Ruotolo, B. T.; Robinson, C. V. Alternate Dissociation Pathways Identified in Charge-Reduced Protein Complex Ions. *Anal. Chem.* **2010**, *82* (12), 5363–5372. <https://doi.org/10.1021/ac101121r>.
- (44) Konermann, L.; Metwally, H.; Duez, Q.; Peters, I. Charging and Supercharging of Proteins for Mass Spectrometry: Recent Insights into the Mechanisms of Electrospray Ionization. *Analyst* **2019**, *144* (21), 6157–6171. <https://doi.org/10.1039/c9an01201j>.
- (45) Barrera, N. P.; Di Bartolo, N.; Booth, P. J.; Robinson, C. V. Micelles Protect Membrane Complexes from Solution to Vacuum. *Science* **2008**, *321* (5886), 243–246. <https://doi.org/10.1126/science.1159292>.
- (46) Hopper, J. T. S.; Yu, Y. T.-C.; Li, D.; Raymond, A.; Bostock, M.; Liko, I.; Mikhailov, V.; Laganowsky, A.; Benesch, J. L. P.; Caffrey, M.; Nietlispach, D.; Robinson, C. V. Detergent-Free Mass Spectrometry of Membrane Protein Complexes. *Nat. Methods* **2013**, *10* (12), 1206–1208. <https://doi.org/10.1038/nmeth.2691>.
- (47) Laganowsky, A.; Reading, E.; Hopper, J. T.; Robinson, C. V. Mass Spectrometry of Intact Membrane Protein Complexes. *Nat Protoc* **2013**, *8* (4), 639–651. <https://doi.org/10.1038/nprot.2013.024>.
- (48) Hedges, J. B.; Vahidi, S.; Yue, X.; Konermann, L. Effects of Ammonium Bicarbonate on the Electrospray Mass Spectra of Proteins: Evidence for Bubble-Induced Unfolding. *Anal. Chem.* **2013**, *85* (13), 6469–6476. <https://doi.org/10.1021/ac401020s>.
- (49) Konermann, L.; Ahadi, E.; Rodriguez, A. D.; Vahidi, S. Unraveling the Mechanism of Electrospray Ionization. *Anal. Chem.* **2013**, *85* (1), 2–9. <https://doi.org/10.1021/ac302789c>.
- (50) McAllister, R. G.; Metwally, H.; Sun, Y.; Konermann, L. Release of Native-like Gaseous Proteins from Electrospray Droplets via the Charged Residue Mechanism: Insights from Molecular Dynamics Simulations. *J. Am. Chem. Soc.* **2015**, *137* (39), 12667–12676. <https://doi.org/10.1021/jacs.5b07913>.
- (51) Heck, A. J. R.; van den Heuvel, R. H. H. Investigation of Intact Protein Complexes by Mass Spectrometry. *Mass Spectrom. Rev.* **2004**, *23* (5), 368–389. <https://doi.org/10.1002/mas.10081>.
- (52) Marty, M. T.; Baldwin, A. J.; Marklund, E. G.; Hochberg, G. K.; Benesch, J. L.; Robinson, C. V. Bayesian Deconvolution of Mass and Ion Mobility Spectra: From Binary Interactions to Polydisperse Ensembles. *Anal Chem* **2015**, *87* (8), 4370–4376. <https://doi.org/10.1021/acs.analchem.5b00140>.
- (53) Mulvaney, R. L. Mass Spectrometry. In *Nitrogen Isotope Techniques*; Elsevier, 1993; pp 11–57. <https://doi.org/10.1016/B978-0-08-092407-6.50007-9>.
- (54) Murray, K. K.; Boyd, R. K.; Eberlin, M. N.; Langley, G. J.; Li, L.; Naito, Y. Definitions of Terms Relating to Mass Spectrometry (IUPAC Recommendations 2013). *Pure Appl. Chem.* **2013**, *85* (7), 1515–1609. <https://doi.org/10.1351/Pac-Rec-06-04-06>.
- (55) Root, K.; Wittwer, Y.; Barylyuk, K.; Anders, U.; Zenobi, R. Insight into Signal Response of Protein Ions in Native ESI-MS from the Analysis of Model Mixtures of Covalently Linked Protein Oligomers. *J. Am. Soc. Mass Spectrom.* **2017**, *28* (9), 1863–1875. <https://doi.org/10.1007/s13361-017-1690-3>.
- (56) Rose, R. J.; Labrijn, A. F.; van den Bremer, E. T.; Loverix, S.; Lasters, I.; van Berkel, P. H.; van de Winkel, J. G.; Schuurman, J.; Parren, P. W.; Heck, A. J. Quantitative Analysis of the Interaction Strength and Dynamics of Human IgG4 Half Molecules by Native Mass Spectrometry. *Structure* **2011**, *19* (9), 1274–1282. <https://doi.org/10.1016/j.str.2011.06.016>.
- (57) Paul, W. Electromagnetic Traps for Charged and Neutral Particles (Nobel Lecture). *Angew. Chem. Int. Ed. Engl.* **1990**, *29* (7), 739–748. <https://doi.org/10.1002/anie.199007391>.
- (58) Chernushevich, I. V.; Loboda, A. V.; Thomson, B. A. An Introduction to Quadrupole-Time-of-Flight Mass Spectrometry. *J. Mass Spectrom.* **2001**, *36* (8), 849–865. <https://doi.org/10.1002/jms.207>.
- (59) Boesl, U. Time-of-Flight Mass Spectrometry: Introduction to the Basics: TIME-OF-FLIGHT MASS SPECTROMETRY. *Mass Spectrom. Rev.* **2017**, *36* (1), 86–109. <https://doi.org/10.1002/mas.21520>.
- (60) Makarov, A. Electrostatic Axially Harmonic Orbital Trapping: A High-Performance Technique of Mass Analysis. *Anal. Chem.* **2000**, *72* (6), 1156–1162. <https://doi.org/10.1021/ac991131p>.
- (61) Hu, Q.; Noll, R. J.; Li, H.; Makarov, A.; Hardman, M.; Graham Cooks, R. The Orbitrap: A New Mass Spectrometer. *J. Mass Spectrom.* **2005**, *40* (4), 430–443. <https://doi.org/10.1002/jms.856>.
- (62) Zubarev, R. A.; Makarov, A. Orbitrap Mass Spectrometry. *Anal. Chem.* **2013**, *85* (11), 5288–5296. <https://doi.org/10.1021/ac4001223>.
- (63) Tamara, S.; den Boer, M. A.; Heck, A. J. R. High-Resolution Native Mass Spectrometry. *Chem. Rev.* **2022**, *122* (8), 7269–7326. <https://doi.org/10.1021/acs.chemrev.1c00212>.

- (64) Nolting, D.; Malek, R.; Makarov, A. Ion Traps in Modern Mass Spectrometry. *Mass Spectrom. Rev.* **2019**, *38* (2), 150–168. <https://doi.org/10.1002/mas.21549>.
- (65) Dienes, T.; Pastor, S. J.; Schürch, S.; Scott, J. R.; Yao, J.; Cui, S.; Wilkins, C. L. Fourier Transform Mass Spectrometry-Advancing Years (1992-Mid. 1996). *Mass Spectrom. Rev.* **1996**, *15* (3), 163–211. [https://doi.org/10.1002/\(SICI\)1098-2787\(1996\)15:3<163::AID-MAS2>3.0.CO;2-G](https://doi.org/10.1002/(SICI)1098-2787(1996)15:3<163::AID-MAS2>3.0.CO;2-G).
- (66) Scigelova, M.; Hornshaw, M.; Giannakopoulos, A.; Makarov, A. Fourier Transform Mass Spectrometry. *Mol. Cell. Proteomics* **2011**, *10* (7), M111.009431. <https://doi.org/10.1074/mcp.M111.009431>.
- (67) Rose, R. J.; Damoc, E.; Denisov, E.; Makarov, A.; Heck, A. J. R. High-Sensitivity Orbitrap Mass Analysis of Intact Macromolecular Assemblies. *Nat. Methods* **2012**, *9* (11), 1084–1086. <https://doi.org/10.1038/nmeth.2208>.
- (68) van de Waterbeemd, M.; Fort, K. L.; Boll, D.; Reinhardt-Szyba, M.; Routh, A.; Makarov, A.; Heck, A. J. High-Fidelity Mass Analysis Unveils Heterogeneity in Intact Ribosomal Particles. *Nat. Methods* **2017**, *14* (3), 283–286. <https://doi.org/10.1038/nmeth.4147>.
- (69) Fort, K. L.; van de Waterbeemd, M.; Boll, D.; Reinhardt-Szyba, M.; Belov, M. E.; Sasaki, E.; Zschoche, R.; Hilvert, D.; Makarov, A. A.; Heck, A. J. R. Expanding the Structural Analysis Capabilities on an Orbitrap-Based Mass Spectrometer for Large Macromolecular Complexes. *The Analyst* **2018**, *143* (1), 100–105. <https://doi.org/10.1039/C7AN01629H>.
- (70) Wörner, T. P.; Snijder, J.; Bennett, A.; Agbandje-McKenna, M.; Makarov, A. A.; Heck, A. J. R. Resolving Heterogeneous Macromolecular Assemblies by Orbitrap-Based Single-Particle Charge Detection Mass Spectrometry. *Nat. Methods* **2020**, *17* (4), 395–398. <https://doi.org/10.1038/s41592-020-0770-7>.
- (71) Wörner, T. P.; Aizikov, K.; Snijder, J.; Fort, K. L.; Makarov, A. A.; Heck, A. J. R. Frequency Chasing of Individual Megadalton Ions in an Orbitrap Analyser Improves Precision of Analysis in Single-Molecule Mass Spectrometry. *Nat. Chem.* **2022**, *14* (5), 515–522. <https://doi.org/10.1038/s41557-022-00897-1>.
- (72) Chowdhury, S. K.; Katta, V.; Chait, B. T. Probing Conformational Changes in Proteins by Mass Spectrometry. *J. Am. Chem. Soc.* **1990**, *112* (24), 9012–9013. <https://doi.org/10.1021/ja00180a074>.
- (73) Fernandez de la Mora, J. Electrospray Ionization of Large Multiply Charged Species Proceeds via Dole's Charged Residue Mechanism. *Anal. Chim. Acta* **2000**, *406* (1), 93–104. [https://doi.org/10.1016/S0003-2670\(99\)00601-7](https://doi.org/10.1016/S0003-2670(99)00601-7).
- (74) Kaltashov, I. A.; Mohimen, A. Estimates of Protein Surface Areas in Solution by Electrospray Ionization Mass Spectrometry. *Anal. Chem.* **2005**, *77* (16), 5370–5379. <https://doi.org/10.1021/ac050511+>.
- (75) Shelimov, K. B.; Clemmer, D. E.; Hudgins, R. R.; Jarrold, M. F. Protein Structure *in Vacuo*: Gas-Phase Conformations of BPTI and Cytochrome c. *J. Am. Chem. Soc.* **1997**, *119* (9), 2240–2248. <https://doi.org/10.1021/ja9619059>.
- (76) Wyttenbach, T.; Bowers, M. T. Structural Stability from Solution to the Gas Phase: Native Solution Structure of Ubiquitin Survives Analysis in a Solvent-Free Ion Mobility–Mass Spectrometry Environment. *J. Phys. Chem. B* **2011**, *115* (42), 12266–12275. <https://doi.org/10.1021/jp206867a>.
- (77) Segev, E.; Wyttenbach, T.; Bowers, M. T.; Gerber, R. B. Conformational Evolution of Ubiquitin Ions in Electrospray Mass Spectrometry: Molecular Dynamics Simulations at Gradually Increasing Temperatures. *Phys. Chem. Chem. Phys.* **2008**, *10* (21), 3077. <https://doi.org/10.1039/b718610j>.
- (78) González Flórez, A. I.; Mucha, E.; Ahn, D.-S.; Gewinner, S.; Schöllkopf, W.; Pagel, K.; von Helden, G. Charge-Induced Unzipping of Isolated Proteins to a Defined Secondary Structure. *Angew. Chem. Int. Ed.* **2016**, *55* (10), 3295–3299. <https://doi.org/10.1002/anie.201510983>.
- (79) Zhou, M.; Lantz, C.; Brown, K. A.; Ge, Y.; Paša-Tolić, L.; Loo, J. A.; Lermyte, F. Higher-Order Structural Characterisation of Native Proteins and Complexes by Top-down Mass Spectrometry. *Chem. Sci.* **2020**, *11* (48), 12918–12936. <https://doi.org/10.1039/D0SC04392C>.
- (80) Silveira, J. A.; Fort, K. L.; Kim, D.; Servage, K. A.; Pierson, N. A.; Clemmer, D. E.; Russell, D. H. From Solution to the Gas Phase: Stepwise Dehydration and Kinetic Trapping of Substance P Reveals the Origin of Peptide Conformations. *J. Am. Chem. Soc.* **2013**, *135* (51), 19147–19153. <https://doi.org/10.1021/ja4114193>.
- (81) Clemmer, D. E.; Russell, D. H.; Williams, E. R. Characterizing the *Conformationome*: Toward a Structural Understanding of the Proteome. *Acc. Chem. Res.* **2017**, *50* (3), 556–560. <https://doi.org/10.1021/acs.accounts.6b00548>.
- (82) Scarff, C. A.; Thalassinos, K.; Hilton, G. R.; Scrivens, J. H. Travelling Wave Ion Mobility Mass Spectrometry Studies of Protein Structure: Biological Significance and Comparison with X-Ray Crystallography and Nuclear Magnetic Resonance Spectroscopy Measurements. *Rapid Commun. Mass Spectrom.* **2008**, *22* (20), 3297–3304. <https://doi.org/10.1002/rcm.3737>.
- (83) Lanucara, F.; Holman, S. W.; Gray, C. J.; Evers, C. E. The Power of Ion Mobility-Mass Spectrometry for Structural Characterization and the Study of Conformational Dynamics. *Nat. Chem.* **2014**, *6* (4), 281–294. <https://doi.org/10.1038/Nchem.1889>.
- (84) Jurneczko, E.; Barran, P. E. How Useful Is Ion Mobility Mass Spectrometry for Structural Biology? The Relationship between Protein Crystal Structures and Their Collision Cross Sections in the Gas Phase. *The Analyst* **2011**, *136* (1), 20–28. <https://doi.org/10.1039/C0AN00373E>.
- (85) Iavarone, A. T.; Parks, J. H. Conformational Change in Unsolvated Trp-Cage Protein Probed by Fluorescence. *J. Am. Chem. Soc.* **2005**, *127* (24), 8606–8607. <https://doi.org/10.1021/ja051788u>.

- (86) Oomens, J.; Polfer, N.; Moore, D. T.; van der Meer, L.; Marshall, A. G.; Eyler, J. R.; Meijer, G.; von Helden, G. Charge-State Resolved Mid-Infrared Spectroscopy of a Gas-Phase Protein. *Phys. Chem. Chem. Phys.* **2005**, *7* (7), 1345. <https://doi.org/10.1039/b502322j>.
- (87) Oomens, J.; Sartakov, B. G.; Meijer, G.; von Helden, G. Gas-Phase Infrared Multiple Photon Dissociation Spectroscopy of Mass-Selected Molecular Ions. *Int. J. Mass Spectrom.* **2006**, *254* (1–2), 1–19. <https://doi.org/10.1016/j.ijms.2006.05.009>.
- (88) Polfer, N. C.; Oomens, J. Vibrational Spectroscopy of Bare and Solvated Ionic Complexes of Biological Relevance. *Mass Spectrom. Rev.* **2009**, *28* (3), 468–494. <https://doi.org/10.1002/mas.20215>.
- (89) Polfer, N. C. Infrared Multiple Photon Dissociation Spectroscopy of Trapped Ions. *Chem. Soc. Rev.* **2011**, *40* (5), 2211. <https://doi.org/10.1039/c0cs00171f>.
- (90) Mikhailov, V. A.; Mize, T. H.; Benesch, J. L. P.; Robinson, C. V. Mass-Selective Soft-Landing of Protein Assemblies with Controlled Landing Energies. *Anal. Chem.* **2014**, *86* (16), 8321–8328. <https://doi.org/10.1021/ac5018327>.
- (91) Longchamp, J.-N.; Rauschenbach, S.; Abb, S.; Escher, C.; Latychevskaia, T.; Kern, K.; Fink, H.-W. Imaging Proteins at the Single-Molecule Level. *Proc. Natl. Acad. Sci.* **2017**, *114* (7), 1474–1479. <https://doi.org/10.1073/pnas.1614519114>.
- (92) Hogan, C. J.; Ruotolo, B. T.; Robinson, C. V.; Fernandez de la Mora, J. Tandem Differential Mobility Analysis-Mass Spectrometry Reveals Partial Gas-Phase Collapse of the GroEL Complex. *J. Phys. Chem. B* **2011**, *115* (13), 3614–3621. <https://doi.org/10.1021/jp109172k>.
- (93) Breuker, K.; McLafferty, F. W. Stepwise Evolution of Protein Native Structure with Electrospray into the Gas Phase, 10^{-12} to 10^2 s. *Proc. Natl. Acad. Sci.* **2008**, *105* (47), 18145–18152. <https://doi.org/10.1073/pnas.0807005105>.
- (94) Shi, L.; Holliday, A. E.; Shi, H.; Zhu, F.; Ewing, M. A.; Russell, D. H.; Clemmer, D. E. Characterizing Intermediates Along the Transition from Polyproline I to Polyproline II Using Ion Mobility Spectrometry-Mass Spectrometry. *J. Am. Chem. Soc.* **2014**, *136* (36), 12702–12711. <https://doi.org/10.1021/ja505899g>.
- (95) Breuker, K.; Oh, H.; Horn, D. M.; Cerda, B. A.; McLafferty, F. W. Detailed Unfolding and Folding of Gaseous Ubiquitin Ions Characterized by Electron Capture Dissociation. *J. Am. Chem. Soc.* **2002**, *124* (22), 6407–6420. <https://doi.org/10.1021/ja012267j>.
- (96) Gavrilidou, A. F. M.; Sokratous, K.; Yen, H.-Y.; De Colibus, L. High-Throughput Native Mass Spectrometry Screening in Drug Discovery. *Front. Mol. Biosci.* **2022**, *9*, 837901. <https://doi.org/10.3389/fmolb.2022.837901>.
- (97) Fiorentino, F.; Rotili, D.; Mai, A. Native Mass Spectrometry-Directed Drug Discovery: Recent Advances in Investigating Protein Function and Modulation. *Drug Discov. Today* **2023**, *28* (5), 103548. <https://doi.org/10.1016/j.drudis.2023.103548>.
- (98) Kitova, E. N.; El-Hawiet, A.; Schnier, P. D.; Klassen, J. S. Reliable Determinations of Protein–Ligand Interactions by Direct ESI-MS Measurements. Are We There Yet? *J. Am. Soc. Mass Spectrom.* **2012**, *23* (3), 431–441. <https://doi.org/10.1007/s13361-011-0311-9>.
- (99) Allison, T. M.; Bechara, C. Structural Mass Spectrometry Comes of Age: New Insight into Protein Structure, Function and Interactions. *Biochem. Soc. Trans.* **2019**, *47* (1), 317–327. <https://doi.org/10.1042/BST20180356>.
- (100) Schulte, J.; Tants, J.-N.; von Ehr, J.; Schlundt, A.; Morgner, N. Determination of Dissociation Constants via Quantitative Mass Spectrometry. *Front. Anal. Sci.* **2023**, *3*. <https://doi.org/10.3389/frans.2023.1119489>.
- (101) Bennett, J. L.; Nguyen, G. T. H.; Donald, W. A. Protein–Small Molecule Interactions in Native Mass Spectrometry. *Chem. Rev.* **2022**, *122* (8), 7327–7385. <https://doi.org/10.1021/acs.chemrev.1c00293>.
- (102) Wang, W.; Kitova, E. N.; Klassen, J. S. Nonspecific Protein–Carbohydrate Complexes Produced by Nanoelectrospray Ionization. Factors Influencing Their Formation and Stability. *Anal. Chem.* **2005**, *77* (10), 3060–3071. <https://doi.org/10.1021/ac048433y>.
- (103) Daubenfeld, T.; Bouin, A. P.; van der Rest, G. A Deconvolution Method for the Separation of Specific versus Nonspecific Interactions in Noncovalent Protein–Ligand Complexes Analyzed by ESI-FT-ICR Mass Spectrometry. *J. Am. Soc. Mass Spectrom.* **2006**, *17* (9), 1239–1248. <https://doi.org/10.1016/j.jasms.2006.05.005>.
- (104) Sun, J.; Kitova, E. N.; Wang, W.; Klassen, J. S. Method for Distinguishing Specific from Nonspecific Protein–Ligand Complexes in Nanoelectrospray Ionization Mass Spectrometry. *Anal. Chem.* **2006**, *78* (9), 3010–3018. <https://doi.org/10.1021/ac0522005>.
- (105) Ozdemir, A.; Gulfen, M.; Lin, J.-L.; Chen, C.-H. A Comparative Study for Sonic Spray and Electrospray Ionization Methods to Determine Noncovalent Protein–Ligand Interactions. *Anal. Lett.* **2019**, *52* (16), 2620–2633. <https://doi.org/10.1080/00032719.2019.1622558>.
- (106) Lim, H.-K.; Hsieh, Y. L.; Ganem, B.; Henion, J. Recognition of Cell-Wall Peptide Ligands by Vancomycin Group Antibiotics: Studies Using Ion Spray Mass Spectrometry. *J. Mass Spectrom.* **1995**, *30* (5), 708–714. <https://doi.org/10.1002/jms.1190300509>.
- (107) Jecklin, M. C.; Schauer, S.; Dumelin, C. E.; Zenobi, R. Label-Free Determination of Protein–Ligand Binding Constants Using Mass Spectrometry and Validation Using Surface Plasmon Resonance and Isothermal Titration Calorimetry. *J. Mol. Recognit.* **2009**, *22* (4), 319–329. <https://doi.org/10.1002/jmr.951>.
- (108) Gabelica, V.; Galic, N.; Rosu, F.; Houssier, C.; De Pauw, E. Influence of Response Factors on Determining Equilibrium Association Constants of Non-Covalent Complexes by Electrospray Ionization Mass Spectrometry. *J. Mass Spectrom.* **2003**, *38* (5), 491–501. <https://doi.org/10.1002/jms.459>.

- (109) Fryčák, P.; Schug, K. A. On-Line Dynamic Titration: Determination of Dissociation Constants for Noncovalent Complexes Using Gaussian Concentration Profiles by Electrospray Ionization Mass Spectrometry. *Anal. Chem.* **2007**, *79* (14), 5407–5413. <https://doi.org/10.1021/ac070519e>.
- (110) Neu, V.; Steiner, R.; Müller, S.; Fattinger, C.; Zenobi, R. Development and Characterization of a Capillary Gap Sampler as New Microfluidic Device for Fast and Direct Analysis of Low Sample Amounts by ESI-MS. *Anal. Chem.* **2013**, *85* (9), 4628–4635. <https://doi.org/10.1021/ac400186t>.
- (111) Przybylski, C.; Benito, J. M.; Bonnet, V.; Mellet, C. O.; García Fernández, J. M. Revealing Cooperative Binding of Polycationic Cyclodextrins with DNA Oligomers by Capillary Electrophoresis Coupled to Mass Spectrometry. *Anal. Chim. Acta* **2018**, *1002*, 70–81. <https://doi.org/10.1016/j.aca.2017.11.034>.
- (112) Báez Bolívar, E. G.; Bui, D. T.; Kitova, E. N.; Han, L.; Zheng, R. B.; Lubner, E. J.; Sayed, S. Y.; Mahal, L. K.; Klassen, J. S. Submicron Emitters Enable Reliable Quantification of Weak Protein–Glycan Interactions by ESI-MS. *Anal. Chem.* **2021**, *93* (9), 4231–4239. <https://doi.org/10.1021/acs.analchem.0c05003>.
- (113) Kaeslin, J.; Brunner, C.; Ghiasikhou, S.; Schneider, G.; Zenobi, R. Bioaffinity Screening with a Rapid and Sample-Efficient Autosampler for Native Electrospray Ionization Mass Spectrometry. *Anal. Chem.* **2021**, *93* (39), 13342–13350. <https://doi.org/10.1021/acs.analchem.1c03130>.
- (114) Bui, D. T.; Li, Z.; Kitov, P. I.; Han, L.; Kitova, E. N.; Fortier, M.; Fuselier, C.; Granger Joly de Boissel, P.; Chatenet, D.; Doucet, N.; Tompkins, S. M.; St-Pierre, Y.; Mahal, L. K.; Klassen, J. S. Quantifying Biomolecular Interactions Using Slow Mixing Mode (SLOMO) Nanoflow ESI-MS. *ACS Cent. Sci.* **2022**, *8* (7), 963–974. <https://doi.org/10.1021/acscentsci.2c00215>.
- (115) Jørgensen, T. J. D.; Roepstorff, P.; Heck, A. J. R. Direct Determination of Solution Binding Constants for Noncovalent Complexes between Bacterial Cell Wall Peptide Analogues and Vancomycin Group Antibiotics by Electrospray Ionization Mass Spectrometry. *Anal. Chem.* **1998**, *70* (20), 4427–4432. <https://doi.org/10.1021/ac980563h>.
- (116) Kempen, E. C.; Brodbelt, J. S. A Method for the Determination of Binding Constants by Electrospray Ionization Mass Spectrometry. *Anal. Chem.* **2000**, *72* (21), 5411–5416. <https://doi.org/10.1021/ac000540e>.
- (117) Annis, D. A.; Nazef, N.; Chuang, C.-C.; Scott, M. P.; Nash, H. M. A General Technique To Rank Protein–Ligand Binding Affinities and Determine Allosteric versus Direct Binding Site Competition in Compound Mixtures. *J. Am. Chem. Soc.* **2004**, *126* (47), 15495–15503. <https://doi.org/10.1021/ja048365x>.
- (118) Wortmann, A.; Jecklin, M. C.; Touboul, D.; Badertscher, M.; Zenobi, R. Binding Constant Determination of High-Affinity Protein–Ligand Complexes by Electrospray Ionization Mass Spectrometry and Ligand Competition. *J. Mass Spectrom.* **2008**, *43* (5), 600–608. <https://doi.org/10.1002/jms.1355>.
- (119) El-Hawiet, A.; Kitova, E. N.; Liu, L.; Klassen, J. S. Quantifying Labile Protein–Ligand Interactions Using Electrospray Ionization Mass Spectrometry. *J. Am. Soc. Mass Spectrom.* **2010**, *21* (11), 1893–1899. <https://doi.org/10.1016/j.jasms.2010.07.008>.
- (120) Kitov, P. I.; Kitova, E. N.; Han, L.; Li, Z.; Jung, J.; Rodrigues, E.; Hunter, C. D.; Cairo, C. W.; Macauley, M. S.; Klassen, J. S. A Quantitative, High-Throughput Method Identifies Protein–Glycan Interactions via Mass Spectrometry. *Commun. Biol.* **2019**, *2* (1), 268. <https://doi.org/10.1038/s42003-019-0507-2>.
- (121) Illes-Toth, E.; Stubbs, C. J.; Siskey, E. K.; Bellamy-Carter, J.; Simmonds, A. L.; Mize, T. H.; Styles, I. B.; Goodwin, R. J. A.; Cooper, H. J. Quantitative Characterization of Three Carbonic Anhydrase Inhibitors by LESA Mass Spectrometry. *J. Am. Soc. Mass Spectrom.* **2022**, *33* (7), 1168–1175. <https://doi.org/10.1021/jasms.2c00024>.
- (122) Garcia-Alai, M. M.; Heidemann, J.; Skruzny, M.; Gieras, A.; Mertens, H. D. T.; Svergun, D. I.; Kaksonen, M.; Uetrecht, C.; Meijers, R. Epsin and Sla2 Form Assemblies through Phospholipid Interfaces. *Nat Commun* **2018**, *9* (1), 328. <https://doi.org/10.1038/s41467-017-02443-x>.
- (123) Yefremova, Y.; Melder, F. T. I.; Danquah, B. D.; Opuni, K. F. M.; Koy, C.; Ehrens, A.; Frommholz, D.; Illges, H.; Koelbel, K.; Sobott, F.; Glocker, M. O. Apparent Activation Energies of Protein–Protein Complex Dissociation in the Gas-Phase Determined by Electrospray Mass Spectrometry. *Anal. Bioanal. Chem.* **2017**, *409* (28), 6549–6558. <https://doi.org/10.1007/s00216-017-0603-4>.
- (124) Douangamath, A.; Fearon, D.; Gehrtz, P.; Krojer, T.; Lukacik, P.; Owen, C. D.; Resnick, E.; Strain-Damerell, C.; Aimon, A.; Ábrányi-Balogh, P.; Brandão-Neto, J.; Carbery, A.; Davison, G.; Dias, A.; Downes, T. D.; Dunnett, L.; Fairhead, M.; Firth, J. D.; Jones, S. P.; Keeley, A.; Keserü, G. M.; Klein, H. F.; Martin, M. P.; Noble, M. E. M.; O'Brien, P.; Powell, A.; Reddi, R. N.; Skyner, R.; Snee, M.; Waring, M. J.; Wild, C.; London, N.; von Delft, F.; Walsh, M. A. Crystallographic and Electrophilic Fragment Screening of the SARS-CoV-2 Main Protease. *Nat. Commun.* **2020**, *11* (1), 5047. <https://doi.org/10.1038/s41467-020-18709-w>.
- (125) Webb, I. K. Recent Technological Developments for Native Mass Spectrometry. *Biochim. Biophys. Acta Proteins Proteomics* **2022**, *1870* (1), 140732. <https://doi.org/10.1016/j.bbapap.2021.140732>.
- (126) Lorenzen, K.; Versluis, C.; van Duijn, E.; van den Heuvel, R. H. H.; Heck, A. J. R. Optimizing Macromolecular Tandem Mass Spectrometry of Large Non-Covalent Complexes Using Heavy Collision Gases. *Int. J. Mass Spectrom.* **2007**, *268* (2–3), 198–206. <https://doi.org/10.1016/j.ijms.2007.06.012>.
- (127) Erba, E. B.; Petosa, C. The Emerging Role of Native Mass Spectrometry in Characterizing the Structure and Dynamics of Macromolecular Complexes. *Protein Sci.* **2015**, *24* (8), 1176–1192. <https://doi.org/10.1002/pro.2661>.
- (128) Brodbelt, J. S. Photodissociation Mass Spectrometry: New Tools for Characterization of Biological Molecules. *Chem Soc Rev* **2014**, *43* (8), 2757–2783. <https://doi.org/10.1039/C3CS60444F>.

- (129) Stiving, A. Q.; VanAernum, Z. L.; Busch, F.; Harvey, S. R.; Sarni, S. H.; Wysocki, V. H. Surface-Induced Dissociation: An Effective Method for Characterization of Protein Quaternary Structure. *Anal. Chem.* **2019**, *91* (1), 190–209. <https://doi.org/10.1021/acs.analchem.8b05071>.
- (130) Lermyte, F.; Valkenburg, D.; Loo, J. A.; Sobott, F. Radical Solutions: Principles and Application of Electron-based Dissociation in Mass Spectrometry-based Analysis of Protein Structure. *Mass Spectrom. Rev.* **2018**, *37* (6), 750–771. <https://doi.org/10.1002/mas.21560>.
- (131) Konijnenberg, A.; Bannwarth, L.; Yilmaz, D.; Kocer, A.; Venien-Bryan, C.; Sobott, F. Top-down Mass Spectrometry of Intact Membrane Protein Complexes Reveals Oligomeric State and Sequence Information in a Single Experiment. *Protein Sci.* **2015**, *24* (8), 1292–1300. <https://doi.org/10.1002/pro.2703>.
- (132) Cruz, E.; Cain, J.; Crossett, B.; Kayser, V. Site-Specific Glycosylation Profile of Influenza A (H1N1) Hemagglutinin through Tandem Mass Spectrometry. *Hum. Vaccines Immunother.* **2018**, *14* (3), 508–517. <https://doi.org/10.1080/21645515.2017.1377871>.
- (133) Hull, P. Notes on DR Snell's Observations Concerning the H-2 Locus Polymorphism. *Heredity* **1970**, *25* (3), 461–465. <https://doi.org/10.1038/hdy.1970.47>.
- (134) The MHC sequencing consortium. Complete Sequence and Gene Map of a Human Major Histocompatibility Complex. *Nature* **1999**, *401* (6756), 921–923. <https://doi.org/10.1038/44853>.
- (135) Younger, R. M.; Amadou, C.; Bethel, G.; Ehlers, A.; Lindahl, K. F.; Forbes, S.; Horton, R.; Milne, S.; Mungall, A. J.; Trowsdale, J.; Volz, A.; Ziegler, A.; Beck, S. Characterization of Clustered MHC-Linked Olfactory Receptor Genes in Human and Mouse. *Genome Res.* **2001**, *11* (4), 519–530. <https://doi.org/10.1101/gr.160301>.
- (136) Günther, E.; Walter, L. The Major Histocompatibility Complex of the Rat (*Rattus Norvegicus*). *Immunogenetics* **2001**, *53* (7), 520–542. <https://doi.org/10.1007/s002510100361>.
- (137) Hurt, P.; Walter, L.; Sudbrak, R.; Klages, S.; Müller, I.; Shiina, T.; Inoko, H.; Lehrach, H.; Günther, E.; Reinhardt, R.; Himmelbauer, H. The Genomic Sequence and Comparative Analysis of the Rat Major Histocompatibility Complex. *Genome Res.* **2004**, *14* (4), 631–639. <https://doi.org/10.1101/gr.1987704>.
- (138) Kaufman, J.; Milne, S.; Göbel, T. W. F.; Walker, B. A.; Jacob, J. P.; Auffray, C.; Zoorob, R.; Beck, S. The Chicken B Locus Is a Minimal Essential Major Histocompatibility Complex. *Nature* **1999**, *401* (6756), 923–925. <https://doi.org/10.1038/44856>.
- (139) Wieczorek, M.; Abualrous, E. T.; Sticht, J.; Alvaro-Benito, M.; Stolzenberg, S.; Noe, F.; Freund, C. Major Histocompatibility Complex (MHC) Class I and MHC Class II Proteins: Conformational Plasticity in Antigen Presentation. *Front Immunol* **2017**, *8*, 292. <https://doi.org/10.3389/fimmu.2017.00292>.
- (140) Bouvier, M.; Wiley, D. C. Importance of Peptide Amino and Carboxyl Termini to the Stability of MHC Class I Molecules. *Science* **1994**, *265* (5170), 398–402. <https://doi.org/10.1126/science.8023162>.
- (141) Effenberger, M.; Stengl, A.; Schober, K.; Gerget, M.; Kampick, M.; Müller, T. R.; Schumacher, D.; Helma, J.; Leonhardt, H.; Busch, D. H. FLEXamers: A Double Tag for Universal Generation of Versatile Peptide-MHC Multimers. *J Immunol* **2019**, *202* (7), 2164–2171. <https://doi.org/10.4049/jimmunol.1801435>.
- (142) Colten, H. R. Expression of the MHC Class III Genes. *Philos. Trans. R. Soc. Lond. B. Biol. Sci.* **1984**, *306* (1129), 355–366. <https://doi.org/10.1098/rstb.1984.0096>.
- (143) Gruen, J.; Weissman, S. Human MHC Class III and IV Genes and Disease Associations. *Front. Biosci. J. Virtual Libr.* **2001**, *6*, D960–72. <https://doi.org/10.2741/gruen>.
- (144) Xie, T. Analysis of the Gene-Dense Major Histocompatibility Complex Class III Region and Its Comparison to Mouse. *Genome Res.* **2003**, *13* (12), 2621–2636. <https://doi.org/10.1101/gr.1736803>.
- (145) Schott, G.; Garcia-Blanco, M. A. MHC Class III RNA Binding Proteins and Immunity. *RNA Biol.* **2021**, *18* (5), 640–646. <https://doi.org/10.1080/15476286.2020.1860388>.
- (146) Townsend, A.; Bodmer, H. Antigen Recognition by Class I-Restricted T Lymphocytes. *Annu. Rev. Immunol.* **1989**, *7*, 601–624. <https://doi.org/10.1146/annurev.iy.07.040189.003125>.
- (147) Comber, J. D.; Philip, R. MHC Class I Antigen Presentation and Implications for Developing a New Generation of Therapeutic Vaccines. *Ther. Adv. Vaccines* **2014**, *2* (3), 77–89. <https://doi.org/10.1177/2051013614525375>.
- (148) Kaufman, J. Generalists and Specialists: A New View of How MHC Class I Molecules Fight Infectious Pathogens. *Trends Immunol.* **2018**, *39* (5), 367–379. <https://doi.org/10.1016/j.it.2018.01.001>.
- (149) Townsend, A.; Öhlén, C.; Bastin, J.; Ljunggren, H.-G.; Foster, L.; Kärre, K. Association of Class I Major Histocompatibility Heavy and Light Chains Induced by Viral Peptides. *Nature* **1989**, *340* (6233), 443–448. <https://doi.org/10.1038/340443a0>.
- (150) Ljunggren, H.-G.; Stam, N. J.; Öhlén, C.; Neefjes, J. J.; Höglund, P.; Heemels, M.-T.; Bastin, J.; Schumacher, T. N. M.; Townsend, A.; Kärre, K.; Ploegh, H. L. Empty MHC Class I Molecules Come out in the Cold. *Nature* **1990**, *346* (6283), 476–480. <https://doi.org/10.1038/346476a0>.
- (151) Montealegre, S.; Venugopalan, V.; Fritzsche, S.; Kulicke, C.; Hein, Z.; Springer, S. Dissociation of β_2 -microglobulin Determines the Surface Quality Control of Major Histocompatibility Complex Class I Molecules. *FASEB J.* **2015**, *29* (7), 2780–2788. <https://doi.org/10.1096/fj.14-268094>.
- (152) Edidin, M.; Achilles, S.; Zeff, R.; Wei, T. Probing the Stability of Class I Major Histocompatibility Complex (MHC) Molecules on the Surface of Human Cells. *Immunogenetics* **1997**, *46* (1), 41–45. <https://doi.org/10.1007/s002510050240>.

- (153) Geng, J.; Altman, J. D.; Krishnakumar, S.; Raghavan, M. Empty Conformers of HLA-B Preferentially Bind CD8 and Regulate CD8+ T Cell Function. *eLife* **2018**, *7*, e36341. <https://doi.org/10.7554/eLife.36341>.
- (154) Elliott, T.; Cerundolo, V.; Elvin, J.; Townsend, A. Peptide-Induced Conformational Change of the Class I Heavy Chain. *Nature* **1991**, *351* (6325), 402–406. <https://doi.org/10.1038/351402a0>.
- (155) Gakamsky, D. M.; Bjorkman, P. J.; Pecht, I. Peptide Interaction with a Class I Major Histocompatibility Complex-Encoded Molecule: Allosteric Control of the Ternary Complex Stability. *Biochemistry* **1996**, *35* (47), 14841–14848. <https://doi.org/10.1021/bi961707u>.
- (156) Arosa, F. A.; Santos, S. G.; Powis, S. J. Open Conformers: The Hidden Face of MHC-I Molecules. *Trends Immunol.* **2007**, *28* (3), 115–123. <https://doi.org/10.1016/j.it.2007.01.002>.
- (157) Campbell, E. C.; Antoniou, A. N.; Powis, S. J. The Multi-Faceted Nature of HLA Class I Dimer Molecules: HLA Class I Dimers. *Immunology* **2012**, *136* (4), 380–384. <https://doi.org/10.1111/j.1365-2567.2012.03593.x>.
- (158) Arosa, F. A.; Esgalhado, A. J.; Reste-Ferreira, D.; Cardoso, E. M. Open MHC Class I Conformers: A Look through the Looking Glass. *Int. J. Mol. Sci.* **2021**, *22* (18), 9738. <https://doi.org/10.3390/ijms22189738>.
- (159) Chakrabarti, A.; Matko, J.; Rahman, N. A.; Barisas, B. G.; Edidin, M. Self-Association of Class I Major Histocompatibility Complex Molecules in Liposome and Cell Surface Membranes. *Biochemistry* **1992**, *31* (31), 7182–7189. <https://doi.org/10.1021/bi00146a022>.
- (160) Capps, G. G.; Robinson, B. E.; Lewis, K. D.; Zúñiga, M. C. In Vivo Dimeric Association of Class I MHC Heavy Chains. Possible Relationship to Class I MHC Heavy Chain-Beta 2-Microglobulin Dissociation. *J. Immunol. Baltim. Md 1950* **1993**, *151* (1), 159–169.
- (161) Matko, J.; Bushkin, Y.; Wei, T.; Edidin, M. Clustering of Class I HLA Molecules on the Surfaces of Activated and Transformed Human Cells. *J. Immunol. Baltim. Md 1950* **1994**, *152* (7), 3353–3360.
- (162) Allen, R. L.; O'Callaghan, C. A.; McMichael, A. J.; Bowness, P. Cutting Edge: HLA-B27 Can Form a Novel Beta 2-Microglobulin-Free Heavy Chain Homodimer Structure. *J. Immunol. Baltim. Md 1950* **1999**, *162* (9), 5045–5048.
- (163) Triantafilou, K.; Triantafilou, M.; Wilson, K. M.; Fernandez, N. Human Major Histocompatibility Molecules Have the Intrinsic Ability to Form Homotypic Associations. *Hum. Immunol.* **2000**, *61* (6), 585–598. [https://doi.org/10.1016/S0198-8859\(00\)00112-9](https://doi.org/10.1016/S0198-8859(00)00112-9).
- (164) Fassett, M. S.; Davis, D. M.; Valter, M. M.; Cohen, G. B.; Strominger, J. L. Signaling at the Inhibitory Natural Killer Cell Immune Synapse Regulates Lipid Raft Polarization but Not Class I MHC Clustering. *Proc. Natl. Acad. Sci.* **2001**, *98* (25), 14547–14552. <https://doi.org/10.1073/pnas.211563598>.
- (165) Bodnar, A. Class I HLA Oligomerization at the Surface of B Cells Is Controlled by Exogenous Beta2-Microglobulin: Implications in Activation of Cytotoxic T Lymphocytes. *Int. Immunol.* **2003**, *15* (3), 331–339. <https://doi.org/10.1093/intimm/dxg042>.
- (166) Antoniou, A. N.; Guiliano, D. B.; Lenart, I.; Burn, G.; Powis, S. J. The Oxidative Folding and Misfolding of Human Leukocyte Antigen-B27. *Antioxid. Redox Signal.* **2011**, *15* (3), 669–684. <https://doi.org/10.1089/ars.2010.3692>.
- (167) Makhadiyeva, D.; Lam, L.; Moatari, M.; Vallance, J.; Zheng, Y.; Campbell, E. C.; Powis, S. J. MHC Class I Dimer Formation by Alteration of the Cellular Redox Environment and Induction of Apoptosis. *Immunology* **2012**, *135* (2), 133–139. <https://doi.org/10.1111/j.1365-2567.2011.03518.x>.
- (168) Lu, X.; Gibbs, J. S.; Hickman, H. D.; David, A.; Dolan, B. P.; Jin, Y.; Kranz, D. M.; Bennink, J. R.; Yewdell, J. W.; Varma, R. Endogenous Viral Antigen Processing Generates Peptide-Specific MHC Class I Cell-Surface Clusters. *Proc. Natl. Acad. Sci.* **2012**, *109* (38), 15407–15412. <https://doi.org/10.1073/pnas.1208696109>.
- (169) Baía, D.; Pou, J.; Jones, D.; Mandelboim, O.; Trowsdale, J.; Muntasell, A.; López-Botet, M. Interaction of the LILRB1 Inhibitory Receptor with HLA Class Ia Dimers. *Eur. J. Immunol.* **2016**, *46* (7), 1681–1690. <https://doi.org/10.1002/eji.201546149>.
- (170) Blumenthal, D.; Edidin, M.; Gheber, L. A. Trafficking of MHC Molecules to the Cell Surface Creates Dynamic Protein Patches. *J. Cell Sci.* **2016**, jcs.187112. <https://doi.org/10.1242/jcs.187112>.
- (171) Armony, G.; Heck, A. J. R.; Wu, W. Extracellular Crosslinking Mass Spectrometry Reveals HLA Class I – HLA Class II Interactions on the Cell Surface. *Mol. Immunol.* **2021**, *136*, 16–25. <https://doi.org/10.1016/j.molimm.2021.05.010>.
- (172) Ferez, M.; Castro, M.; Alarcon, B.; van Santen, H. M. Cognate Peptide–MHC Complexes Are Expressed as Tightly Apposed Nanoclusters in Virus-Infected Cells To Allow TCR Crosslinking. *J. Immunol.* **2014**, *192* (1), 52–58. <https://doi.org/10.4049/jimmunol.1301224>.
- (173) Berman, H. M.; Westbrook, J.; Feng, Z.; Gilliland, G.; Bhat, T. N.; Weissig, H.; Shindyalov, I. N.; Bourne, P. E. The Protein Data Bank. *Nucleic Acids Res.* **2000**, *28* (1), 235–242. <https://doi.org/10.1093/nar/28.1.235>.
- (174) Saini, S. K.; Tamhane, T.; Anjanappa, R.; Saikia, A.; Ramskov, S.; Donia, M.; Svane, I. M.; Jakobsen, S. N.; Garcia-Alai, M.; Zacharias, M.; Meijers, R.; Springer, S.; Hadrup, S. R. Empty Peptide-Receptive MHC Class I Molecules for Efficient Detection of Antigen-Specific T Cells. *Sci Immunol* **2019**, *4* (37). <https://doi.org/10.1126/sciimmunol.aau9039>.
- (175) Thomas, C.; Tampé, R. MHC I Chaperone Complexes Shaping Immunity. *Curr. Opin. Immunol.* **2019**, *58*, 9–15. <https://doi.org/10.1016/j.coi.2019.01.001>.
- (176) Madden, D. R. The Three-Dimensional Structure of Peptide-MHC Complexes. *Annu Rev Immunol* **1995**, *13*, 587–622. <https://doi.org/10.1146/annurev.iy.13.040195.003103>.

- (177) Garrett, T. P.; Saper, M. A.; Bjorkman, P. J.; Strominger, J. L.; Wiley, D. C. Specificity Pockets for the Side Chains of Peptide Antigens in HLA-Aw68. *Nature* **1989**, *342* (6250), 692–696. <https://doi.org/10.1038/342692a0>.
- (178) Batalia, M. A.; Collins, E. J. Peptide Binding by Class I and Class II MHC Molecules. *Biopolymers* **1997**, *43* (4), 281–302. [https://doi.org/10.1002/\(SICI\)1097-0282\(1997\)43:4<281::AID-BIP3>3.0.CO;2-R](https://doi.org/10.1002/(SICI)1097-0282(1997)43:4<281::AID-BIP3>3.0.CO;2-R).
- (179) Hunt, D. F.; Henderson, R. A.; Shabanowitz, J.; Sakaguchi, K.; Michel, H.; Sevilir, N.; Cox, A. L.; Appella, E.; Engelhard, V. H. Characterization of Peptides Bound to the Class I MHC Molecule HLA-A2.1 by Mass Spectrometry. *Science* **1992**, *255* (5049), 1261–1263. <https://doi.org/10.1126/science.1546328>.
- (180) Guo, H.-C.; Jardetzky, T. S.; Garrett, T. P. J.; Lane, W. S.; Strominger, J. L.; Wiley, D. C. Different Length Peptides Bind to HLA-Aw68 Similarly at Their Ends but Bulge out in the Middle. *Nature* **1992**, *360* (6402), 364–366. <https://doi.org/10.1038/360364a0>.
- (181) Chen, Y.; Sidney, J.; Southwood, S.; Cox, A. L.; Sakaguchi, K.; Henderson, R. A.; Appella, E.; Hunt, D. F.; Sette, A.; Engelhard, V. H. Naturally Processed Peptides Longer than Nine Amino Acid Residues Bind to the Class I MHC Molecule HLA-A2.1 with High Affinity and in Different Conformations. *J. Immunol.* **1994**, *152* (6), 2874–2881. <https://doi.org/10.4049/jimmunol.152.6.2874>.
- (182) Urban, R. G.; Chiczy, R. M.; Lane, W. S.; Strominger, J. L.; Rehm, A.; Kenter, M. J.; UytdeHaag, F. G.; Ploegh, H.; Uchanska-Ziegler, B.; Ziegler, A. A Subset of HLA-B27 Molecules Contains Peptides Muchlonger than Nonamers. *Proc. Natl. Acad. Sci.* **1994**, *91* (4), 1534–1538. <https://doi.org/10.1073/pnas.91.4.1534>.
- (183) Tynan, F. E.; Borg, N. A.; Miles, J. J.; Beddoe, T.; El-Hassen, D.; Silins, S. L.; van Zuylen, W. J. M.; Purcell, A. W.; Kjer-Nielsen, L.; McCluskey, J.; Burrows, S. R.; Rossjohn, J. High Resolution Structures of Highly Bulged Viral Epitopes Bound to Major Histocompatibility Complex Class I. *J. Biol. Chem.* **2005**, *280* (25), 23900–23909. <https://doi.org/10.1074/jbc.M503060200>.
- (184) Trowitzsch, S.; Tampé, R. Multifunctional Chaperone and Quality Control Complexes in Adaptive Immunity. *Annu. Rev. Biophys.* **2020**, *49* (1), 135–161. <https://doi.org/10.1146/annurev-biophys-121219-081643>.
- (185) Thomas, C.; Tampé, R. MHC I Assembly and Peptide Editing — Chaperones, Clients, and Molecular Plasticity in Immunity. *Curr. Opin. Immunol.* **2021**, *70*, 48–56. <https://doi.org/10.1016/j.coi.2021.02.004>.
- (186) Williams, A. P.; Peh, C. A.; Purcell, A. W.; McCluskey, J.; Elliott, T. Optimization of the MHC Class I Peptide Cargo Is Dependent on Tapasin. *Immunity* **2002**, *16* (4), 509–520. [https://doi.org/10.1016/S1074-7613\(02\)00304-7](https://doi.org/10.1016/S1074-7613(02)00304-7).
- (187) Elliott, T.; Williams, A. The Optimization of Peptide Cargo Bound to MHC Class I Molecules by the Peptide-Loading Complex. *Immunol. Rev.* **2005**, *207* (1), 89–99. <https://doi.org/10.1111/j.0105-2896.2005.00311.x>.
- (188) Neerincx, A.; Boyle, L. H. Properties of the Tapasin Homologue TAPBPR. *Curr. Opin. Immunol.* **2017**, *46*, 97–102. <https://doi.org/10.1016/j.coi.2017.04.008>.
- (189) Fleischmann, G.; Fiset, O.; Thomas, C.; Wieneke, R.; Tumulka, F.; Schneeweiss, C.; Springer, S.; Schafer, L. V.; Tampe, R. Mechanistic Basis for Epitope Proofreading in the Peptide-Loading Complex. *J Immunol* **2015**, *195* (9), 4503–4513. <https://doi.org/10.4049/jimmunol.1501515>.
- (190) Blees, A.; Janulienė, D.; Hofmann, T.; Koller, N.; Schmidt, C.; Trowitzsch, S.; Moeller, A.; Tampé, R. Structure of the Human MHC-I Peptide-Loading Complex. *Nature* **2017**, *551* (7681), 525–528. <https://doi.org/10.1038/nature24627>.
- (191) Domnick, A.; Winter, C.; Sušac, L.; Hennecke, L.; Hensen, M.; Zitzmann, N.; Trowitzsch, S.; Thomas, C.; Tampé, R. Molecular Basis of MHC I Quality Control in the Peptide Loading Complex. *Nat. Commun.* **2022**, *13* (1), 4701. <https://doi.org/10.1038/s41467-022-32384-z>.
- (192) Hulpke, S.; Tampé, R. The MHC I Loading Complex: A Multitasking Machinery in Adaptive Immunity. *Trends Biochem. Sci.* **2013**, *38* (8), 412–420. <https://doi.org/10.1016/j.tibs.2013.06.003>.
- (193) Blum, J. S.; Wearsch, P. A.; Cresswell, P. Pathways of Antigen Processing. *Annu. Rev. Immunol.* **2013**, *31* (1), 443–473. <https://doi.org/10.1146/annurev-immunol-032712-095910>.
- (194) Sadasivan, B.; Lehner, P. J.; Ortmann, B.; Spies, T.; Cresswell, P. Roles for Calreticulin and a Novel Glycoprotein, Tapasin, in the Interaction of MHC Class I Molecules with TAP. *Immunity* **1996**, *5* (2), 103–114. [https://doi.org/10.1016/S1074-7613\(00\)80487-2](https://doi.org/10.1016/S1074-7613(00)80487-2).
- (195) Dong, G.; Wearsch, P. A.; Peaper, D. R.; Cresswell, P.; Reinisch, K. M. Insights into MHC Class I Peptide Loading from the Structure of the Tapasin-ERp57 Thiol Oxidoreductase Heterodimer. *Immunity* **2009**, *30* (1), 21–32. <https://doi.org/10.1016/j.immuni.2008.10.018>.
- (196) Chen, M.; Bouvier, M. Analysis of Interactions in a Tapasin/Class I Complex Provides a Mechanism for Peptide Selection. *EMBO J.* **2007**, *26* (6), 1681–1690. <https://doi.org/10.1038/sj.emboj.7601624>.
- (197) Praveen, P. V. K.; Yaneva, R.; Kalbacher, H.; Springer, S. Tapasin Edits Peptides on MHC Class I Molecules by Accelerating Peptide Exchange. *Eur. J. Immunol.* **2009**, *40* (1), 214–224. <https://doi.org/10.1002/eji.200939342>.
- (198) Ortmann, B.; Copeman, J.; Lehner, P. J.; Sadasivan, B.; Herberg, J. A.; Grandea, A. G.; Riddell, S. R.; Tampé, R.; Spies, T.; Trowsdale, J.; Cresswell, P. A Critical Role for Tapasin in the Assembly and Function of Multimeric MHC Class I-TAP Complexes. *Science* **1997**, *277* (5330), 1306–1309. <https://doi.org/10.1126/science.277.5330.1306>.
- (199) Abualrous, E. T.; Fritzsche, S.; Hein, Z.; Al-Balushi, M. S.; Reinink, P.; Boyle, L. H.; Wellbrock, U.; Antoniou, A. N.; Springer, S. F Pocket Flexibility Influences the Tapasin Dependence of Two Differentially Disease-Associated MHC Class I Proteins. *Eur J Immunol* **2015**, *45* (4), 1248–1257. <https://doi.org/10.1002/eji.201445307>.

- (200) Bouvier, M.; Wiley, D. C. Structural Characterization of a Soluble and Partially Folded Class I Major Histocompatibility Heavy Chain/B2m Heterodimer. *Nat. Struct. Biol.* **1998**, *5* (5), 377–384. <https://doi.org/10.1038/nsb0598-377>.
- (201) Springer, S.; Döring, K.; Skipper, J. C. A.; Townsend, A. R. M.; Cerundolo, V. Fast Association Rates Suggest a Conformational Change in the MHC Class I Molecule H-2D^b upon Peptide Binding. *Biochemistry* **1998**, *37* (9), 3001–3012. <https://doi.org/10.1021/bi9717441>.
- (202) Hansen, T. H.; Lybarger, L.; Yu, L.; Mitaksov, V.; Fremont, D. H. Recognition of Open Conformers of Classical MHC by Chaperones and Monoclonal Antibodies. *Immunol. Rev.* **2005**, *207* (1), 100–111. <https://doi.org/10.1111/j.0105-2896.2005.00315.x>.
- (203) Neefjes, J.; Jongasma, M. L. M.; Paul, P.; Bakke, O. Towards a Systems Understanding of MHC Class I and MHC Class II Antigen Presentation. *Nat. Rev. Immunol.* **2011**, *11* (12), 823–836. <https://doi.org/10.1038/nri3084>.
- (204) Hewitt, E. W. The MHC Class I Antigen Presentation Pathway: Strategies for Viral Immune Evasion. *Immunology* **2003**, *110* (2), 163–169. <https://doi.org/10.1046/j.1365-2567.2003.01738.x>.
- (205) Rock, K. L.; Reits, E.; Neefjes, J. Present Yourself! By MHC Class I and MHC Class II Molecules. *Trends Immunol.* **2016**, *37* (11), 724–737. <https://doi.org/10.1016/j.it.2016.08.010>.
- (206) Spiliotis, E. T.; Osorio, M.; Zúñiga, M. C.; Eddidin, M. Selective Export of MHC Class I Molecules from the ER after Their Dissociation from TAP. *Immunity* **2000**, *13* (6), 841–851. [https://doi.org/10.1016/S1074-7613\(00\)00081-9](https://doi.org/10.1016/S1074-7613(00)00081-9).
- (207) Szeto, C.; Lobos, C. A.; Nguyen, A. T.; Gras, S. TCR Recognition of Peptide–MHC-I: Rule Makers and Breakers. *Int. J. Mol. Sci.* **2020**, *22* (1), 68. <https://doi.org/10.3390/ijms22010068>.
- (208) Cole, D. K.; Laugel, B.; Clement, M.; Price, D. A.; Wooldridge, L.; Sewell, A. K. The Molecular Determinants of CD8 Co-Receptor Function. *Immunology* **2012**, *137* (2), 139–148. <https://doi.org/10.1111/j.1365-2567.2012.03625.x>.
- (209) Gao, G. F.; Tormo, J.; Gerth, U. C.; Wyer, J. R.; McMichael, A. J.; Stuart, D. I.; Bell, J. I.; Jones, E. Y.; Jakobsen, B. K. Crystal Structure of the Complex between Human CD8 $\alpha\alpha$ and HLA-A2. *Nature* **1997**, *387* (6633), 630–634. <https://doi.org/10.1038/42523>.
- (210) Leahy, D. J.; Axel, R.; Hendrickson, W. A. Crystal Structure of a Soluble Form of the Human T Cell Coreceptor CD8 at 2.6 Å Resolution. *Cell* **1992**, *68* (6), 1145–1162. [https://doi.org/10.1016/0092-8674\(92\)90085-Q](https://doi.org/10.1016/0092-8674(92)90085-Q).
- (211) Omilusik, K. D.; Goldrath, A. W. The Origins of Memory T Cells. *Nature* **2017**, *552* (7685), 337–339. <https://doi.org/10.1038/d41586-017-08280-8>.
- (212) Tunghland, B. Role of Gut Microbiota in Immune Homeostasis. In *Human Microbiota in Health and Disease*; Elsevier, 2018; pp 135–154. <https://doi.org/10.1016/B978-0-12-814649-1.00004-1>.
- (213) Farber, D. L.; Yudanin, N. A.; Restifo, N. P. Human Memory T Cells: Generation, Compartmentalization and Homeostasis. *Nat. Rev. Immunol.* **2014**, *14* (1), 24–35. <https://doi.org/10.1038/nri3567>.
- (214) Corran, P.; Griffith, E. *Guidelines for the Production and Quality Control of Synthetic Peptide Vaccines, Annex 1*; Technical Report Series; 48; World Health Organization: Geneva, Switzerland, 1999; pp 24–43.
- (215) Sidney, J.; Southwood, S.; Mann, D. L.; Fernandez-Vina, M. A.; Newman, M. J.; Sette, A. Majority of Peptides Binding HLA-A*0201 with High Affinity Crossreact with Other A2-Supertypes Molecules. *Hum Immunol* **2001**, *62* (11), 1200–1216. [https://doi.org/10.1016/s0198-8859\(01\)00319-6](https://doi.org/10.1016/s0198-8859(01)00319-6).
- (216) Bassani-Sternberg, M.; Coukos, G. Mass Spectrometry-Based Antigen Discovery for Cancer Immunotherapy. *Curr Opin Immunol* **2016**, *41*, 9–17. <https://doi.org/10.1016/j.coi.2016.04.005>.
- (217) Attermann, A. S.; Bjerregaard, A. M.; Saini, S. K.; Grønbaek, K.; Hadrup, S. R. Human Endogenous Retroviruses and Their Implication for Immunotherapeutics of Cancer. *Ann Oncol* **2018**, *29* (11), 2183–2191. <https://doi.org/10.1093/annonc/mdy413>.
- (218) Jurtz, V.; Paul, S.; Andreatta, M.; Marcatili, P.; Peters, B.; Nielsen, M. NetMHCpan-4.0: Improved Peptide-MHC Class I Interaction Predictions Integrating Eluted Ligand and Peptide Binding Affinity Data. *J Immunol* **2017**, *199* (9), 3360–3368. <https://doi.org/10.4049/jimmunol.1700893>.
- (219) Paul, S.; Kolla, R. V.; Sidney, J.; Weiskopf, D.; Fleri, W.; Kim, Y.; Peters, B.; Sette, A. Evaluating the Immunogenicity of Protein Drugs by Applying *In Vitro* MHC Binding Data and the Immune Epitope Database and Analysis Resource. *Clin. Dev. Immunol.* **2013**, *2013*, 1–7. <https://doi.org/10.1155/2013/467852>.
- (220) Lyngaa, R.; Pedersen, N. W.; Schrama, D.; Thruue, C. A.; Ibrani, D.; Met, Ö.; thor Straten, P.; Nghiem, P.; Becker, J. C.; Hadrup, S. R. T-Cell Responses to Oncogenic Merkel Cell Polyomavirus Proteins Distinguish Patients with Merkel Cell Carcinoma from Healthy Donors. *Clin. Cancer Res.* **2014**, *20* (7), 1768–1778. <https://doi.org/10.1158/1078-0432.CCR-13-2697>.
- (221) Saini, S. K.; Ostermeier, K.; Ramnarayan, V. R.; Schuster, H.; Zacharias, M.; Springer, S. Dipeptides Promote Folding and Peptide Binding of MHC Class I Molecules. *Proc Natl Acad Sci U S A* **2013**, *110* (38), 15383–15388. <https://doi.org/10.1073/pnas.1308672110>.
- (222) Hein, Z.; Uchtenhagen, H.; Abualrous, E. T.; Saini, S. K.; Janssen, L.; Van Hateren, A.; Wiek, C.; Hanenberg, H.; Momburg, F.; Achour, A.; Elliott, T.; Springer, S.; Boulanger, D. Peptide-Independent Stabilization of MHC Class I Molecules Breaches Cellular Quality Control. *J Cell Sci* **2014**, *127* (Pt 13), 2885–2897. <https://doi.org/10.1242/jcs.145334>.

- (223) Saini, S. K.; Schuster, H.; Ramnarayan, V. R.; Rammensee, H. G.; Stevanovic, S.; Springer, S. Dipeptides Catalyze Rapid Peptide Exchange on MHC Class I Molecules. *Proc Natl Acad Sci U A* **2015**, *112* (1), 202–207. <https://doi.org/10.1073/pnas.1418690112>.
- (224) Dirscherl, C.; Hein, Z.; Ramnarayan, V. R.; Jacob-Dolan, C.; Springer, S. A Two-Hybrid Antibody Micropattern Assay Reveals Specific in Cis Interactions of MHC I Heavy Chains at the Cell Surface. *Elife* **2018**, *7*. <https://doi.org/10.7554/eLife.34150>.
- (225) Schwarzenbacher, M.; Kaltenbrunner, M.; Brameshuber, M.; Hesch, C.; Paster, W.; Weghuber, J.; Heise, B.; Sonnleitner, A.; Stockinger, H.; Schütz, G. J. Micropatterning for Quantitative Analysis of Protein-Protein Interactions in Living Cells. *Nat. Methods* **2008**, *5* (12), 1053–1060. <https://doi.org/10.1038/nmeth.1268>.
- (226) Sevcsik, E.; Brameshuber, M.; Fölser, M.; Weghuber, J.; Honigsmann, A.; Schütz, G. J. GPI-Anchored Proteins Do Not Reside in Ordered Domains in the Live Cell Plasma Membrane. *Nat. Commun.* **2015**, *6* (1), 6969. <https://doi.org/10.1038/ncomms7969>.
- (227) Bahadur, R. P.; Zacharias, M. The Interface of Protein-Protein Complexes: Analysis of Contacts and Prediction of Interactions. *Cell. Mol. Life Sci.* **2008**, *65* (7–8), 1059–1072. <https://doi.org/10.1007/s00018-007-7451-x>.
- (228) Lin, W.-C.; Iversen, L.; Tu, H.-L.; Rhodes, C.; Christensen, S. M.; Iwig, J. S.; Hansen, S. D.; Huang, W. Y. C.; Groves, J. T. H-Ras Forms Dimers on Membrane Surfaces via a Protein–Protein Interface. *Proc. Natl. Acad. Sci.* **2014**, *111* (8), 2996–3001. <https://doi.org/10.1073/pnas.1321155111>.
- (229) Fooksman, D. R.; Grönvall, G. K.; Tang, Q.; Edidin, M. Clustering Class I MHC Modulates Sensitivity of T Cell Recognition. *J. Immunol.* **2006**, *176* (11), 6673–6680. <https://doi.org/10.4049/jimmunol.176.11.6673>.
- (230) Chen, B.; Li, J.; He, C.; Li, D.; Tong, W.; Zou, Y.; Xu, W. Role of HLA-B27 in the Pathogenesis of Ankylosing Spondylitis. *Mol. Med. Rep.* **2017**, *15* (4), 1943–1951. <https://doi.org/10.3892/mmr.2017.6248>.
- (231) Schell, T. D. The Assembly of Functional Beta2-Microglobulin-Free MHC Class I Molecules That Interact with Peptides and CD8+ T Lymphocytes. *Int. Immunol.* **2002**, *14* (7), 775–782. <https://doi.org/10.1093/intimm/14.7.775>.
- (232) Dulberger, C. L.; McMurtrey, C. P.; Hölzemer, A.; Neu, K. E.; Liu, V.; Steinbach, A. M.; Garcia-Beltran, W. F.; Sulak, M.; Jabri, B.; Lynch, V. J.; Altfeld, M.; Hildebrand, W. H.; Adams, E. J. Human Leukocyte Antigen F Presents Peptides and Regulates Immunity through Interactions with NK Cell Receptors. *Immunity* **2017**, *46* (6), 1018–1029.e7. <https://doi.org/10.1016/j.immuni.2017.06.002>.
- (233) Goodridge, J. P.; Lee, N.; Burian, A.; Pyo, C.-W.; Tykodi, S. S.; Warren, E. H.; Yee, C.; Riddell, S. R.; Geraghty, D. E. HLA-F and MHC-I Open Conformers Cooperate in a MHC-I Antigen Cross-Presentation Pathway. *J. Immunol.* **2013**, *191* (4), 1567–1577. <https://doi.org/10.4049/jimmunol.1300080>.
- (234) Mahmutefendić, H.; Blagojević, G.; Tomaš, M. I.; Kučić, N.; Lučin, P. Segregation of Open Major Histocompatibility Class I Conformers at the Plasma Membrane and during Endosomal Trafficking Reveals Conformation-Based Sorting in the Endosomal System. *Int. J. Biochem. Cell Biol.* **2011**, *43* (4), 504–515. <https://doi.org/10.1016/j.biocel.2010.12.002>.
- (235) Zacharias, M.; Springer, S. Conformational Flexibility of the MHC Class I Alpha1-Alpha2 Domain in Peptide Bound and Free States: A Molecular Dynamics Simulation Study. *Biophys J* **2004**, *87* (4), 2203–2214. <https://doi.org/10.1529/biophysj.104.044743>.
- (236) Mage, M. G.; Dolan, M. A.; Wang, R.; Boyd, L. F.; Revilla, M. J.; Robinson, H.; Natarajan, K.; Myers, N. B.; Hansen, T. H.; Margulies, D. H. A Structural and Molecular Dynamics Approach to Understanding the Peptide-Receptive Transition State of MHC-I Molecules. *Mol. Immunol.* **2013**, *55* (2), 123–125. <https://doi.org/10.1016/j.molimm.2012.10.021>.
- (237) Yaneva, R.; Schneeweiss, C.; Zacharias, M.; Springer, S. Peptide Binding to MHC Class I and II Proteins: New Avenues from New Methods. *Mol. Immunol.* **2010**, *47* (4), 649–657. <https://doi.org/10.1016/j.molimm.2009.10.008>.
- (238) Pettersen, E. F.; Goddard, T. D.; Huang, C. C.; Couch, G. S.; Greenblatt, D. M.; Meng, E. C.; Ferrin, T. E. UCSF Chimera—a Visualization System for Exploratory Research and Analysis. *J Comput Chem* **2004**, *25* (13), 1605–1612. <https://doi.org/10.1002/jcc.20084>.
- (239) Moritz, A.; Anjanappa, R.; Wagner, C.; Bunk, S.; Hofmann, M.; Pszolla, G.; Saikia, A.; Garcia-Alai, M.; Meijers, R.; Rammensee, H. G.; Springer, S.; Maurer, D. High-Throughput Peptide-MHC Complex Generation and Kinetic Screenings of TCRs with Peptide-Receptive HLA-A*02:01 Molecules. *Sci Immunol* **2019**, *4* (37). <https://doi.org/10.1126/sciimmunol.aav0860>.
- (240) Saini, S. K.; Abualrous, E. T.; Tigan, A. S.; Covella, K.; Wellbrock, U.; Springer, S. Not All Empty MHC Class I Molecules Are Molten Globules: Tryptophan Fluorescence Reveals a Two-Step Mechanism of Thermal Denaturation. *Mol Immunol* **2013**, *54* (3–4), 386–396. <https://doi.org/10.1016/j.molimm.2013.01.004>.
- (241) Keller, B. O.; Sui, J.; Young, A. B.; Whittall, R. M. Interferences and Contaminants Encountered in Modern Mass Spectrometry. *Anal Chim Acta* **2008**, *627* (1), 71–81. <https://doi.org/10.1016/j.aca.2008.04.043>.
- (242) McDonald, G. R.; Hudson, A. L.; Dunn, S. M.; You, H.; Baker, G. B.; Whittall, R. M.; Martin, J. W.; Jha, A.; Edmondson, D. E.; Holt, A. Bioactive Contaminants Leach from Disposable Laboratory Plasticware. *Science* **2008**, *322* (5903), 917. <https://doi.org/10.1126/science.1162395>.
- (243) Watson, J.; Greenough, E. B.; Leet, J. E.; Ford, M. J.; Drexler, D. M.; Belcastro, J. V.; Herbst, J. J.; Chatterjee, M.; Banks, M. Extraction, Identification, and Functional Characterization of a Bioactive Substance from Automated

- Compound-Handling Plastic Tips. *J Biomol Screen* **2009**, *14* (5), 566–572. <https://doi.org/10.1177/1087057109336594>.
- (244) Glithero, A.; Tormo, J.; Doering, K.; Kojima, M.; Jones, E. Y.; Elliott, T. The Crystal Structure of H-2Db Complexed with a Partial Peptide Epitope Suggests a Major Histocompatibility Complex Class I Assembly Intermediate. *J. Biol. Chem.* **2006**, *281* (18), 12699–12704. <https://doi.org/10.1074/jbc.M511683200>.
- (245) Garstka, M. A.; Fritzsche, S.; Lenart, I.; Hein, Z.; Jankevicius, G.; Boyle, L. H.; Elliott, T.; Trowsdale, J.; Antoniou, A. N.; Zacharias, M.; Springer, S. Tapasin Dependence of Major Histocompatibility Complex Class I Molecules Correlates with Their Conformational Flexibility. *FASEB J.* **2011**, *25* (11), 3989–3998. <https://doi.org/10.1096/fj.11-190249>.
- (246) Thomas, C.; Tampé, R. Structure of the TAPBPR–MHC I Complex Defines the Mechanism of Peptide Loading and Editing. *Science* **2017**, *358* (6366), 1060–1064. <https://doi.org/10.1126/science.aao6001>.
- (247) Jiang, J.; Natarajan, K.; Boyd, L. F.; Morozov, G. I.; Mage, M. G.; Margulies, D. H. Crystal Structure of a TAPBPR–MHC I Complex Reveals the Mechanism of Peptide Editing in Antigen Presentation. *Science* **2017**, *358* (6366), 1064–1068. <https://doi.org/10.1126/science.aao5154>.
- (248) Hafstrand, I.; Sayitoglu, E. C.; Apavaloaei, A.; Josey, B. J.; Sun, R.; Han, X.; Pellegrino, S.; Ozkazanc, D.; Potens, R.; Janssen, L.; Nilvebrant, J.; Nygren, P. A.; Sandalova, T.; Springer, S.; Georgoudaki, A. M.; Duru, A. D.; Achour, A. Successive Crystal Structure Snapshots Suggest the Basis for MHC Class I Peptide Loading and Editing by Tapasin. *Proc Natl Acad Sci U S A* **2019**, *116* (11), 5055–5060. <https://doi.org/10.1073/pnas.1807656116>.
- (249) Ostermeir, K.; Springer, S.; Zacharias, M. Coupling between Side Chain Interactions and Binding Pocket Flexibility in HLA-B*44:02 Molecules Investigated by Molecular Dynamics Simulations. *Mol Immunol* **2015**, *63* (2), 312–319. <https://doi.org/10.1016/j.molimm.2014.07.021>.
- (250) Shimizu, A.; Kawana-Tachikawa, A.; Yamagata, A.; Han, C.; Zhu, D.; Sato, Y.; Nakamura, H.; Koibuchi, T.; Carlson, J.; Martin, E.; Brumme, C. J.; Shi, Y.; Gao, G. F.; Brumme, Z. L.; Fukai, S.; Iwamoto, A. Structure of TCR and Antigen Complexes at an Immunodominant CTL Epitope in HIV-1 Infection. *Sci. Rep.* **2013**, *3* (1), 3097. <https://doi.org/10.1038/srep03097>.
- (251) Sun, X.; Shi, Y.; Akahoshi, T.; Fujiwara, M.; Gatanaga, H.; Schönbach, C.; Kuse, N.; Appay, V.; Gao, G. F.; Oka, S.; Takiguchi, M. Effects of a Single Escape Mutation on T Cell and HIV-1 Co-Adaptation. *Cell Rep.* **2016**, *15* (10), 2279–2291. <https://doi.org/10.1016/j.celrep.2016.05.017>.
- (252) Huang, E. C.; Pramanik, B. N.; Tsarbopoulos, A.; Reichert, P.; Ganguly, A. K.; Trotta, P. P.; Nagabhusan, T. L.; Covey, T. R. Application of Electrospray Mass Spectrometry in Probing Protein-Protein and Protein-Ligand Noncovalent Interactions. *J Am Soc Mass Spectrom* **1993**, *4* (8), 624–630. [https://doi.org/10.1016/1044-0305\(93\)85026-T](https://doi.org/10.1016/1044-0305(93)85026-T).
- (253) Zhang, S.; Van Pelt, C. K.; Wilson, D. B. Quantitative Determination of Noncovalent Binding Interactions Using Automated Nanoelectrospray Mass Spectrometry. *Anal Chem* **2003**, *75* (13), 3010–3018. <https://doi.org/10.1021/ac034089d>.
- (254) Yin, S.; Xie, Y.; Loo, J. A. Mass Spectrometry of Protein-Ligand Complexes: Enhanced Gas-Phase Stability of Ribonuclease-Nucleotide Complexes. *J Am Soc Mass Spectrom* **2008**, *19* (8), 1199–1208. <https://doi.org/10.1016/j.jasms.2008.05.012>.
- (255) Mehmood, S.; Allison, T. M.; Robinson, C. V. Mass Spectrometry of Protein Complexes: From Origins to Applications. *Annu Rev Phys Chem* **2015**, *66*, 453–474. <https://doi.org/10.1146/annurev-physchem-040214-121732>.
- (256) Stern, L. J.; Wiley, D. C. Antigenic Peptide Binding by Class I and Class II Histocompatibility Proteins. *Structure* **1994**, *2* (4), 245–251. [https://doi.org/10.1016/s0969-2126\(00\)00026-5](https://doi.org/10.1016/s0969-2126(00)00026-5).
- (257) Gras, S.; Saulquin, X.; Reiser, J. B.; Debeaupuis, E.; Echasserieau, K.; Kissenpfennig, A.; Legoux, F.; Chouquet, A.; Le Gorrec, M.; Machillot, P.; Neveu, B.; Thielens, N.; Malissen, B.; Bonneville, M.; Housset, D. Structural Bases for the Affinity-Driven Selection of a Public TCR against a Dominant Human Cytomegalovirus Epitope. *J Immunol* **2009**, *183* (1), 430–437. <https://doi.org/10.4049/jimmunol.0900556>.
- (258) Vita, R.; Mahajan, S.; Overton, J. A.; Dhanda, S. K.; Martini, S.; Cantrell, J. R.; Wheeler, D. K.; Sette, A.; Peters, B. The Immune Epitope Database (IEDB): 2018 Update. *Nucleic Acids Res.* **2019**, *47* (D1), D339–D343. <https://doi.org/10.1093/nar/gky1006>.
- (259) Williams, J. D.; Flanagan, M.; Lopez, L.; Fischer, S.; Miller, L. A. Using Accurate Mass Electrospray Ionization-Time-of-Flight Mass Spectrometry with in-Source Collision-Induced Dissociation to Sequence Peptide Mixtures. *J Chromatogr A* **2003**, *1020* (1), 11–26. <https://doi.org/10.1016/j.chroma.2003.07.019>.
- (260) Liu, J.; Konermann, L. Protein-Protein Binding Affinities in Solution Determined by Electrospray Mass Spectrometry. *J Am Soc Mass Spectrom* **2011**, *22* (3), 408–417. <https://doi.org/10.1007/s13361-010-0052-1>.
- (261) Niebling, S.; Burastero, O.; Burgi, J.; Gunther, C.; Defelipe, L. A.; Sander, S.; Gattkowsky, E.; Anjanappa, R.; Wilmanns, M.; Springer, S.; Tidow, H.; Garcia-Alai, M. FoldAffinity: Binding Affinities from NDSF Experiments. *Sci Rep* **2021**, *11* (1), 9572. <https://doi.org/10.1038/s41598-021-88985-z>.
- (262) Saikia, A.; Springer, S. Peptide-MHC I Complex Stability Measured by Nanoscale Differential Scanning Fluorimetry Reveals Molecular Mechanism of Thermal Denaturation. *Mol. Immunol.* **2021**, *136*, 73–81. <https://doi.org/10.1016/j.molimm.2021.04.028>.
- (263) Gautschi, M.; Just, S.; Mun, A.; Ross, S.; Rücknagel, P.; Dubaquié, Y.; Ehrenhofer-Murray, A.; Rospert, S. The Yeast N(Alpha)-Acetyltransferase NatA Is Quantitatively Anchored to the Ribosome and Interacts with Nascent

- Polypeptides. *Mol. Cell. Biol.* **2003**, 23 (20), 7403–7414. <https://doi.org/10.1128/MCB.23.20.7403-7414.2003>.
- (264) Arnesen, T. Towards a Functional Understanding of Protein N-Terminal Acetylation. *PLoS Biol.* **2011**, 9 (5), e1001074–e1001074. <https://doi.org/10.1371/journal.pbio.1001074>.
- (265) Matsumura, M.; Fremont, D. H.; Peterson, P. A.; Wilson, I. A. Emerging Principles for the Recognition of Peptide Antigens by MHC Class I Molecules. *Science* **1992**, 257 (5072), 927–934. <https://doi.org/10.1126/science.1323878>.
- (266) Gillanders, W. E.; Hanson, H. L.; Rubocki, R. J.; Hansen, T. H.; Connolly, J. M. Class I-Restricted Cytotoxic T Cell Recognition of Split Peptide Ligands. *Int. Immunol.* **1997**, 9 (1), 81–89. <https://doi.org/10.1093/intimm/9.1.81>.
- (267) Knapman, T. W.; Morton, V. L.; Stonehouse, N. J.; Stockley, P. G.; Ashcroft, A. E. Determining the Topology of Virus Assembly Intermediates Using Ion Mobility Spectrometry-Mass Spectrometry. *Rapid Commun. Mass Spectrom.* **2010**, 24 (20), 3033–3042. <https://doi.org/10.1002/rcm.4732>.
- (268) Falk, K.; Rötzschke, O.; Stevanović, S.; Jung, G.; Rammensee, H.-G. Allele-Specific Motifs Revealed by Sequencing of Self-Peptides Eluted from MHC Molecules. *Nature* **1991**, 351 (6324), 290–296. <https://doi.org/10.1038/351290a0>.
- (269) Parker, K. C.; Bednarek, M. A.; Hull, L. K.; Utz, U.; Cunningham, B.; Zweerink, H. J.; Biddison, W. E.; Coligan, J. E. Sequence Motifs Important for Peptide Binding to the Human MHC Class I Molecule, HLA-A2. *J. Immunol.* **1992**, 149 (11), 3580.
- (270) Parker, K. C.; Bednarek, M. A.; Coligan, J. E. Scheme for Ranking Potential HLA-A2 Binding Peptides Based on Independent Binding of Individual Peptide Side-Chains. *J. Immunol.* **1994**, 152 (1), 163.
- (271) Morita, D.; Yamamoto, Y.; Mizutani, T.; Ishikawa, T.; Suzuki, J.; Igarashi, T.; Mori, N.; Shiina, T.; Inoko, H.; Fujita, H.; Iwai, K.; Tanaka, Y.; Mikami, B.; Sugita, M. Crystal Structure of the N-Myristoylated Lipopeptide-Bound MHC Class I Complex. *Nat. Commun.* **2016**, 7 (1), 10356. <https://doi.org/10.1038/ncomms10356>.
- (272) Shima, Y.; Morita, D.; Mizutani, T.; Mori, N.; Mikami, B.; Sugita, M. Crystal Structures of Lysophospholipid-Bound MHC Class I Molecules. *J Biol Chem* **2020**. <https://doi.org/10.1074/jbc.RA119.011932>.
- (273) Kim, C. R.; Kim, H. S.; Choi, S. J.; Kim, J. K.; Gim, M. C.; Kim, Y. J.; Shin, D. H. Erucamide from Radish Leaves Has an Inhibitory Effect Against Acetylcholinesterase and Prevents Memory Deficit Induced by Trimethyltin. *J Med Food* **2018**, 21 (8), 769–776. <https://doi.org/10.1089/jmf.2017.4117>.
- (274) Tamilmani, E.; Radhakrishnan, R.; Sankaran, K. 13-Docosamide Release by Bacteria in Response to Glucose during Growth-Fluorescein Quenching and Clinical Application. *Appl Microbiol Biotechnol* **2018**, 102 (15), 6673–6685. <https://doi.org/10.1007/s00253-018-9127-x>.
- (275) Chaparro, R. J.; Burton, A. R.; Serreze, D. V.; Vignali, D. A. A.; DiLorenzo, T. P. Rapid Identification of MHC Class I-Restricted Antigens Relevant to Autoimmune Diabetes Using Retrogenic T Cells. *J. Immunol. Methods* **2008**, 335 (1–2), 106–115. <https://doi.org/10.1016/j.jim.2008.03.007>.
- (276) Harndahl, M.; Rasmussen, M.; Roder, G.; Buus, S. Real-Time, High-Throughput Measurements of Peptide–MHC-I Dissociation Using a Scintillation Proximity Assay. *J. Immunol. Methods* **2011**, 374 (1), 5–12. <https://doi.org/10.1016/j.jim.2010.10.012>.
- (277) Haj, A. K.; Breitbach, M. E.; Baker, D. A.; Mohns, M. S.; Moreno, G. K.; Wilson, N. A.; Lyamichev, V.; Patel, J.; Weisgrau, K. L.; Dudley, D. M.; O'Connor, D. H. High-Throughput Identification of MHC Class I Binding Peptides Using an Ultradense Peptide Array. *J. Immunol. Baltim. Md 1950* **2020**, 204 (6), 1689–1696. <https://doi.org/10.4049/jimmunol.1900889>.
- (278) Purcell, A. W.; McCluskey, J.; Rossjohn, J. More than One Reason to Rethink the Use of Peptides in Vaccine Design. *Nat. Rev. Drug Discov.* **2007**, 6 (5), 404–414. <https://doi.org/10.1038/nrd2224>.
- (279) Yang, H.; Kim, D. S. Chapter One - Peptide Immunotherapy in Vaccine Development: From Epitope to Adjuvant. In *Advances in Protein Chemistry and Structural Biology*; Donev, R., Ed.; Academic Press, 2015; Vol. 99, pp 1–14. <https://doi.org/10.1016/bs.apcsb.2015.03.001>.
- (280) Sun, T.; Han, H.; Hudalla, G. A.; Wen, Y.; Pompano, R. R.; Collier, J. H. Thermal Stability of Self-Assembled Peptide Vaccine Materials. *Acta Biomater* **2016**, 30, 62–71. <https://doi.org/10.1016/j.actbio.2015.11.019>.
- (281) Luimstra, J. J.; Franken, K. L. M. C.; Garstka, M. A.; Drijfhout, J. W.; Neefjes, J.; Ovaa, H. Production and Thermal Exchange of Conditional Peptide-MHC I Multimers. *Curr. Protoc. Immunol.* **2019**, 126 (1). <https://doi.org/10.1002/cpim.85>.
- (282) Falk, K.; Lau, J. M.; Santambrogio, L.; Esteban, V. M.; Puentes, F.; Rötzschke, O.; Strominger, J. L. Ligand Exchange of Major Histocompatibility Complex Class II Proteins Is Triggered by H-Bond Donor Groups of Small Molecules. *J. Biol. Chem.* **2002**, 277 (4), 2709–2715. <https://doi.org/10.1074/jbc.M109098200>.
- (283) Haderler, A.; Saikia, A.; Zacharias, M.; Springer, S. Rapid Peptide Exchange on MHC Class I by Small Molecules Elucidates Dynamics of Bound Peptide. *Curr. Res. Immunol.* **2022**, 3, 167–174. <https://doi.org/10.1016/j.crimmu.2022.08.002>.
- (284) Wang, R.-F.; Rosenberg, S. A. Human Tumor Antigens for Cancer Vaccine Development. *Immunol. Rev.* **1999**, 170 (1), 85–100. <https://doi.org/10.1111/j.1600-065X.1999.tb01331.x>.
- (285) Wang, R.; Doolan, D. L.; Le, T. P.; Hedstrom, R. C.; Coonan, K. M.; Charoenvit, Y.; Jones, T. R.; Hobart, P.; Margalith, M.; Ng, J.; Weiss, W. R.; Sedegah, M.; de Taisne, C.; A. Norman, J.; Hoffman, S. L. Induction of Antigen-Specific

- Cytotoxic T Lymphocytes in Humans by a Malaria DNA Vaccine. *Science* **1998**, 282 (5388), 476–480. <https://doi.org/10.1126/science.282.5388.476>.
- (286) Berzofsky, J. A.; Ahlers, J. D.; Derby, M. A.; Pendleton, C. D.; Arichi, T.; Belyakov, I. M. Approaches to Improve Engineered Vaccines for Human Immunodeficiency Virus and Other Viruses That Cause Chronic Infections. *Immunol. Rev.* **1999**, 170 (1), 151–172. <https://doi.org/10.1111/j.1600-065X.1999.tb01336.x>.
- (287) Gulukota, K.; DeLisi, C. HLA Allele Selection for Designing Peptide Vaccines. *Genet Anal* **1996**, 13 (3), 81–86. [https://doi.org/10.1016/1050-3862\(95\)00156-5](https://doi.org/10.1016/1050-3862(95)00156-5).
- (288) Larsen, M. V.; Lundegaard, C.; Lamberth, K.; Buus, S.; Brunak, S.; Lund, O.; Nielsen, M. An Integrative Approach to CTL Epitope Prediction: A Combined Algorithm Integrating MHC Class I Binding, TAP Transport Efficiency, and Proteasomal Cleavage Predictions. *Eur. J. Immunol.* **2005**, 35 (8), 2295–2303. <https://doi.org/10.1002/eji.200425811>.
- (289) Rammensee, H.-G.; Bachmann, J.; Emmerich, N. P. N.; Bachor, O. A.; Stevanović, S. SYFPEITHI: Database for MHC Ligands and Peptide Motifs. *Immunogenetics* **1999**, 50 (3–4), 213–219. <https://doi.org/10.1007/s002510050595>.
- (290) Saethang, T.; Hirose, O.; Kimkong, I.; Tran, V. A.; Dang, X. T.; Nguyen, L. A. T.; Le, T. K. T.; Kubo, M.; Yamada, Y.; Satou, K. EpicCapo: Epitope Prediction Using Combined Information of Amino Acid Pairwise Contact Potentials and HLA-Peptide Contact Site Information. *BMC Bioinformatics* **2012**, 13 (1), 313. <https://doi.org/10.1186/1471-2105-13-313>.
- (291) Sette, A.; Sidney, J.; del Guercio, M.-F.; Southwood, S.; Ruppert, J.; Dahlberg, C.; Grey, H. M.; Kubo, R. T. Peptide Binding to the Most Frequent HLA-A Class I Alleles Measured by Quantitative Molecular Binding Assays. *Mol. Immunol.* **1994**, 31 (11), 813–822. [https://doi.org/10.1016/0161-5890\(94\)90019-1](https://doi.org/10.1016/0161-5890(94)90019-1).
- (292) Nair, S. K.; Tomaras, G. D.; Sales, A. P.; Boczkowski, D.; Chan, C.; Plonk, K.; Cai, Y.; Dannull, J.; Kepler, T. B.; Pruitt, S. K.; Weinhold, K. J. High-Throughput Identification and Dendritic Cell-Based Functional Validation of MHC Class I-Restricted Mycobacterium Tuberculosis Epitopes. *Sci Rep* **2014**, 4, 4632. <https://doi.org/10.1038/srep04632>.
- (293) Zhang, G. L.; Ansari, H. R.; Bradley, P.; Cawley, G. C.; Hertz, T.; Hu, X.; Jojic, N.; Kim, Y.; Kohlbacher, O.; Lund, O.; Lundegaard, C.; Magaret, C. A.; Nielsen, M.; Papadopoulos, H.; Raghava, G. P. S.; Tal, V.-S.; Xue, L. C.; Yanover, C.; Zhu, S.; Rock, M. T.; Crowe, J. E.; Panayiotou, C.; Polycarpou, M. M.; Duch, W.; Brusica, V. Machine Learning Competition in Immunology – Prediction of HLA Class I Binding Peptides. *J. Immunol. Methods* **2011**, 374 (1–2), 1–4. <https://doi.org/10.1016/j.jim.2011.09.010>.
- (294) Trolle, T.; Metushi, I. G.; Greenbaum, J. A.; Kim, Y.; Sidney, J.; Lund, O.; Sette, A.; Peters, B.; Nielsen, M. Automated Benchmarking of Peptide-MHC Class I Binding Predictions. *Bioinformatics* **2015**, 31 (13), 2174–2181. <https://doi.org/10.1093/bioinformatics/btv123>.
- (295) Caron, E.; Kowalewski, Daniel J.; Chiek Koh, C.; Sturm, T.; Schuster, H.; Aebbersold, R. Analysis of Major Histocompatibility Complex (MHC) Immunopeptidomes Using Mass Spectrometry*. *Mol. Cell. Proteomics* **2015**, 14 (12), 3105–3117. <https://doi.org/10.1074/mcp.0115.052431>.
- (296) Gfeller, D.; Bassani-Sternberg, M. Predicting Antigen Presentation-What Could We Learn From a Million Peptides? *Front Immunol* **2018**, 9, 1716. <https://doi.org/10.3389/fimmu.2018.01716>.
- (297) Loo, R. R. O.; Goodlett, D. R.; Smith, R. D.; Loo, J. A. Observation of a Noncovalent Ribonuclease S-Protein/S-Peptide Complex by Electrospray Ionization Mass Spectrometry. *J. Am. Chem. Soc.* **1993**, 115 (10), 4391–4392. <https://doi.org/10.1021/ja00063a079>.
- (298) Lan, H.; Abualrous, E. T.; Sticht, J.; Fernandez, L. M. A.; Werk, T.; Weise, C.; Ballaschk, M.; Schmieder, P.; Loll, B.; Freund, C. Exchange Catalysis by Tapasin Exploits Conserved and Allele-Specific Features of MHC-I Molecules. *Nat. Commun.* **2021**, 12 (1), 4236. <https://doi.org/10.1038/s41467-021-24401-4>.
- (299) Sagert, L.; Hennig, F.; Thomas, C.; Tampé, R. A Loop Structure Allows TAPBPR to Exert Its Dual Function as MHC I Chaperone and Peptide Editor. *eLife* **2020**, 9, e55326. <https://doi.org/10.7554/eLife.55326>.
- (300) Van Pelt, C. K.; Zhang, S.; Fung, E.; Chu, I.; Liu, T.; Li, C.; Korfmacher, W. A.; Henion, J. A Fully Automated Nanoelectrospray Tandem Mass Spectrometric Method for Analysis of Caco-2 Samples. *Rapid Commun. Mass Spectrom.* **2003**, 17 (14), 1573–1578. <https://doi.org/10.1002/rcm.1087>.
- (301) Zhang, S.; Van Pelt, C. K.; Henion, J. D. Automated Chip-Based Nanoelectrospray-Mass Spectrometry for Rapid Identification of Proteins Separated by Two-Dimensional Gel Electrophoresis. *ELECTROPHORESIS* **2003**, 24 (21), 3620–3632. <https://doi.org/10.1002/elps.200305585>.
- (302) Santini, B. L.; Zacharias, M. Rapid Rational Design of Cyclic Peptides Mimicking Protein-Protein Interfaces. In *Computational Peptide Science*; Simonson, T., Ed.; Methods in Molecular Biology; Springer US: New York, NY, 2022; Vol. 2405, pp 231–244. https://doi.org/10.1007/978-1-0716-1855-4_12.
- (303) Lenci, E.; Trabocchi, A. Peptidomimetic Toolbox for Drug Discovery. *Chem. Soc. Rev.* **2020**, 49 (11), 3262–3277. <https://doi.org/10.1039/D0CS00102C>.
- (304) Mera, T.; Faustman, D. L. Removal of Donor Human Leukocyte Antigen Class I Proteins With Papain: Translation for Possible Whole Organ Practices. *Transplantation* **2015**, 99 (4), 724–730. <https://doi.org/10.1097/TP.0000000000000436>.
- (305) Storkus, W. J.; Zeh, H. J.; Salter, R. D.; Lotze, M. T. Identification of T-Cell Epitopes: Rapid Isolation of Class I-Presented Peptides from Viable Cells by Mild Acid Elution. *J. Immunother. Emphas. Tumor Immunol. Off. J. Soc. Biol. Ther.* **1993**, 14 (2), 94–103.

- (306) Torabi-Pour, N.; Nouri, A. M. E.; Saffie, R.; Oliver, R. T. D. Comparative Study between Direct Mild Acid Extraction and Immunobead Purification Technique for Isolation of HLA Class I-Associated Peptides. *Urol. Int.* **2002**, *68* (1), 38–43. <https://doi.org/10.1159/000048415>.
- (307) Sturm, T.; Sautter, B.; Wörner, T. P.; Stevanović, S.; Rammensee, H.-G.; Planz, O.; Heck, A. J. R.; Aebbersold, R. Mild Acid Elution and MHC Immunoaffinity Chromatography Reveal Similar Albeit Not Identical Profiles of the HLA Class I Immunopeptidome. *J. Proteome Res.* **2021**, *20* (1), 289–304. <https://doi.org/10.1021/acs.jproteome.0c00386>.
- (308) Hoffmeister, B. Mapping T Cell Epitopes by Flow Cytometry. *Methods* **2003**, *29* (3), 270–281. [https://doi.org/10.1016/S1046-2023\(02\)00349-3](https://doi.org/10.1016/S1046-2023(02)00349-3).
- (309) Andersen, R. S.; Kvistborg, P.; Frøsig, T. M.; Pedersen, N. W.; Lyngaa, R.; Bakker, A. H.; Shu, C. J.; Straten, P. thor; Schumacher, T. N.; Hadrup, S. R. Parallel Detection of Antigen-Specific T Cell Responses by Combinatorial Encoding of MHC Multimers. *Nat. Protoc.* **2012**, *7* (5), 891–902. <https://doi.org/10.1038/nprot.2012.037>.
- (310) Newell, E. W.; Sigal, N.; Nair, N.; Kidd, B. A.; Greenberg, H. B.; Davis, M. M. Combinatorial Tetramer Staining and Mass Cytometry Analysis Facilitate T-Cell Epitope Mapping and Characterization. *Nat. Biotechnol.* **2013**, *31* (7), 623–629. <https://doi.org/10.1038/nbt.2593>.
- (311) Cimen Bozkus, C.; Blazquez, A. B.; Enokida, T.; Bhardwaj, N. A T-Cell-Based Immunogenicity Protocol for Evaluating Human Antigen-Specific Responses. *STAR Protoc.* **2021**, *2* (3), 100758. <https://doi.org/10.1016/j.xpro.2021.100758>.
- (312) Bentzen, A. K.; Marquard, A. M.; Lyngaa, R.; Saini, S. K.; Ramskov, S.; Donia, M.; Such, L.; Furness, A. J. S.; McGranahan, N.; Rosenthal, R.; Straten, P. thor; Szallasi, Z.; Svane, I. M.; Swanton, C.; Quezada, S. A.; Jakobsen, S. N.; Eklund, A. C.; Hadrup, S. R. Large-Scale Detection of Antigen-Specific T Cells Using Peptide-MHC-I Multimers Labeled with DNA Barcodes. *Nat. Biotechnol.* **2016**, *34* (10), 1037–1045. <https://doi.org/10.1038/nbt.3662>.
- (313) Schachner, L. F.; Phung, W.; Han, G.; Darwish, M.; Bell, A.; Mellors, J. S.; Srzentic, K.; Huguet, R.; Blanchette, C.; Sandoval, W. High-Throughput, Quantitative Analysis of Peptide-Exchanged MHCI Complexes by Native Mass Spectrometry. *Anal. Chem.* **2022**, *acs.analchem.2c02423*. <https://doi.org/10.1021/acs.analchem.2c02423>.
- (314) van den Heuvel, R. H. H.; van Duijn, E.; Mazon, H.; Synowsky, S. A.; Lorenzen, K.; Versluis, C.; Brouns, S. J. J.; Langridge, D.; van der Oost, J.; Hoyes, J.; Heck, A. J. R. Improving the Performance of a Quadrupole Time-of-Flight Instrument for Macromolecular Mass Spectrometry. *Anal. Chem.* **2006**, *78* (21), 7473–7483. <https://doi.org/10.1021/ac061039a>.
- (315) Morgner, N.; Robinson, C. V. Mass Ign: An Assignment Strategy for Maximizing Information from the Mass Spectra of Heterogeneous Protein Assemblies. *Anal. Chem.* **2012**, *84* (6), 2939–2948. <https://doi.org/10.1021/ac300056a>.
- (316) Strohal, M.; Hassman, M.; Kosata, B.; Kodicek, M. MMass Data Miner: An Open Source Alternative for Mass Spectrometric Data Analysis. *Rapid Commun Mass Spectrom* **2008**, *22* (6), 905–908. <https://doi.org/10.1002/rcm.3444>.
- (317) McIlvaine, T. C. A BUFFER SOLUTION FOR COLORIMETRIC COMPARISON. *J. Biol. Chem.* **1921**, *49* (1), 183–186. [https://doi.org/10.1016/S0021-9258\(18\)86000-8](https://doi.org/10.1016/S0021-9258(18)86000-8).
- (318) Hunter, J. D. Matplotlib: A 2D Graphics Environment. *Comput. Sci. Eng.* **2007**, *9* (3), 90–95. <https://doi.org/10.1109/MCSE.2007.55>.
- (319) Caswell, T. A.; Droettboom, M.; Lee, A.; Hunter, J.; Firing, E.; Andrade, E. S. D.; Hoffmann, T.; Stansby, D.; Klymak, J.; Varoquaux, N.; Nielsen, J. H.; Root, B.; Elson, P.; May, R.; Dale, D.; Jae-Joon Lee; Seppänen, J. K.; McDougall, D.; Straw, A.; Hobson, P.; Gohlke, C.; Yu, T. S.; Ma, E.; Vincent, A. F.; Silvester, S.; Moad, C.; Kniazev, N.; Hannah; Ernest, E. *Matplotlib/Matplotlib: REL: V3.2.2*; Zenodo, 2020. <https://doi.org/10.5281/ZENODO.3898017>.
- (320) van Rossum, G. Python Tutorial. **1995**, No. R 9526.
- (321) Deutsch, E. W.; Csordas, A.; Sun, Z.; Jarnuczak, A.; Perez-Riverol, Y.; Ternent, T.; Campbell, D. S.; Bernal-Llinares, M.; Okuda, S.; Kawano, S.; Moritz, R. L.; Carver, J. J.; Wang, M.; Ishihama, Y.; Bandeira, N.; Hermjakob, H.; Vizcaíno, J. A. The ProteomeXchange Consortium in 2017: Supporting the Cultural Change in Proteomics Public Data Deposition. *Nucleic Acids Res.* **2017**, *45* (D1), D1100–D1106. <https://doi.org/10.1093/nar/gkw936>.
- (322) Perez-Riverol, Y.; Csordas, A.; Bai, J.; Bernal-Llinares, M.; Hewapathirana, S.; Kundu, D. J.; Inuganti, A.; Griss, J.; Mayer, G.; Eisenacher, M.; Pérez, E.; Uszkoreit, J.; Pfeuffer, J.; Sachsenberg, T.; Yilmaz, Ş.; Tiwary, S.; Cox, J.; Audain, E.; Walzer, M.; Jarnuczak, A. F.; Ternent, T.; Brazma, A.; Vizcaíno, J. A. The PRIDE Database and Related Tools and Resources in 2019: Improving Support for Quantification Data. *Nucleic Acids Res.* **2019**, *47* (D1), D442–D450. <https://doi.org/10.1093/nar/gky1106>.

Supplement

Supplemental figures

Parts of the following chapter have been published in:

Anjanappa, R., Garcia-Alai, M., **Kopicki, J. D.**, Lockhauserbäumer, J., Aboelmagd, M., Hinrichs, J., Nemtanu, I. M., Uetrecht, C., Zacharias, M., Springer, S., & Meijers, R. (2020). Structures of peptide-free and partially loaded MHC class I molecules reveal mechanisms of peptide selection. *Nature communications*, 11(1), 1314².

Reprinted from ANJANAPPA *et al.* (2020). Copyright © 2020, The Author(s).

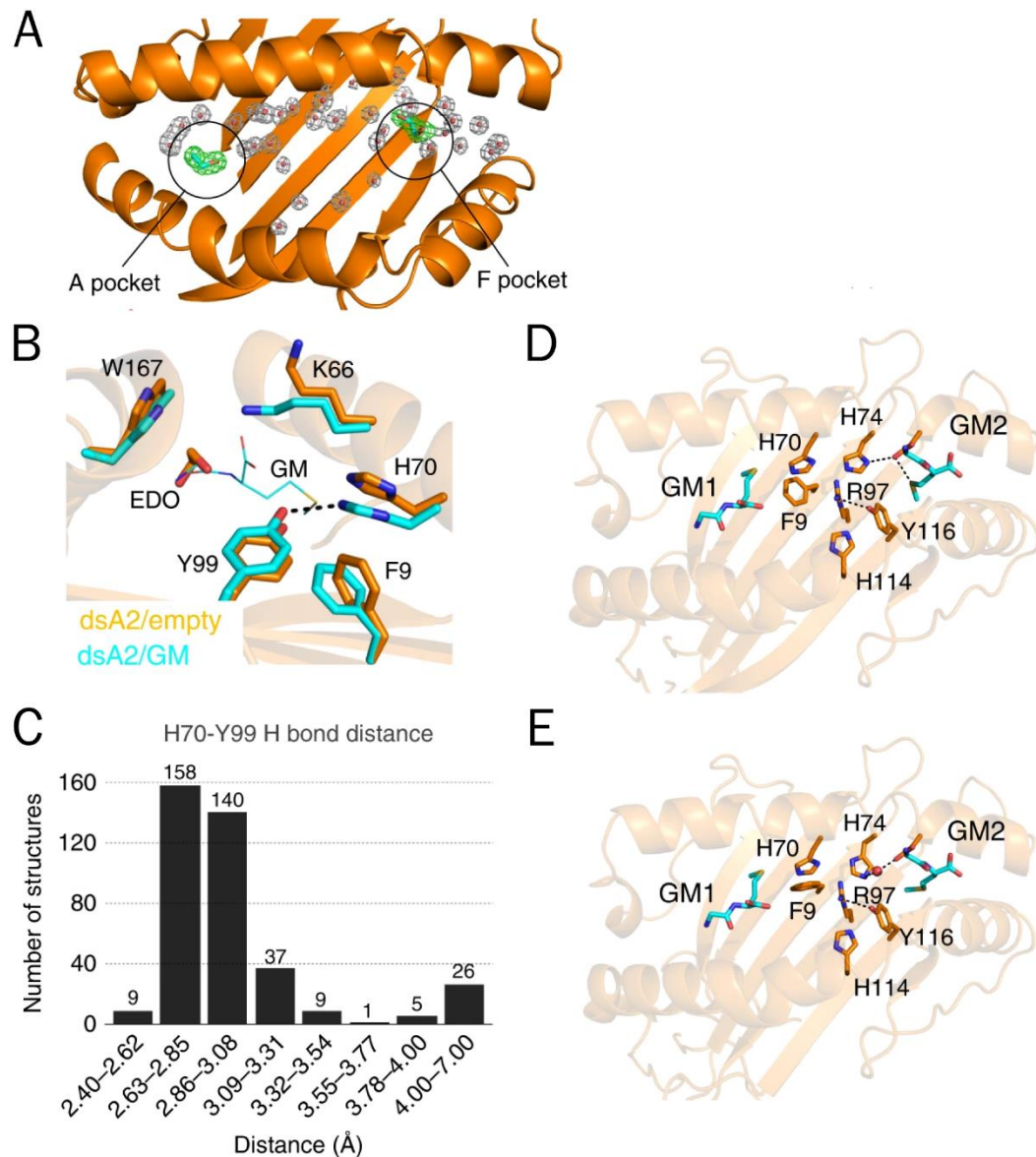


Figure 53 | The locked and unlocked states of the A and F pockets of A2.

A: Ribbon diagram of the dsA2_peptide_free-1 crystal structure, showing electron density from a $2mF_o-DF_c$ map for the water molecules (gray) and the EDO molecules (green) in the peptide-binding groove at a contour level of 1σ . **B:** Close-up of the A pocket in the locked (cyan, from the dsA2+GM structure) and the unlocked (gold, from the peptide-free structure) states. In the unlocked state, the hydrogen bond between Y99 and H70 is broken and the side chains of H70 and F9 move into the peptide-binding groove, whereas the side chain of Y99 moves downwards. **C:** Systematic analysis of the distance distribution between the OH group on Y99 and the closest nitrogen atom on the imidazole side chain of H70 for all peptide-loaded HLA-A*02:01 molecules observed in the PDB. The histogram shows that > 90% of the deposited structures contain a hydrogen bond between H70 and Y99. **D, E:** Two alternate hydrogen bond networks that are formed as a result of the presence of the methionine side chain in the F pocket are seen in each dsA2+GM+GM molecule. This leads to conformational changes in the side chains of residues H74 and F9.

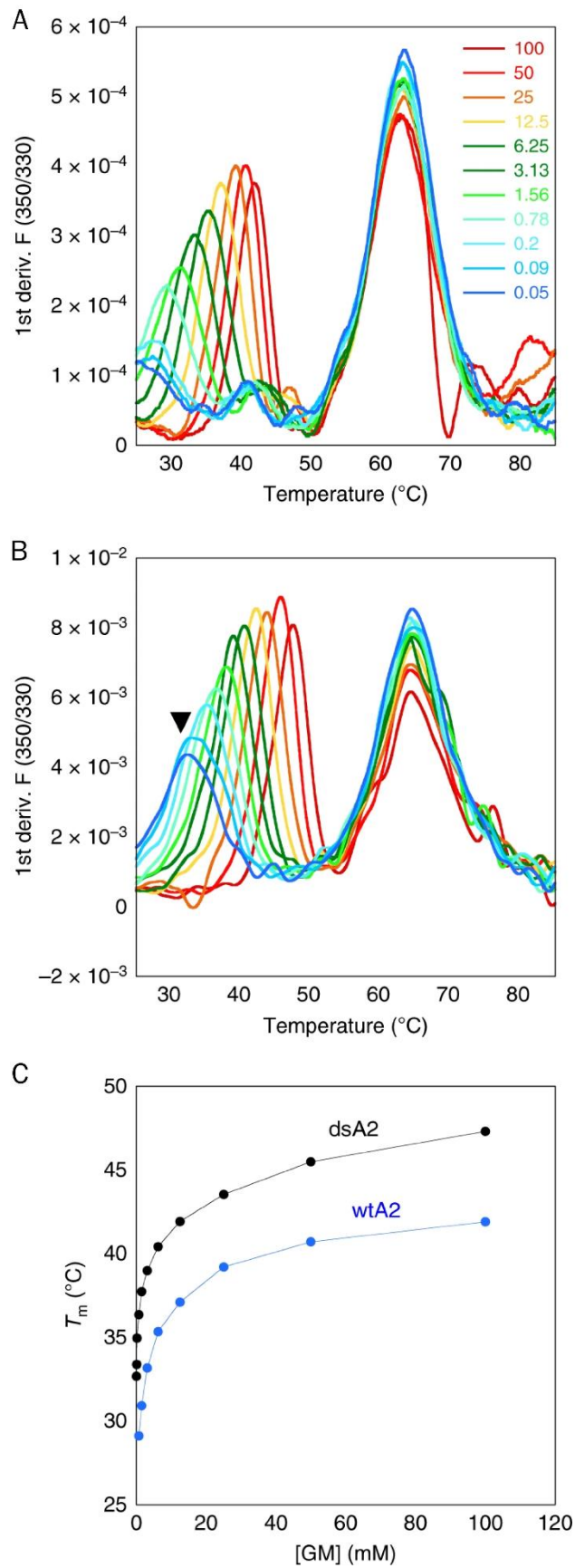


Figure 54 | dsA2 is stable at very low dipeptide concentrations.

Thermal denaturation of A2 in the presence of increasing concentrations of GM measured by nDSF (tryptophan fluorescence). **A, B:** First derivatives of the F_{350}/F_{330} (ratio of fluorescence emissions at 350 nm and 330 nm) curves for wtA2 and dsA2 with the maxima reporting the melting temperatures (T_m). The concentration of GM (in mM) is indicated in rainbow colors from red (maximum, 100 mM) to blue (minimum, 0.05 mM). The arrow points to the transition of the dsA2 heavy chain that is visible even at very low dipeptide concentration. **C:** Scatter plot of the T_m obtained for the A2 heavy chain (first unfolding event) as a function of GM concentration.

Supplemental tables

Table 7 | M_{exp} of the different α_3 domain protein species

The masses were determined from at least three independent MS measurements. They are listed together with the respective values for standard deviation (SD) along with the theoretically calculated M_{th} .

mass species	M_{th} (Da)	M_{exp} (Da) \pm SD (Da)
α_3 monomer	11,475	11,472.7 \pm 0.4
α_3 monomer _{short}	10,623	10,062.1 \pm 1
α_3 dimer	22,950	22,947 \pm 1
α_3 dimer _{short}	22,098	22,094 \pm 1

Table 8 | M_{exp} of the different wtA2 and dsA2 protein species.

The masses were determined from at least three independent MS measurements. They are listed together with the respective values for SD and average FWHM along with the theoretically calculated M_{th} . FWHM values are given for the whole peak area where individual species were not fully resolved. $\beta_2\text{m-M1}$ and A2-M1 represent $\beta_2\text{m}$ and A2 respectively, containing the N-terminal methionine.

	mass species	M_{th} (Da)	M_{exp} (Da) \pm SD (Da)	FWHM (Da) \pm SD (Da)
wtA2	$\beta_2\text{m-M1}$	11,731	11,729 \pm 1	2.4 \pm 0.5
	$\beta_2\text{m}$	11,862	11,860.0 \pm 0.5	2.1 \pm 0.4
	HC	31,808	31,799 \pm 4	7.3 \pm 0.7
	A2-M1	43,539	43,548 \pm 5	6.3 \pm 0.4
	A2	43,670	43,680 \pm 2	6 \pm 1
dsA2	A2+erucamide	44,009	44,017 \pm 4	20 \pm 10
	HC	33,977	33,971 \pm 2	7 \pm 4
	A2-M1	45,708	45,703 \pm 2	4.1 \pm 0.4
	A2	45,839	45,834 \pm 3	4 \pm 1
	A2+erucamide	46,178	46,172 \pm 2	11 \pm 7
	A2+NV9	46,782	46,778 \pm 1	4 \pm 1
	A2+NV9+NV9	47,725	47,723 \pm 3	8 \pm 4

Table 9 | AUC for the detected dsA2 mass species at different acceleration voltages.

The AUC is determined over the entire spectrum for the respective mass species at 10 V, 25 V and 50 V. The mean value of the AUC presence of the different peptides (protein-peptide ratio 1:5, 1:10:10 in dual peptide approach) from at least three independent measurements is listed together with their corresponding SD. "dsA2" corresponds to the empty HLA-A*02:01(Y84C/A139C) disulfide mutant complex, "dsA2+pep" to dsA2 bound to one peptide, "dsA2+pep+pep" to dsA2 bound to two molecules of this certain peptide, "dsA2+pep2" to dsA2 bound to another peptide when two different peptides were present, "dsA2+pep2+pep2" to dsA2 bound to two molecules of the second peptide, "dsA2+pep1+pep2" to dsA2 bound to one molecule of each of both peptides and "dsA2+erucamide" to dsA2 bound to the erucamide respectively. ¹NV9 – high affinity control, ²YF9 – low affinity control, ³GV9 – minimal binding motif, ⁴Ac-NV9 – modified N-terminus, ⁵Ac-NV9-NH₂ – modified N- and C-terminus, ⁶NV9-NH₂ – modified C-terminus.

peptide	acc. volt.	dsA2		dsA2+pep		dsA2+pep+pep		dsA2+pep2		dsA2+pep2+pep2		dsA2+pep1+pep2		dsA2+erucamide	
		AUC	SD	AUC	SD	AUC	SD	AUC	SD	AUC	SD	AUC	SD	AUC	SD
NV9 ¹	10 V	31%	2%	64%	3%	4%	4%							2%	2%
	25 V	28%	4%	64%	5%	7%	6%							0.5%	0.5%
	50 V	59%	5%	40%	4%	1%	2%							0%	0%
YF9 ²	10 V	56%	3%	4%	2%	0%	0%							39%	2%
	25 V	51%	4%	5%	2%	0%	0%							44%	3%
	50 V	95%	5%	5%	2%	0%	0%							2%	2%
GV9 ³	10 V	52%	2%	43%	2%	1.5%	0.4%							4.3%	0.6%
	25 V	50%	1%	43%	3%	2.2%	0.9%							5%	2%
	50 V	62%	3%	35%	3%	1.1%	0.3%							1.7%	0.2%
Ac-NV9 ⁴	10 V	24%	2%	63%	3%	11%	2%							2.1%	0.5%
	25 V	23%	2%	64%	1%	9%	1%							3%	2%
	50 V	33%	2%	57%	2%	8%	1%							1.7%	0.9%
Ac-NV9-NH ₂ ⁵	10 V	55%	2%	27.9%	0.5%	2.4%	0.6%							15%	1%
	25 V	57%	2%	28%	1%	1%	1%							14%	1%
	50 V	72%	3%	25%	3%	1%	1%							2.2%	0.4%
NV9-NH ₂ ⁶	10 V	36%	2%	59%	2%	5%	1%							0.4%	0.2%
	25 V	36%	2%	58%	2%	5%	1%							0.3%	0.3%
	50 V	61%	1%	38%	1%	1.6%	0.3%							0.1%	0.2%

Table 9 | continued.

peptide	acc. volt.	dsA2		dsA2+pep		dsA2+pep+pep		dsA2+pep2		dsA2+pep2+pep2		dsA2+pep1+pep2		dsA2+erucamide	
		AUC	SD	AUC	SD	AUC	SD	AUC	SD	AUC	SD	AUC	SD	AUC	SD
NP4	10 V	55%	2%	11%	1%	0.6%	0.2%							33.8%	0.6%
	25 V	57.8%	0.9%	10.4%	0.5%	0.69%	0.06%							31.1%	0.5%
	50 V	92.4%	0.5%	2.6%	0.1%	0.8%	0.1%							4.3%	0.3%
NM5	10 V	62%	2%	17.9%	0.6%	1.0%	0.2%							19%	1%
	25 V	64%	3%	18.0%	0.7%	1.2%	0.2%							17%	2%
	50 V	90.3%	0.6%	8.1%	0.3%	0.3%	0.6%							1.3%	0.1%
NV6	10 V	66%	1%	10%	2%	0.5%	0.1%							24%	1%
	25 V	66%	1%	11%	2%	0.69%	0.08%							22%	2%
	50 V	91.2%	0.5%	4.1%	0.8%	1.9%	0.3%							2.9%	0.4%
NA7	10 V	75%	3%	16%	2%	0.8%	0.3%							8%	1%
	25 V	68%	3%	19%	2%	1.4%	0.7%							11%	1%
	50 V	86%	4%	12%	3%	0.5%	0.5%							1.8%	0.2%
NT8	10 V	47.3%	0.9%	28%	1%	0.6%	0.5%							24%	1%
	25 V	50%	3%	28.2%	0.9%	1%	1%							21%	1%
	50 V	75%	2%	23%	1%	0.2%	0.3%							1.6%	0.3%
LV8	10 V	42%	6%	54%	5%	2.8%	0.3%							1.7%	0.9%
	25 V	40%	3%	54%	3%	3.9%	0.8%							1.5%	0.7%
	50 V	53%	2%	45%	2%	1.6%	0.2%							0.4%	0.4%
VV7	10 V	61.8%	0.5%	17%	2%	1.7%	0.3%							19%	3%
	25 V	62%	3%	17%	3%	1.16%	0.06%							20.2%	0.7%
	50 V	96%	3%	3%	2%	0%	0%							1.3%	0.6%
PV6	10 V	68%	6%	12%	2%	0.5%	0.6%							19%	3%
	25 V	68%	6%	13%	3%	0.5%	0.2%							19%	3%
	50 V	90%	3%	5%	1%	0.1%	0.1%							5%	1%
MV5	10 V	64%	3%	23%	2%	3.2%	0.7%							10.4%	0.2%
	25 V	63%	4%	23%	2%	3.7%	1.0%							10.4%	0.4%
	50 V	80%	3%	15%	2%	1.5%	0.6%							3.3%	0.3%
VV4	10 V	68%	1%	14%	1%	0%	0%							18.093%	0.007%
	25 V	68%	2%	14%	1%	0%	0%							17.6%	1.0%
	50 V	92%	1%	4.1%	1.0%	0%	0%							4.0%	0.4%

Table 9 | continued.

peptide	acc. volt.	dsA2		dsA2+pep		dsA2+pep+pep		dsA2+pep2		dsA2+pep2+pep2		dsA2+pep1+pep2		dsA2+erucamide	
		AUC	SD	AUC	SD	AUC	SD	AUC	SD	AUC	SD	AUC	SD	AUC	SD
AV9	10 V	57%	2%	39.9%	0.7%	2.1%	0.7%							1.2%	0.8%
	25 V	57%	4%	39%	2%	2.0%	0.9%							2%	2%
	50 V	80.0%	0.8%	17.77%	1.00%	1.2%	0.2%							1.0%	0.6%
GL9	10 V	32%	2%	62%	4%	3.8%	1.0%							2%	3%
	25 V	30%	3%	65%	3%	3.2%	1.0%							2%	1%
	50 V	40%	2%	56%	1%	2.3%	1.0%							1.0%	0.9%
LV9	10 V	12%	1%	68%	1%	19%	1%							0.9%	0.9%
	25 V	15%	2%	68%	1%	16%	1%							1.0%	0.5%
	50 V	32%	2%	55%	1%	13%	1%							0.5%	0.4%
FV9	10 V	20%	2%	78%	2%	2%	1%							0.9%	0.5%
	25 V	19%	2%	79%	3%	2%	1%							0.8%	0.4%
	50 V	22%	2%	75%	2%	2%	1%							0.7%	0.2%
YL9	10 V	40%	3%	52%	4%	7%	4%							0.91%	0.10%
	25 V	42%	4%	52%	2%	5%	2%							1.3%	0.2%
	50 V	74%	2%	23%	2%	2.6%	0.5%							0.8%	0.2%

Table 9 | continued.

peptide	acc. volt.	dsA2		dsA2+pep		dsA2+pep+pep		dsA2+pep2		dsA2+pep2+pep2		dsA2+pep1+pep2		dsA2+erucamide	
		AUC	SD	AUC	SD	AUC	SD	AUC	SD	AUC	SD	AUC	SD	AUC	SD
NP4 +	10 V	54%	2%	9%	3%	1.1%	0.5%	10%	1%	1.2%	1.0%	2.1%	0.5%	22%	4%
	25 V	56%	2%	8%	2%	0.5%	0.5%	10%	1%	0.7%	0.7%	1.6%	0.5%	22%	4%
	50 V	87%	2%	5%	1%	0%	0%	4.4%	0.6%	0%	0%	0%	0%	3.1%	0.4%
NP4 +	10 V	42.9%	0.9%	6%	2%	1.8%	0.3%	27%	1%	5.6%	0.3%	5.2%	0.8%	10%	1%
	25 V	43%	2%	5%	1%	1%	2%	27%	2%	6.4%	0.6%	5.3%	0.9%	10.5%	0.8%
MV5	50 V	76%	5%	3%	1%	0.5%	0.9%	14%	2%	1.9%	0.8%	1%	1%	1.8%	0.3%
	10 V	48%	3%	8%	1%	1.7%	0.3%	13%	2%	0.9%	0.8%	2.8%	0.2%	25%	2%
NP4 +	25 V	49%	1%	8.5%	0.6%	1.4%	0.2%	13.6%	0.5%	0.4%	0.7%	2.1%	0.1%	24.5%	0.9%
	50 V	90.8%	0.3%	3.0%	0.3%	0%	0%	3.5%	0.1%	0%	0%	0%	0%	2.5%	0.1%
NM5 +	10 V	56%	3%	13%	2%	1%	1%	8.9%	0.8%	0.5%	0.8%	1.8%	1.6%	18%	4%
	25 V	55.7%	0.7%	14.2%	0.9%	0%	0%	8.6%	0.4%	0%	0%	2.0%	1.9%	19%	2%
VV4	50 V	86%	4%	8%	1%	0%	0%	2.8%	1.0%	0%	0%	0%	0%	4%	2%
	10 V	46%	7%	8%	3%	5%	4%	20%	1%	4.9%	0.8%	6%	1%	9%	1%
NM5 +	25 V	51%	9%	6%	3%	3%	3%	20%	3%	4.5%	0.5%	5%	3%	9%	2%
	50 V	75%	7%	6%	5%	0%	0%	11.7%	0.4%	4%	2%	2%	2%	1%	1%
NM5 +	10 V	58%	2%	11.9%	0.6%	1%	2%	9%	2%	0%	0%	0.4%	0.7%	18%	1%
	25 V	60.3%	0.5%	12.0%	0.8%	1%	1%	8.9%	0.4%	0%	0%	0.4%	0.7%	17.3%	0.4%
PV6	50 V	91.1%	0.7%	5.6%	0.2%	0%	0%	2.4%	0.2%	0%	0%	0%	0%	0.9%	0.8%
	10 V	47%	8%	6%	1%	1%	0%	17%	4%	7%	4%	3%	0%	18%	1%
NV6 +	25 V	48%	4%	6%	0%	1%	2%	16%	2%	5%	1%	2%	1%	21%	3%
	50 V	81%	7%	3%	1%	0%	0%	7%	4%	2%	1%	0%	0%	7%	2%
NV6 +	10 V	47%	5%	8%	2%	4%	2%	21%	1%	6.5%	0.8%	3.0%	0.3%	10%	2%
	25 V	42%	8%	9%	3%	4%	2%	20%	3%	8%	2%	5%	3%	10.2%	0.8%
MV5	50 V	71%	5%	6%	2%	1%	1%	12.5%	0.9%	2.1%	0.7%	1.4%	0.6%	6%	1%

Table 10 | Apparent K_d for dsA2 and different peptides obtained by native MS and iDSF.

The K_d was calculated from the respective AUC values at 1.0 V acceleration voltage (protein-peptide ratio 1:5). $K_{d,high}$ is an affinity determined on the basis of a real experiment at a cone voltage of 150 V, while a theoretical cone voltage of 48 V is assumed for $K_{d,low}$ to correct for ion-source decay. $K_{d,iDSF}$ was derived by two independent measurements. Protein concentration is 2.2 μ M. For each ligand, a two-fold serial dilution series was prepared using eleven concentrations depending on their predicted or assumed K_d range. The listed SD for K_d was determined using common equations, which estimate the propagation of uncertainty. ¹NV9 – high affinity control, ²GV9 – minimal binding motif, ³Ac-NV9 – modified N-terminus, ⁴Ac-NV9-NH₂ – modified N- and C-terminus, ⁵NV9-NH₂ – modified C-terminus; * iDSF reaches its limits at affinities below 200 nm.

peptide	sequence	$K_{d,high}$		$K_{d,low}$		$K_{d,iDSF}$	
		K_d (μ M)	SD (μ M)	K_d (μ M)	SD (μ M)	K_d (μ M)	SD (μ M)
NV9 ¹	NLVPVATV	8	2	0.06	0.08	0.04*	0.01
GV9 ²	GLGGGGGV	35	2	0.5	0.2	0.36	0.06
Ac-NV9 ³		4.5	1.0	0.11	0.05	0.61	0.08
Ac-NV9-NH ₂ ⁴		80	7	7	3	4	1
NV9-NH ₂ ⁵		10	1	0.004	0.003	0.001*	0.001
NP4	NLVP	350	60	110	80	50	20
NM5	NLVP	180	30	15	6	11	3
NV6	NLVP	380	70	30	20	9	2
NA7	NLVP	210	40	1.6	0.7	3.6	0.5
NT8	NLVP	92	5	30	20	2.6	0.4
LV8	LVPMVATV	17	3	0.07	0.06	0.008*	0.005
VV7	VPMVATV	180	30	15	7	7.8	1.0
PV6	PMVATV	300	200	15	7	15	2
MV5	MVATV	110	10	3	1	1.6	0.2
VV4	VATV	270	30	13	5	50	20
AV9	ALFDIESKV	40	2	0.03	0.03		
GL9	GLYDMEHL	9	1	0.1	0.2		
LV9	LLFGYFVYV	0.9	0.2	0.02	0.03		
FV9	FLYDDNQRV	2.6	0.3	0.02	0.02		
YL9	YLLEMLMRL	14	3	0.020	0.008		
NP4+VV4				90	30		
NP4+MV5				11	3		
NP4+PV6				130	50		
NM5+VV4				50	20		
NM5+MV5				9	3		
NM5+PV6				50	10		
NV6+VV4				50	10		
NV6+MV5				13	4		

Table 11 | T_m for dsA2 and different peptides obtained by nDSF.

The T_m as well as the resulting SD for dsA2 in absence or presence of the different peptides was defined by at least two independent measurements. Protein concentration is 2 μM . ¹NV9 – high affinity control, ²VF9 – low affinity control, ³GV9 – minimal binding motif, ⁴Ac-NV9 – modified N-terminus, ⁵Ac-NV9-NH₂ – modified N-terminus, ⁶NV9-NH₂ – modified C-terminus.

peptide	0.2 μM		2 μM		20 μM		1 mM		2 mM	
	T_m ($^{\circ}\text{C}$)	SD ($^{\circ}\text{C}$)	T_m ($^{\circ}\text{C}$)	SD ($^{\circ}\text{C}$)	T_m ($^{\circ}\text{C}$)	SD ($^{\circ}\text{C}$)	T_m ($^{\circ}\text{C}$)	SD ($^{\circ}\text{C}$)	T_m ($^{\circ}\text{C}$)	SD ($^{\circ}\text{C}$)
empty	35.7	0.6								
NV9 ¹	35.8	0.8	58.96	0.07	59.1	0.1	60.698	0.007		
YF9 ²	36.1	0.8	36.1	0.8	36.2	0.8				
GV9 ³	36.4	0.6	38.8	0.4	42.1	0.2	47.6	0.1		
Ac-NV9 ⁴	36.6	0.7	39.6	0.6	43.2	0.6	48.420	0.001		
Ac-NV9-NH ₂ ⁵	36.0	0.8	36.6	0.4	38.4	0.3				
NV9-NH ₂ ⁶	36.0	0.9	46.9	0.2	50.3	0.3	55.53	0.04		
NP4	35.6	0.4	35.7	0.5	35.8	0.4	38.95	0.04	42.10	0.06
NM5	35.6	0.5	35.9	0.4	37.3	0.3	45.04	0.07	45.93	0.03
NV6	35.5	0.1	35.9	0.2	37.61	0.05	44.1	0.6	44.6	0.2
NA7	35.51	0.09	35.9	0.1	37.95	0.06	45.442	0.007		
NT8	35.5	0.1	36.02	0.09	38.78	0.02	46.89	0.02		
LV8	35.40	0.08	43.5	0.1	47.28	0.04	53.30	0.04		
VV7	35.5	0.1	35.7	0.2	37.0	0.1	42.29	0.01		
PV6	35.5	0.2	35.62	0.09	36.40	0.02	42.2	0.3	43.6	0.5
MV5	35.64	0.08	36.5	0.1	39.31	0.07	47.90	0.01	49.253	0.003
VV4	35.475	0.002	35.1	0.6	35.5	0.2	41.47	0.03	42.6	0.1
NP4+VV4							44.99	0.05	47.93	0.10
NP4+MV5							47.55	0.06	50.35	0.05
NP4+PV6							43.88	0.05	46.47	0.08
NM5+VV4							47.22	0.05	47.26	0.08
NM5+MV5							47.59	0.03	49.900	0.002
NM5+PV6							45.45	0.02	47.295	0.010

Exemplary experimental files

Q-Tof 2

Acquisition Experiment Report
File:d:\mass spec data\q-tof - janines data\mhc\20201120 - mhc - 10um alpha3 dimer fraction\201120 jdk009.raw
Header
Acquired File Name: 201120 JDK009
Acquired Date: 20-Nov-2020
Acquired Time: 15:18:40
Job Code:
Task Code:
User Name:
Laboratory Name:
Instrument: QTOF
Conditions:
Submitter:
SampleID:
Bottle Number:
Description: 20uM alpha3 monomer (dimer fraction), 10V (150V)
Instrument Calibration:
Calibration File:
Parameters
MS1 Static: None
MS1 Scanning: None
MS1 Scan Speed Compensation: None
MS2 Static: None
MS2 Scanning: None
MS2 Scan Speed Compensation: None
Calibration Time: 11:16
Calibration Date: 01/29/20
Coefficients
MS1 Static: None
MS2 Static: None
Function 1: None
Parameters for C:\MassLynx\Qtof\tuneexp.exp
Temperature Correction Is Disabled
TDC Gain Control 0.0
TDC Amp Edge Control 0.0
Using 4 GHz TDC NO
Using TTP 4 GHz TDC NO
Instrument Parameters - Function 1:
Polarity ES+
Calibration Dynamic 2
Capillary 1.45 1.45
Cone 150 162
Extractor 0 10
RF Lens 0.10 9.65
Source Temp (°C) 80 79
Desolvation Temp (°C) 20 1020
LM Resolution5.0
HM Resolution5.0
Collision Energy 10.0 9.6
Ion Energy 1.0
Steering 0.00 -1.09
Entrance 70.0 -70.6
Pre-filter 5.0 4.8
Transport 10.0 -11.4
Aperture2 15.0 -16.7
Acceleration 200 -199
Focus 0 -1
Tube Lens 80 -80
Offset1 -0.8 -68.1
Offset2 0.0 -70.3
Pusher 980 924

```
TOF (kV)      9.10  -9.29
Reflectron    35.00  2.05
Pusher Cycle Time (µs)  96
Pusher Frequency (Hz)  10416.6667
Multiplier    550  -552
MCP           1900  1908
Centroid Threshold  0.0
Min Points    2.0
Np Multiplier 0.70
Resolution    4000.0
Lock Mass     0.0000
Mass Window +/- 1.0000
Lteff         450.6400
Veff          9100.0000
              1.0000
TDC Start (mV) 700.0000
TDC Stop (mV) 42.0000
TDC Threshold 0.0000
Pirani Pressure(mbar) 2.77e0
Penning Pressure(mbar) 1.42e-4
Tof Penning Pressure(mbar) 6.89e-7
Function Parameters - Function 1 - TOF MSMS FUNCTION
Set Mass      1914.0
Start Mass    100.0
End Mass      10000.0
Start Time (mins) 0.0
End Time (mins) 0.0
Data Format    Continuum
Ion Mode      ES Mode
Polarity      Positive
Instrument Parameter Filename C:\MassLynx\lotte.PRO\ACQUDB\TOF_jh_2020.ipr
Scans To Sum  1000000
Scan Time (sec) 1.0
InterScan Time (sec) 0.1
Use Tune Page Collision Energy YES
Collision Energy (eV) 30.0
Use Tune Page Cone Voltage YES
Cone Voltage (V) 35.0
Function 1
Scans in function: 106
Cycle time (secs): 1.100
Scan duration (secs): 1.000
Inter Scan Delay (secs): 0.100
Start and End Time(mins): Always on
Ionization mode: ES+
Data type: Accurate Mass
Function type: TOF Daughter
Mass range: 100 to 10000
Collision Energy: 0.0
```

Q Exactive™ UHMR Hybrid Quadrupole Orbitrap™

```
20230207_01_10uMdsA21uMeachcoronamix #1 RT: 0.0134
Total Ion Current: 9584210.00
Scan Low Mass: 500.00
Scan High Mass: 15000.00
Scan Start Time (min): 0.01
Scan Number: 1
Base Peak Intensity: 436523.22
Base Peak Mass: 4556.91
Scan Mode: FTMS + p NSI Full ms2 1000.00@hcd50.00 [500.00-15000.00]
Q Exactive UHMR Orbitrap Data:
=====
Multiple Injection: ce:ace:ace:a
Multi Inject Info: IT=41;30;30
AGC: Off
Micro Scan Count: 5
Scan Segment:0
Scan Event: 0
```

```
Master Index:0
Charge State:0
Monoisotopic M/Z: 0.0000
Ion Injection Time (ms): 100.000
Max. Ion Time (ms): 5.00
FT Resolution (m/z=200): 17500
FT Resolution (m/z=400): 12500
MS2 Isolation Width: 0.00
MS2 Isolation Offset: 0.00
AGC Target: 1000000
HCD Energy: 50.00
Analyzer Temperature: 28.57
=== Mass Calibration: ===:
Conversion Parameter B: 67839294.1611
Conversion Parameter C: -6344750.9683
Temperature Comp. (ppm): -4.07
RF Comp. (ppm): 0.00
Space Charge Comp. (ppm): -0.48
Resolution Comp. (ppm): 0.13
Number of Lock Masses: 0
Lock Mass #1 (m/z): 0.0000
Lock Mass #2 (m/z): 0.0000
Lock Mass #3 (m/z): 0.0000
LM Search Window (ppm): 0.0
LM Search Window (mmu): 0.0
Number of LM Found: 0
Last Locking (sec): 0.0
LM m/z-Correction (ppm): 0.00
=== Ion Optics Settings: ===:
S-Lens RF Level: 200.00
S-Lens Voltage (V): 21.00
Skimmer Voltage (V): 15.00
Inject Flatapole Offset (V): 5.00
Bent Flatapole DC (V): 2.00
MP2 and MP3 RF (V): 900.00
Gate Lens Voltage (V): 1.80
C-Trap RF (V): 2950.0
==== Diagnostic Data: ====:
APD: On
Dynamic RT Shift (min): 0.00
Intens Comp Factor: 0.7997
Res. Dep. Intens: 1.000
CTCD NumF: 0
CTCD Comp: 1.000
CTCD ScScr: 0.000
RawOvFtT: 499346.6
LC FWHM parameter: 30.0
Rod: 0
PS Inj. Time (ms): 0.000
AGC PS Mode: 0
AGC PS Diag: 0
HCD Energy eV: 50.000
AGC Fill: 1.00
Injection t0:0.000
t0 FLP: 0.00
Access Id: 0
Analog Input 1 (V): 0.000
Analog Input 2 (V): 0.000
RF-Only: On
Extended Trapping: -1.000
Direct Mass: AIC Density Target (%): 0.00
Direct Mass: Manual Inject Time (ms): 0.00
==== Overall Status: ====:
Status: Instrument status Ok
Performance: Warn: Mass and eFT Calibrations - Posi...ion (pos) -
Overdue (2023-02-01 15:47)
===== Ion Source: =====:
Spray Voltage (V) 1468.4
Spray Current (ÅµA) 0.16
Spray Current std. dev. (ÅµA) 0.04
Capillary Temperature (Å°C) 50.39
```

```
Sheath gas flow rate          0.06
Aux gas flow rate             0.08
Sweep gas flow rate          0.00
Aux. Temperature (Å°C)       1.59
===== Ion Optics: =====:
Capillary Voltage (V)        -0.4
Bent Flatapole DC (V)        1.9
Inj Flatapole A DC (V)       -150.0
Inj Flatapole B DC (V)       -76.6
Trans Multipole DC (V)       0.2
HCD Multipole DC (V)         -54.7
Inj. Flat. RF Amp (V)        699.3
Inj. Flat. RF Freq (kHz)     514.430
Bent Flat. RF Amp (V)        938.1
Bent Flat. RF Freq (kHz)     1081.990
RF2 and RF3 Amp (V)         897.3
RF2 and RF3 Freq (kHz)      800.270
Inter Flatapole DC (V)       59.77
Quad Exit DC (V)            -20.12
C-Trap Entrance Lens DC (V)  1.16
C-Trap RF Amp (V)           2944.4
C-Trap RF Freq (kHz)        2.190
C-Trap RF Curr (A)          0.554
C-Trap Exit Lens DC (V)     -19.87
HCD Exit Lens DC (V)        34.76
===== Vacuum: =====:
Fore Vacuum Sensor (mbar)    1.75
High Vacuum Sensor (mbar)   3.30e-09
UHV Sensor (mbar)           3.68e-10
Source TMP Speed            1000.0
UHV TMP Speed               1000.0
===== Temperatures: =====:
Analyzer Temperature (Å°C)   28.66
Ambient Temperature (Å°C)    31.2
Ambient Humidity (%)         20.9
Source TMP Motor Temperature 50.0
Source TMP Bottom Temperatur 40.0
UHV TMP Motor Temperature (Å 51.0
IOS Heatsink Temp. (Å°C)    32.2
HVPS Peltier Temp. (Å°C)    37.22
Quad. Det. Temp. (Å°C)      34.25
===== Diagnostic Data: =====
Performance ld               0.664
Performance me               1427.285
Performance cy:              0.801
CTCD mV                      6.50
```

Hazardous substances according to the GHS

Table 12 | Overview of all hazardous substances used in this work.

All substances are listed along with their hazard pictograms as well as hazard and precautionary statements according to the Globally Harmonized System of Classification and Labelling of Chemicals (GHS). The information was retrieved from safety data sheets provided by respective manufacturers.



substance (CAS)	hazard pictogram	hazard statements	precautionary statements
2-mercaptoethanol (60-24-2)		<p>H301 + H331 Toxic if swallowed or if inhaled.</p> <p>H310 Fatal in contact with skin.</p> <p>H315 Causes skin irritation.</p> <p>H317 May cause an allergic skin reaction.</p> <p>H318 Causes serious eye damage.</p> <p>H361d Suspected of damaging the unborn child.</p> <p>H373 May cause damage to organs (Liver, Heart) through prolonged or repeated exposure if swallowed.</p> <p>H410 Very toxic to aquatic life with long lasting effects.</p>	<p>P273 Avoid release to the environment.</p> <p>P280 Wear protective gloves/protective clothing/eye protection/face protection.</p> <p>P301 + P310 IF SWALLOWED: Immediately call a POISON CENTER/doctor.</p> <p>P302 + P352 + P310 IF ON SKIN: Wash with plenty of water. Immediately call a POISON CENTER/doctor.</p> <p>P304 + P340 + P311 IF INHALED: Remove person to fresh air and keep comfortable for breathing. Call a POISON CENTER/doctor.</p> <p>P305 + P351 + P338 IF IN EYES: Rinse cautiously with water for several minutes. Remove contact lenses, if present and easy to do. Continue rinsing.</p>
acetic acid (64-19-7)		<p>H226 Flammable liquid and vapor.</p> <p>H314 Causes severe skin burns and eye damage.</p>	<p>P210 Keep away from heat, hot surfaces, sparks, open flames, and other ignition sources. No smoking.</p> <p>P280 Wear protective gloves/protective clothing/eye protection/face protection.</p> <p>P303+P361+P353 IF ON SKIN (or hair): Take off immediately all contaminated clothing. Rinse skin with water.</p> <p>P305+P351+P338+P310 IF IN EYES: Rinse cautiously with water for several minutes. Remove contact lenses, if present and easy to do. Continue rinsing. Immediately call a poison center/doctor.</p>

Table 12 | continued.


substance (CAS)	hazard pictogram	hazard statements	precautionary statements
ammonium acetate (631-61-8)		Not a hazardous substance or mixture according to Regulation (EC) No 1272/2008.	
ammonium hydroxide solution (1336-21-6)		<p>H314 Causes severe skin burns and eye damage.</p> <p>H335 May cause respiratory irritation.</p> <p>H410 Very toxic to aquatic life with long lasting effects.</p>	<p>P261 Avoid breathing dust/fume/gas/mist/vapors/spray.</p> <p>P271 Use only outdoors or in a well-ventilated area.</p> <p>P273 Avoid release to the environment.</p> <p>P280 Wear protective gloves/protective clothing/eye protection/face protection.</p> <p>P303+P361+P353 IF ON SKIN (or hair): Take off immediately all contaminated clothing. Rinse skin with water.</p> <p>P305+P351+P338 IF IN EYES: Rinse cautiously with water for several minutes. Remove contact lenses, if present and easy to do. Continue rinsing.</p>
arginine (74-79-3)		Not a hazardous substance or mixture according to Regulation (EC) No 1272/2008.	
bromophenol blue (115-39-9)		Not a hazardous substance or mixture according to Regulation (EC) No 1272/2008.	

Table 12 | continued.



substance (CAS)	hazard pictogram	hazard statements	precautionary statements
<p>cesium iodide (7789-17-5)</p>		<p>H361fd Suspected of damaging fertility. Suspected of damaging the unborn child.</p> <p>H400 Very toxic to aquatic life.</p>	<p>P201 Obtain special instructions before use.</p> <p>P202 Do not handle until all safety precautions have been read and understood.</p> <p>P273 Avoid release to the environment.</p> <p>P280 Wear protective gloves/protective clothing/eye protection/face protection.</p> <p>P308 + P313 IF exposed or concerned: Get medical advice/attention.</p> <p>P391 Collect spillage.</p>
<p>dithiothreitol, DTT (3483-12-3)</p>		<p>H302 Harmful if swallowed.</p> <p>H315 Causes skin irritation.</p> <p>H318 Causes serious eye damage.</p>	<p>P264 Wash skin thoroughly after handling.</p> <p>P270 Do not eat, drink or smoke when using this product.</p> <p>P280 Wear protective gloves/eye protection/face protection.</p> <p>P301 + P312 IF SWALLOWED: Call a POISON CENTER/doctor if you feel unwell.</p> <p>P302 + P352 IF ON SKIN: Wash with plenty of water.</p> <p>P305 + P351 + P338 IF IN EYES: Rinse cautiously with water for several minutes. Remove contact lenses, if present and easy to do. Continue rinsing.</p>

Table 12 | continued.



substance (CAS)	hazard pictogram	hazard statements	precautionary statements
ethylenediaminetetraacetic acid, EDTA (60-00-4)		H319 Causes serious eye irritation.	P264 Wash skin thoroughly after handling. P280 Wear eye protection/face protection. P305 + P351 + P338 IF IN EYES: Rinse cautiously with water for several minutes. Remove contact lenses, if present and easy to do. Continue rinsing. P337 + P313 If eye irritation persists: Get medical advice/attention.
glutathione, oxidized (27025-41-8)		Not a hazardous substance or mixture according to Regulation (EC) No 1272/2008.	
glutathione, reduced (70-18-8)		Not a hazardous substance or mixture according to Regulation (EC) No 1272/2008.	
glycerol (56-81-5)		Not a hazardous substance or mixture according to Regulation (EC) No 1272/2008.	
guanidine hydrochloride (50-01-1)		H302 + H332 Harmful if swallowed or if inhaled. H315 Causes skin irritation. H319 Causes serious eye irritation.	P261 Avoid breathing dust. P264 Wash skin thoroughly after handling. P301 + P312 IF SWALLOWED: Call a POISON CENTER/doctor if you feel unwell. P302 + P352 IF ON SKIN: Wash with plenty of water. P304 + P340 + P312 IF INHALED: Remove person to fresh air and keep comfortable for breathing. Call a POISON CENTER/doctor if you feel unwell. P305 + P351 + P338 IF IN EYES: Rinse cautiously with water for several minutes. Remove contact lenses, if present and easy to do. Continue rinsing.
HEPES (7365-45-9)		Not a hazardous substance or mixture according to Regulation (EC) No 1272/2008.	

Table 12 | continued.



substance (CAS)	hazard pictogram	hazard statements	precautionary statements
isopropyl- β -D-1-thiogalactopyranosid, IPTG (367-93-1)		H319 Causes serious eye irritation. H351 Suspected of causing cancer.	P281 Use personal protective equipment as required. P305 + P351 + P338 IF IN EYES: Rinse cautiously with water for several minutes. Remove contact lenses, if present and easy to do. Continue rinsing.
phenylmethylsulfonyl fluoride, PMSF (329-98-6)		H301 Toxic if swallowed. H314 Causes severe skin burns and eye damage.	P260 Do not breathe dusts or mists. P270 Do not eat, drink or smoke when using this product. P280 Wear protective gloves/protective clothing/eye protection/face protection. P303 + P361 + P353 IF ON SKIN (or hair): Take off immediately all contaminated clothing. Rinse skin with water. P304 + P340 + P310 IF INHALED: Remove person to fresh air and keep comfortable for breathing. Immediately call a POISON CENTER/doctor. P305 + P351 + P338 IF IN EYES: Rinse cautiously with water for several minutes. Remove contact lenses, if present and easy to do. Continue rinsing.
sodium chloride, NaCl (7647-14-5)		Not a hazardous substance or mixture according to Regulation (EC) No 1272/2008.	

Table 12 | continued.



substance (CAS)	hazard pictogram	hazard statements	precautionary statements
<p>sodium dodecyl sulfate, SDS (151-21-3)</p>		<p>H228 Flammable solid.</p> <p>H302 + H332 Harmful if swallowed or if inhaled.</p> <p>H315 Causes skin irritation.</p> <p>H318 Causes serious eye damage.</p> <p>H335 May cause respiratory irritation.</p> <p>H412 Harmful to aquatic life with long lasting effects.</p>	<p>P210 Keep away from heat, hot surfaces, sparks, open flames and other ignition sources. No smoking.</p> <p>P273 Avoid release to the environment.</p> <p>P280 Wear protective gloves/protective clothing/eye protection/face protection.</p> <p>P301 + P312 IF SWALLOWED: Call a POISON CENTER/doctor if you feel unwell.</p> <p>P304 + P340 + P312 IF INHALED: Remove person to fresh air and keep comfortable for breathing. Call a POISON CENTER/doctor if you feel unwell.</p> <p>P305 + P351 + P338 IF IN EYES: Rinse cautiously with water for several minutes. Remove contact lenses, if present and easy to do. Continue rinsing.</p>
<p>sucrose (57-50-1)</p>		<p>Not a hazardous substance or mixture according to Regulation (EC) No 1272/2008.</p>	
<p>tris(hydroxymethyl)aminomethane hydrochloride, Tris-HCl (1185-53-1)</p>		<p>Not a hazardous substance or mixture according to Regulation (EC) No 1272/2008.</p>	

Table 12 | continued.

substance (CAS)	hazard pictogram	hazard statements	precautionary statements
<p>Triton™ X-100 (9036-19-5)</p>		<p>H302 Harmful if swallowed.</p> <p>H315 Causes skin irritation.</p> <p>H318 Causes serious eye damage.</p> <p>H410 Very toxic to aquatic life with long lasting effects.</p>	<p>P264 Wash skin thoroughly after handling.</p> <p>P273 Avoid release to the environment.</p> <p>P280 Wear protective gloves/eye protection/face protection.</p> <p>P301 + P312 IF SWALLOWED: Call a POISON CENTER/doctor if you feel unwell.</p> <p>P302 + P352 IF ON SKIN: Wash with plenty of water.</p> <p>P305 + P351 + P338 IF IN EYES: Rinse cautiously with water for several minutes. Remove contact lenses, if present and easy to do. Continue rinsing.</p>
<p>urea (57-13-6)</p>	<p>Not a hazardous substance or mixture according to Regulation (EC) No 1272/2008.</p>		

Contributions

Data presented in this thesis results from highly collaborative work mainly together with the Springer lab (Constructor University Bremen). The data and results shown in this thesis are primarily based on native mass spectrometry experiments designed and performed by me (JDK). If not stated otherwise, the work (design, implementation, evaluation of the experiments, etc.) was carried out by me. In some respects, the work is complemented by results from my collaborators to support the research findings.

For the first part of the introduction (**Chapter 1.1**), a small section was taken from a review that I co-authored. For the second part of the introduction (**Chapter 1.2**), minor sections from the publications listed below, in which I was the main author or co-author, were adopted.

The following lists for each chapter which co-authors contributed to this work and to what extent.

Chapter 1.1 Structural mass spectrometry

Dülfer, J., Kádek, A., **Kopicki, J.-D.**, Krichel, B., & Uetrecht, C. (2019). Structural mass spectrometry goes viral. *Advances in virus research*, 105, 189–238. doi: 10.1016/bs.aivir.2019.07.003¹.

JD, AK, JDK and BK did literature research and wrote the manuscript. JD, AK, and CU revised and edited the manuscript.

Chapter 1.2 Immune regulation via the major histocompatibility complex

Anjanappa, R., Garcia-Alai, M., **Kopicki, J.-D.**, Lockhauserbäumer, J., Aboelmagd, M., Hinrichs, J., Nemtanu, I. M., Uetrecht, C., Zacharias, M., Springer, S., & Meijers, R. (2020). Structures of peptide-free and partially loaded MHC class I molecules reveal mechanisms of peptide selection. *Nature communications*, 11(1), 1314².

SS and RM wrote the manuscript with input from all authors.

Dirscherl, C., Löchte, S., Hein, Z., **Kopicki, J.-D.**, Harders, A. R., Linden, N., Karner, A., Preiner, J., Weghuber, J., Garcia-Alai, M., Uetrecht, C., Zacharias, M., Piehler, J., Lanzerstorfer, P., & Springer, S. (2022). Dissociation of β_2m from MHC class I triggers formation of noncovalent transient heavy chain dimers. *Journal of cell science*, 135(9), jcs259489³.

CD, SL, JDK, NL wrote the manuscript. MGA, CU, MZ, JPi, PL, and SS revised and edited the manuscript.

Kopicki, J.-D., Saikia, A., Niebling, S., Günther, C., Anjanappa, R., Garcia-Alai, M., Springer, S., & Uetrecht, C. (2022). Opening opportunities for K_d determination and screening of MHC peptide complexes. *Communications biology*, 5(1), 488⁴.

JDK wrote the manuscript. CU and SS revised and edited the manuscript.

Chapter 3.1 MHC-I heavy chains form noncovalent dimers in absence of β_2m

Dirscherl, C., Löchte, S., Hein, Z., **Kopicki, J.-D.**, Harders, A. R., Linden, N., Karner, A., Preiner, J., Weghuber, J., Garcia-Alai, M., Uetrecht, C., Zacharias, M., Piehler, J., Lanzerstorfer, P., & Springer, S. (2022). Dissociation of β_2m from MHC class I triggers formation of noncovalent transient heavy chain dimers. *Journal of cell science*, 135(9), jcs259489³.

JDK collected and analyzed all native mass spectrometry data. Protein production and other investigational work was executed by CD, SL, ZH, ARH, AK, JPr, MZ, and PL. CD, SL, JDK, NL wrote the manuscript. MGA, CU, MZ, JPi, PL, and SS revised and edited the manuscript.

Chapter 3.2 Peptide-free, disulfide-stabilized MHC-I molecules

Anjanappa, R., Garcia-Alai, M., **Kopicki, J.-D.**, Lockhauserbäumer, J., Aboelmagd, M., Hinrichs, J., Nemtanu, I. M., Uetrecht, C., Zacharias, M., Springer, S., & Meijers, R. (2020). Structures of peptide-free and partially loaded MHC class I molecules reveal mechanisms of peptide selection. *Nature communications*, 11(1), 1314².

JDK collected and analyzed all native mass spectrometry data. Protein production and other investigational work was executed by AR, MGA, MA, JH, IMN, MZ, and RM. SS and RM wrote the manuscript with input from all authors.

Chapter 3.3 MHC-I peptide binding

Kopicki, J.-D., Saikia, A., Niebling, S., Günther, C., Anjanappa, R., Garcia-Alai, M., Springer, S., & Uetrecht, C. (2022). Opening opportunities for K_d determination and screening of MHC peptide complexes. *Communications biology*, 5(1), 488⁴.

JDK collected and analyzed all native mass spectrometry data. Protein production and other investigational work was executed by AS, SN, CG, AR. JDK wrote the manuscript. CU and SS revised and edited the manuscript.

Chapter 3.4 Establishing a high-throughput peptide screening

Kopicki, J.-D., Springer, S., & Uetrecht, C. (in preparation).

Chapter 5 Materials and methods

Anjanappa, R., Garcia-Alai, M., **Kopicki, J.-D.**, Lockhauserbäumer, J., Aboelmagd, M., Hinrichs, J., Nemtanu, I. M., Uetrecht, C., Zacharias, M., Springer, S., & Meijers, R. (2020). Structures of peptide-free and partially loaded MHC class I molecules reveal mechanisms of peptide selection. *Nature communications*, 11(1), 1314².

SS and RM wrote the manuscript with input from all authors.

Dirscherl, C., Löchte, S., Hein, Z., **Kopicki, J.-D.**, Harders, A. R., Linden, N., Karner, A., Preiner, J., Weghuber, J., Garcia-Alai, M., Uetrecht, C., Zacharias, M., Piehler, J., Lanzerstorfer, P., & Springer, S. (2022). Dissociation of β_2m from MHC class I triggers formation of noncovalent transient heavy chain dimers. *Journal of cell science*, 135(9), jcs259489³.

CD, SL, JDK, NL wrote the manuscript. MGA, CU, MZ, JPi, PL, and SS revised and edited the manuscript.

Kopicki, J.-D., Saikia, A., Niebling, S., Günther, C., Anjanappa, R., Garcia-Alai, M., Springer, S., & Uetrecht, C. (2022). Opening opportunities for K_d determination and screening of MHC peptide complexes. *Communications biology*, 5(1), 488⁴.

JDK wrote the manuscript. CU and SS revised and edited the manuscript.

Acknowledgements

So now it's in sight – the real end of my chemistry studies. Honestly, I wouldn't do it again, it was really exhausting and retrospectively I could have achieved much more, in much shorter time and especially with much less effort, but well, I never really had any other plan. When I was just able to write and started to sign friendship books, there was a clear policy for the field "When I grow up, I'm going to be ...": a researcher! Sometimes it was undefined, sometimes it said marine biologist, sometimes paleontologist (Jurassic Park was still quite new), but sometimes I actually wrote virologist. I wish I still had a photo of that, it would be super funny for this very moment. Meanwhile I've become something of a virologist myself – yeah ok, this dissertation here doesn't even involve viral proteins, but after now seven years in the "Dynamics of Viral Structures" group I kind of count myself as one too. After all, there are a few viral peptides in my work. Actually, my PhD, like my master's thesis before, was supposed to be about Ebola virus capsid assembly, but that didn't work out fast enough and then the MHC project came around the corner and suddenly I could easily collect one cool result after the other. I definitely want to thank **Sebastian** for that. I am glad that I was allowed to become a part of your MHC research. I love working with dsA2. Everyone here is always envious of how beautifully the proteins fly. Thanks for the great ideas and thanks also to your team for producing the protein and all the measurements that complement my work. In this context, I would also like to thank **all the collaboration partners** for making it possible to publish my own data. Many thanks also to my student **Luca** for helping me with some of the screening measurements.

Thank you, **Charlotte**, for taking me in as a little master's student and not kicking me out right after. Thank you also for always being kind and understanding when I had a tough time. I learned so much (mass spectrometry had been only a small incomprehensible part of the annoying spectro lecture for me before and there were no more associations) and besides I had by far the best time of my academic life working for you. I clearly owe that to all my AG77 homies. **Johannes**, you were a great tutor for my master thesis. **Boris**, come back to our WhatsApp group, we miss you a lot! **Alan**, no matter what you were asked, you always had a smart tip and were willing to help – that's what we miss! **Jasmin**, my soulmate, thank you for proofreading, but thank you especially for being such a nice colleague, happy to do business with you again, 10/10. **Ronja**, my real work-wifey, congratulations for winning the race – never had any doubts about it, but in the end, you really made it exciting again. Thanks for cheering me up with a cake or two when I was feeling down. **Kira**, thanks to you, after a long injury break, I was able to play soccer in a jersey again. That was super cool, but now I'd rather stay with roller derby. Don't lose your spirit and keep doing your

boomer dad jokes! Speaking of boomers: **Jürgen**, thanks for sticking with us a little longer. We need you. **Alice**, on behalf of the animals, thank you for becoming vegan and for farming all your bad karma on Twitter instead. **Lennart**, you are just the funniest person in the world, thank you for that. In my heart, you've had a permanent office desk for a long time. **Lars**, thank you for every ich_iel meme and all the lovely conversations. Lok'tar ogar! **Marius**, even though you haven't even been around that long, it's like I've known you forever. Thanks for every Wednesday scream and every obscene picture under my mouse. Thanks to the **whole AG77 crew!**

All dear friends out there, thank you for giving me stress-free time away from work and worries. **Mama and Papa**, I don't know what you had in mind for me, but I think it's pretty decent. I never felt like you guys ever doubted me in terms of my academic career, so thanks for that and thanks for every cent that helped to make this possible. **Gina**, the last few years you've grown into such a wonderful person, and we understand each other better than ever. Thank you for that. **Pierre**, you too have been a part of my academic career since school days. Every high, every low, you were there and always loved me. Thank you for that. By now I've learned so much and can explain many things of our world to you, but *why* derivatives work the way they do, I still don't know. Stay tuned!

Declaration of authorship | Eidesstattliche Versicherung

I hereby declare, on oath, that I have written the present dissertation by my own and have not used other than the acknowledged resources and aids. The submitted written document corresponds to the file on the electronic storage medium. I further declare that this thesis has not been presented previously to another examination board.

Hiermit versichere ich an Eides statt, die vorliegende Dissertation selbst verfasst und keine anderen als die angegebenen Hilfsmittel benutzt zu haben. Die eingereichte schriftliche Fassung entspricht der auf dem elektronischen Speichermedium. Ich versichere, dass diese Dissertation nicht in einem früheren Promotionsverfahren eingereicht wurde

20.03.2023

